Pushing the Boundaries of Condensed Matter Electron Momentum Spectroscopy

A thesis submitted for the degree
of Doctor of Philosophy of
the Australian National University

Cameron M. A. Bowles

March, 2008

This thesis contains no material which has been accepted for the award of any other degree or diploma in any university. To the best of the author's knowledge and belief, it contains no material previously published or written by another person, except where due reference is made in the text.

Cameron M. A. Bowles
March, 2008

Contents

Acknowledgements

A doctoral project never completes itself, nor can it be completed without support from a wide range of people. From professional guidance and help from supervisors and technicians to the support of loved ones, so many people play some part in its completion.

Foremost I would like to acknowledge and thank the support of my supervisor Dr Maarten Vos, without his guidance and input the project would never have gotten off the ground. A sincere thankyou to my laboratory mate Dr Michael Went, who taught me so much about breaking down large problems into simple logical steps, and provided a good deal of feedback and advice about those small problems that happen daily in the laboratory. A warm thankyou to Dr Anotoli Kheifets for his time and patience in explaining a lot of the theoretical aspects used in his calculations.

With the building of any new experimental equipment there is always glitches and problems that seem insurmountable. I was fortunate enough to work with a wonderful technician Graeme Cornish, who always had an answer to any problem. His help in the design and building of the spin polarised electron source was absolutely invaluable.

There were many family and friends who supported me not only throughout the last 4 years but also to get me to where I am today. A special thanks to my mother and step father, my father and my pseudo-parents Ron and Kaye Baldock. To all my friends that are to numerous to mention, who have kept me sane throughout my academic journey I cant thankyou all enough.

Abstract

An electron momentum spectrometer at the Australian National University has been used to study various aspects of different solid state systems. EMS is a transmission mode technique and involves the collision of the incident electron with a bound electron, after which both electrons are ejected and measured in coincidence. Through well defined reaction kinematics the complete valence spectral momentum density ($A(\varepsilon, \mathbf{q})$) can be measured . The spectrometer has been used to measure the spectral momentum densities (spectral functions) of single crystal targets, as well as targets in disordered states. A new spin polarised electron source was constructed and implemented in the ANU spectrometer, which was used to measure spin dependent features of ferromagnetic samples.

This thesis is divided into seven chapters, the first chapter is an introduction into the field of electron momentum spectroscopy, highlighting what has been measured before and how the technique has progressed to its present state. Some comparisons to other experimental techniques will be made.

The second chapter describes the ANU EMS spectrometer in detail. The technique requires some technical and advanced equipment that is often used in novel ways. The production of thin (20 nm) free standing targets will be detailed, along with the experimental chamber and electronics used to run the apparatus and collect data. The determination of the energy and momentum resolution of the experiment is also described.

The third chapter will detail the design and construction of the new spin polarised

electron source. The results of commissioning and characterizing the new source will be presented.

Chapters four through six will present the measured results. The fourth chapter will detail the single crystalline measurements for the group eleven noble metals (Cu, Ag and Au). Each sample was measured along three high symmetry directions and compared to a DFT calculation using the LDA and a FP-LMTO basis. The fifth chapter will include the results from samples that were in disordered states, a measurement which is unique to the EMS technique. The polycrystalline and amorphous states of the Si and Ge semiconductors are presented and conclusions are made to the degree of difference in the results and to which theoretical approach to the unique amorphous state of the semiconductors best matches the EMS results. The sixth chapter includes results of ferromagnetic iron, measured using the spin polarised electron source. The spectrometer was used to measure spin-polarised electron-energy-loss-spectroscopy (SPEELS) and magnetic electron-Compton profiles. A theoretical investigation is also presented in chapter six which details the advancements required in the spin polarised electron gun to measure an accurate spin-polarised EMS spectra of a ferromagnetic Fe sample.

Chapter 7 includes the summary of all the results presented and conclusions reached from the comparison of the measured EMS spectra and various theoretical calculations. A discussion is presented about the future directions and possibilities of the EMS technique.

Glossary of Abbreviations

The following tables contain a majority of the abbreviations and variables used throughout this thesis. It is intended for readers to have a quick point of reference, to avoid the need to unnecessarily repeat definitions throughout the text.

abbrev.	definition	abbrev.	definition
(e,2e)	electron interaction, 1 incident, 2 emitted electrons	FWHM	full-width-half-maximum
		HV	high voltage
(p,2p)	proton interaction, 1 incident, 2 emitted protons	IPA	independent particle approximation
		LCR	liquid crystal retarder
amC/a-C	amorphous carbon	LDA	local density approximation
ANU	Australian National University	linear-DOS	linear density of states
AREDC	angular-resolved energy-distribution -curve	LSDA	local spin density approximation
		MCP	micro-channel plate
ARPES	angular-resolved photoemission spectroscopy	MFP	mean free path
		NEA	negative electron affinity
au	atomic units	PSD	position sensitive detector
BCC	body-centred cubic	PWIA	plane wave impulse approximation
BZ	Brillouin zone	QE	quantum efficiency
CFD	constant fraction discriminator	RAE	resistive anode encoder
CP	Compton profile	RGA	residual gas analyser
CRN	continuous random network	RMS	root-mean-squared
DAQ	data acquisition card	SCCD	self-consistent charge density
DFT	density functional theory	SIC	self interaction correction
DOS	density of states	SMD	spectral-momentum density
EELS	electron-energy-loss spectroscopy	SPEELS	spin-polarised electron-energy-loss spectroscopy
EMS	electron momentum spectroscopy		
eV	electron volt	SPEMS	spin-polarised electron momentum spectroscopy
FCC	face-centred cubic		
FESEM	field-emission scanning-electron -microscope	TAC	time to amplitude convertor
		UHV	ultra high vacuum
FP-LMTO	full-potential linear-muffin-tin-orbital	XPS	x-ray photoemission spectroscopy

Variable	Definition
$A(\varepsilon,\mathbf{q})$	spectral momentum density
$e_{0,1,2}$	the incident and outgoing electrons
$E_{0,1,2}$	energy of incident and outgoing electrons
ε	binding energy of bound electron
$\varepsilon(\mathbf{q})$	band dispersion
$f(\mathbf{k}_0,\mathbf{k}_1,\mathbf{k}_1)$	scattering amplitude function
f_{ee}	spin-averaged Mott-scattering cross section
$\mathbf{G}$	the reciprocal-space lattice vector
$\Gamma-\mathbf{X}$	the 100 direction from a FCC sample in momentum space
$\Gamma-\mathbf{K}$	the 110 direction from a FCC sample in momentum space
$\Gamma-\mathbf{L}$	the 111 direction from a FCC sample in momentum space
$\Gamma-\mathbf{H}$	the 100 direction from a BCC sample in momentum space
$\Gamma-\mathbf{N}$	the 110 direction from a BCC sample in momentum space
$\Gamma-\mathbf{P}$	the 111 direction from a BCC sample in momentum space
$I(q_x,q_y)$	the momentum profile as measured by positron annihilation
$J(q_z)$	the Compton profile
$\mathbf{k}_{0,1,2}$	momentum of incoming and outgoing electrons
K	momentum transfer from incident electron to ejected electron
$\mathbf{p}$	momentum of residual target ion
$\mathbf{q}$	momentum of bound electron an instant before collision
$\rho(\mathbf{q})$	momentum distribution
$\mathrm{S}(\vartheta)$	Sherman function
$S(E_s,\mathbf{p}_s)$	the solid target
$S^+(E_s,\mathbf{p}_s)$	the residual ion
T	transition matrix element
θ	polar angle of outgoing electrons in xz plane (44.3^o)
$\phi_{1,2}$	azimuthal angles of 2 outgoing electrons in yz plane
$\phi_i(\mathbf{q})$	momentum space one-electron wavefunction of electron in orbital i

Chapter 1

Introduction

Electron momentum spectroscopy (EMS) is a vital experimental technique for understanding and determining the physical and electronic properties of all states of matter. Through simple electronic collisions the binding energy and/or momentum of the bound electrons in atoms, molecules and solids can be determined. This is of fundamental interest as electrons determine the physical properties of atoms, molecules and, the subject of this thesis, solids. By being able to experimentally probe these states, knowledge is acquired about many-body systems that are impossible to exactly solve theoretically. This means the experimental observations provide a database of information to which theorists can test their latest approximations.

With non-coincidence techniques the information measured is either restricted to one variable or a projection which is integrated over two axes, like differences in energy levels (Auger spectroscopy), momentum profiles (Compton scattering) or energy loss profiles (electron energy loss spectroscopy). With coincidence techniques more than one degree of information can be measured, normally at the cost of detection efficiency and increased complexity of the experiment. In EMS, the energy and momentum of the bound electrons are determined by simple conservation equations and given the correct geometrical configuration of the experiment the relative band density can also be measured. Thus EMS is a unique experimental tool that can determine all facets of the electronic structure in many-body systems.

1.1 Electron Momentum Spectroscopy

EMS is a kinematically-complete ionisation experiment, meaning the energy and momentum of all particles involved are known. EMS is an experiment where high energy incident electrons impinge upon a thin solid film colliding with a bound electron from the solid system which results in the bound electron being ejected and the incident electron being scattered. The two outgoing electrons are detected in coincidence to ensure they resulted from the same ionisation event, and through conservation of energy and momentum;

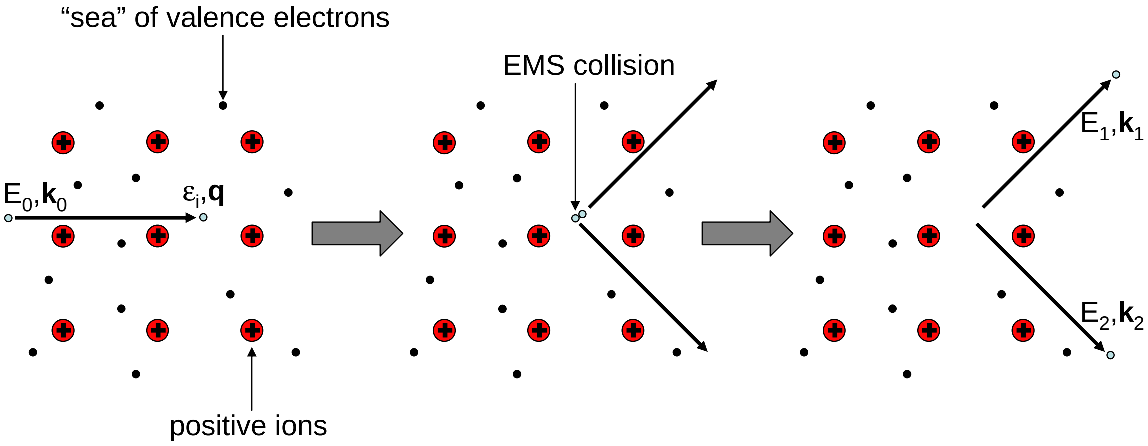

Figure 1.1: schematic diagram of an (e,2e) collision in a metallic solid.

$$\begin{aligned} \varepsilon_i &= E_0 - E_1 - E_2, \\ \mathbf{p} = -\mathbf{q} &= \mathbf{k}_0 - \mathbf{k}_1 - \mathbf{k}_2, \end{aligned} \tag{1.1}$$

we can determine the electronic state of the solid, which is equal to the binding energy (ε) of the ejected electron, and the momentum ($\mathbf{q}$) of the bound electron prior to collision. The incident electron energy (E_0) and momentum ($\mathbf{k}_0$) are defined by the electron beam and the two outgoing electron’s energy (E_1, E_2) and momentum ($\mathbf{k}_1, \mathbf{k}_2$) which can be measured. Hence the only unknowns in the conservation of energy and momentum equations (Eq. 1.1) are the binding energy (ε) and the momentum the ejected electron had an instant before the collision took place ($\mathbf{q}$), which is the opposite of the recoil momentum ($\mathbf{p}$) of the target.

$$\mathbf{q} = -\mathbf{p}. \tag{1.2}$$

It is shown later that the collision between the incoming and bound electron is essentially a clean binary collision, where the two electrons can be treated as plane waves and the target solid does not affect the EMS collision. The clean binary collision infers that the recoil momentum of the target is equal and opposite to the momentum the ejected electron had before impact. Through many EMS collisions the energy-momentum resolved electron density of a sample can be measured, otherwise referred to as the spectral momentum density (SMD). It will be shown later that the differential cross section of the EMS interaction is directly proportional to the spectral momentum density of the target ($A(\varepsilon_i, \mathbf{q})$).

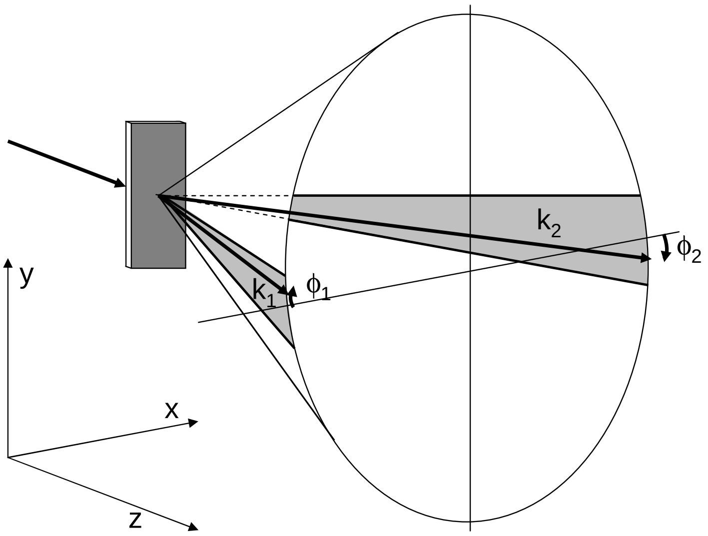

Figure 1.2: The EMS geometry, showing the subtended cone of the outgoing electrons, the shaded areas are where the two detectors are positioned. The incident electron travels in the z-direction, and for coincidences the two shaded components of the cone correspond to a zero recoil momentum of the residual ion along the x, and z axes. Thus the measured recoil momentum component is along the y-axis.

For the ANU EMS spectrometer the range of outgoing electrons that are measured are shown in Fig. 1.2 by the shaded surface areas of the subtending cone. The ANU spectrometer is designed for a 50 keV incoming electron beam ($\mathbf{k}_0$ = 62.07 au, where 1 atomic unit of momentum (au) is equivalent to the inverse of the Bohr radius, 1.89 Å^{-1}). The high energy outgoing electrons (25 keV) mean that the angle of the outgoing subtended cone is corrected for relativistic effects from 90° to 88.6°. Two outgoing electrons in these shaded regions (Fig. 1.2) that originate from the same EMS event are symmetrically scattered (E_1 = E_2 = 0.5 E_0). This geometry minimises the effect of multiple scattering by maximising the energy of the outgoing electrons which increases the average distance that the electron can travel through the sample before undergoing a secondary collision (mean free path). The two shaded areas of the conical surface represent the limited range over which the two detectors measure. The advantage of measuring over this limited range is that the change of momentum in the x-direction and z-direction (1.2) of each measured EMS event is zero;

$$\begin{aligned}
\mathbf{p}_x &= |\mathbf{k}_1|\sin\theta\cos\phi_1 + |\mathbf{k}_2|\sin(-\theta)\cos\phi_2 \\
&\approx |\mathbf{k}_1|\sin\theta - |\mathbf{k}_2|\sin\theta \qquad \text{as } \cos\phi_1 \approx \cos\phi_2 \approx 1 \\
&\approx 0 \qquad \text{as } |\mathbf{k}_1| \approx |\mathbf{k}_2| \qquad (1.3) \\
\mathbf{p}_z &= |\mathbf{k}_1|\cos\theta\cos\phi_1 + |\mathbf{k}_2|\cos(-\theta)\cos\phi_2 \\
&\approx |\mathbf{k}_1|\cos\theta + |\mathbf{k}_2|\cos\theta \\
&\approx 2|\mathbf{k}_1|\cos\theta = 62.07 \text{ au} = |\mathbf{k}_0|. \qquad (1.4)
\end{aligned}$$

Where θ is the angle between the incident electron vector and the outgoing electron vector (44.3°). As $\mathbf{k}_1 \approx \mathbf{k}_2 \approx 43.38$ au it follows from equations 1.3 and 1.4 that the total outgoing momentum in the x and z directions is equal to the total incoming momentum in those directions. So $\Delta\mathbf{p}_{x,z}$ for an EMS interaction with two outgoing electrons measured along the shaded surface areas of the cone is zero. So the only momentum measured is the difference of momenta in the y-direction, which enables the ANU EMS spectrometer to measure along single crystal directions.

$$\mathbf{p}_y = \mathbf{k}_1 \sin\phi + \mathbf{k}_2 \sin(-\phi) \approx \mathbf{k}_1(\phi_1 - \phi_2). \qquad (1.5)$$

Another feature of EMS is that it measures the real momentum of the bound electron rather than the crystal momentum, and hence does not require long range order in the target solid. This enables EMS to measure electronic band structures of ordered (crystalline) as well as disordered (amorphous, polycrystalline) samples, a feature which the more common photonic equivalent, angular-resolved photoemission spectroscopy (ARPES), does not possess.

1.2 EMS History

EMS was first conceptualised in the 1960's and was developed in analogy to the nuclear physics reaction of (p,2p), in which an incident proton scatters from and ejects another proton from the nucleus. Theoretical investigation by Neudachin *et. al.* [1], in 1969, into the EMS experiment concluded that "interpretation is particularly simple when no multiple scattering is present", and that the cross section would directly yield the modulus square of the momentum-space wavefunction of the bound electron. Neudachin *et. al.* also stated that because (e,2e) was a very direct technique for measuring the wavefunction it should become "a leading method of investigation of electronic states", though performing the experiments would be difficult. The first experimental results came from Italy with Amaldi *et.al.* [2] in 1969 and Camilloni *et.al.* [3] in 1972. These experimental studies showed that the technique was feasible although several experimental problems were highlighted. The biggest problem was the energy resolution ($\approx$ 90 eV), which was so poor that experiments were only barely able to separate the core from the valence electrons. Another problem was the effect of multiple scattering, meaning that the incoming or outgoing electrons undergo secondary collisions. These secondary collisions cause a loss of energy or a change of momentum from the incoming/outgoing electrons which means the determined binding energy and momentum of the bound electron will be incorrect (Eq. 1.1) and the measured event will contribute to the background. To reduce the effect of multiple scattering, higher energy electrons were used. However increasing the incident electron's energy also had the effect of reducing the scattering cross section, increasing the measurement time and worsening the already poor energy resolution. These experimental problems could not be easily overcome and so the focus shifted to gaseous targets [4]. The lower density of gaseous targets meant multiple scattering was not a problem and lower energies could be used, resulting in more resolved results. A series of successful experiments on gases followed including a measurement on atomic hydrogen [5]. The (e,2e) results showed near perfect agreement to the Schrödinger equation, which can be solved exactly for atomic hydrogen, validating the theoretical interpretation of the (e,2e) technique.

The success of the application of the (e,2e) technique to gas phase targets continued to drive experimentalists back towards solid targets. The ability to resolve valence bands which are accountable for the properties of solids was the driving force behind the push. Over the following 25 years many experimental groups contributed to improving the energy resolution of the technique [6, 7, 8, 9].

In 1979 Persiantseva *et. al.* [6] improved the energy resolution remarkably by slowing down the ejected electrons prior to detection, this resulted in an overall energy resolution of 11 eV (for their aluminium spectra). In 1984 the first measurements resolving structure within the valence band of amorphous carbon (amC) were reported by Ritter *et. al.* [7], with an energy resolution of 6 eV and momentum resolution of 0.3 au. Ritter measured the dispersion effects in the valence band, which is the binding energy of the valence electrons varying as a function of their momentum ($\varepsilon(\mathbf{q})$). For free electrons in a potential well these dispersion effects (Fig. 1.3) are seen as a parabola corresponding to the equation of kinetic energy of a free particle $E = \frac{q^2}{2m}$. In a metallic solid the valence electrons can be thought of as a free electron gas in a periodic potential array of the positively charged atomic cores (Fig. 1.3). The total energy of the bound electron is given by the sum of its kinetic energy (E_k) and its potential energy (E_p) determined by the atomic cores around it ($E_{total} = E_k + E_p$), where the kinetic energy of the electron is the kinetic energy of a free particle $E = \frac{q^2}{2m}$. Hence for a free electron solid the expected valence electronic structure is a parabolic curve from the kinetic energy term with a small perturbation from the atomic core potential well (Fig. 1.3).

In 1988 Gao *et. al.* [11] published the first experimental results for a single crystal

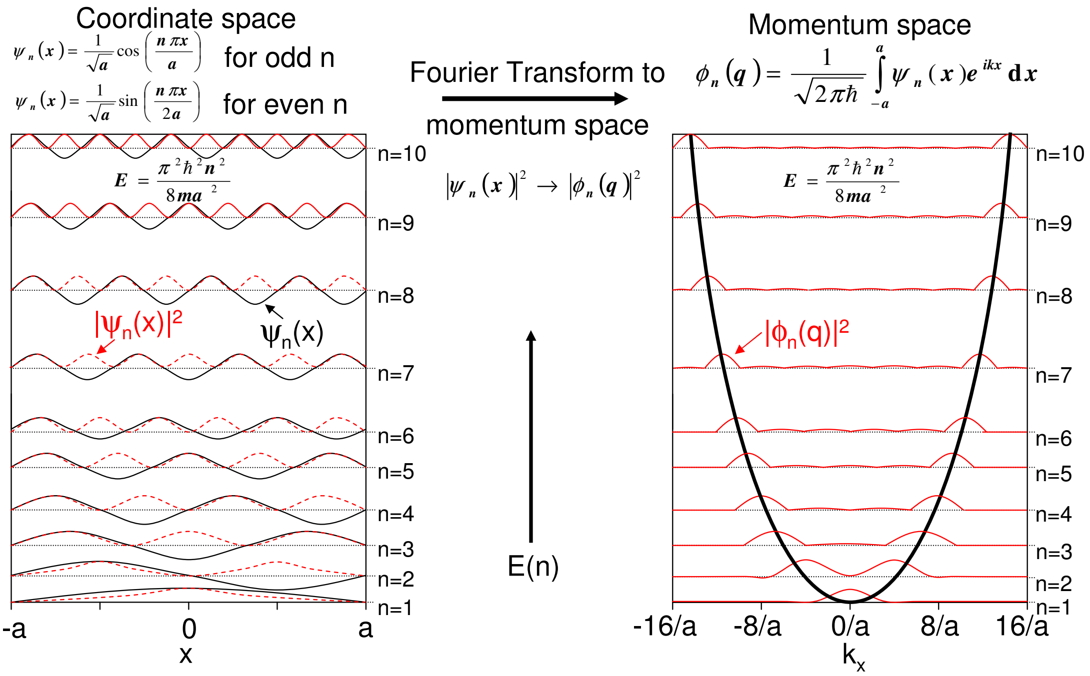

Figure 1.3: A particle in a box is analogous to a valence electron in a free electron solid. The solution to the probability of finding an electron in momentum space $|\phi_n(q)|^2$ results in a parabola, with the positions of the maxima in the momentum densities increasing with the square root of the energies ($\mathbf{q} \propto$ E). For a system of many electrons the energy levels are so close together that they form a continuous band. The shape of the band is called the band dispersion $\varepsilon(\mathbf{q})$ [10].

target (graphite). The experimental energy resolution was 8.6 eV with momentum resolutions of 0.25 au and 0.39 au for the out of plane and planar directions measured. This experiment successfully showed that (e,2e) could be used as an experimental technique to measure anisotropy in single crystal targets as well as the disordered targets, that had been previously measured.

The major breakthrough was the application of two-dimensional electron detectors [12], meaning the electron detectors could simultaneously measure a range of energies and angles (ϕ, Fig. 1.2). This reduced the data collection time from months to days as shown by the group at the Flinders University of South Australia [12, 13] who also improved energy resolution to 1 eV. The Flinders group has measured a variety of targets including carbon and silicon in both amorphous and crystalline states, and some alkali-oxides [14, 15, 16, 17, 18]. The results still suffered from the effects of multiple scattering mainly due to the low-energy asymmetric-kinematics, as the slowly ejected electron (1.2 keV) has a very short mean free path relative to the sample thickness. The multiple scattering clouded interpretation of results, and many approximations were made in an attempt to remove the effects of multiple scattering.

The ANU solid state spectrometer is an improvement over the Flinders spectrometer. The ANU spectrometer, not only achieves energy resolutions of 1 eV and momentum resolutions of 0.1 au, it also uses much higher energy and symmetric kinematics. This results in much less multiple scattering, meaning more direct and more easily interpreted data when compared to those of the Flinders spectrometer. For a more detailed comparison see Vos and Weigold [19]. The ANU spectrometer is discussed in more detail in chapter 2.

1.3 Related Techniques

Using electrons as spectroscopic probes into solid structures often results in more direct and easily interpreted results than the photonic equivalent. EMS measures the energy and momentum resolved electronic densities in solids. Such depth of information means that there are many ways in which to analyse the EMS results, and compare them with sophisticated theoretical techniques at a level not possible by any other method. In such a way EMS can also be a bridging technique between other experiments. In this section EMS will be briefly compared with some of the other main experimental techniques, namely angular-resolved photoemission spectroscopy (ARPES), Compton scattering and positron annihilation. These following techniques omit at least one of the measurable quantities that EMS can measure, but they have advantages in other areas like energy resolution or the number of targets that can be measured.

Angular-resolved Photoemission Spectroscopy

ARPES is a technique capable of measuring the change in the binding energy of a band as a function of the momentum of the electrons in the crystal (band dispersion). ARPES involves ionising a single crystal target with a well defined incident photon and measuring the energy and angle of the photoemitted electrons. Photoelectron peaks can then be extracted as a function of incident photon energy or outgoing photoelectron angle, so that each peak corresponds to one point on an experimental band structure measurement. ARPES has the distinct advantages of not requiring thin, free-standing films and as such has a larger range of possible single crystal targets, and the advantage of having a much better energy resolution (up to 1 meV). The disadvantages of ARPES compared to EMS are numerous, the main disadvantages include the need for long range order in targets, thus only crystalline targets can be studied. ARPES is a very useful experimental tool, but it is a theoretically very complicated process and for many years an over simplified 3-step photoemission treatment was used. Quantum mechanically a 1-step process is required, and after many years theorists are finally achieving accurate predictions with this model [20, 21]. ARPES is extremely sensitive, as low energy photoelectrons have very small escape depths, so the signal from the surface states can sometimes dominates the signal from the bulk states [22, 23], hence the bulk and surface contributions are hard to separate. ARPES generally has a poorer momentum resolution on a whole as the experiment does not conserve the momentum contribution perpendicular to the surface. When the low energy photoelectrons escape the surface into the vacuum they are perturbed by the potential step at the surface and lose $\mathbf{k}_\perp$ information. This loss of $\mathbf{k}_\perp$ information results in some bands with a momentum component perpendicular to the surface normal becoming suppressed in the ARPES results. EMS is not noticeably affected by the surface potential step, as the electrons leaving the surface have 25 keV of energy and the small surface potential ($\approx$ 4 eV) is negligible at that energy. As ARPES extracts the band structure from the measured energy distribution curves, it can only measure a series of points along the band structure and not the relative intensities of different bands, or the variation in intensity across a band as EMS can. However recent developments in toroidal analysers is enabling photoemission to measure relative intensities in momentum space one energy at a time. Measurement of the intensities in different Brillouin zones have only been done near the Fermi surface [24] and energies slightly above the Fermi surface [25]. Through very stable experimental parameters it may be possible to scan across different energies and measure a full valence band structure with relative intensities.

ARPES is still the most widely used technique for band structure ($\varepsilon(\mathbf{q})$) measurements [22] and in detailed comparison with EMS measured band structures, which are bulk sensitive, elucidation of surface contributions to the band structure may be possible.

Compton Scattering

Compton scattering is generally performed by irradiating a solid target with high energy photons and measuring the change in wavelength (energy) of the outgoing photons [26]. In order to conserve momentum the reflected photons will become Doppler shifted by an amount that corresponds to the momentum of the bound electron prior to collision. The measured momentum distribution of the electrons in the solid is known as a Compton profile ($J(q)$). The Compton profile of a target is a partially integrated momentum density given for all bound electrons by:

$$J(q_z) = \int dq_x \int \rho(\mathbf{q}) dq_y \tag{1.6}$$

Where $\rho(\mathbf{q})$ is the momentum density distribution, which is the same as the spectral momentum density that has been integrated over all binding energies. By only measuring one outgoing particle the experiment is restricted to one degree of information and in the case of Compton scattering that is a momentum profile that is integrated over two axial directions. Thus the Compton profile is the projection of the momentum density in the momentum transfer direction that is effectively integrated over all binding energies.

EMS momentum profiles are differentiated as a function of energy and also measured along a single momentum direction so direct comparison to Compton profiles is difficult. EMS measurements normally only encompass the valence electrons with small binding energies (typically 0-80 eV below the Fermi level) where as Compton profiles include the core electrons as well. The advantage of Compton scattering is that multiple scattering effects are small, so the intensity at higher momentum comes from bound electrons with higher momentum, and not from electrons with lower momentum that have been multiple scattered to higher momentum values. Experiments are also much less complicated and are not restricted in target selection or preparation.

Positron Annihilation

Positron annihilation is the process of a positron combining with a bound electron to produce two, momentum conserving, photons which can be analysed to determine the momentum information of the initial electron and positron combined. Prior to annihilation positrons thermalise down to room temperature [27] which corresponds to a momentum of 0.05 au. The momentum of the positron prior to annihilation is not exactly known and hence the bound electron's momentum is also only measured with a momentum resolution no better than the order of the thermalisation momentum. The cooling of the samples down to liquid nitrogen temperatures, can greatly lower the thermalisation momentum, and hence improve the resolution. If both particles are stationary then the two resulting photons travel at 180° to each other. If, however, either particle is moving then the non-zero momentum is conserved by emitting the two photons at an angle (θ) less than 180°. Thus the emission angle of the two emitted photons are measured in coincidence, and can be related to the momentum profile of the bound electrons in the target. In addition the momentum conservation also gives rise to a Doppler shift in the energy of the emitted photons, however the resolution of measuring energy shift of the photons is 10 times less resolved than measuring the emission angles of the photons [28]. The momentum profiles ($I(q_x,q_y)$) measured by positron annihilation are given by

$$I(q_x,q_y) \propto \int \rho_{\pm}(\mathbf{q})dq_z. \tag{1.7}$$

Where $\rho_{\pm}(\mathbf{q})$ is the momentum distribution of electrons in the presence of a positron. It is given by the square modulus of the Fourier transform of the products of the electron and positron wavefunction.

$$\rho_{\pm}(\mathbf{q}) = \sum_j \left| \int \mathrm{e}^{-i\mathbf{q}\cdot\mathbf{r}} \psi_j(\mathbf{r})\psi_p(\mathbf{r})d^3\mathbf{r} \right|^2 \tag{1.8}$$

Positron annihilation may not represent the true target momentum profile. As positron annihilation involves a slow moving positron and target electron, the positron wavefunction ψ_p interacts with the wavefuntion of the bound electron ψ_j prior to annihilation via Coulomb attraction effectively perturbing the bound electron's wavefunction. However, these correlation effects as discussed by West [28], have a sizeable effect on the lifetimes but have only a very small contribution to the momentum density.

The other feature of positron annihilation is that the positrons tend to move towards vacancies in the crystal lattice because of the lower atomic density there, or lacking vacancies in the lattice the positron annihilation will occur with the outer most valence electrons that are closest to the Fermi level. This means that the measured momentum profiles will come from either defects in the crystal or from near the Fermi surface. This feature can be an advantage when studying defects in crystals, but otherwise it hinders these measurements in comparison to EMS momentum profiles. Positron annihilation would be a good comparison to EMS if the measurements were performed on a perfect crystal. As the measured momentum profiles are direction dependent and more sensitive to lower momentum electrons, although EMS would generally have a better momentum resolution, and be able to differentiate the momentum profiles as a function of binding energy. For further information on Compton scattering or positron annihilation see Cooper *et. al.* [29].

1.4 Theory of EMS

Electron Momentum Spectroscopy (EMS) is based upon a kinematically complete ionisation reaction, where a high energy incident electron interacts with a bound electron to produce two indistinguishable emitted electrons (Fig. 1.4) [30, 31]. These two emitted electrons are then detected in coincidence to ensure that they originated from the same collision event. The energy and momentum of the two outgoing electrons are measured and the energy and momentum of the incident electron is well defined, so the binding energy and momentum of the bound electron can be determined. Measuring many EMS reactions, the differential cross section is determined [30, 31] and under the right kinematic conditions the cross section is directly proportional to the modulus square of the wavefunction in momentum space. From this method spectral information such as the spectral momentum density (SMD) and the band dispersion, $\varepsilon(\mathbf{q})$, can be directly measured.

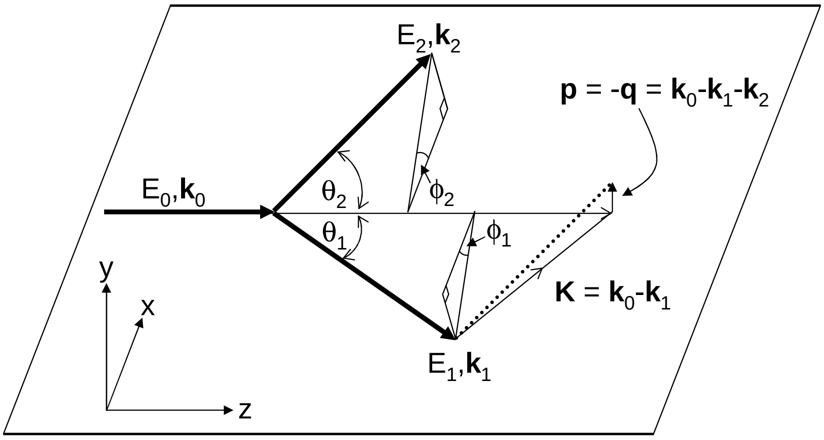

Figure 1.4: The EMS kinematics for the ANU solid state spectrometer. The variables mentioned throughout this chapter are defined, as well as the geometrical arrangement which is symmetric non-coplanar which ensures that the energy and momentum transfer of the outgoing electrons are as high as possible to satisfy the theoretical approximations.

The band information is determined from the conservation of energy and momentum equations, as the energy and momentum must be conserved. The (e,2e) reaction is described by the following equation:

$$e_0(\mathrm{E}_0,\mathbf{k}_0)+S(\mathrm{E}_S,\mathbf{p}_S)\rightarrow S^+(\mathrm{E}_{S^+},\mathbf{p}_{S^+})+e_1(\mathrm{E}_1,\mathbf{k}_1)+e_2(\mathrm{E}_2,\mathbf{k}_2) \tag{1.9}$$

where an incident electron (e_0) is scattered from the target sample (S), to produce a scattered electron (e_1) and an ejected electron (e_2) resulting in an ionised target (S^+) in a final state (ψ_f) [32]. We can take this equation further to say that both conservation of momentum and energy requires:

$$\begin{aligned} \mathrm{E}_0 &= \mathrm{E}_1+\mathrm{E}_2+(\mathrm{E}_{S^+}-\mathrm{E}_S) \\ \mathbf{k}_0 &= \mathbf{k}_1+\mathbf{k}_2+(\mathbf{p}_{S^+}-\mathbf{p}_S) \end{aligned} \tag{1.10}$$

Where the difference in energy between the final and initial states of the target can be denoted by ε, the energy required for ionisation, and can be referred to as the binding energy of the ionised electron. The difference in momentum between the final and initial states of the target is denoted **p**, and is the momentum gained by the ion due to the ejection of an electron, commonly referred to as the recoil momentum. Using the binary encounter approximation, a reaction can be set up where there is a large and very sudden transfer of energy and momentum to only the target electron and not the target itself. This implies, due to conservation of momentum, that the recoil momentum (**p**) of the target must be equal and opposite to the momentum of the target electron (**q**) an instant before the collision.

$$\mathbf{p} = -\mathbf{q} \tag{1.11}$$

So we can rewrite equations 1.10 as:

$$\begin{aligned} \varepsilon &= \mathrm{E}_0 - (\mathrm{E}_1 + \mathrm{E}_2) \\ \mathbf{q} &= \mathbf{k}_1 + \mathbf{k}_2 - \mathbf{k}_0 \end{aligned} \tag{1.12}$$

The binding energy of the ejected electron and its momentum can be directly measured. Using multiparameter data acquisition both of these quantities can be measured simultaneously to obtain the spectral momentum density (SMD) of the target electrons.

An (e,2e) collision is described by the cross section which is a measure of the probability of recording a true coincident count for each unit of incident electronic flux, outgoing solid angle and energy interval. This differential equation for two outgoing electrons is referred to as the triple differential cross section [33]:

$$\frac{d^5\sigma}{d\Omega_1 d\Omega_2 dE_1} = \frac{k_1 k_2}{k_0} |f(\mathbf{k}_0, \mathbf{k}_1, \mathbf{k}_2)|^2. \tag{1.13}$$

Where $f(\mathbf{k}_0, \mathbf{k}_1, \mathbf{k}_2)$ is the scattering amplitude and contains information about the ionisation event. Under the independent particle approximation (IPA), which assumes that the EMS reaction is not affected by the many body system, the scattering amplitude can be separated into an electron-electron collision term and a structural term that contains information about the electron orbitals of the target. The IPA allows the structural term to be written as a product of one particle wavefunctions. Incorporating the plane wave impulse approximation (PWIA), which assumes that the electron wavefunctions of the incoming and outgoing electrons can be described by plane waves, as they are at sufficiently high enough energy, the scattering amplitude can be simplified to [32]:

$$\frac{d^5\sigma}{d\Omega_1 d\Omega_2 dE_1} = \frac{k_1 k_2}{k_0}(2\pi)^4 f_{ee} \sum_{av} |\langle \mathbf{q}i|0\rangle|^2. \tag{1.14}$$

Where f_{ee} is the electron-electron collision term and has been shown [34] to be equal to the spin averaged Mott scattering cross section for a free electron-electron collision;

$$\begin{aligned} f_{ee} &= \frac{1}{(2\pi^2)^2}\frac{2\pi\eta}{e^{2\pi\eta}-1}\left[\frac{1}{|\mathbf{k}_0-\mathbf{k}_1|^4}+\frac{1}{|\mathbf{k}_0-\mathbf{k}_2|^4}-\frac{1}{|\mathbf{k}_0-\mathbf{k}_1|^2|\mathbf{k}_0-\mathbf{k}_2|^2}\right] \\ &\quad \times \cos\left(\eta \ln\frac{|\mathbf{k}_0-\mathbf{k}_2|^2}{|\mathbf{k}_0-\mathbf{k}_1|^2}\right) \end{aligned} \tag{1.15}$$

Where $\eta = |\mathbf{k}_1 - \mathbf{k}_2|^{-1}$, and as this term approaches zero the $\frac{2\pi\eta}{e^{2\pi\eta}-1}$ term approaches 1. For symmetric kinematics the momentum transfer quantities are equal $|\mathbf{k}_0 - \mathbf{k}_1| = |\mathbf{k}_0 - \mathbf{k}_2| = K$. As such the electron-electron collision factor reduces to

$$f_{ee} = \frac{1}{(2\pi^2)^2 K^4}. \tag{1.16}$$

The other term in equation 1.14 ($\langle \mathbf{q}i|0\rangle$), is the structural term, and contains information about the target. Under the IPA the structural term simplifies to a product of one electron wavefunctions that can be equated to the momentum space wavefunction of a target electron in the i^{th} band ($\langle \mathbf{q}i|0\rangle \equiv \phi_i(\mathbf{q})$). And the absolute modulus squared of this momentum space wavefunction is the probability of finding an electron at a given energy and momentum combination in momentum space, which is the most direct experimental information that can be obtained.

$$\frac{d^5\sigma}{d\Omega_1 d\Omega_2 dE_1} = \frac{(2\pi)^4 k_1 k_2}{k_0} f_{ee} \sum_{av} |\phi_i(\mathbf{q})|^2. \tag{1.17}$$

For atoms there is a discrete energy level for each orbital, so the modulus square of the orbital momentum space wavefunction is just a momentum distribution at one energy. When changing from an atom to a solid the complexity of the system increases from one atom with a few discrete energy levels to infinite atoms with an infinite number of energy levels. These energy levels become so closely packed that they form a continuous band. This transition has been explained in more depth in literature [35] with the use of fictitious hydrogen chains, the H_2 molecules has one energy level with one momentum distribution, a H_{32} molecule chain has 16 different energy levels, each with a different momentum distribution. Taking this trend further, a solid will have an infinite number of discreet energy levels that form a continuous band. This means that for a solid the differential cross section is better expressed in terms of a spectral momentum density ($\mathrm{A}(\varepsilon_i, \mathbf{q})$) which is the absolute square of a continuum of one electron momentum space wavefunctions ($|\phi_i(\mathbf{q})|^2$).

$$\frac{d^5\sigma}{d\Omega_1 d\Omega_2 dE_1} = \frac{(2\pi)^4 k_1 k_2}{k_0} f_{ee} \mathrm{A}(\varepsilon_i, \mathbf{q}). \tag{1.18}$$

Application to crystalline solids

For crystalline solids the atomic cores form a periodic potential and the problem can be simplified even further. The solution to the Schrödinger equation of a charged particle in a periodic potential can be given in terms of Bloch functions. These Bloch functions describe the motion of an electron in the periodic crystal lattice;

$$\psi_{i\mathbf{k}}(\mathbf{r}) = u_{i\mathbf{k}}(\mathbf{r}) e^{i\mathbf{k}\cdot\mathbf{r}} = \sum_{\mathrm{G}} c_{\mathrm{G}} e^{i(\mathbf{k}+\mathbf{G})\cdot\mathbf{r}}. \tag{1.19}$$

Where $u_{i\mathbf{k}}(\mathbf{r})$ is a function that is periodic in the crystal lattice. By taking the square modulus of the wavefunction, which gives the electronic density, the $e^{i\mathbf{k}\cdot\mathbf{r}}$ term equates to 1, so the $u_{i\mathbf{k}}(\mathbf{r})$ term contains the periodicity and electron intensity information.

$$u_{i\mathbf{k}}(\mathbf{r}) = \sum_{\mathrm{G}} c_{\mathrm{G}} e^{i\mathbf{G}\cdot\mathbf{r}}. \tag{1.20}$$

where the sum is over all reciprocal space lattice vectors and, in three dimensions, $\mathbf{G}$ is a basis set of vectors that incorporates the translational symmetry of the crystal in momentum space. Integer amounts (a) of the reciprocal lattice vector ($\mathbf{G}$) relates real (measured) momentum ($\mathbf{q}$) to the crystal momentum ($\mathbf{k}$);

$$\mathbf{q} = \mathbf{k} \pm a\mathbf{G} \tag{1.21}$$

The normalised wavefunction for a single crystal sample under the BEA and IPA approximations in positional space is given by [32];

$$\psi_{i\mathbf{k}}(\mathbf{r}) = N^{-\frac{1}{2}} \sum_{n=0}^{N-1} \psi_i(\mathbf{r} - \mathbf{R}_n) e^{i\mathbf{k}\cdot\mathbf{R}_n}. \tag{1.22}$$

which is a summation over N identical unit cells of the unit cell orbital ($\psi_i(\mathbf{r} - \mathbf{R}_n)$). Taking the Fourier transform of the positional space wavefunction ($\psi_{i\mathbf{k}}(\mathbf{r})$) will yield the momentum space wavefunction of the entire crystal solid ($\Phi_{i\mathbf{k}}(\mathbf{q})$). As previously shown under the PWIA, the momentum space wavefunction ($|\Phi_{i\mathbf{k}}(\mathbf{q})|^2$) is equal to the structure factor ($|\langle \mathbf{q}i|0\rangle|^2$) in the EMS differential cross section (Eq. 1.17). Taking the Fourier transform of the positional space wavefunction (Bloch function) gives;

$$\begin{aligned} \Phi_{i\mathbf{q}}(\mathbf{q}) &= N^{-\frac{1}{2}}(2\pi)^{-\frac{3}{2}} \int d\mathbf{r} e^{-i\mathbf{q}\cdot\mathbf{r}} \sum_{n=0}^{N-1} \psi_i(\mathbf{r} - \mathbf{R}_n) e^{i\mathbf{r}\cdot\mathbf{R}_n} \\ &= N^{\frac{1}{2}} \phi_i(\mathbf{q}) \delta_{\mathbf{k}-\mathbf{q}\pm a\mathbf{G}}. \end{aligned} \tag{1.23}$$

where $|\Phi_{i\mathbf{k}}(\mathbf{q})|^2$ is the momentum space wavefunction for the solid and is equal to the momentum-space orbital of the unit cell ($\phi_i(\mathbf{q})$) multiplied by the square root of the number of unit cells in the crystal ($N^{\frac{1}{2}}$), and a delta function that relates the crystal momentum ($\mathbf{k}$) to the observed momentum ($\mathbf{q}$). The momentum-space orbital of the unit cell is given by;

$$\phi_i(\mathbf{q}) = (2\pi)^{-\frac{3}{2}} \int d\mathbf{r} e^{-i\mathbf{q}\cdot\mathbf{r}} \psi_i(\mathbf{r}) \tag{1.24}$$

and the delta function which ensures the unit cells are correctly centred in relation to each other by maintaining the relationship between the observed momentum and crystal momentum is given by;

$$\delta_{\mathbf{k}-\mathbf{q}\pm a\mathbf{G}} = N^{-1} \sum_{n=0}^{N-1} e^{i(\mathbf{k}-\mathbf{q}\pm a\mathbf{G})\cdot\mathbf{R}_n} \tag{1.25}$$

Given the periodicity of a single crystal sample with many repeating unit cells the EMS differential cross section (Eq. 1.18) can be simplified to the absolute square of the momentum space orbital of the unit cell. For a symmetric EMS spectrometer the triple differential cross section becomes;

$$\frac{d^5\sigma}{d\Omega_1 d\Omega_2 dE_1} = \frac{4N' k_1 k_2}{k_0 K^4} |\phi_i(\mathbf{q})|^2 \delta_{\mathbf{k}-\mathbf{q}\pm a\mathbf{G}}. \tag{1.26}$$

Which is very similar to the EMS cross section for atoms and molecules.

Effects of multiple scattering

External effects on the incoming or outgoing plane wave electrons will cause perturbations to either their energy or their momentum. Perturbations caused by the EMS electrons interacting with the nucleus is most common via Bragg scattering. The result is to effectively shift the measured momentum by a reciprocal lattice vector (**G**). Perturbations caused by the EMS electrons interacting with other bound electrons is most common via plasmon losses. The result is a loss in energy to one of the EMS electrons and in incorrect determination of the binding energy (ε) of the sample (Eq. 1.12). These external experimental effects are not included in this theoretical formulation as they occur outside of the EMS interaction.

To avoid these external effects EMS is performed at high energies, in the case of the ANU EMS spectrometer it is performed at 50 keV, and measurements are performed on thin samples (<200 Å). For a majority of EMS interactions in the ANU spectrometer neither the incoming or outgoing electrons have further interactions with the target system. These distortions will be discussed as multiple scattering (Section 4.3).

The theoretical formulation shown in this chapter is a single particle notation to reduce the complexity, the single particle notation is not a limit of the experimental technique. This chapter was intended to give the reader some understanding of what is measured in the EMS technique and what is meant by the term spectral function. For a more in depth formulation see Weigold *et. al.* [32] or McCarthy *et. al.* [30].

Chapter 2

Apparatus

To date only one reference exists that explains some of the more novel aspects in the design of the ANU spectrometer [36]. There is no comprehensive reference of the ANU spectrometer in literature, so the experimental apparatus will be explained in detail in this chapter. Electron momentum spectroscopy (EMS) is a complex experimental technique that combines many aspects of physics, so the experimental apparatus is quite intricate.

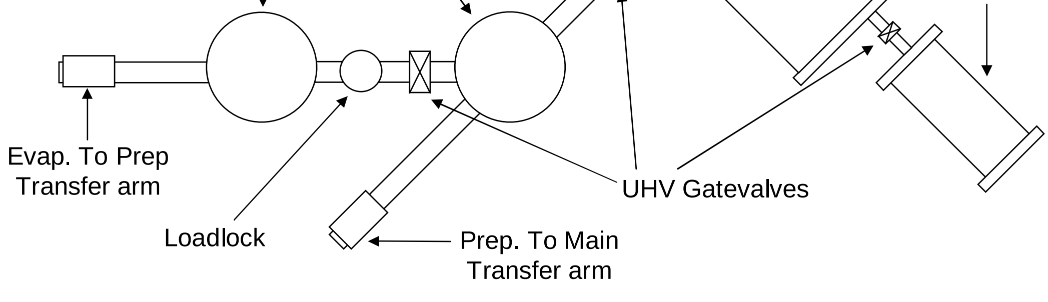

Figure 2.1: An overview of the ANU spectrometer layout. Showing the relative positioning of each of the chambers and the connections between them by UHV gatevalves.

The design of the ANU spectrometer was based around the need for good energy and momentum resolution in the multi-parameter and coincident detection of two outgoing electrons, whilst minimising the multiple scattering effects in the interaction region. This chapter will explain the key features of the main experimental chamber and give a brief description of the sample preparation chambers and the ultra high vacuum (UHV) transfer system between the chambers (Fig. 2.1).

2.1 Main Chamber

The main experimental chamber is used to perform EMS, EELS (electron energy loss spectrometry), electron diffraction and electron-Compton scattering experiments. Of those experiments EMS is the most difficult and requires the most stringent experimental conditions. To obtain an EMS spectral function with significant statistics the measurement requires 3-4 days of collection time, and a very well collimated electron beam. Thus an extremely good vacuum is required to both minimise the amount of background scattering and minimise surface contamination of the target over the measurement period. The main chamber is pumped to the 60-100 torr range with a venturi pump run from pressurised nitrogen (N_2). A sorption pump, which is cleaner than a rotary pump, is then used to achieve pressures of the order of 10^{-3} torr. The main chamber can be further pumped to the 10^{-6} torr region via the UHV preparation chamber (10^{-10} torr). A 320 L/s ion pump (Physical Electronics 3088322) mounted from the main chamber is then turned on to achieve the 10^{-9} torr range. At the end of the bakeout cycle a non-evaporative getter (NEG)(Physical electronics 2150300) can be activated which reduces the partial pressure of gases which are difficult to pump by other means (i.e. hydrogen, oxygen). The combination of the NEG and ion pump quickly brings the pressure of the main chamber into the low 10^{-10} torr range and after a few cycles of the titanium sublimation pump (Physical Electronics 224-0550) and a few weeks seasoning of the vacuum the base pressure of the chamber reaches the low 10^{-11} torr region, which increases to the mid 10^{-11} torr region during operation. The gatevalve to the preparation chamber is closed at all times except

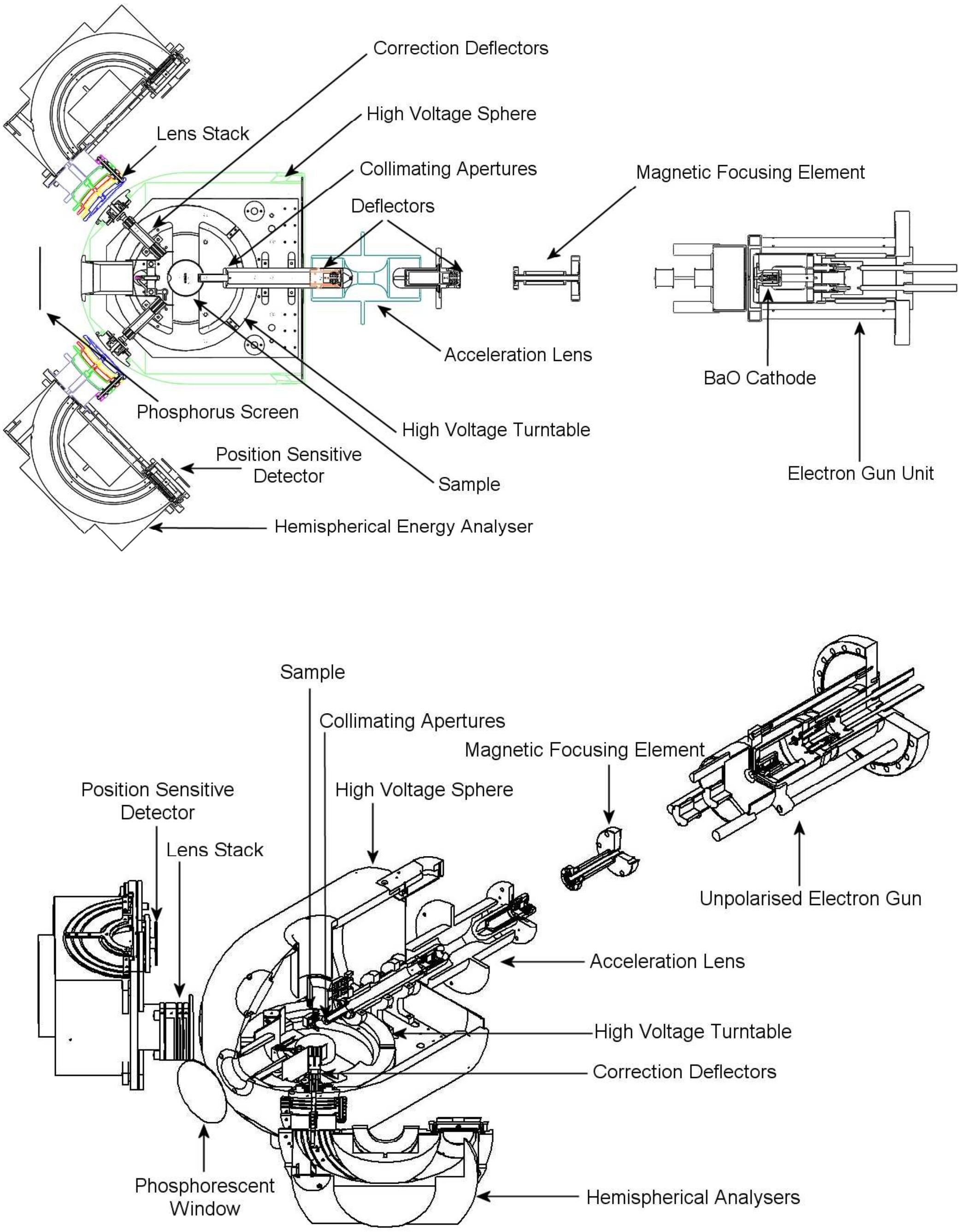

Figure 2.2: The main experimental chamber cut in the plane of the EMS interaction (top view). With the key features being the high voltage sphere (green), the sample position, the phosphorus screen, the outgoing correction deflectors and the two hemispherical electron detection systems. Am isometric view (below) shows the three dimensional shape of the components.

during sample transfer to help to maintain the UHV in the main chamber.

The pressure is sufficient to maintain clean surfaces on even the more reactive samples such as Fe over the period of the EMS measurement. In the case of a breach of UHV conditions an interlock is also designed around this system so that the high voltage supplies, analysing power supplies and pumps will be protected. As high voltages are dealt with, the power supplies also have other interlock criteria that will switch them off as a safety precaution. If the door of the high voltage cage, which acts as a safety barrier and to prevent pickup, is opened or the voltages of the DC batteries that power the electronics in the HV region, become too low for stable operation then the power will be switched off.

The high voltage configuration of this chamber (Fig. 2.3) is designed to minimise any high voltage drift or ripple that would worsen the energy resolution of an EMS experiment. This configuration is explained in detail in Vos *et. al.* 2000 [36], and involves the electron gun being held at a potential of -25.5 kV and the electrons being accelerated to 50 kV in the target region by holding the target region at a potential of +24.5 kV. The gun high voltage region involves a -24.5 kV power supply floating on a -1 kV supply to achieve a total potential of -25.5kV. The offset voltage circuit measures the voltage offset through a resistor chain $\left(\mathrm{V_{offset}}\ (\mathrm{keV}) = 24.5 * \frac{\mathrm{R_{offset}}}{90.09\times10^{6}}\right)$. This configuration allows the -24.5 kV supply of the gun and the +24.5 kV supply of the target region to go through voltage dividers and then be analysed by a drift and ripple compensator. If any long term drift occurs then the drift and ripple compensator, which the gun voltage floats upon, will output a correction voltage to ensure that the difference between the two high voltage power supplies is 0 V. These HV power supplies are kept inside a HV cage to prevent pickup and also for safety precautions.

The reason the gun voltage is 1 kV higher in magnitude is due to the configuration of the analysing electronics. The symmetrically scattered outgoing electrons each have approximately +25 keV of energy, and upon leaving the HV target region (+24.5 kV) they are decelerated to 400 eV (analysers float at -100 V, see section 2.1.3). This dictates that the target HV region must be +24.5 kV, and hence to achieve the required 50 keV electron beam the gun region must be at -25.5 kV.

The electron gun is a barium oxide (BaO) cathode which is mounted in a side chamber

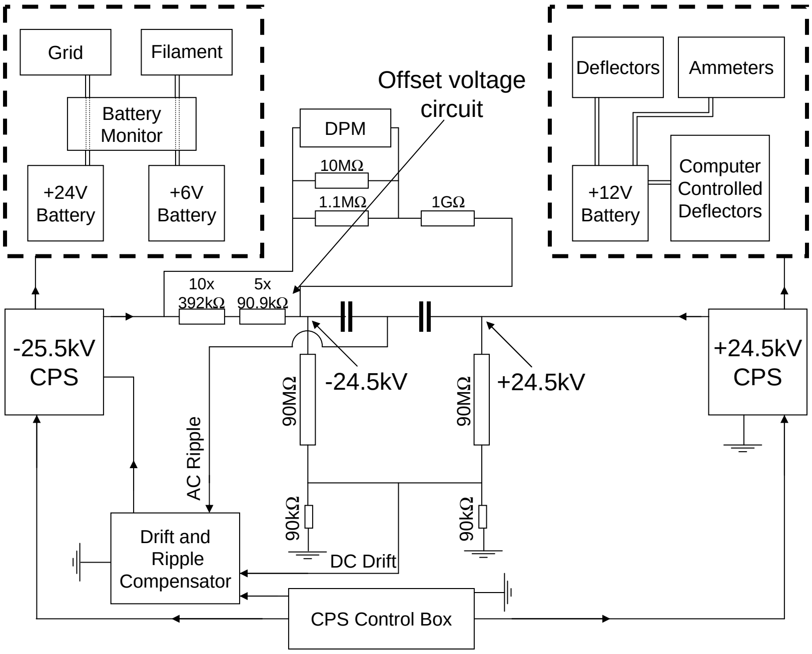

Figure 2.3: Overview of the high voltage electronics for the gun and target region. The HV dividers reduce the input voltage to the drift and ripple compensator which can analyse the difference of these two voltages and output a correction voltage that the gun HV floats on.

connected to the main chamber through a mini flange with a gatevalve (MDC GV-625M-P) for isolation if necessary. The gun chamber has its own ion pump (Physical electronics 3096150) to maintain a UHV environment in the gun chamber at all times to prevent contamination of the BaO cathode.

The sphere in the main chamber is designed to float up to +24.5 kV so that everything inside the chamber is at the same potential, so the focusing capabilities of the electron beam can be simplified and maximised by requiring only two focusing elements, one upon entering and one upon exiting this region. This is achieved by having a high voltage sphere, made from machined aluminium (12 mm thick), mounted with a 15 mm gap inside the chamber (Figs. 2.2 and 2.1). The sample is lowered into this region, prior to turning on the high voltage, via a xyzθ manipulator (Thermionics Northwest FM103/104-2-2/16/B8T/PL-.75) that has a 30 kV insulator that transverses across the HV sphere, so that the lower section of the manipulator which holds the sample, is held at the same potential as the HV sphere.

Components inside the HV sphere include collimating apertures and deflectors for the incident electron beam (see section 2.1.2). A Faraday cup which is in the path of the electron beam positioned behind the sample and a turntable for selecting between 3 different entrance slits for the detectors. The turntable is inside the HV sphere but is rotatable via an externally mounted linear motion feedthrough (MDC BLM-275-1) that is electrically isolated from the target HV region by a ceramic insulator. The different entrance slits (Fig. 2.4) that can be selected by rotating the turntable are the calibration slits which consist of a series of small holes, a 0.5 mm wide slit for measurements in which the coincidence countrate is low, and a 0.2 mm wide entrance slit that gives a better energy resolution at the cost of coincidence countrate. Also mounted in the HV sphere are two sets of momentum offset correction deflectors [36, 37] that allow corrections for small errors in alignment and stray magnetic fields, these deflectors are used to ensure the sample is measured through the zero momentum position in the crystal (see section 4). The Faraday cup is on a mount that is attached via a 30 kV insulator to an externally mounted vertical manipulator (MDC BLM-275-1). It is important that the Faraday cup is moveable so that the measured electron diffraction images, that are taken on the phosphor screen positioned along the direction of the incident electron beam behind the Faraday cup, are not blocked or distorted by fringing effects from the Faraday cup.

Outside of the HV sphere in the main chamber is a phosphorous screen that shows an electron diffraction image from the target sample which enables us to see what atomic arrangement that sample has. It is clearly evident whether the sample is in a single crystal (dots), polycrystalline (rings) or amorphous (broad rings) state. Via analysis with a computer program (processdiffraction [38]) it is also possible to determine the interatomic spacing, this has been used in the preparation of single crystal vanadium oxide [39] to determine which oxidation state the vanadium was in. The hemispherical energy analysers (see section 2.1.3) are mounted outside of the HV sphere with a decelerating lens stack separating the analysers from the HV sphere. They are positioned here so the outgoing electrons are decelerated from 25 keV to 400 eV which allows more resolved detection of their energies and hence a better energy resolution in the experiment, a successful technique first employed in (e,2e) by Persiantseva *et. al.* [6]. The position sensitive detectors

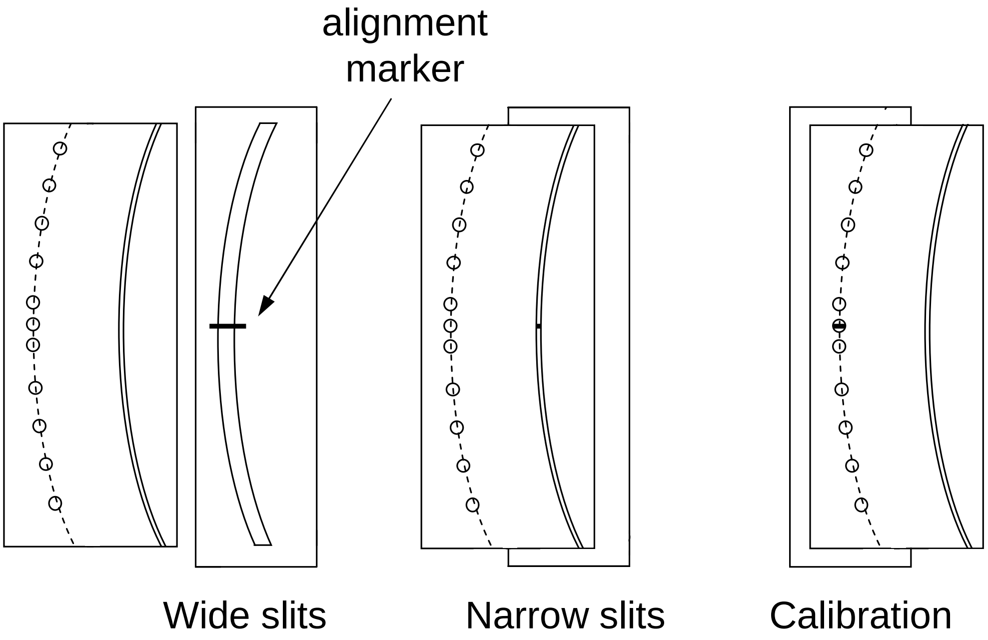

Figure 2.4: The three different slits available on the main chamber turntable. The wide slit is fixed in position with the sample alignment marker. The narrow slit and calibration apertures can be positioned in front of the wide slits by the turntable that they are mounted on. The curvature of the slits corresponds to the 88.6° measurement cone.

(PSD's)(see section 2.1.4) are also located outside of the HV sphere at the exit of the energy selective hemispheres.

2.1.1 Sample Alignment

Sample alignment is essential to ensure that the sample of interest is correctly centred in the interaction region. If the sample is moved forwards or backwards of the zero position, then offsets in the energy and momentum scales are created, as the measurement will effectively sample over a different exiting cone than the one that the spectrometer is setup to measure (see Fig. 1.2). Misalignment also reduces the energy and momentum resolution as the measurement is then measuring over kinematics that the spectrometer is not precisely calibrated for.

To have a repeatable sample position, two pins are internally mounted in the chamber,

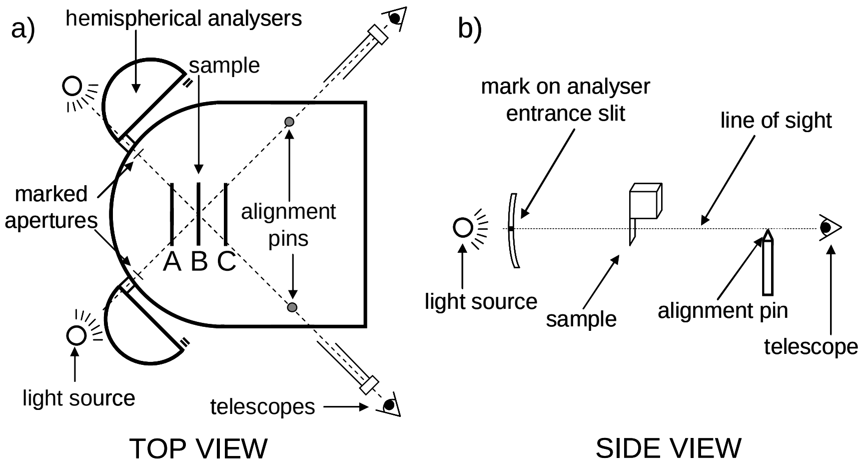

Figure 2.5: Sample alignment schematic. a) from the top view, firstly each of the telescopes are positioned so that the pinhead and analyser entrance slit is aligned. Then the sample is put into the position where the telescopes intersect, this procedure results in a 0.1mm sample position accuracy. b) a side view showing height alignment.

and each set of entrance slits to the analysers has a horizontal bar. Two externally mounted telescopes (Leica NA820), one per analyser, are aligned so that the cross hairs align with both the closely positioned pin and the distantly mounted analyser entrance slits. Where the line of sight of the two telescopes intercept is the well defined sample position (Fig. 2.5). Prior to any measurement the sample is carefully positioned so that each of the telescopes cross hairs are aligned with the same position on the sample. In Fig. 2.5, three sample positions labelled A, B and C are shown. For sample position A the line of sight of the two telescopes will view different positions on the sample, alternately for sample position C the line of sight of the two telescopes will view the opposite sides of the sample than they did in position A. It is only for position B that the line of sight of the two telescopes will view the same position on the sample. It is this position that the electron beam passes through, easily enabling the selection of a desirable part of the sample to measure. This alignment procedure can replicate sample position to within ≈ 0.1 mm in each axis. The sample is also rotatable in the θ angle (about the y-axis, Fig. 1.4), this rotation axis is also checked with the marked angular scale prior to each measurement with an angular resolution of approximately 1°.

2.1.2 Electron Beam

For accurate kinematics and energy resolution a well defined electron beam with a well known energy, small spot size and minimal transverse energy is required. The electron beam used in the ANU spectrometer is produced by a barium oxide (Heatwave, HWES 101263) cathode that is designed for UHV use, where low light emission and a low thermal energy spread is required. Heating currents on the order of 1.0-1.2 A would result in a typical operating temperature of 1200 K for this cathode as stated in the Heatwave Laboratories data sheet. The operating conditions are typically on the order of 0.7 A, hence the operating temperatures would be approximately 0.5-0.7 times the quoted 1200 K. For thermionic emitters the energy resolution of the emitted beam is given as a function of their operating temperature [32]:

$$\Delta E = 2.54 k_B T, \tag{2.1}$$

which would indicate that the energy resolution of the incident electron beam would be on the order of 150-250 meV. This does not take into account the effect of space-charge broadening on the resolution, which is kept to a minimum by the high extraction voltage (25.5 kV) and the relatively large emission area of the cathode (2.2×10^{-6} m^2), or the energy resolution broadening due to collisions between the electron beam and background particles within the UHV. As the electrons are extracted towards the grounded electron optics they first pass through a circular grid focusing element that has a typical voltage of -140 V below the negative high voltage (-HV) of the gun. The grid reduces the area of emission of the cathode by reducing the extraction field away from the central axis of the electron beam, this results in the emitted electron beam being more tightly focussed, however the space charge broadening contribution to the energy resolution will be also be larger. The electron beam is then accelerated through an anode which acts as a grounding plate to stop the fringing effect of the negative high voltage field from affecting the following electron optics.

The electron beam has several sets of deflectors and a magnetic focusing element to compensate for slight experimental misalignments and stray magnetic fields, before being accelerated in the positive high voltage (+HV) region in the main chamber. To obtain a focussed beam the magnetic focussing element is used in combination with an acceleration lens which maintains the focussing of the electron beam as it enters the +HV target region. Once into the target region the electrons have 50 keV of kinetic energy relative to the target sample. In the collimation region, just prior to the target position, there are two fine apertures, 400 μm and 100 μm, that are separated by 200 mm. These apertures collimate the incident electron to a beam spot at the sample of less than 200 μm. This ensures that the transverse momentum is very small, and hence the momentum along the direction of the electron beam (z-direction) is well defined (62.07 au). The well collimated incident electron beam then impinges on the sample and a small fraction will undergo a symmetric EMS collision with the two outgoing electrons heading off towards the hemispherical energy analysers (see section 2.1.3).

A specially designed set of deflectors are positioned along the outgoing electron trajectories that are used to correct for any slight misalignment or stray magnetic field and ensure that the momentum offsets in the x-axis and z-axis are zero so the sample is truly measured through zero momentum. These two sets of deflectors can also be used to sample through different momentum regions of a single crystal sample [40]. These final correction deflectors were explained in more detail in Vos *et. al* [36].

2.1.3 Analysers

The two outgoing electrons (Fig. 2.6) that have been decelerated to 400 V upon leaving the HV target region first pass through an energy selective hemispherical analyser before striking the position sensitive detector (PSD). The energy analysers separate the energy out across the horizontal axis of the PSD, whilst not affecting the vertical component which is a measure of momentum in the y-direction. Criteria for the hemispherical energy analyser include obtaining the best possible energy resolution whilst maintaining a reasonable sized entrance slit to increase the coincidence countrate and reduce data acquisition time. These two criteria are conflicting as shown by Imhof *et. al.* [41], as to increase the entrance slit width (x_a) increases the range of acceptable angle (pencil angle, α) and hence decreases the energy resolution (ΔE). The electron optics have been designed to achieve a good energy resolution whilst maintaining a reasonable countrate.

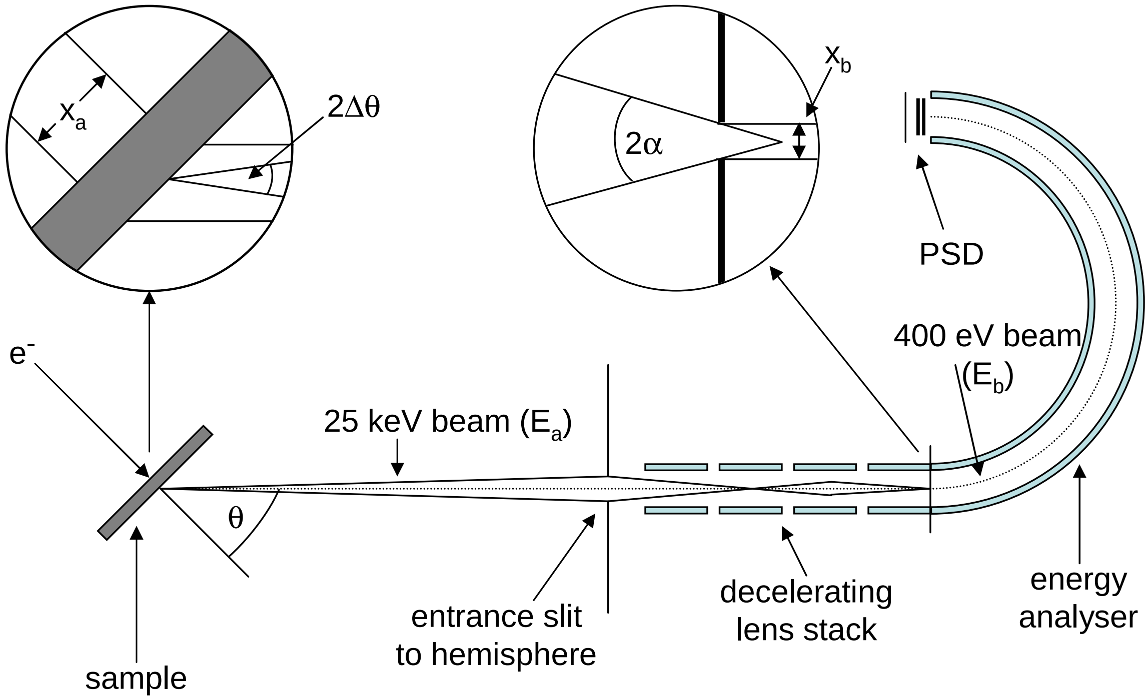

Figure 2.6: The incident beam spot (x_a), with an outgoing angle of $2\Delta\theta$ that can still pass through the entrance slit to the analysers. The decelerating lens stack then slows the electrons down to 400 V and focuses them to an effective slit size of 0.05 mm (x_b). This lens stack design achieves energy resolutions of down to 160 meV whilst not affecting the momentum information.

Prior to entering the energy analyser the incoming electrons are slowed to a kinetic energy of approximately 400 eV (E_b), by raising the hemispherical analysers and lens stack to a potential of -100 V and using a conical slit lens system to maintain a focussed beam. By slowing the electrons prior to the hemispherical energy analyser, the required pass energy is lowered and this dramatically increases the energy resolution [6]. The other properties of this conical lens is to focus the incoming electron beam in the θ angle down to an entrance distance of 0.05 mm (x_b), which is ten times smaller than the entrance slit (x_a = 0.5 mm, or 0.2 mm for fine entrance slit) to the lens system. The lens system is conical so that the electron beam only sees a focusing field in the θ direction, the ϕ direction (Fig. 1.2) sees no effective field, and thus the ϕ angular (i.e. momentum) information is conserved. By observing the given geometry and knowing the beam spot size (0.1 mm) and the width of the entrance slits 0.5 mm (0.2 mm fine), $\Delta\theta$ can be calculated to be 2.1 mrad (1.1 mrad). The pencil angle created by the focusing lens elements can be determined from the Helmholtz-Lagrange relationship [42]:

$$\Delta x_a \Delta\theta \sqrt{E_a} = \Delta x_b \Delta\alpha \sqrt{E_b} \tag{2.2}$$

hence, an effective pencil angles of $2\alpha = 33.9$ mrad for the coarse slit, and $2\alpha = 17.3$ mrad for the fine slit are determined. Using the energy resolution equation for a dispersive energy analyser given by Moore *et. al.* [43];

$$\Delta E_{FWHM} = E_{pass}\left(\frac{x_b}{2R_{mean}} + 0.5\alpha^2\right) \tag{2.3}$$

we obtain analyser energy resolutions of 330 meV for the wide slit and 160 meV for the narrow slit. The narrow slit is far better for the energy resolution of the analyser but reduces the singles countrate by a factor of 2.5 in each detector. In effect reducing the coincidence countrate by a factor of 6.25, which increases the data collection time by the same factor.

The hemispherical energy analysers have first order angular focussing [44], meaning that small deviations of the entrance angle α will still image on approximately the same exit position as the α term in the exiting radial position equations is effectively zero.

$$\begin{aligned} R_f &= -w_i + 2R_{mean}\left(\frac{E - E_{pass}}{E_{pass}}\right) + R_{mean}\alpha^2 \\ R_f &\simeq 2R_{mean}\left(\frac{E - E_{pass}}{E_{pass}}\right), \end{aligned} \tag{2.4}$$

where R_{mean} is the mean radial path of the hemisphere, E_{pass} is the mean pass energy of the hemisphere and E is the energy of the electron being analysed. The focussing properties of the entrance lenses to the hemisphere minimises the image of the incoming radial position ($w_i \leq 0.025$ mm) and the angle of the imaged electron terms ($R_{mean}\alpha^2 \leq 0.09$ mm). So the pass energy term ($2R_{mean}\left(\frac{E-E_0}{E_0}\right) \leq 20$ mm) determines the radial exit position (R_f). This implies that the radial exit position is linearly proportional to the energy of the electron traversing around the hemisphere (E).

The higher energy electrons will move to the outside of the hemisphere and have a longer pathlength resulting in a longer transit time [41] due to the radial exit positions relation to the electron's energy. The higher energy electrons will also have a larger potential energy in the hemispherical analyser, which limits their kinetic energy meaning they actually travel more slowly, and again take longer to travel through the hemisphere. Another factor in determining transit times is the orbital path in which the electrons take. Should all the electrons enter the hemisphere at R_{mean} with E_{mean} and perpendicular to the entrance plane ($\alpha = 0$) then all orbits would be circular. However as the ANU EMS spectrometers hemispherical energy analyser accepts entry positions of $w_i = R_{mean} \pm 0.025mm$, energies and entry angles of $\alpha = \pm 0.033rad$, then there will be some electrons that have an elliptical path that strike the same position with the same energy as electrons that had a circular path. This results in slightly longer pathlengths and hence transit times, resulting in a spread of transit times that are not separable by their detected positions, and hence sets a lower limit to the width of the timing peak.

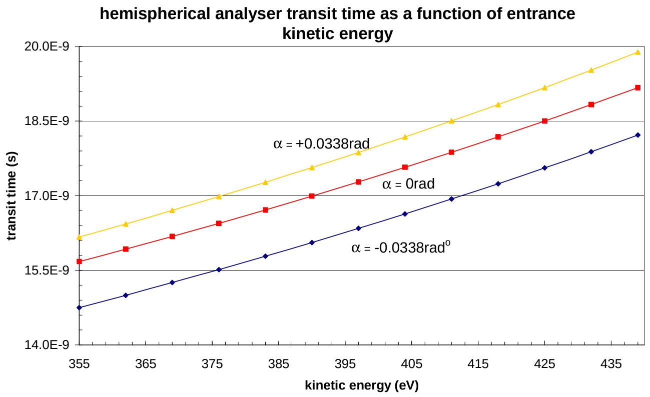

Figure 2.7: The transit time through the hemispherical analysers calculated from the equations of Kepler orbits shown by Caprari [45], showing a timing spread of 1.5 ns depending on the incoming pencil angle (α)

The pass energy of the analysers is 400 eV, and the distance between the inner ($R_i = 80$ mm) and outer hemispheres ($R_o = 120$ mm) is 40 mm, at the exit of the hemispheres are 40 mm diameter PSD's (see section 2.1.4) which cover the full exit width of the hemispherical analysers. This means that whilst the mean pass energy is 400 V electrons over a broad energy range are detected. Combined with the ability to measure a range of momentum values simultaneously means that the detection efficiency is significantly increased. Electrons entering a hemispherical analyser at a the radial position (R_{mean}) with an energy E, will be detected at a radial position R_f which is given by the relation in Eq. 2.4 [44]. This means that for a mean pass energy of 400 eV and an inner and outer radii of 80 mm and 120 mm respectively energies over the range of 355-436 eV can be measured. In addition to this range the hemisphere can be biased by up to -1 kV by a power supply which changes the potential of the entire hemispherical analyser allowing the analyser to be scanned over a larger range of values. For example, outgoing electrons with 500 eV of energy will be slowed by the value of the bias voltage, if the bias voltage is -100 V then the electron will have a kinetic energy of 400 eV (500-100), and will be detected in the middle of the plate. If a bias voltage of 120 V is now applied, the same electron will have an effective energy of 380 eV (500-120) and will now be detected on the low energy side of the PSD. This enables us to scan across the PSD so that any variations in the sensitivity of the PSD across the plate will be averaged out. It also allows the measurement of the spectral function of the core level electrons by changing the pass energy of the hemisphere to accept lower energy outgoing electrons (ie. measure target electrons with higher binding energy).

2.1.4 Detectors

Position sensitive detectors (PSD's) are at the exit of the hemispherical energy analysers. These PSD's consist of a set of micro channel plates (MCP's) and a resistive anode encoder (RAE) (Fig. 2.8). The PSD determines the position at which the outgoing electron strikes the channel plate, which can be calibrated so each position corresponds to an energy and momentum value of the measured electron. This arrangement of position sensitive detectors has been previously used in EMS for parallel detection of energy and momentum [12]. The ANU spectrometer described here uses the same position sensitive detection scheme as the Flinders EMS solid state spectrometer. Firstly the electron leaving the hemisphere strikes two chevron mounted micro-channel plates (Burle, 40/12/8/D/EDR/60:1/MS/CH/None) [46] creating a cascade of electrons resulting in a charge cloud that is large enough to be detected by the resistive anode encoder (Quantar Technology, 40mm). MCP's contain very thin electron multiplier tubes that are tilted at a small angle (8°) to optimise the cascade of electrons. Chevron mounting is when two MCP's are mounted back to back so the angular offsets in the electron multiplier tubes are in opposite directions (Fig. 2.8). Chevron mounting achieves a higher degree of accuracy by minimising the effect of stray ions emitted from the MCP, whilst squaring the intensity of the outgoing charge cloud. The MCP's have a 60:1 length to diameter ratio, resulting in a more intense and space-confined charge cloud than the standard 40:1 aspect ratio MCP's. The charge cloud that strikes the resistive anode encoder disperses over the resistive element and the electronic signal is measured at the four corners as discussed later.

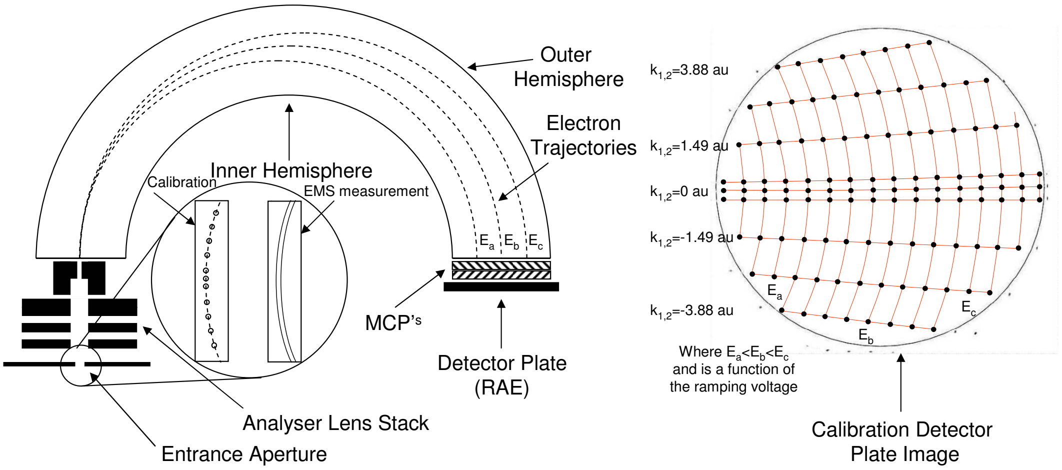

Figure 2.8: Left: the hemisphere and PSD configurations showing the entrance focusing lenses and the chevron mounted MCP's at the exit. Right: a detector image taken by using the calibration slits to look at an elastic peak, and then scanning the biased power supply so the image shifts across the plate. The red lines correspond to positions of equal energy and equal momentum, using this image the detector can now be calibrated.

In section 2.1.3 it was explained how the horizontal axis of the PSD corresponded to the energy scale. It can also be said that the vertical axis on the PSD corresponds to an angle (ϕ) that can be related back to a momentum component along the y-direction using Eq. 1.5. Thus the vertical deflection can be used (Fig. 2.8) to determine the momentum of the bound electron. The experiment is arranged so that only bound electrons with $\mathbf{q}_x \approx 0$ and $\mathbf{q}_z \approx 0$ are measured. If the bound electron has any momentum in the x-axis ($\mathbf{q}_x$) or z-axis ($\mathbf{q}_z$) then the outgoing electrons will be filtered out at the narrow entrance slit, which is positioned before the lens stack leading into the hemispherical energy analyser. Thus the position that the electron is detected is related to the outgoing electron's energy (horizontal axis) and momentum in the y-axis (vertical axis). A precise calibration procedure can be performed on each detector to map the real energy and momentum axes onto the detection plate.

The calibration procedure for the PSD's involves a specially designed set of calibration apertures (Fig. 2.4), with accurately known positions, which correspond to a well known ϕ angle (and hence momentum) in the y-direction of the experimental frame of reference. An elastic peak is measured through these calibration apertures, which produces a series of dots on the PSD, each corresponding to a well known ϕ angle (Fig. 2.8). The typical voltage offset on the detector is 100 V, this offset can be ramped up or down to change the effective energy of the elastically scattered electrons from the EELS measurement. For example at 100 V the elastically scattered electrons from an EELS measurement have 400 eV of energy passing through the detector. The elastic peak is then remeasured with the detector offset voltage at 102 V, so the effective energy of the elastic peak is now 398 V. Through a series of measurements of the elastic peak at different energies, a series of dots (aperture projections) are measured which correspond to well known energies and momenta which acts as a calibration grid for the momentum and energy axes (Fig. 2.8).

2.2 Data Collection System

The manipulation of the electronic data collection signals can be broken into two main sections, a fast pulse section that determines the coincidence criteria, and a slow pulse section that contains the information about where the electrons have struck the PSD

(Fig. 2.9).

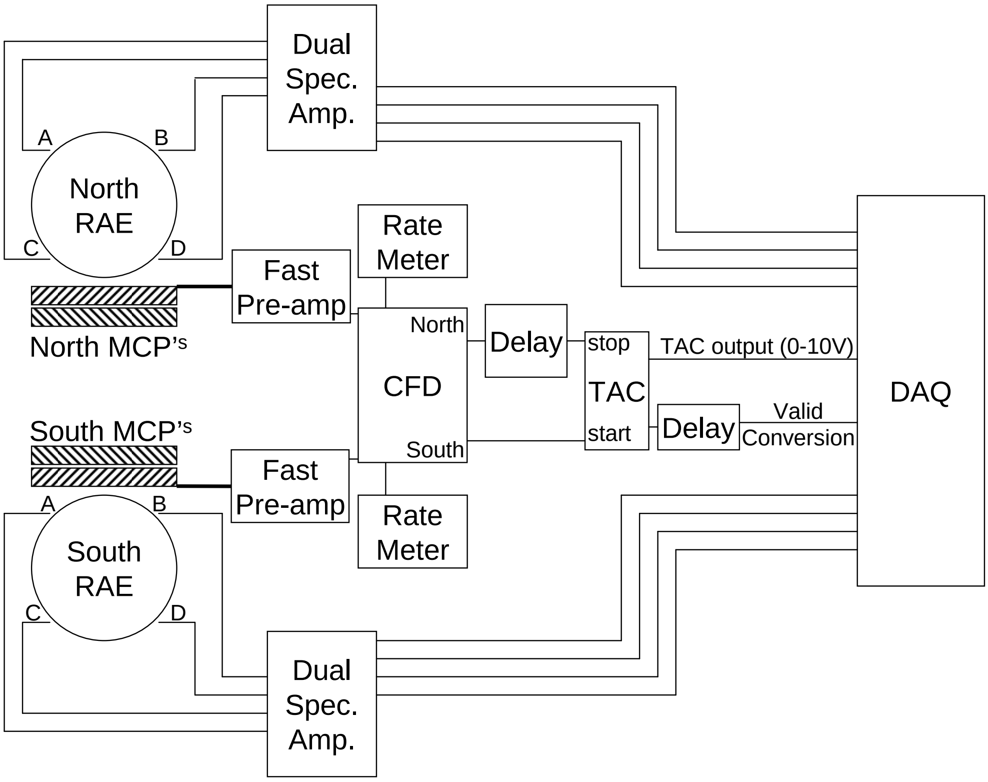

Figure 2.9: The analysing electronics configuration. Showing the slow four corner pulses of the RAE being amplified and analysed by the DAQ. The fast timing signal leaves the exit of the MCP's to be analysed by the time-to-amplitude convertor that defines the coincidence timing criteria and timing window.

The fast signal processing begins when a pulse is generated, from the conservation of charge, when the charge cloud leaves the second chevron mounted MCP in each detector. The pulse is used to indicate the arrival time of the electron in that detector, and is used in correlation with a fast timing pulse from the other detector to determine whether the two measured electrons came from a single event or whether the two measured electrons are from different scattering events. The two fast signals are put through a fast inverting pulse transformer to ensure the fast pulse is an acceptable negative pulse that has been decoupled from the high voltage of the MCP. The two signals are then amplified by a fast pre-amplifier (ORTEC VT120) and sent to a constant fraction discriminator (CFD)(ORTEC 935) which converts the pulses into a NIM pulse (negative). The South pulse is then sent to start a time to amplitude convertor (TAC)(ORTEC 566) which outputs a pulse whose height (0-10 V) is related to the time difference between the arrival times of the two fast pulses. The North fast pulse is then delayed (ORTEC 425A) before being used as a stop pulse for the TAC. If these two pulses arrived in coincidence then the height of the timing pulse from the TAC should correspond to the delay set on the North fast pulse. The accepted timing delay is typically 43-49 ns, out of a 200 ns TAC timing range, most of the other non-coincidence counts are used for background correction for non-coincident counts that accidently fall into the accepted timing window (see Fig. 2.10). The black areas (**B**) on a timing spectrum (fig 2.10) correspond to areas where events due to secondary electrons from collisions with the MCP surface [36] may have been recorded, these counts are not used for either true counts or background counts and are rejected. The red areas (**A**) in the timing spectrum is a background of accidental coincidences. The counts measured in this area (**A**) are used to correct for accidental coincidences that fall into the coincidence window (**C**, Fig. 2.10). The other signal to come from the TAC is a +5 V TTL pulse which is sent every time the TAC receives a start and stop pulse within 200 ns of each other. This pulse is delayed so it arrives at the data acquisition card (DAQ) at the same time as the corner pulses and acts as a trigger for the DAQ to record the four corner pulses from each detector and the analog TAC output at that time.

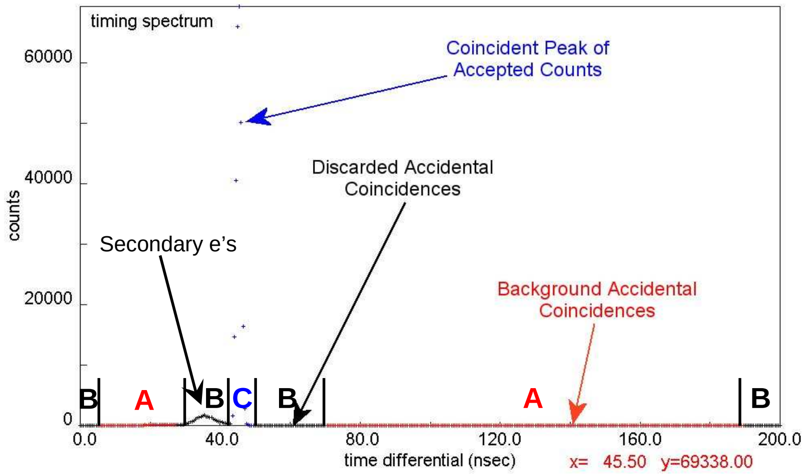

Figure 2.10: A typical timing spectrum from the data acquisition system. Showing the coincidence peak and a small background corresponding to accidental coincidences which can be used for a background correction.

The slow signal processing begins when the electron cloud strikes the resistive anode encoder (RAE) in the position sensitive detector (PSD). The pulse reaching each of the four corners is sent to a pre-amplifier (Canberra 2005) which converts the charge cloud to a voltage pulse. This signal is then amplified by spectroscopic amplifiers (ORTEC 855), which have been calibrated with a test pulse produced from a precision pulse generator (ORTEC 419) so that each corner pulse is amplified by the same amount. This calibration ensures that there are no differences in amplification between the four corner pulses that would lead to the incorrect impact position of the electron on the PSD being calculated. The output of the spectroscopic amplifiers are then fed into the DAQ, and if they came from a coincidence event, they should arrive there as the trigger pulse, produced form the TAC, arrives there and the relative height of the four corner pulses are measured. The ratio of heights of the four corner pulses can be related to an (x,y) position on the resistive anode [47] which corresponds to a specific energy and momentum combination as determined during the calibration procedure:

$$\begin{aligned} x &= \frac{A+D}{A+B+C+D} \\ y &= \frac{A+B}{A+B+C+D} \end{aligned} \tag{2.5}$$

The (x,y) position is determined by the above ratios where A, B, C, D are the intensities of the signal measured at the corners indicated in Fig. 2.9. The height of the four corner pulses undergo a logic test to ensure that either of the two measured counts didn't originate from noise across the plate or from two electrons striking the same detector at the same time. The logic test involves determining the impact position (x,y) and then calculating the expected heights of the four corner pulses which are then compared to the four measured corner pulses. Any measured events that have sufficient discrepancies, between the calculated and measured heights of the corner pulses, are rejected.

Every coincidence pair that successfully passes all the timing and coincidence criteria is written to file, a typical EMS measurement requires 250 000 to 300 000 coincidence counts to achieve sufficient statistics at an average coincidence countrate of 1-2Hz, most measurements are completed in 3-4 days. To ensure uniform sensitivity across the MCPs the power supply upon which the hemisphere is biased is scanned over an energy range in 1 eV steps every minute. Thus the energy scale of the PSD shifts throughout the measurement, averaging out any areas of non-uniform sensitivity in the PSD. Each complete scan across the PSD stores the range of coincidence counts that were measured over that scan, enabling reanalysis of the data as a function of time. Data should be consistent over time, so this re-analysis allows both the long term voltage stability and sample quality to be examined over the time of the measurement.

The software used to collect this data into a matrix, graphically view and manipulate the data was written by Dr Maarten Vos in visual C at the ANU. The software involves correction algorithms by which the accidental counts recorded in the coincident timing spectra can be corrected for and an algorithm that can remove some multiple scattering contributions (section 4.3). In the timing spectrum (Fig. 2.10), counts from the accidental coincidence region (**A**) can be measured as a separate spectra which can be used to correct for the accidental coincidences that would occur under the true coincidence region (**C**). The accidental coincidence contribution (Fig. 2.10, **A**) is very small.

The more common background correction to use on the data is to correct for the relative sensitivity of different momentum and energy combinations. For example if the bound electron has zero momentum then the sum of the measured angles (ϕ) of the two detected electrons must also be zero. There are many more possible combinations of ϕ-angles that result in a total momentum difference of zero, than there is, for say a total momentum difference of 4 au ($\phi_1 \pm \phi_2 \approx 5^\circ$), as the limit of the detectors is generally $\pm 5^\circ$. So to account for the difference in the sensitivity of our detectors, to different combinations of binding energy and momentum, a background spectra can be determined by convoluting the two detector images. This correction is known as a convoluted singles correction and is measured independently from the EMS measurement. All data presented in this thesis will have this sensitivity correction applied to it.

The data collection software also corrects for variations in transit times (section 2.1.3) of the two coincident electrons through the hemispherical energy analysers. The software alters the effective time separation between the two coincident electrons as a linear function of their x-coordinate, before testing for coincidence timing criteria. This data correction procedure is essential for obtaining an accurate timing spectrum and timing coincidence technique. This correction procedure reduces the width of the measured timing peak, minimising the accepted timing window and hence reducing the amount of accidental coincidence counts that contribute to the targets measured spectral function.

2.3 Performance

The performance of the spectrometer can be determined by its resolution in both energy and momentum and the rate at which data is measured (coincidence countrate). These criteria can be theoretically determined to a good approximation, however many effects can not be individually determined in this spectrometer such as space-charge density effects of the electron beam and the effect of sample thickness on the coincidence countrate.

2.3.1 Energy Resolution

The energy resolution of the spectrometer (ΔE_{tot}) can be approximated by the summation in quadrature of the full width half maximum (FWHM) of the energy resolution of the individual components, assuming the energy resolution of each component can be approximated by a gaussian distribution.

$$\begin{aligned} \Delta E_{tot} &= \sqrt{\Delta E_0^2 + \Delta E_1^2 + \Delta E_2^2} \\ &= \sqrt{\Delta E_{thermal} + \Delta E_{sc}^2 + \Delta E_{HV}^2 + \Delta E_{analyser1}^2 + \Delta E_{analyser2}^2} \end{aligned} \tag{2.6}$$

The energy resolution of the incident electron beam (ΔE_0) is made up of many components including the thermal broadening from the cathode ($\Delta E_{thermal}$) which has been calculated to be approximately 150-250 meV given the standard operating temperature of the cathode and the specifications of the cathode provided by Heatwave Laboratories.

The space charge effects (ΔE_{sc}) [48], which are difficult to calculate as each electron gun has its own characteristics. For this analysis the space charge effects will be estimated by comparing the measured experimental resolution to the energy resolution of the individual components. The energy resolution of the high voltage stability (ΔE_{sc}), which includes long term drift and short term ripple, which is minimised by the HV arrangement as described earlier, and is expected to be on the order of 100 meV (2 ppm) [49].

The energy resolution of the two outgoing electrons ($\Delta E_{1,2}$) is completely determined by how accurately there energies can be measured, so it is determined by the energy resolution of the analysers ($\Delta E_{analyser1,2}$). The energy resolution of the analysers is a combination of the width of the entrance slits, the calibration of the position sensitive detector and the pass energy of the analyser. The base energy resolution for the hemispherical energy analysers can be calculated (equation 2.3) [32, 50] to be 330 meV under standard operating conditions. This value however does not include the contribution caused by the calibration of the position sensitive detector which can be determined by the fitting parameters used during calibration to be on the order of 60-100 meV. The overall energy resolution of each detector is expected to be on the order of 400 meV. This energy resolution can be improved by changing the width of the entrance slits (0.5 mm) to the fine entrance slits (0.2 mm) resulting in a drop of the base analyser resolution from 330 meV to 160 meV. This improvement in energy comes at a cost of coincidence countrate which drops by over a factor of 6.

The overall energy resolution of the spectrometer (Eq. 2.6) is experimentally measured to be on the order of 1 eV. By using the measured analyser resolutions and the theoretical resolutions of the thermal broadening and high voltage stabilities, an upper limit on the space charge resolution can be determined to be on the order of 600 meV. The space charge contribution was determined from the experimental resolution of the EMS spectrometer, and as such includes other contributions such as sample effects. So whilst the space charge approximation is expected to be an upper limit, it is still clearly the limiting factor in the experimental resolution.

Source	Theoretical	Experimental
Thermal Broadening	150-250 meV	-
Space Charge	<600 meV	-
High Voltage	100 meV	-
Analyser 1	330 meV	400 meV
Analyser 2	330 meV	400 meV
Total	$\approx$ 1.0 eV	1.0 eV

Table 2.1: An overview of the different energy resolution components. A total energy resolution is obtained by adding the components in quadrature, due to their gaussian nature. The experimentally measured energy resolution (1.0 eV) was used to approximate the space charge resolution (600 meV)

2.3.2 Momentum Resolution

The momentum resolution of the EMS spectrometer is measured along 3 directions (x,y,z) as defined in Fig. 1.2. For disordered samples the vector dependance on the momentum resolution is more relaxed as x and z momentum components are indistinguishable, and to a reasonable approximation the resolution can be expressed in terms of a spherical average, for single crystal samples however the momentum resolution along different axes is important. The incoming and outgoing momentum resolution of the x-components can be individually calculated and then added in quadrature:

$$\Delta q_x = \sqrt{(\Delta q_{x\ incoming})^2 + (\Delta q_{x\ outgoing})^2} \tag{2.7}$$

In the same method the y and z-components can also be determined.

The incoming electron's momentum resolution parallel to the electron beam (z-axis) can be assumed to be negligible as it is related to the energy spread of the beam which is under 11 ppm. Its momentum resolution perpendicular to the propagation direction is determined by the final two beam collimating apertures of 0.4 mm and 0.1 mm which are separated by 200 mm. A Monte Carlo simulation [51] of electrons that are able to pass through these apertures produces a distribution that is near Gaussian and has an RMS value of 0.030 au.

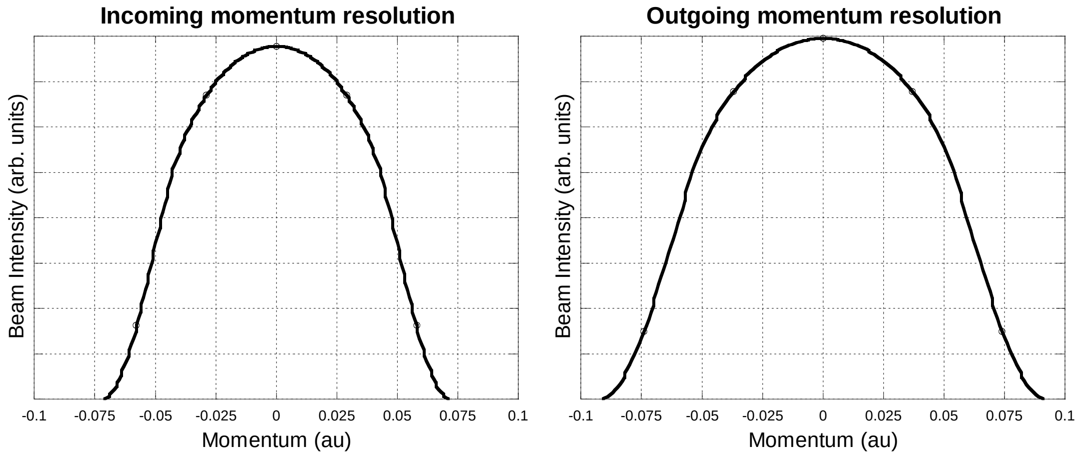

Figure 2.11: The momentum resolution profiles as determined by a Monte Carlo simulation using the incoming and outgoing apertures. The RMS of these near-Gaussian curves is taken as the momentum resolution for the x and y components of the incoming beam and the x and z components of the outgoing beams.

The momentum resolution of the outgoing electrons are again determined by the geometrical configuration of the analysers and also by the calibration of the PSD. The momentum resolution in the x-axis and z-axis is determined using a Monte Carlo code to simulate the outgoing geometries of the beam size on the sample (0.2 mm) and the acceptance slit (0.5 mm) that are separated by 150 mm. The resulting RMS values of each of the x and z components from this calculation was determined to be 0.0375 au. This resolution includes the fact that there are 2 outgoing electrons and that each outgoing electron is at 45° to the x and z axes.

The y-axis momentum resolution can be determined by calibrating the image on the detector plate. By placing the 0.1 mm calibration holes (apertures, see Fig. 2.4) in front of the entrance slit of the analysers, the dots imaged on the detector plate can be used to determine the $\Delta\phi_y$ which can be converted to an overall momentum resolution in the y-direction. The width of the image on the detector plate after correcting for the non-zero entrance aperture width (0.1 mm) was shown to be 0.1648 mm which corresponded to a momentum resolution of 0.0120 au. When taking the two detectors into account the

	x-axis	y-axis	z-axis	spherically averaged
Incoming	0.030 au	0.030 au	0.00 au	0.020 au
Outgoing	0.0375 au	0.0170 au	0.0375 au	0.0307 au
Total RMS	0.048 au	0.0355 au	0.0375 au	0.0366 au
Total FWHM	0.105 au	0.0781 au	0.0825 au	0.0885 au

Table 2.2: The momentum resolution components along the three axes, determined for the wide analyser slits which are more commonly used. The spherical averaged result (0.089 au) is applicable for disordered samples, to determine the momentum resolution for crystalline samples (≈0.1 au) is more complicated. These components have been added in quadrature to achieve a total momentum resolution which is an approximation of their near gaussian distribution.

overall momentum resolution in the y-axis is 0.0170 au RMS.

To obtain the momentum resolution of the whole experiment the incoming and outgoing momentum resolutions must be added in quadrature to obtain the following momentum resolutions (0.048 au, 0.0355 au, 0.0375 au) for the (x,y,z) axes respectively. Taking the spherical average of these momentum resolution components an overall resolution of 0.0653 au is obtained. Converting these values to FWHM values the momentum resolutions of (0.105 au, 0.0781 au, 0.0825 au) respectively and a spherical average of 0.0885 au are obtained.

The total FWHM values quoted in the above table are assuming the momentum distributions are a Gaussian distribution. As seen in Fig. 2.11 this assumption is not completely true, but is a reasonable first approximation. The conversion of the momentum resolution into FWHM values was performed to allow comparison with other techniques that quote momentum resolution in terms of the FWHM.

2.3.3 Coincidence Countrates

Coincidence countrates are affected by the cross section of the target, the incoming current density and the area on the target which is being measured over. All of these effects could be improved in this spectrometer but doing so would reduce other aspects of the spectrometers performance.

The electronic structure of a target is fixed for any given target, but the reaction kinematics are not. It is possible to change the reaction kinematics so that the measured energy transfer and scattering angle is near the maximum of the Bethe ridge ([52]). The Bethe ridge is a ridge in the theoretically calculated surface for the magnitude of the cross section of an electron scattering experiment as a function of energy transfer and scattering angle. Whilst the symmetric scattering conditions lie on the Bethe ridge, they are at a point further down the Bethe ridge which has a lower cross section than the equivalent (50 kV) asymmetric scattering conditions would have. By changing the kinematics from symmetric to a non-symmetric configuration the coincidence countrate can be increased, however this also increases the effect of multiple scattering as one of the outgoing electrons would be much lower in energy. Multiple scattering plagued early attempts at solid state (e,2e), so this spectrometers design was specifically aimed at reducing the effect of multiple scattering as much as possible, hence the high energy and symmetric scattering geometry.

Increasing the incoming current density would linearly increase the coincident countrate. Driving the cathode filament at a higher operating current would also increases the effect of thermal broadening and space charge effects of the incident electron beam. Current operating criteria require 500-600 nA of current on the sample to achieve acceptable coincident countrates for most samples. This is much higher than the Flinders EMS spectrometer [12], which uses an asymmetric (20 kV) scattering geometry which is further up the Bethe ridge and hence at a higher scattering cross section, which only requires an incident electron beam of 100 nA to reach the sample. The advantage of the ANU spectrometer is the symmetric scattering conditions minimises the effect of multiple

Slit width	Energy Resolution	Relative Countrate
0.2 mm	160 meV	1
0.5 mm	330 meV	6.25
0.8 mm	641 meV	16

Table 2.3: The effect on the energy resolution and detection efficiency of the analysers by changing the size of the entrance slits. The typically used entrance slit (0.5 mm) is a compromise between energy resolution (Eq. 2.2) and detection efficiency.

scattering.

The volume of phase space, over which the spectrometer measures, can be increased or decreased by changing the size of the entrance slits to the detectors. Enlarging the area of phase space measured by the detectors would result in a higher coincidence countrate. However increasing the size of the entrance slits on the detectors would have an adverse effect on the momentum and energy resolution (Tab. 2.3):

The standard entrance slit (0.5 mm) yields a moderate coincidence countrate whilst still maintaining an acceptable energy resolution. If a sample with a high cross section is measured then the thin slits (0.2 mm) may be used at a reduced coincident countrate. Alternatively a wider slit, (eg. 0.8 mm) could be used to obtain a higher coincidence countrate (2.5 times) than the 0.5 mm slit, however this would result in a decrease of the energy resolution of the analysers from 330 meV to 641 meV. The analyser energy resolution would then be the dominant factor in the overall energy resolution, meaning the increased energy resolution would be directly visible in the EMS results (Table 2.3).

Designing an electron spectrometer is a compromise between various aspects such as resolution, acquisition time and simplicity. The ANU EMS spectrometer was designed to minimise multiple scattering, whilst still maintaining good energy and momentum resolution and a moderate coincident countrate. Those design criteria have been well met.

2.4 Sample Preparation and Characterisation Chambers

The experimental results will only be as clear as the sample is pure, hence sample preparation is critical. If there is contamination in the sample or the sample is not in the correct atomic arrangement then the results will either be contaminated or interpreted incorrectly. A transmission EMS experiment requires thin, flat, free standing films in order to perform a measurement that is not dominated by multiple scattering. Atomically clean samples are required in order to ensure accurate results. To achieve this all of the final stages of sample preparation are preformed under UHV in either the evaporation chamber for materials which are prepared via evaporation deposition. Or in the preparation chamber where techniques such as sputter thinning, plasma etching, annealing and Auger spectrometry are performed to produce and characterise thinner and cleaner samples. There is a sample storage carousel in the preparation chamber so that many samples can be stored under a UHV environment, to ensure contamination is minimised, before a measurement takes place.

Sample preparation differs vastly depending on the atomic arrangement required (single crystal, polycrystalline or amorphous), the availability of commercially made products and aspects of the growth mechanisms. As each sample mentioned in this thesis was prepared using different methods, a complete description for each sample will be given in the relevant sections in chapters 4, 5 and 6. In this section a brief description will be given of the preparation techniques and experimental layouts that were used for samples produced in this thesis. This following section is in no way a complete description of the preparation facilities at the ANU EMS laboratory.

The evaporation and preparation chambers are the two main sample preparation chambers on the ANU EMS spectrometer (Fig. 2.1). Both are kept at a UHV state by turbomolecular (turbo) pumps (Pfeiffer, TMU260IS) which are backed by a rotary roughing pump (Pfeiffer, DUO10). The pressures of both chambers are monitored with an ion gauge controlled by a Granville-Phillips controller (model 307). The ion gauge controllers have built in set points that control interlock boxes for each system, that will shut off the power to the electronic units associated with each chamber and also close pneumatic gatevalves to protect the turbo pumps.

2.4.1 Evaporation Chamber

Many samples can be prepared by evaporative deposition. The samples produced by this method are either amorphous, polycrystalline or single crystalline dependant upon the growth mechanism of the individual targets and the substrate they are being deposited onto. A UHV vacuum is needed to prevent contaminants adhering to the sample during the evaporation procedure. The required evaporation system must be able to control both the rate of evaporation and the total thickness of deposition.

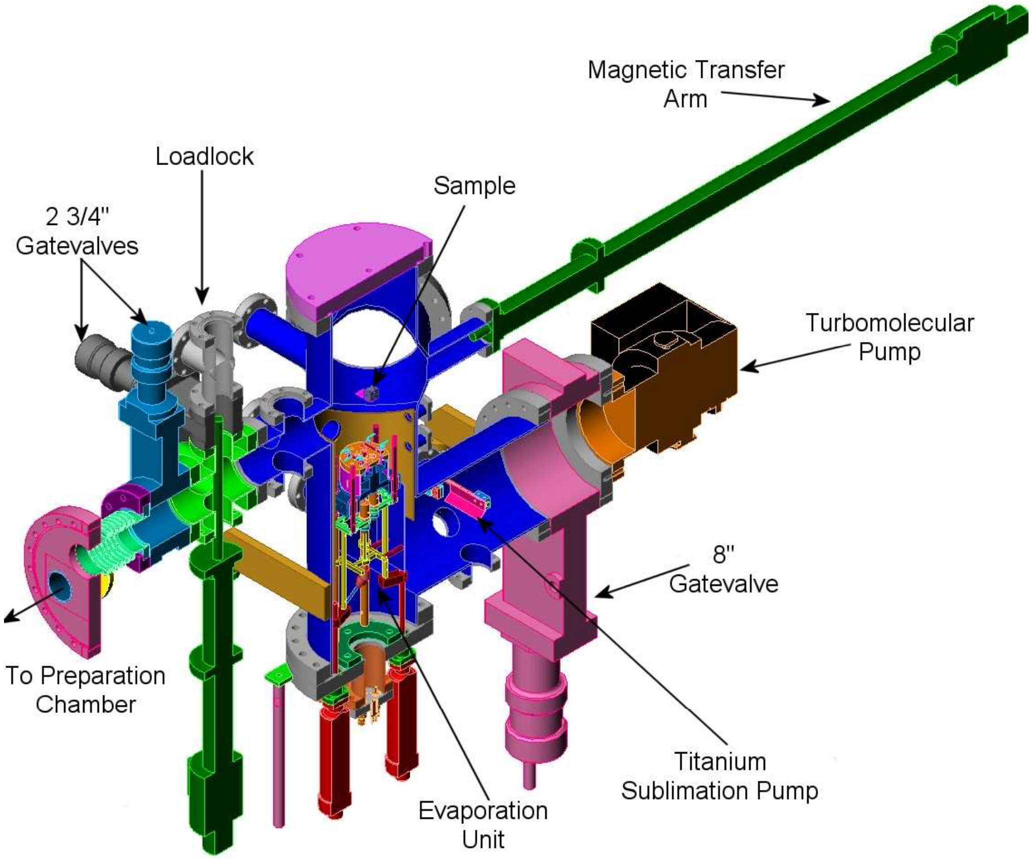

Figure 2.12: The layout of the evaporation chamber, showing the positions of the loadlock, magnetic transfer arm, pumping system and relative position of the preparation chamber.

The loadlock is a purpose built system that enables samples to be transported into and out of the UHV system without having to break the evaporation chambers vacuum. The loadlock is a $2\frac{3}{4}$" four way cross that is separated from the evaporation chamber by a gatevalve (MDC GV-1500M-04). The loadlock is brought up to atmospheric pressure by introducing nitrogen through a leak valve, then the viton sealed port is opened and the sample is placed onto a vertical transfer arm. As the loadlock chamber is only open to the atmosphere for a few seconds it is easily roughed back down to 10^{-3} torr. The gatevalve is then slowly opened to the evaporation chamber and as there is only a very small volume in the loadlock the evaporation chamber remains under 1x10^{-6} torr. When the gatevalve is fully open the sample can be transferred to the evaporation chamber. The vertical manipulator is then retracted back into the loadlock and the gatevalve once again closed. The pressure in the evaporation chamber recovers back to its base pressure over the next few hours. This method minimises the amount of contamination in the UHV system.

2.4.2 Evaporation Unit

The evaporation unit was designed and built at the ANU. It is able to house four different materials for evaporation at any one time and can evaporate one material individually or two materials simultaneously. This allows the preparation of alloys, prepared with differing ratios of constituent species (section 5.2). To monitor and calibrate the rate of evaporation there is a vibrating quartz crystal monitor (Maxtek inc.) near the top of the chamber. This quartz crystal monitor is 195 mm ($d_{crystal}$) from the evaporating material and thus using Eq. 2.8, the rate of evaporation onto the sample which is 90 mm (d_{sample}) away from the evaporating material can be measured.

$$Th = A \times TF \times \Delta P \times \Delta t. \tag{2.8}$$

Where Th is the thickness of material evaporated, A is a constant of the quartz crystal that is determined in the factory. ΔP is the ratio in density of quartz to density of evaporated material and must be set before evaporation on the quartz crystal monitor controller (MaxTek TM 100). Δt is the difference in the period of oscillation, which is a measure of the amount of material that has been evaporated. TF is a tooling factor which includes the differences in distance from the evaporating material to the quartz crystal monitor and sample. The deposition drops off as r^2 from the source, so the tooling factor is given by;

$$TF = \left(\frac{d_{crystal}}{d_{sample}}\right)^2 \times 100\%. \tag{2.9}$$

By measuring the amount deposited and then differentiating with respect to time, an evaporation rate can be determined.

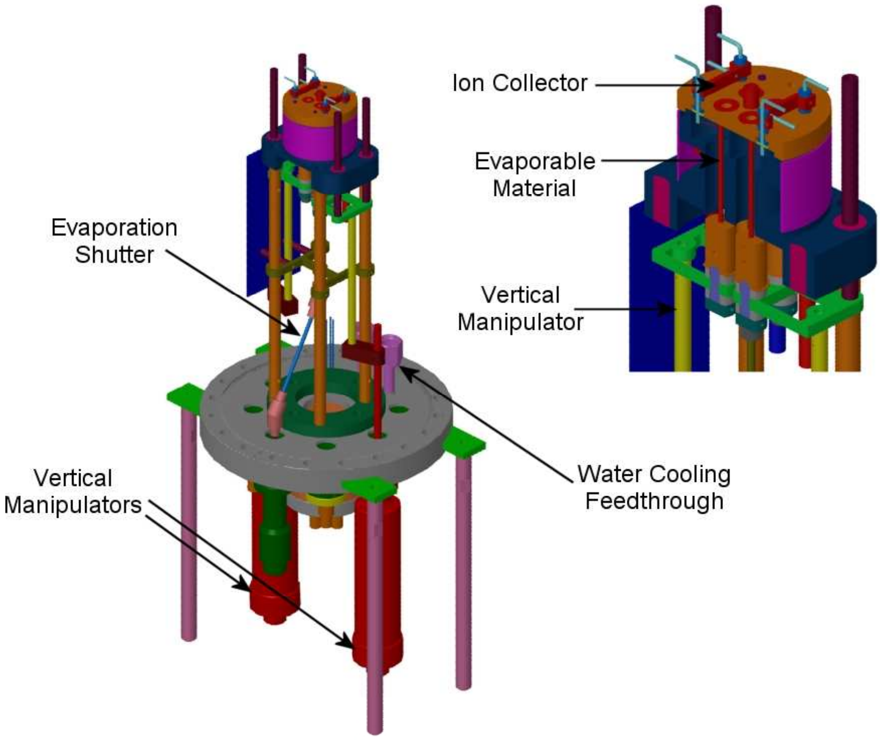

Figure 2.13: The Evaporator unit, showing the position of the tungsten filaments, evaporating materials, ion collectors and vertical manipulators used to move that evaporable materials into position.

The evaporation unit consists of a tungsten filament, which is coiled closely around the evaporable material. A current is passed through the filament and the source material is held at a potential of 3 kV, thus electrons that are emitted from the filament bombard the material. This electron bombardment heats the material turning it into a vapour. A certain fraction of the atomic beam is ionised thus the rate of evaporation is proportional to the amount of ions produced by the evaporating material, which is measured with an ion collector biased at -36 V. When the sample is in position the computer controlled filament can vary its emission to maintain a constant rate of evaporation based on the measured ion current. The computer program also tracks the total amount deposited on the sample and when the desired thickness is reached the evaporation can be terminated. The typical evaporation rate is normally of the order of 0.1 Å/sec.

The evaporable materials are each mounted onto the end of a vertical manipulator so they can be moved into the correct position for evaporation with the tungsten filament. This generally enables many evaporations out of each material before the material needs to be replaced. During evaporation the tungsten filament heats the surrounding area, as a result the pressure in the evaporation chamber is increased due to outgassing. To dampen this effect the evaporation unit has a water cooling jacket built into the region surrounding the tungsten filaments. This jacket helps to maintain pressures on the order of 10^{-9} torr during evaporation.

2.4.3 Preparation Chamber

The preparation chamber is where the final stages of sample preparation take place including sputter thinning and annealing, which are used to thin and clean the surface and rearrange the atomic order of samples. Characterisation of the surface cleanliness with Auger spectroscopy (Physical Electronics) is also performed in the preparation chamber prior to insertion into the main chamber. For this reason the preparation chamber must be maintained at the lowest possible pressure to prevent surface contamination of both the prepared samples and samples stored on the storage rack mounted in this chamber.

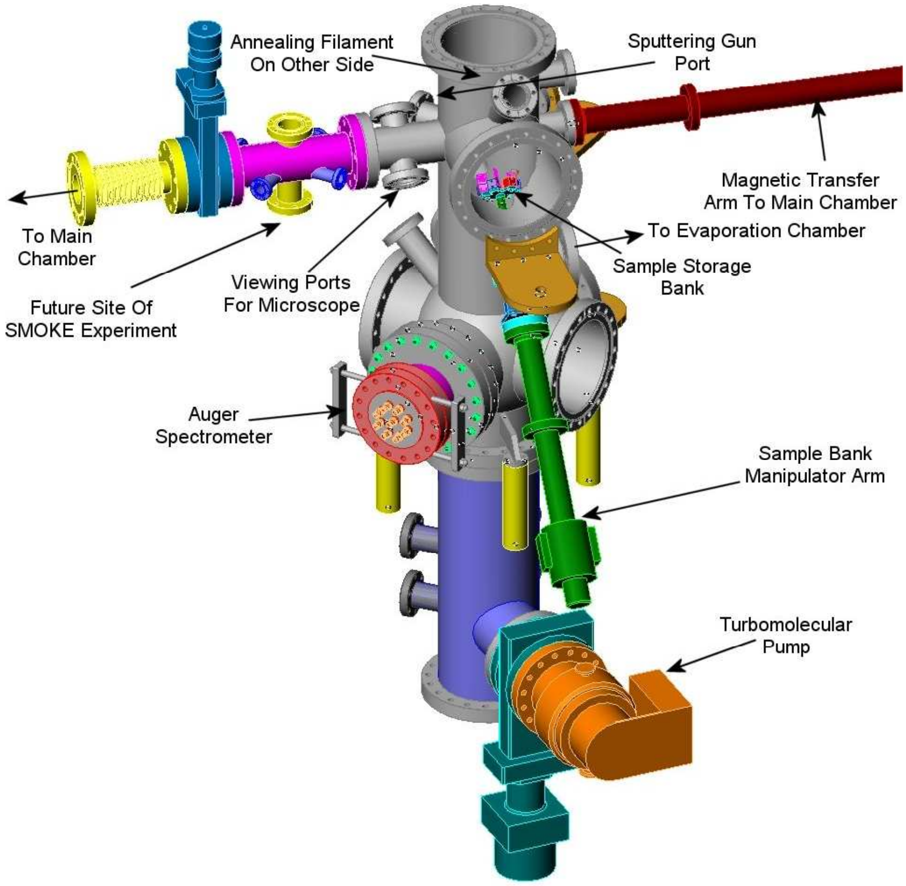

Figure 2.14: The preparation chamber, showing the configuration of the sputtering and annealing preparation systems. As well as the Auger characterisation and microscope viewing ports. Also the position of the sample storage bank, and connections to the evaporation chamber and main experimental chamber. The future site of a potential SMOKE magnetisation characterising system is also shown.

Annealing

The preparation chamber houses an annealing filament that is mounted onto a 1” horizontal manipulator which can extend the annealing filament close to the sample mount. Annealing can be used to clean loosely bonded contaminants from the surface of samples or to change the bonding configuration for some samples, from amorphous to polycrystalline. Solid state recrystallisation [53], or atomic rearrangement, via annealing is a well documented process having been first noticed by metal workers in the early 19th century, and was later modeled to other solids [54]. The annealing setup in the ANU EMS apparatus was not designed to measure effects such as transition temperatures, and is thus unable to do so. The annealing filament is used to just induce the transition so the sample is heated and then characterised and if it has not yet fully recrystallised then it can be taken back for further heating. Recrystallisation in the preparation chamber can be a trial and error method, but most metals and semi-conductors can be generally recrystallised quite easily (1W, 10 min).

Sputtering

Sputter thinning samples is performed in the preparation chamber by introducing argon (Ar) ions through a sputtering gun (LK technologies NGI3000). This sputtering gun is designed to work at low background pressures (1×10^{-6} torr) so there is no need for any differential pumping stage in the preparation chamber. The sputtering gun is capable of accelerating the Ar ions up to 3 kV, which would increase the rate of sputtering. The disadvantage is that the penetration depth of the sputtering beam is greatly increased and this results in a greater depth of disorder at the surface (see section 4.1).

For polycrystalline or amorphous samples the sputtering induced surface disorder does not matter, however for single crystal samples the effect adds a small amount of the disordered state results to the measured single crystal spectral function. The resulting signal from the disordered layer overlaps the sharp features seen in the single crystal spectra, producing a mixed spectra that would look less resolved.

To position a sample for sputter thinning the sample mount in the preparation chamber has a Faraday cup mounted on it, that is used to measure the Ar^{+} flux. The Faraday cup is placed in line with the sputtering beam by maximising the current measured on the Faraday cup. This position is aligned by line of sight with an externally mounted telescope. Using the cross hairs of the telescope for horizontal and vertical alignment and the focus for the small adjustment in depth required, the sample can be positioned in the correct position in line with the sputtering beam. The progression of the sputter thinning process is monitored by an externally mounted telescope, once a sample appears near the desired thickness it can be transferred into the main chamber and have an EELS spectrum taken to give a more quantitative indication of its thickness.

Chapter 3

Spin-Polarised Electron Source

Spin-polarised electron sources are becoming more common and more widely used in different areas of physics such as surface, solid state, atomic and high-energy physics [55]. The development of such sources is allowing these different areas of physics to directly probe spin dependent phenomena. A GaAs spin-polarised electron source has been designed and built to be used on the solid state EMS spectrometer at the ANU. The primary goal is to increase the energy resolution of the experiment, with a secondary aim to probe magnetic samples in future work.

3.1 History

For a long time polarised electrons could only be produced from high-energy Mott scattering, but in the 1970's a variety of techniques developed. These techniques can be subdivided into two classes, the first uses electrons that have been extracted from materials with orientated spins like ferromagnetic solids, the second class uses electrons that have been photoemitted from unpolarised sources where spin-orbit coupling leads to an electronic spin polarisation. The most successful method was photoemission from the surface of a p-type GaAs crystal, which belongs to the second of the two classes. The reason why the GaAs polarised electron sources are considered so successful is due to the sources high figure of merit (P^2I). The figure of merit is an arbitrary concept used to compare the effectiveness of different sources of spin polarised electrons, using the two pre-requisites of a spin polarised electron source, the polarisation (P) and the intensity (I). GaAs sources have the added benefit of being able to quickly reverse the polarisation of the produced electron beam, which is done by changing the state of the circularly polarised incident light.

Production of spin-polarised electrons from the photoemission of a GaAs p-type crystal was first suggested in 1974 [56, 57, 58]. The first working prototype was developed in early 1975 [57, 59] by Pierce *et. al.*. They demonstrated an electron polarisation of 45% near the photothreshold. This was achieved by using a p-type crystal that had been covered in many consecutive layers of caesium and then oxygen to bend the conduction band and achieve a NEA near the surface (Fig. 3.2). The method of applying the caesium and oxygen would later become affectionately known as the “Yo-Yo” method, which aptly describes the intensity fluctuations of emission current during the NEA activation. Groups have since used this method of producing polarised electrons and have achieved short term (minutes) DC emission in the range of milliamps [60, 61] and pulsed emission in the range of amps [62].

The limitation in the GaAs polarised electron source has always been the theoretical maximum polarisation of 50%, many groups have overcome the problem by producing strained crystals which are typically alloyed with phosphour [63, 64], or by using superlattices [65, 66]. Both these new types of crystals remove the degeneracy of the $P_{3/2}$ orbitals (Fig. 3.1) and hence the maximum achievable polarisation increases [66]. Recently theoretical work is being done in this area to try to recognise new crystal structures that will completely remove degeneracy via spin-orbit splitting and crystal-field splitting [67]. The remaining restricting factor being spin relaxation times and transmission times of the excited electrons in the crystal, which can be minimised by emission from ultra thin crystals.

3.2 Theory of GaAs Polarised Electrons

GaAs is a semiconductor with its valence band 1.52 eV (816 nm) below the conduction band at the Γ point at 0 K [55]. This represents the threshold energy of the crystal, that is the lowest amount of energy that can possibly excite an electron into the conduction band. The transition probabilities at the Γ point from the P state to the S state (Fig. 3.1) are shown with the relative intensity of each of the transitions.

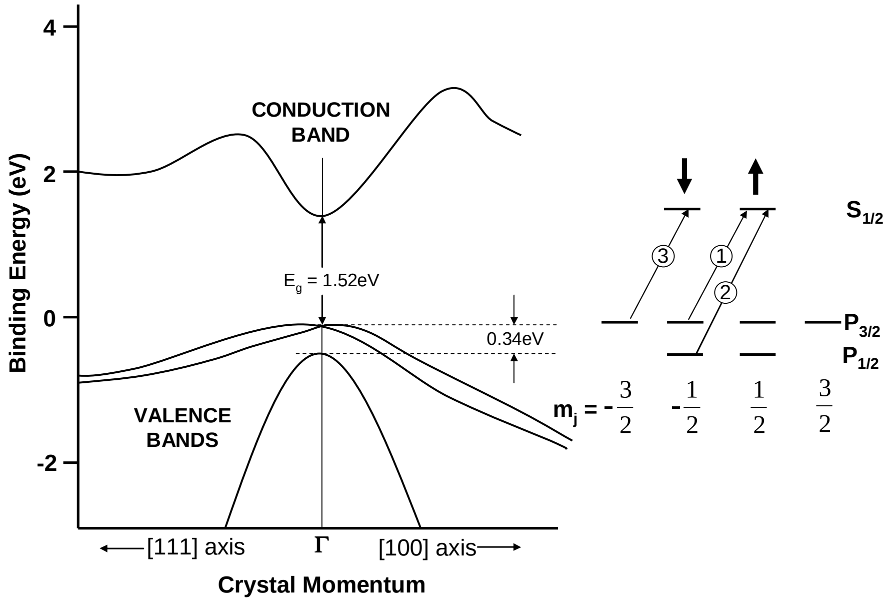

Figure 3.1: Left: An overview of the band structure of the GaAs crystal [68, 55]. Showing the spin-orbit splitting at the Γ point of the P orbital. Right: The relative intensities of the different transitions for σ^+ initiated excitation (shown in circles).

The relative probabilities of the different transitions shown in the above figure come from the calculation of the matrix elements of the transitions $\langle\Psi_f|H_{int}|\Psi_i\rangle$, which can be solved for by using spherical harmonics for the wavefunctions. Selection rules govern that for circularly polarised light (σ^+) only transitions with $\Delta m_j = +1$ are allowed, these transitions are shown in Fig. 3.1 (solid lines). Irradiating with σ^+ light will produce photoemission of electrons with a spin asymmetry of 3:1 (spin $\downarrow$: spin $\uparrow$). Using the definition of spin polarisation (Eq. 3.1) where $N\uparrow$ ($N\downarrow$) are the number of electron magnetic moments parallel (anti-parallel), the GaAs source will yield a theoretical 50%

spin polarised electron beam. Whilst the theoretical maximum is 50% polarisation, in reality GaAs sources often have a much smaller polarisation due to spin relaxation that occurs during photoelectron transmission through the crystal.

$$P = \frac{N\uparrow - N\downarrow}{N\uparrow + N\downarrow} \tag{3.1}$$

The work function for a GaAs crystal is on the order of 4 eV, and depending on the wavelength of light used the free electron will, at most, have only a few hundred meV of energy which is insufficient to overcome the potential at the surface and escape into the vacuum. To get the crystal to photoemit, a negative electron affinity (NEA) must be induced at the surface. This can be achieved by coating the crystal with caesium and oxygen, to form a caesium oxide compound [69, 70], which bends the conduction band to below the vacuum level (figure 3.2), allowing the excited electrons to easily escape the surface and become photoemitted. The spins of the electrons are either parallel or anti-parallel to the surface normal of the crystal.

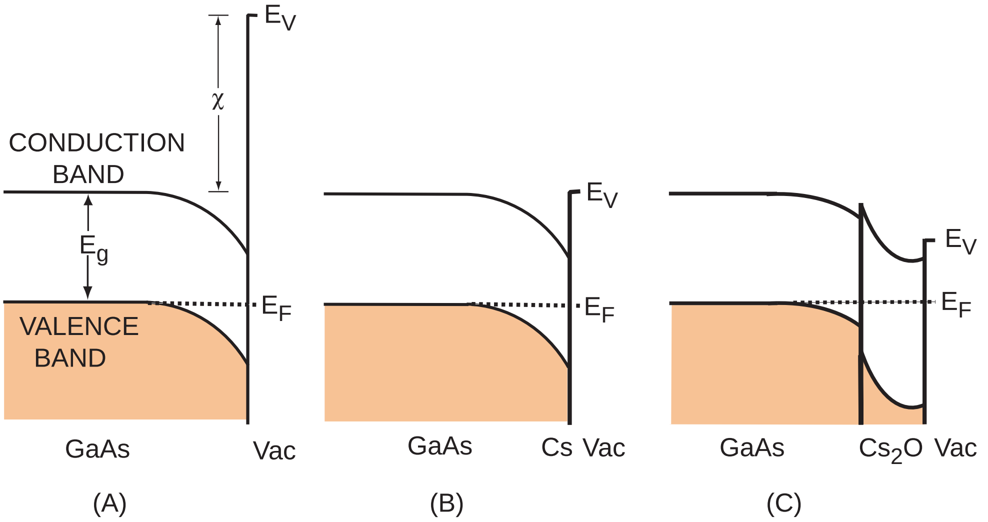

Figure 3.2: The effect on the band diagram of Cs and O_2 being added to the surface of a GaAs crystal. Initially the vacuum level (χ) is large ($\approx$4 eV), but by adding Cs and then O_2 the outer most region of the crystal is bent to a level lower than the vacuum potential to achieve a negative electron affinity (-χ), meaning excited electrons near the surface will be extracted from the crystal.

3.3 Design

The GaAs polarised electron source which was developed for the ANU solid state EMS spectrometer had many key design criteria, including a high intensity (10 μA) with a long activation lifetime (1 week). The crystal is required to be held at a potential of -25 kV, and this restricts the design. As in most polarised electron sources the electron polarisation is required to be switched from spin-up polarisation to spin-down polarisation relative to the experimental y-axis, so that the electrons will be polarised parallel to the sample surface. For EMS a narrow, well collimated beam size is also required to help the energy and momentum resolution of the experiment, so several collimating apertures and focusing elements are used.

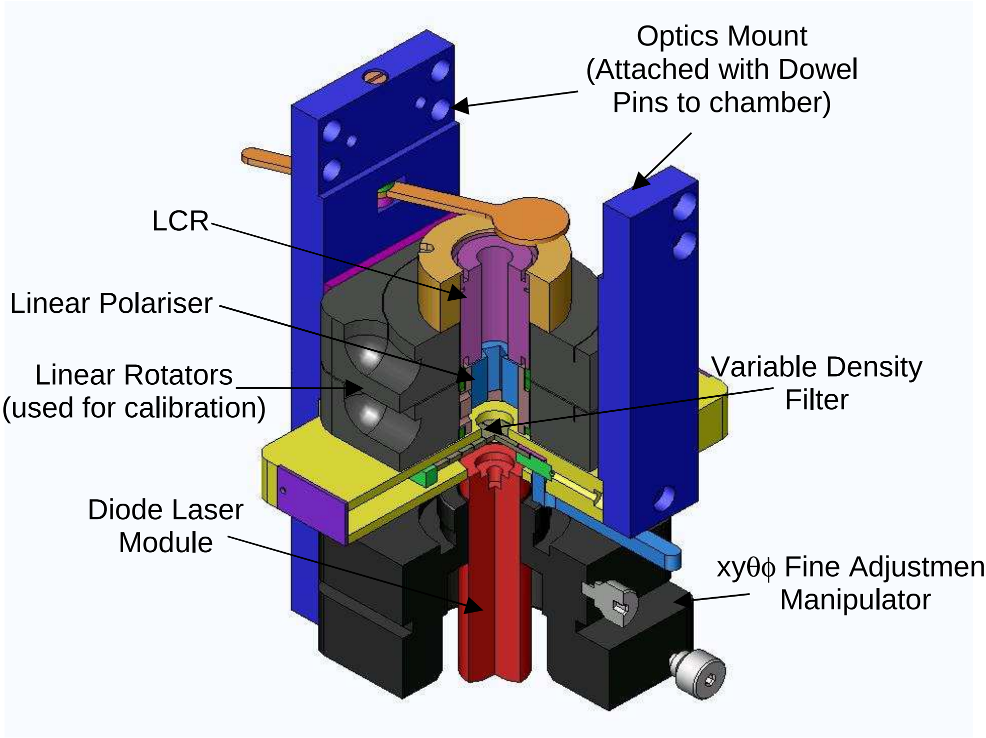

Figure 3.3: The laser mount area with optics, that achieves circularly polarised light whilst also being able to quickly change the direction of circular polarisation.

The production of the polarised electron beam begins with the laser and optics (Fig. 3.3) which produce the circularly polarised photons that initiate the photoemission process. The laser passes through a stepped density filter (Edmund scientific J32-599). The density filter enables a variation of the laser power, so as the crystal emission degrades with time the laser power reaching the crystal can be increased to maintain approximately the same emission current. This maximises the activation lifetime of the crystal.

A Glan-Thompson linear polariser (Melles Griot 03PTH109/C) ensures the laser is linearly polarised, prior to passing through the liquid crystal retarder (LCR)(Meadowlark LVR-100) which can vary the retardation between $\frac{\lambda}{4}$ and $\frac{3\lambda}{4}$ in 5-20 ms. These different retardation values correspond to the σ^+ and σ^- polarised light which will produce spin parallel and spin anti-parallel electrons with respect to the surface normal of the GaAs crystal. During measurements the spin-up and spin-down electrons will be switched once every minute to minimise the effect that any experimental drifts or fluctuations will have on the measurements. The fast switching time of the LCR enables fast switching between the produced spin up and spin down electrons, minimising the dead time in the data collection process.

The crystal area and the grid focussing element are both floating at -24.5 kV which will be referred to as the negative high voltage (-HV) area. The grid can be biased at a higher potential than the crystal area to act as a focussing element. The crystal is insulated from the grid by M3 ceramic shoulder washers, and the grid is insulated from the ground mesh by 35 kV insulators (ISI 9951208). The GaAs crystal sits inside the -HV region above a 4 mm diameter hole. Above the crystal a thin sheet of molybdenum is used to separate the crystal from the UHV button heater (Heatwave 101136). The button heater is held in place with a spring that provides pressure on the button heater from a macor barrier that is screwed in place above the button heater. The spring's force constant is gradually reduced by the heat produced during the crystal cleaning cycle, so the spring is required to be replaced upon changing the crystal in order to maintain a reasonable amount of downward pressure in the button heater. To help overcome the loss of tension in the spring a specially designed tungsten wire was incorporated as the return wire for the button heater, which is also used to provide a downward force which keeps the button heater in place.

Initially a thermocouple was attached in the region between the button heater and the

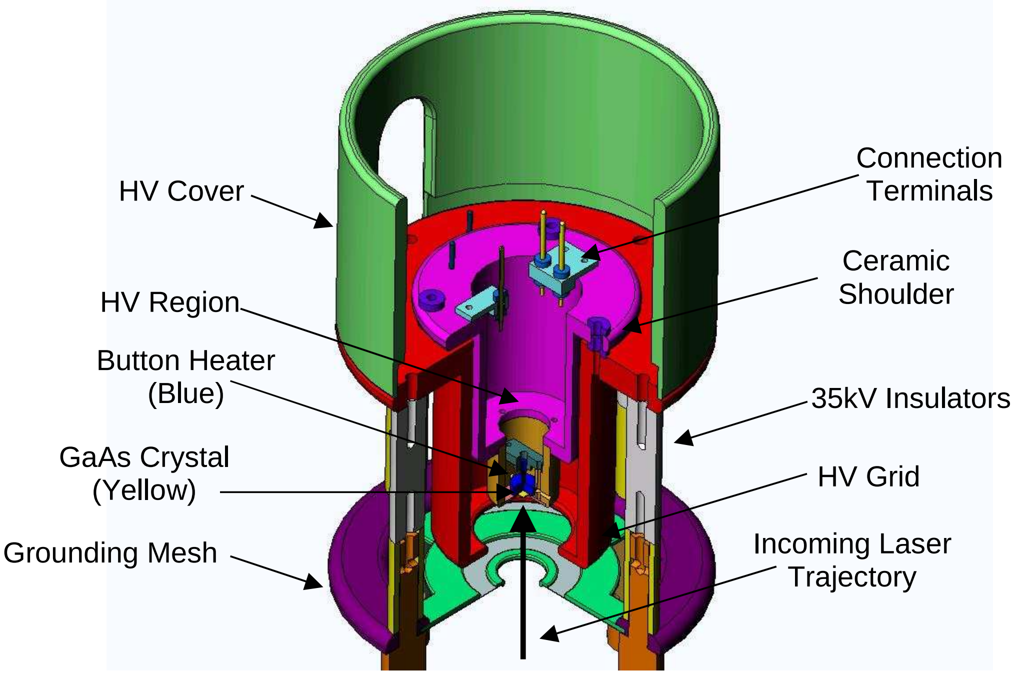

Figure 3.4: The crystal mounting stage incorporates the HV crystal region (purple and orange), that is electrically isolated from the HV grid region (red). The button heater (blue) and GaAs crystal (yellow) can be seen inside the HV crystal region. The 35kV aluminium oxide insulators can be seen and below those is a 50% transmission grounding mesh that creates a uniform electric field between the grid and ground to avoid any adverse affects on the electron beam.

crystal to monitor the crystal temperature during the heat cleaning cycle. The thermocouple system was inadequate to determine the temperature on the far surface of the crystal, as too much heat was being lost to the surrounding area, so a new method to determine the temperature of the crystal surface was required. the crystal temperature can be monitored using a pyrometer [71], but that requires having a window in the chamber so the crystal surface is easily viewable. As this design was based around the thermocouples to measure the temperature of the crystal there was no side window from which the crystal surface was viewable. There was however a hole through the base of the hemispherical deflector and along the electron beam that was designed for the incoming laser beam to pass through. This path was too small for any conventional pyrometer to be effective, so instead a CMOS (complementary metal oxide semiconductor) camera (Electrim EDC-1000) was used to measure the intensity of the blackbody radiation emitted by the crystal during heating (section 3.4).

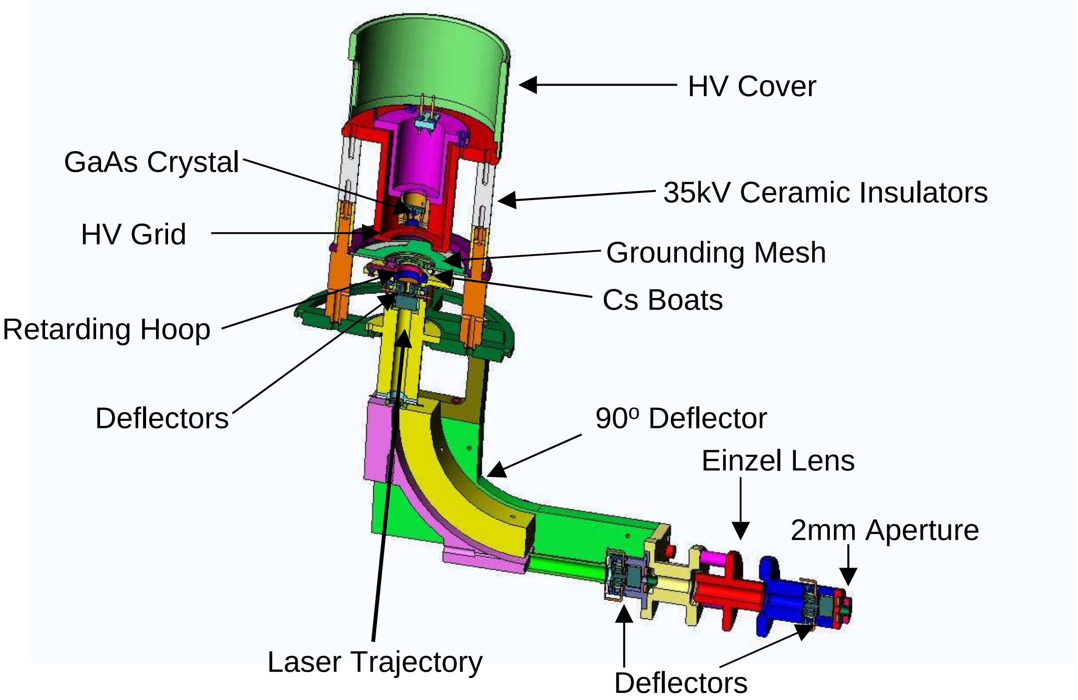

Figure 3.5: The whole polarised electron source, showing the relative positions of the crystal region (see Fig.3.4), the 90° deflector for making the spin polarisation axis and electron beam direction orthogonal, and the einzel lens for focussing prior to entering the main chamber.

The overview of the production of spin polarised electrons from this design begins when the laser strikes the crystal via small apertures drilled through the 90° deflector. This then initiates an electron excitation from the valence band (P) to the conduction band (S). The excited electron then heads towards the surface and is emitted due to the negative electron affinity (NEA) [72]. Due to the transition probabilities the electrons will have a preferential spin orientation (see section 3.2) resulting in a spin polarised electron beam. The emitted electron beam is focused by a grid element, before passing through a collimation aperture and two sets of deflectors. The electron's spin orientations are parallel to the incident light source and hence the electron beam must undergo a rotation of 90° so they strike the sample with the electron spin polarisation parallel to the sample surface. For this purpose the polarised electrons then pass through a 90° hemispherical deflector (Fig. 3.5). Upon exiting the hemispherical deflector the electron beam is focussed by an einzel lens, and then passes through a final collimation aperture, before entering into the main chamber. All these apertures and deflectors were designed to ensure a finely focused beam whilst still maintaining a relatively high transmission of electrons through to the target region.

3.4 Activation

Activation of the GaAs crystal into a spin-polarised photocathode requires obtaining a NEA at the crystal surface to enable the excited electrons to escape from the solid to the vacuum. This is achieved by coating the surface with caesium and oxygen which induces a bending in the vacuum level, so that the vacuum level becomes lower than the conduction band, allowing free electrons to easily escape from the surface.

Each activation begins with a heat cleaning cycle, to remove impurities from the surface that have accumulated there from transfer into the chamber or from impurities gathering onto the surface over time since the previous heat clean. The heat clean is the most critical process of the whole activation cycle. Too cold and the surface will not be clean enough to re-activate, too hot (above 660°C) and arsenic (As) can preferentially evaporate from the surface [73, 74] changing the stoichiometry and band structure of the crystal rendering the crystal useless for polarised emission. In an ideal heat clean the crystal surface is heated to 600-650 degrees and held there for a few minutes [73, 75]. The crystal surface temperature measuring technique required the camera to have the same focus, position and stray light acceptance for every single measurement. As these conditions were unable to be met in the current configuration a modified technique was used. A hot mirror filter (700 nm, high energy pass) was placed in front of the camera and the ratio of the unfiltered intensity to the filtered intensity was measured.

The ratio of filtered to unfiltered emission intensities should be reasonably constant between measurements, despite external effects such as a slight misalignment of the camera, stray light or focussing conditions. These ratios were experimentally determined from several heat cleaning cycles that were conducted at successively higher tempera-

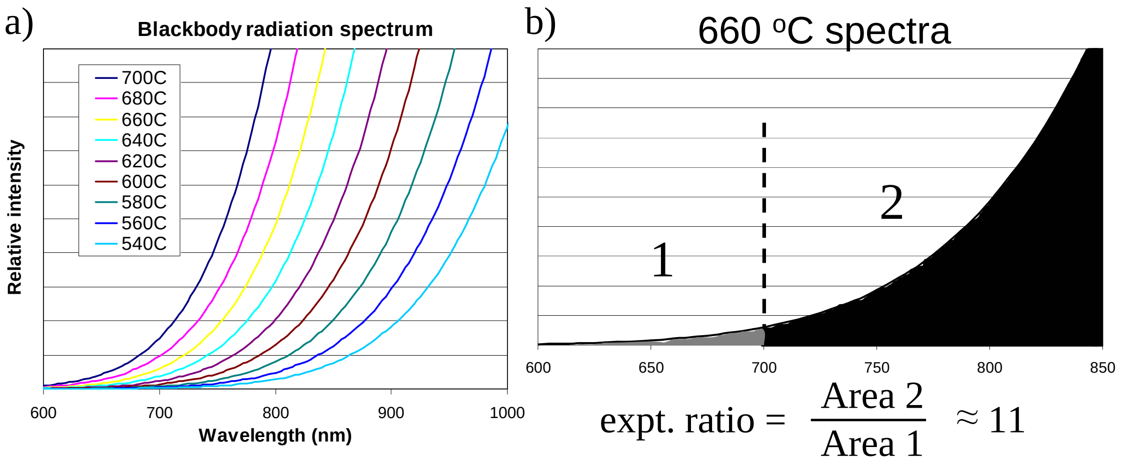

Figure 3.6: a) The blackbody radiation curves for objects at different temperatures, $I = \left(\frac{2\pi hc}{\lambda^3}\frac{1}{e^{\frac{h\nu}{\lambda kT}}-1}\right)$. b) A representation of the different emission intensities for the 660 °C blackbody radiation curve, the ratio for these intensity ranges 350 nm-700 nm:350 nm-1000 nm was experimentally determined to be 11:1.

tures (button heater input power) until the resulting emission from the activated crystal began to decrease. Upon opening the experimental chamber and examining the GaAs crystal it was evident that at this point the crystal had been overheated as the surface of the crystal had changed appearance, a sign that arsenic had begun to evaporate from the surface. From this calibration the resulting optimised blackbody emission ratio (with and without hot mirror) of approximately 11:1 was determined. Heating a crystal to this emission ratio would result in a heat cleaning temperature that would not damage the crystal stoichiometry but would still produce a clean crystal surface.

Once the crystal surface is heat cleaned the caesium (Cs) boats (SAES Cs-NF-5.4-17-FT) are heated to a low Cs emission rate whilst the crystal cools. After about 12 hours the crystal is sufficiently cool for Cs to begin to stick to the surface of the crystal. At this time the Cs emission is increased to around 4A (see section 3.5.2). The emission current from the crystal is then continuously monitored until the maximum electron emission is reached and then drops to 50-70% of that maximum. Oxygen (O_2) is then added and the emission increases to a new, higher, maximum before once again decaying to 50-70% of the new maximum at which time the O_2 is turned off. The Cs cycle then begins again and the process is repeated until no further increase in emission is evident.

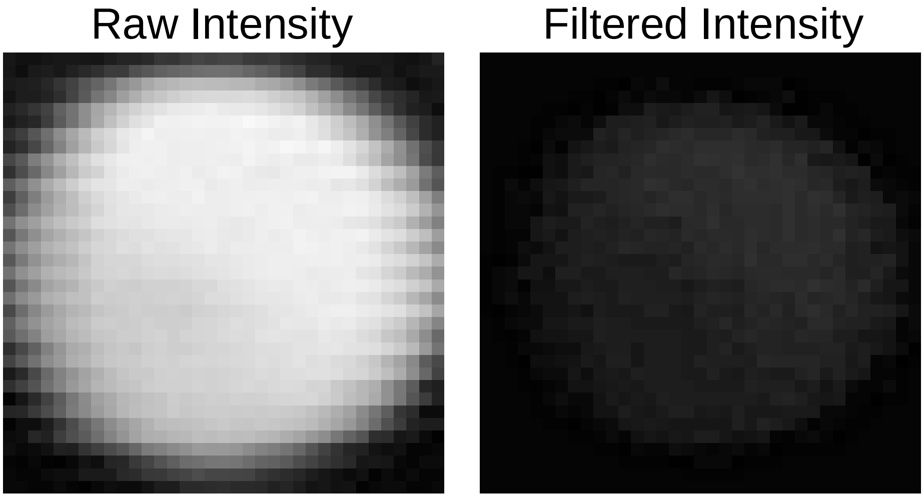

Figure 3.7: Left: the blackbody radiation emission from the crystal. right: the same emission picture but with the hot mirror filter in position. The ratio of the average intensity of these two pictures gives an indication to the temperature of the crystal surface.

This procedure is well known as the “Yo-Yo” method [57, 76], typically this cyclic process would require 30-40 cycles for a maximum emission to be reached, which is higher than other groups have found [73, 77]. The whole activation process takes between 36-48 hours to produce a renewed polarised electron source. Once the maximum quantum efficiency has been obtained by this method the crystal is over caesiated by about 10-20% to increase the activation lifetime [73].

3.5 Calibration and Performance

To achieve a consistent, efficient and high quality spin polarised electron source many components need to be well calibrated. In this section the calibration method and results for the electron optics, caesium and oxygen flow rates and the activation process of the crystal will be discussed.

3.5.1 Circularly Polarised Light Calibration

Circularly polarised light is required to produce spin polarised electrons, and for this experiment the ability to switch between spin up and spin down electrons is required, this means switching between σ^+ (righthand polarised) and σ^- (lefthand polarised) light. To achieve this the following optics are used:

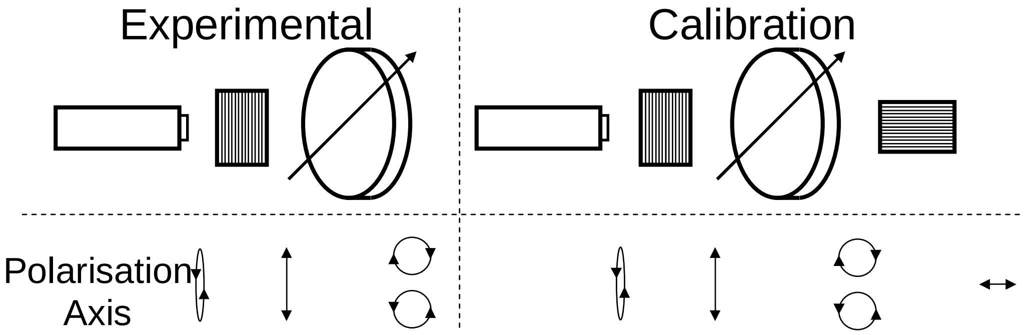

Figure 3.8: Left: The laser optics for the experimental configuration with the polarisation axis of the laser at each stage below. Right: The laser optics for the calibration configuration. The second linear polariser is 90° to the first, and the intensity of transmission through this polariser should be 50% if the light is circularly polarised before hand.

In the experimental configuration a linear polariser (Glan-Thompson polarising prism) is placed directly in front of the laser and aligned so the polarisation axis of the laser and polariser are parallel, this insures the light from the laser is 100 % polarised. The LCR then switches the linearly polarised light to σ^+ or σ^- polarisations, by changing the retardance from $\frac{\lambda}{4}$ to $\frac{3\lambda}{4}$. The LCR is a solid state device that can act as a variable retarder by applying different voltages across it.

In the calibration configuration the only difference to the experimental configuration is the final linear polariser which is perpendicular to the first linear polariser. In the calibration procedure the LCR must have its fast axis at 45° to the first linear polariser, and the LCR voltages for $\frac{\lambda}{4}$ and $\frac{3\lambda}{4}$ retardation must be determined. The fast axis is aligned by iteratively rotating the LCR and then varying the voltage across the LCR until an absolute maximum intensity is measured after the second linear polariser. This current configuration ensures the fast axis is at 45°, and the voltage applied to the LCR gives it a $\frac{\lambda}{2}$ retardation value, at this point the LCR is aligned. For voltage calibration of the LCR the transmitted laser intensity after the second linear polariser is measured as a function of the voltage applied to the LCR to produce a calibration graph (Fig. 3.9).

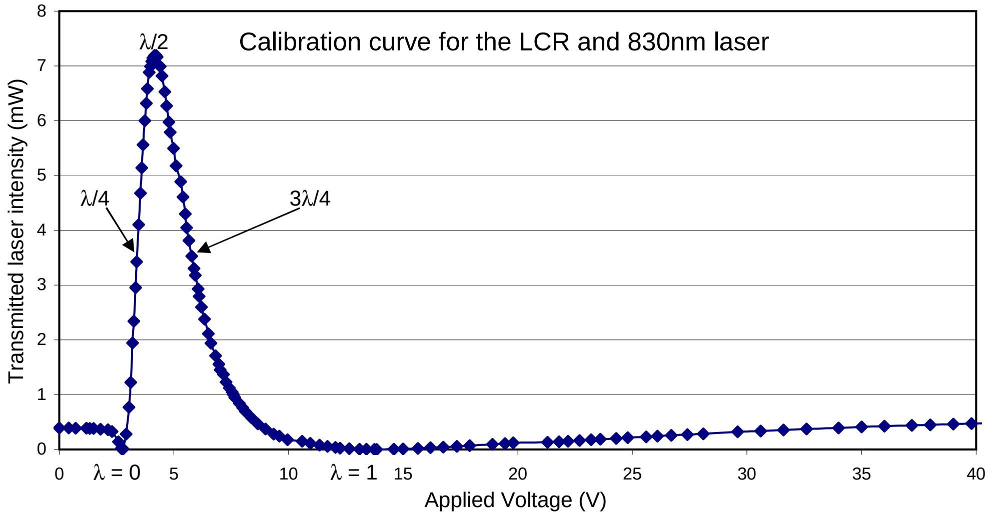

Figure 3.9: LCR calibration graph which shows the laser (830 nm) intensity transmitted through the second linear polariser in the calibration configuration (Fig. 3.8) as a function of the voltage applied to the LCR. The $\frac{\lambda}{4}$ and $\frac{3\lambda}{4}$ voltages are measured from when the calibration curve is at half maximum.

In the calibration graph (Fig. 3.9) it can be seen that the intensity initially decreases to a minimum at 2.90 V. This corresponds to a retardation of 0λ, implying that at 0 V the retardation is slightly negative (or less than λ). The emission then sharply increases to a maximum which corresponds to when the laser has changed its polarisation axis by 90°, so a maximum intensity is transmitted through the second linear polariser which is at 90° to the first. This indicates that 4.30 V corresponds to a retardation of $\frac{\lambda}{2}$. The intensity then drops as the voltage (retardation) increases, until a minimum is again realised when the retardation is λ and there is no effect on the axis of polarisation. It is seen (Fig. 3.9) that applying further voltage (after $\lambda = 1$) has a minimal effect on the retardation. Values of the voltages required for $\frac{\lambda}{4}$ and $\frac{3\lambda}{4}$ retardation can be extracted from half the maximum intensity points from the graph. These voltage values were found to be $\frac{\lambda}{4} = 3.50$ V (p-p) and $\frac{3\lambda}{4} = 5.80$ V (p-p).

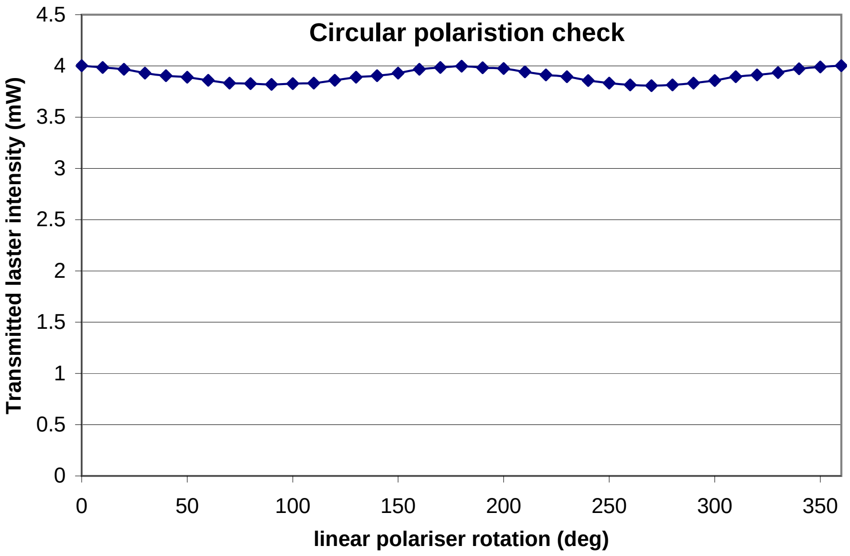

Figure 3.10: The transmitted light intensity as a function of the angle of the second linear polariser when the LCR is at its calibrated retardance ($\frac{\lambda}{4}$). This is a measure of the degree of circular polarisation of the outgoing light.

These voltages (3.5 and 5.8 V) were then applied to the LCR and the intensity emitted was measured as a function of the angle of the second linear polariser. If the retardation is accurate and the light is truly circularly polarised then the emission should be constant and independent of the angle of the second linear polariser. Several checks were done at voltages around the optimum voltages as determined from the calibration curve. The final values which resulted in the highest degree of circularly polarised light were $\frac{\lambda}{4}$ = 3.81 V (p-p) and $\frac{3\lambda}{4}$ = 5.86 V (p-p), both of which produced higher than 97% circularly polarised light (Fig. 3.10) for the 830 nm laser used. Retardation is wavelength dependant so each laser used must be re-calibrated using this procedure to determine the new LCR voltages.

3.5.2 Oxygen and Caesium Deposition

To achieve NEA at the crystal surface activation of the crystal with Cs and O_2 is required. To get an understanding of the amount of these materials needed a calibration the Cs and O_2 sources was needed. The Cs was produced from a commercially available alkali metal dispenser. In the experimental set-up it was impossible to measure the Cs evaporation rate, however the evaporation rate of these Cs dispensers has been accurately measured elsewhere [78]. In that study they looked at a longer dispenser, but as the cross-sectional area of the two dispensers are identical and the Cs activation is dependant on cross sectional area. Then the ratio of applied current to the Cs evaporation rate per unit length is expected to be the same for the two different length dispensers. So by scaling the Cs evaporation rate by the ratio of the two lengths of the dispensers an evaporation rate calibration was obtained (Fig. 3.11).

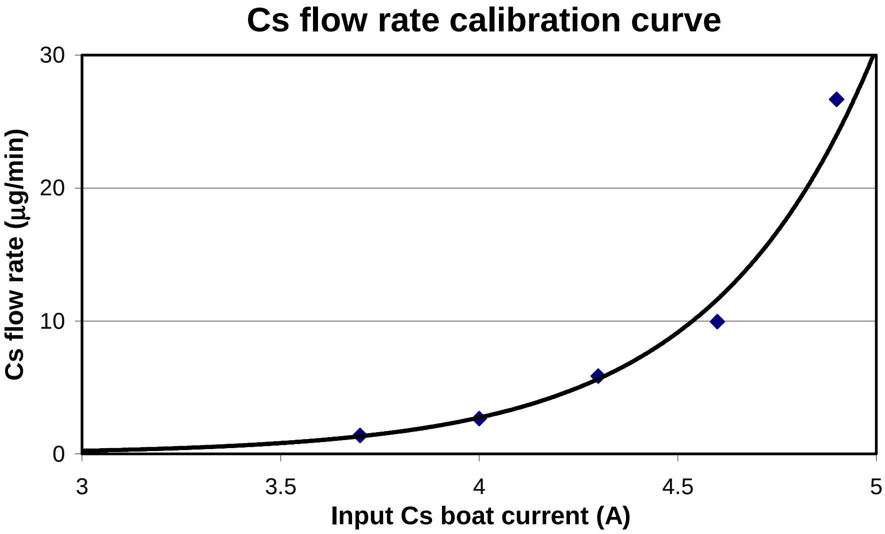

Figure 3.11: Cs flow rate calibration graph as obtained from [78]. Typical activation currents were 4.2 A, and typical background Cs flow rates after activation were between 3-3.8 A depending on the laser intensity and emission from the crystal.

Each activation was slightly different but the required current applied to the Cs dispensers for GaAs activation was on the order of 3.8 - 4.2 A. A residual Cs evaporation rate was required to maintain a high emission from the crystal and to increase the lifetime of each activation. The residual Cs evaporation rate was dependent upon the laser power applied (due to laser induced ablation [79]) and the emission current from the crystal (bombardment from backstreaming ions [77]). The residual Cs evaporation rate was between 3.0 - 3.8 A, which is a typical steady state Cs flux as seen by other groups [74, 80]. Occasionally the required steady state Cs flux would get even higher as the crystal aged. At these rates the Cs boats lasted from 4-6 months of constant use before signs of Cs depletion occurred. The gun chamber has 4 Cs boats mounted inside the UHV, that can be used individually, so the lifetime of the Cs boats means that continued operation for up to 2 years is possible.

Oxygen was introduced into the UHV system from a tank containing highly pure oxygen via a variable leak valve (Granville-Phillips 203), so calibration of the leak valve was required. A residual gas analyser (RGA)(SRS RGA100) was added to the system, and the chamber environment background was measured with the RGA. The variable leak valve was incrementally opened and an RGA spectrum was taken at each setting. Each measurement had the background subtracted. This enabled the purity of the oxygen to be measured as well as the partial pressure. The oxygen purity is in excess of 99.5% pure. The continual outgassing of the RGA filament adds impurities to this reading, so 99.5% is expected to be a severe underestimation. After one measurement the vacuum was left to settle, and then a new measurement at a different leak valve setting was taken. The results are shown in figure 3.12.

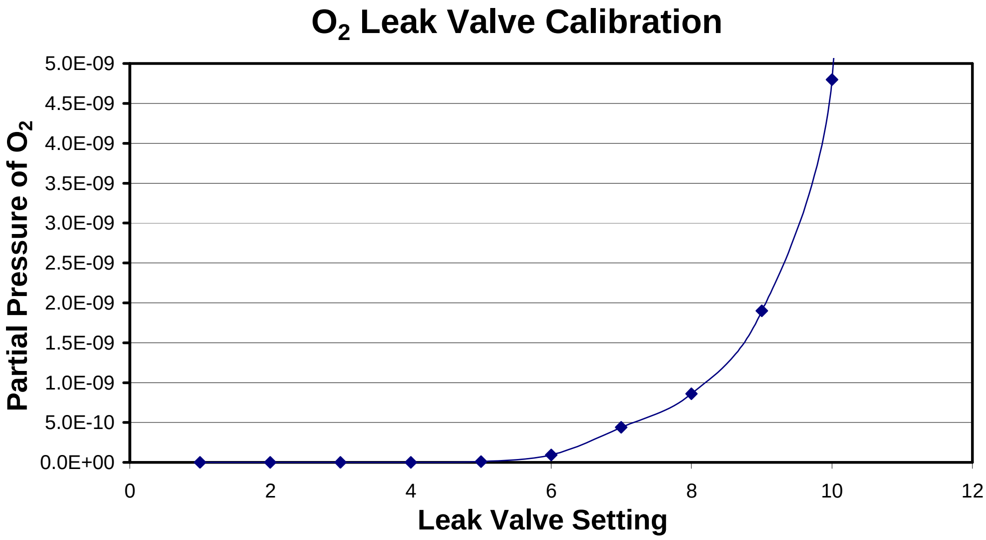

Figure 3.12: O_2 flow rate calibration graph as a function of the variable leak valve setting. Typical settings during activation were between 6-7, and no residual oxygen was required to maintain emission from the crystal.

Typical leak valve settings during activation were between 6 to 7, which corresponded to a partial pressure of about 2.5x10^{-10} torr. It was found that no residual O_2 flow was required to maintain the crystal emission. Any oxygen in the system after the activation is completed resulted in dramatically reduced activation lifetimes [79, 81].

3.5.3 Polarisation, Yield and Lifetimes

The degree of polarisation of the electron beam is determined by Mott scattering from a solid gold (Au) film. The Mott principle states that when an electron beam is scattered from a target of high atomic number (Z) with a polarisation that is normal to the scattering plane a left/right asymmetry (A) will be observed:

$$A = \frac{L - R}{L + R} \tag{3.2}$$

Where L and R are the intensities scattered left and right respectively through the same scattering angle (θ). This scattering asymmetry originates from a change in the sign of the spin-orbit coupling interaction term between the incident electron and target nuclei [55]. This scattering asymmetry can be used to determine the polarisation (P) of the incoming electron beam if the asymmetric scattering factor (Sherman function, S) of the target is known [55, 82].

$$P.S = A \tag{3.3}$$

The implication of measuring the spin polarisation of the incident electron beam in this way is that the uncertainty in the Sherman function carries through to the error in the determination of the polarisation. Typically the effects of multiple scattering hinder an accurate measurement of the Sherman function, and the Sherman function must be extrapolated to zero thickness. Even this extrapolation procedure carries an accuracy of no better than $\pm 5\%$ [82].

The polarisation of the EMS GaAs polarised electron source was determined by using the Sherman function calculated from the ELSEPA Dirac partial-wave calculation of elastic scattering of electrons from atoms, which was written by Salvat *et. al* [83]. The experimental configuration of a scattering angle of 45° and energy of 25 kV, corresponded to an asymmetric scattering function of 5.247×10^{-2} (Fig. 3.13).

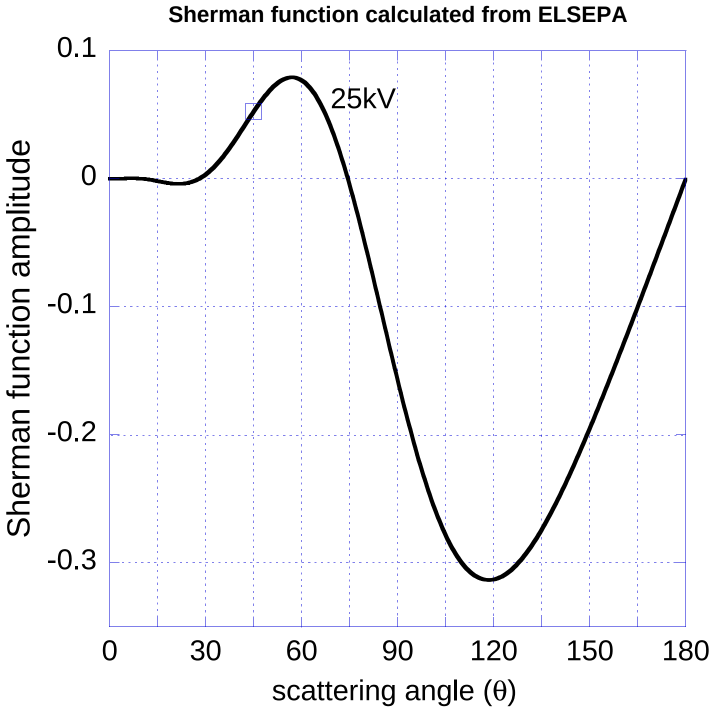

Figure 3.13: The calculated Sherman function for elastic scattering from a gold nucleus at 25 kV incident energy over a scattering angle of 0 to 180°, using the ELSEPA program [83]. The square at 45° marks the experimental conditions and the Sherman function that was used to determine the polarisation of the GaAs spin polarised electron source.

The experimental configuration used to measure the asymmetry was a transmission mode EELS experiment measured at a scattering angle of 45°. The experimental energy resolution of this experiment was on the order of 350 meV, so the elastic and inelastic contributions could be easily separated, meaning that the extrapolation of results to zero thickness was not required. By only taking the ratio of the areas under the elastic peaks, it was ensured that the contributing counts had not been inelastically multiple scattered.

The spin polarisation of the beam was flipped every two minutes and around 200 measurements of each spin direction were taken in an experiment lasting approximately 13 hours. The flipping of the polarisation prevented any long term drift in the experiment from affecting the determination of the beam polarisation. From this measurement the ratio of the areas under the elastic scattering peaks for both the spin up and the spin down case, in each detector, was determined. By taking the ratio of the spin up case minus the spin down case in each detector any differences in the efficiency between the two detectors can be prevented from affecting the spin polarisation determination.

$$P = \frac{N_{1\,up} - N_{1\,down}}{N_{1\,up} + N_{1\,down}} \times \frac{1}{S} \tag{3.4}$$

Using the areas under the elastic peaks for the spin up and spin down asymmetries in each detector and equation 3.4, the polarisation of the electron beam with a 780 nm incident laser was determined to be 14.37 (±0.49)%. A higher degree of electron beam polarisation is expected when using a laser with a higher wavelength, as both the probability of exciting an electron from the $P_{\frac{1}{2}}$ state and the probability of a thermal induced spin flip of the electron is also further reduced. Measuring the area under the elastic peaks obtained using a 830 nm wavelength laser and again using equation 3.4 the electron spin polarisation for the 830 nm laser induced electron emission was determined to be 21.85 (±0.53) %.

Yield

The yield of a photocathode is measured in terms of the quantum efficiency (QE), which is the percentage of electrons emitted per incident photon. The laser intensity was measured accurately on the bench using a laser power meter (Newport 818-SL). The QE can be calculated from the following equation:

$$\begin{aligned} QE &= \frac{\text{electrons/s}}{\text{photons/s}} \times 100\% \\ &= C \times \frac{I_{\text{cryst}}(\mu\text{A})}{P_{\text{laser}}(\text{mW})\lambda(nm)}\% \end{aligned} \tag{3.5}$$

Where the constant C incorporates the conversion of the current in μA to electrons per second, the conversion of the laser intensity and wavelength to photons per second and also the conversion from a fraction to a percentage. The value of the conversion constant C is 124.15.

The QE measurement for the 780 nm laser was conducted at a small laser power (0.352 mW), which produced a maximum of 5.5 μA emission and typically produces emission on the order of 2.5-3 μA. The measured QE (Eq. 3.5) for the 780 nm laser was typically in the range of 1.13-1.34 %, with a maximum QE measurement of 2.48 %. This is similar to values quoted in literature of between 1-5 % [74, 84, 85].

The quantum efficiency measurement for the 830 nm laser was also conducted at a small laser power (0.207 mW), which produced a maximum of 1.8 μA emission and typically produced emission on the order of 1.4-1.6 μA. Using Eq. 3.5 the measured QE was typically in the range of 1.01-1.16 %, with a maximum QE of 1.30 %.

Activation Lifetimes

The activation lifetimes of the NEA on the surface of the crystal varied widely depending upon the mode of operation of the gun. The main three variables included the power of the laser, the amount of emission from the crystal, and the vacuum quality in the chamber.

The power of the laser is believed to thermally excite the caesium in the caesium oxide, enabling the caesium to desorb from the surface of the crystal which affects the surface NEA [86, 87]. The power of the laser controls the rate of the Cs desorption, thus the lower the power of the laser the longer the activation lifetimes. A small proportion of the electrons emitted from the crystal collide with apertures positioned along the electron beam pathway. The amount of electrons colliding with the apertures increases more than linearly as a function of emission from the crystal due to space charge effects broadening the electron beam. The high energy electrons (25 keV) that do collide with an aperture create secondary ions, these positively charged ions then backstream up to the crystal surface which is at a -25 kV potential [77]. The backstreaming ions sputter the NEA layer from the surface resulting in a reduced lifetime of the activated cathode. A retarding hoop (+200 V) was positioned behind the anode which acted as a potential barrier for the low energy backstreaming ions without adversely affecting the focus of the high energy electron beam. The hoop is seen to have a positive effect on the decay rate of an activated crystal (Fig. 3.14), however the hoop did not entirely resolve the problem of backstreaming ions.

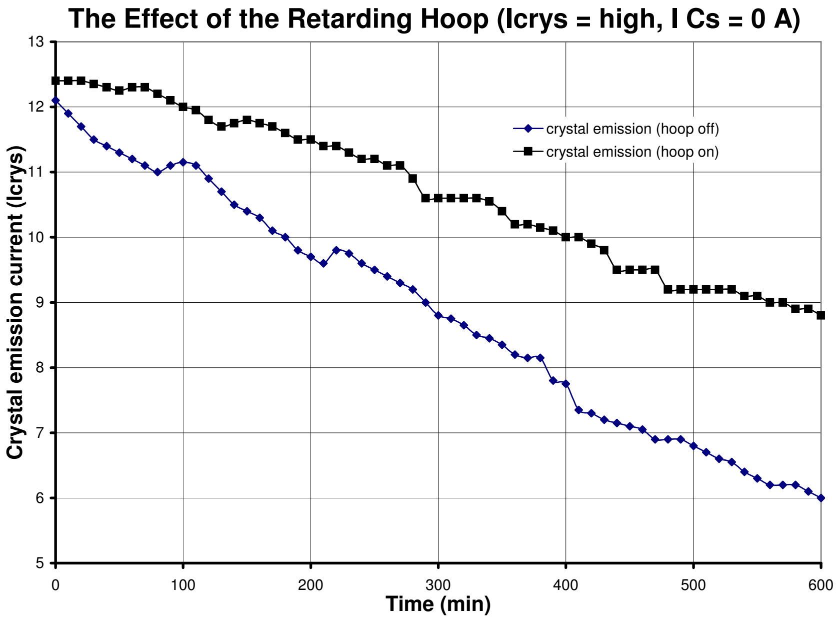

Figure 3.14: The rate of decay of an activated crystal as a function of the state of the retarding hoop. A positive effect is seen on the activation lifetime when there is a positive voltage applied to the retarding hoop. No residual Cs flux and high crystal emissions were used to speed up this effect.

The vacuum quality is critical in maintaining good lifetimes from an activated GaAs crystal [88], not just total pressure but also partial pressures of damaging species. The most damaging species being any oxides [79, 81, 86] which destroy the NEA stoichiometry on the surface. Collisions between the electron beam and apertures in the system meant that the pressure of the chamber increased as a function of emission current from the crystal. Thus longer activation lifetimes were obtained by limiting the crystal emission current to the minimum required.

Once the crystal is activated the two controllable variables are the laser intensity and the residual Cs flux. The best activation lifetime was found when the laser intensity was kept to the required minimum, this resulted in half-lives of the activation lifetimes on the order of 14 days with an emission current on the order of 700 nA. A standard activation life-time measured at a mid ranged laser emission resulted in a lifetime around 3-4 days with a crystal emission on the order of 5 μA.

Chapter 4

Single Crystal Results

In this chapter results will be presented for single crystal copper, silver, and gold, which are all group 11 noble metals. These results have been taken with a non-polarised thermionic electron emission source. All the samples had measurements taken along the three high symmetry directions: $\langle 100\rangle$(Γ-X), $\langle 110\rangle$(Γ-K) and $\langle 111\rangle$(Γ-L), these results will be compared to full potential linear-muffin-tin-orbital (FP-LMTO) calculations [89]. Trends for the group 11 noble metals (Cu, Ag, Au) will be presented, and theoretical predictions for these progressively more charge dense and atomically heavy systems will be discussed.

4.1 Sample Preparation

The single crystal samples were grown on a [110] NaCl crystal at the University of Aarhus to a thickness of 100 nm. The samples were placed in deionised water to dissolve the NaCl substrate and float off the crystalline films, which were then placed onto a sample holder comprised of a stainless steel mesh with 0.3 mm diameter holes. It is through these holes that the transmission EMS experiment occurs. The samples were left to dry before being introduced into the UHV preparation chamber via a loadlock (section 2.4.1). At 100 nm, the samples are still too thick to perform an EMS measurement that won't be dominated by multiple scattering, so they are carefully thinned by a controlled argon sputtering technique to approximately 20 nm. The optimal thickness for a Si sample was experimentally investigated (Fig. 4.1) and it was found that if the sample is still too thick then the outgoing electrons will have a high chance of undergoing multiple scattering which contributes to the background intensity in the EMS results. Alternatively if the sample is too thin then the depth of the surface disorder created from the destructive sputter thinning technique will start to become a large proportion of the overall sample thickness. The surface disorder causes a polycrystalline contribution to the spectra, contaminating the sharp features that a single crystal spectra produces. The depth of this polycrystalline disorder created by sputter thinning is directly related to the ion penetration depth which can be controlled by changing the energy of the sputtering beam. Even with a low sputtering energy it can be seen for Si that the resolution of the spectral function is most resolved for the plot of a 20 nm thick sample (Fig. 4.1, 2t). This indicates that at thicknesses around 10 nm the surface disorder caused by sputtering becomes a non-negligible percentage of the overall thickness, but at 20 nm the surface disorder is still a negligible effect (Fig. 4.2). These measurements produced a maximum

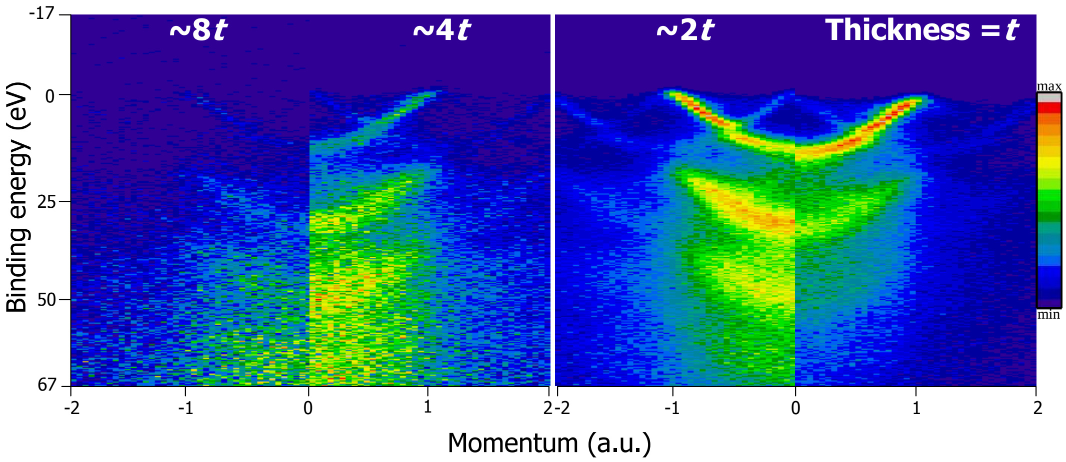

Figure 4.1: Spectral functions for single crystal silicon, where t is approximately 10 nm. As sample thickness decreases (left to right) the intensity of the spectral function increases compared to the contribution of the multiple scattering. Although the clearest spectrum is not produced from the thinnest target.

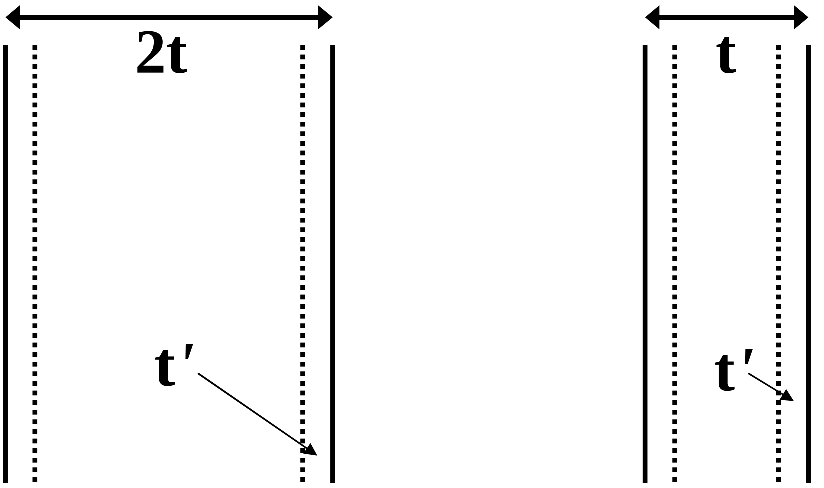

$$\text{Relative disorder} = \frac{\text{Polycrystalline disorder}}{\text{Single crystal order}}$$

$$\frac{1}{2t/2t' - 1} \qquad \frac{1}{t/2t' - 1}$$

Figure 4.2: This diagram shows the increase in the relative amount of disorder in the sample as a function of total sample thickness. For example if the surface disorder (t') is 1nm, and film thickness (t) is 10 nm then the relative disorder is 2t film = 11%, and the 1t film = 25%.

coincidence count rate for the 20 nm thick measurement of 5.3 Hz, compared to the coincidence countrate of the same sample at 10 nm (3.5 Hz), 40 nm (2.8 Hz) and 80 nm (0.4 Hz). The decrease in coincidence countrate can be explained by considering the effects of multiple scattering. If an outgoing electron undergoes excessive multiple scattering, then its energy or momentum can be shifted outside of the spectrometers detection range and the preceding EMS event will not contribute to the coincidence countrate. The probability of multiple scattering occurring increases with the thickness of the sample. Alternatively, thinner samples are less likely to have as many EMS events occur as the interaction region is shorter. These two opposing loss mechanisms for coincidence countrates produce a maximum coincident countrate for a single crystal silicon target, at a thickness around 20 nm. The noble metals discussed in this chapter are more dense than the silicon test subject, thus multiple scattering is expected to be more intense, so the sample needs to be thinner. The thicknesses of the noble metal samples should be less than 20 nm to achieve the best results.

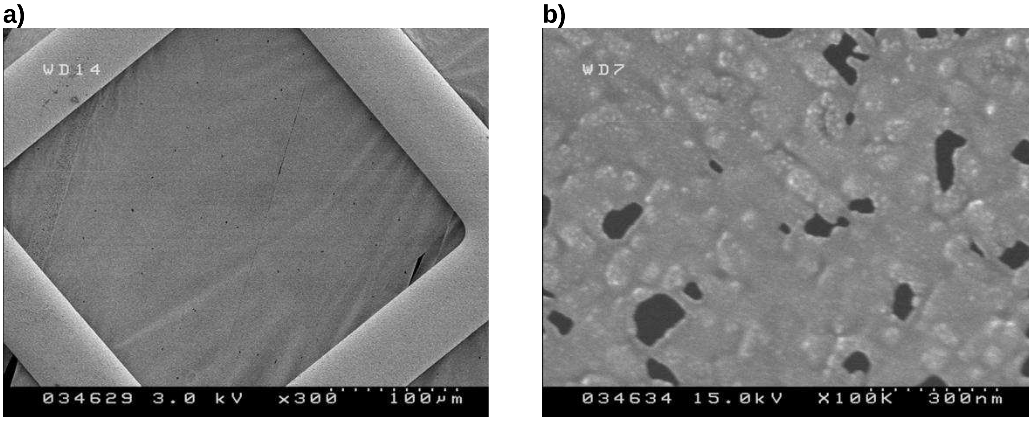

Figure 4.3: A single crystal Cu sample sputter thinned to approximately 10 nm. a) 300x magnification looks very uniform, b) at 100 000x magnification the surface disorder can be clearly seen with thin “holes” (dark areas) and thick islands (light areas).

Field-emission scanning electron microscopy (FESEM) images were taken (Fig. 4.3) on a thin Cu single crystal sample (thickness $\approx$10 nm). Samples are examined at around 300x magnification with an in situ optical microscope prior to an EMS measurement. At that magnification, as shown by the FESEM image (Fig. 4.3), the sample looks to be of a uniform thickness, with no obvious defects, hence this sample would typically be used in an EMS measurement. When the sample is examined more closely (100 000x magnification), it is quickly seen that the surface disorder was quite large (Fig. 4.3b). There is a large range of thicknesses across the sample with dark areas corresponding to “holes” and light areas corresponding to “islands”. These “holes” appear to be complete tears through the sample, it is assumed that the stresses on the thin film during the dramatic pressure change from the UHV EMS chamber to atmosphere created these miniature tears. It is believed that prior to bringing the sample up to atmosphere that these “holes” were just areas of thin film. The “islands” are thicker areas on the sample from which the sputtering thinning technique has removed fewer atoms.

The depth of the surface disorder is determined by the penetration depth of the Ar ions used in the sputter thinning technique. To investigate the sputtering depth a computer simulation (SRIM [90]) was used. The results of the computer simulation (Fig. 4.4)

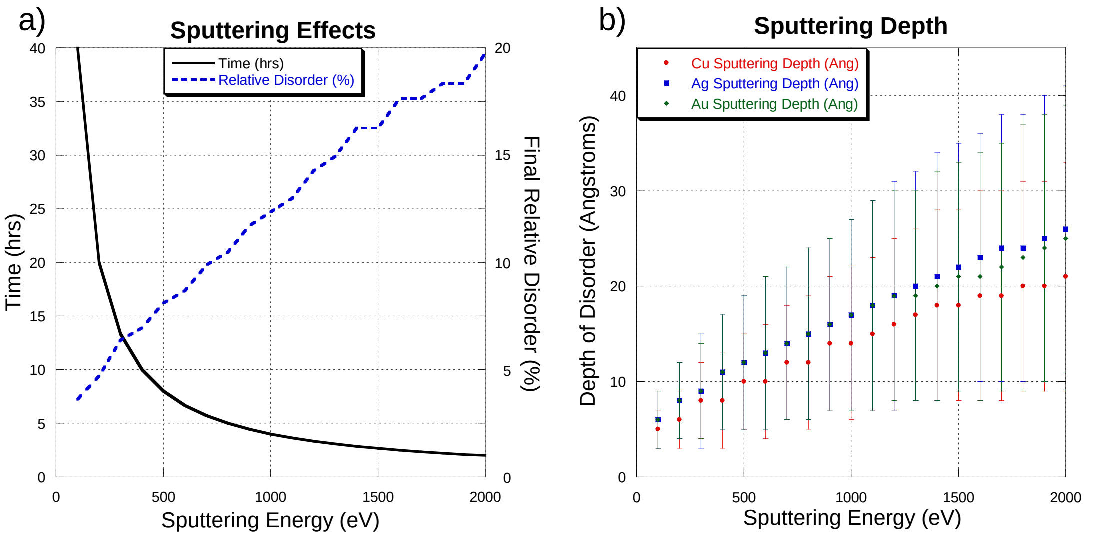

Figure 4.4: (a) The time taken to sputter thin a Cu sample compared to the final percentage of surface disorder (for a 200 Å sample). The sputtering time was experimentally measured for 400 eV and 800 eV sputtering energies, and then extracted using a sputtering simulation (SRIM [90]). (b) The depth of the surface disorder for sputter thinning Cu (●), Ag (■) and Au (♦) samples, as calculated using SRIM [90]. These values were used to determine the final relative percentage disorder in (a).

clearly show that a trade off between sputtering time and the resulting relative disorder of the sample is required. For the preparation of a Cu sample, at the lowest practical (in terms of total sputtering time) sputtering energy (400 eV), the mean sputtering depth was determined to be 8 Å with an average deviation from the mean (straggle) of 5 Å. At 400 eV sputtering energy the relative disorder of the Cu sample of 10 nm thickness would be 8 %.

Through the FESEM, EMS experiments and SRIM simulations into sample preparation it was concluded that samples that were over sputtered developed a large percentage of surface disorder that influenced the EMS results. The values determined to yield the best sample quality are a sputtering energy of 400 eV, and a thinning of the sample to the order of 200 Å.

4.2 Brillouin Zones

At this stage some basic knowledge of solid state theory is necessary to proceed with the explanation of the features seen in the experimentally measured spectral functions of single crystal samples. Solids are large collections of bonded atoms that range from 10^9 atoms in the smallest of metallic solids visible with the naked eye up to 10^{25} atoms in a 1 kg solid. In solid state physics it is far more convenient to take the Fourier transform of the real (positional) space functions and refer to them in reciprocal (momentum) space. The most simple unit cell in real space is the Wigner-Seitz cell, which one obtains by drawing orthogonal planes at the midpoints of the vectors which adjoin equivalent lattice-points between neighbouring unit cells. In reciprocal space (**k**-space) the most simple unit cell obtained in the same way as the Wigner-Seitz cell is called the first Brillouin zone, a 2-dimensional representation of this is shown in Fig. 4.5, and the translational vectors are called reciprocal lattice vectors (**G**). The Brillouin zone boundary has many interesting features associated with it, such as diffraction and energy band splitting (Fig. 4.5).

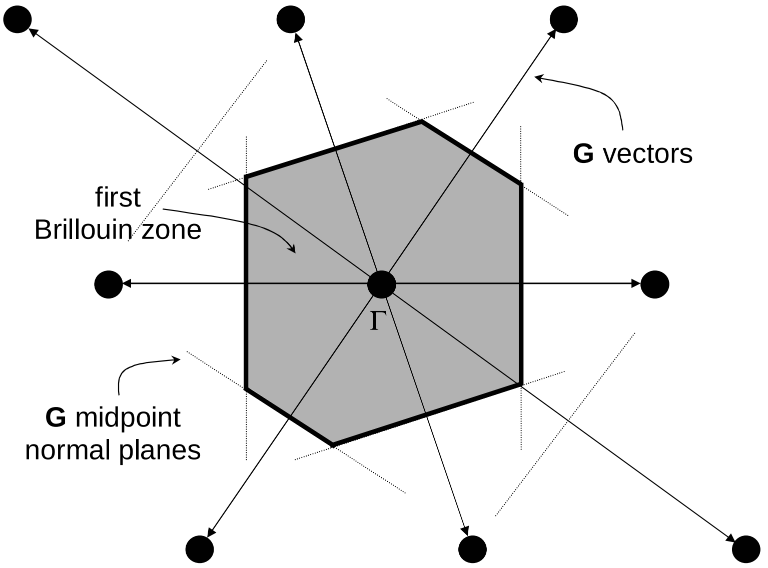

Figure 4.5: A 2-D construction of the first Brillouin zone (shaded). This is the same construction method as a Wigner-Seitz cell in real space. In 3 dimensions it becomes more complicated as you get planes coming from **G** vectors which lie out of this 2 dimensional plane.

The Brillouin zone boundary is determined by the midpoints of the reciprocal-lattice-point to reciprocal-lattice-point vectors. Alternatively the Brillouin zone boundary can be considered as a geometrical representation of the solution to the Bragg scattering condition [10];

$$\mathbf{k} \cdot \mathbf{G} = \frac{1}{2} G^2. \tag{4.1}$$

This Brillouin zone surface represents all momentum vectors ($\mathbf{k}$) which can be diffracted (Bragg scattered) from the crystal. Hence for an EMS measurement along a vector in momentum space the intensity inside the first Brillouin zone may be diffracted into higher order Brillouin zones by the reciprocal lattice vector in that direction.

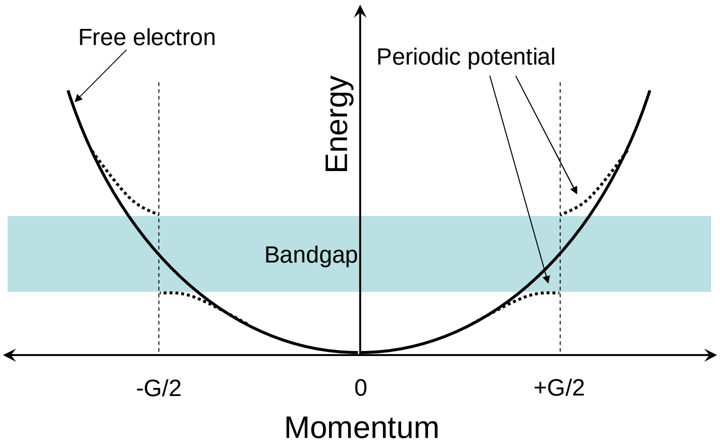

Figure 4.6: The dispersion for a free electron solid (parabola) and a solid with a periodic potential (distorted away from a parabola). The perturbations in the periodic crystal array are caused by Bragg reflections at the Brillouin zone boundary. These reflections lead to a forbidden energy region known as a band gap.

Due to the wave-particle duality of electrons, a valence electron in a solid can be described by a moving wave. As has been previously discussed, at the Brillouin zone boundary these waves can be reflected and depending on the phase relation of the reflected and original waves, two different standing waves are possible, one which has a higher probability of the electron being near the ionic core and one with a higher probability of the electron being away from the ionic core. These two different solutions have different potential energies due to the periodic potentials of the ionic cores, one standing wave will have a potential energy lower than the travelling wave and conversely the other standing wave will have a potential energy higher than the travelling wave. Hence where the Bragg reflection occurs (Brillouin zone boundary) a forbidden energy region forms due to the potential energy splitting, this forbidden region is known as the band gap (Fig. 4.6).

4.3 Multiple Scattering

In an (e,2e) experiment multiple scattering occurs when either the incoming or outgoing electron(s) scatter from another particle. This scattering can change either the electron's momentum (elastic scattering) or the electron's energy (inelastic scattering), which results respectively in an incorrect momentum or binding energy interpretation from the conservation equations (Eq. 1.1).

The most common elastic multiple scattering event is diffraction. Electron wave-particle duality allows electrons to be treated as waves, and the periodic structure of atoms in a single crystal solid can act as a diffraction grating. The resulting diffraction can shift the incoming or outgoing electron(s) momentum by the reciprocal lattice vector (**G**). In the case that the reciprocal lattice vector is directed along the measurement direction we can try to correct for diffraction effects due to this specific **G** vector. If correction is necessary then a fraction of the spectra from the first Brillouin zone ($-\frac{\mathbf{G}}{2}$ to $\frac{\mathbf{G}}{2}$) can be subtracted from higher order Brillouin zones.

$$\mathrm{A}(\mathbf{q}_{\mathrm{y}},\mathrm{E})_{\mathrm{corr}} = \mathrm{A}(\mathbf{q}_{\mathrm{y}},\mathrm{E}) - a\mathrm{A}(\mathbf{q}_{\mathrm{y}}+\mathbf{G}_{\mathrm{y}},\mathrm{E}) - a'\mathrm{A}(\mathbf{q}_{\mathrm{y}}-\mathbf{G}_{\mathrm{y}},\mathrm{E}). \tag{4.2}$$

This diffraction correction procedure is shown mathematically in Eq. 4.2 and the results are shown graphically in Fig. 4.7. The fraction of intensity (a,a') used for subtraction is dependant upon the amount of diffraction. Experimentally (a,a') are determined by the amount of intensity required to reduce the intensity of the diffracted sp-band at $\mathrm{q} = \pm\mathbf{G}$ to zero, as theoretically there should be no intensity at this position (see Fig. 4.7).

A diffraction corrected spectral function of Cu can be seen in Fig. 4.7. After diffraction correction there is still some intensity at higher momenta, this intensity is due to the

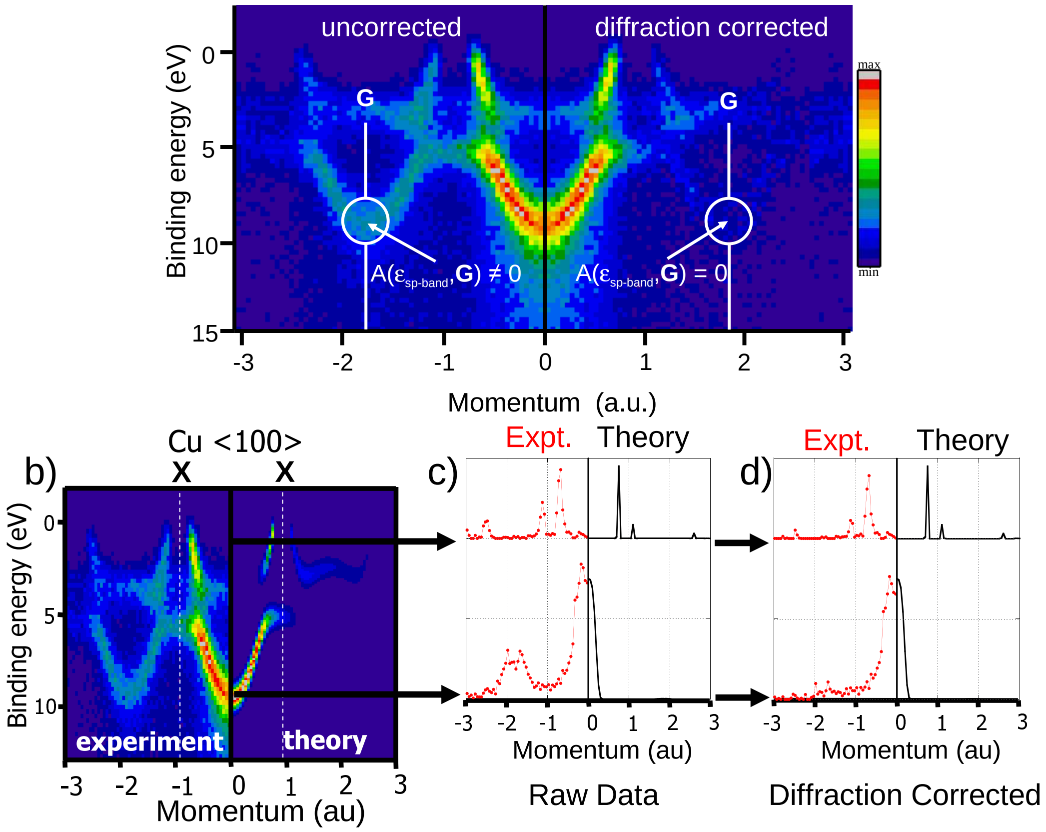

Figure 4.7: a) The raw EMS spectral function for a crystalline Cu ⟨100⟩ measurement (left), and corrected for diffraction effects (right). The correction is applied so that the experimental intensity of the sp-band at q = G is 0, in accordance to the intensity estimated by theory. After diffraction correction there a much better agreement between theory and experiment (b,c,d) for the whole spectrum.

3d electrons that extend out further in momentum space and also due to lattice potential effects which produces a small fraction of the Bloch function intensity shifted by **G** out to higher order Brillouin zones.

The most common inelastic multiple scattering event is plasmon excitation. The electrons in any solid can be collectively excited to oscillate with a frequency proportional to the square root of the electron density, the EMS electrons can interact with the plasmon oscillation and lose a characteristic amount of energy. Inelastic scattering can strongly affect the EMS spectra, and is the main reason for the requirement of very thin samples. The correction procedure involves measuring an EELS spectrum from the sample and fitting

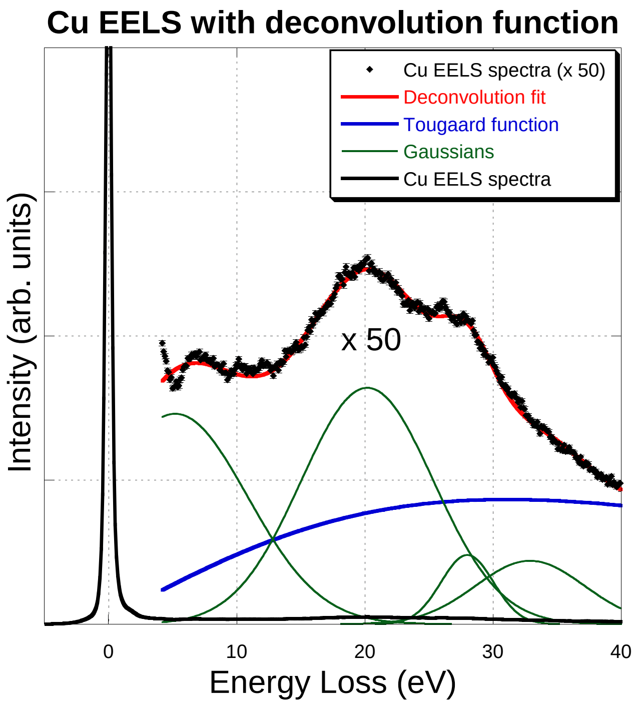

Figure 4.8: the EELS spectrum for a Cu sample (⧫) fitted with a Tougaard (-) and 4 gaussian functions (-) that combine to produce the deconvolution fit (-). The match is not perfect due to the complex inelastic scattering mechanisms in the noble metals, but still more the adequate for a correction function.

the EELS spectrum with a universal Tougaard function and several Gaussian functions [91, 92] (see Fig. 4.8).

$$\rho(\mathrm{E}) = \left(\sum_n A_n e^{\frac{-(x_n - x_0)^2}{2\sigma_n^2}}\right) + \frac{Bx}{(C+x^2)^2} \tag{4.3}$$

The inelastic deconvolution correction function (Eq. 4.3) comprises of a set of Gaussian peaks $\left(\sum_n A_n e^{\frac{-(x_n - x_0)^2}{2\sigma_n^2}}\right)$ to describe the plasmon oscillation, and a Tougaard function $\left(\frac{Bx}{(C+x^2)^2}\right)$ that describes other inelastic losses [93, 94]. While the fitting function ($\rho(\mathrm{E})$) is obtained from a 25 keV EELS spectrum, the inelastic losses are caused by the same processes as in an EMS spectrum with 50 keV incoming and 25 keV outgoing electrons. The major differences between the inelastic processes of the two experiments are the effective sample thickness which changes because of the differences in the inelastic mean free paths of the different energy electrons, and the path length through the sample. This effect has been previously examined in detail [95], and it has been determined that a sample in the coincident EMS experiment appears to be 1.4 times thicker than the same sample in the singles experiment (EELS) [95].

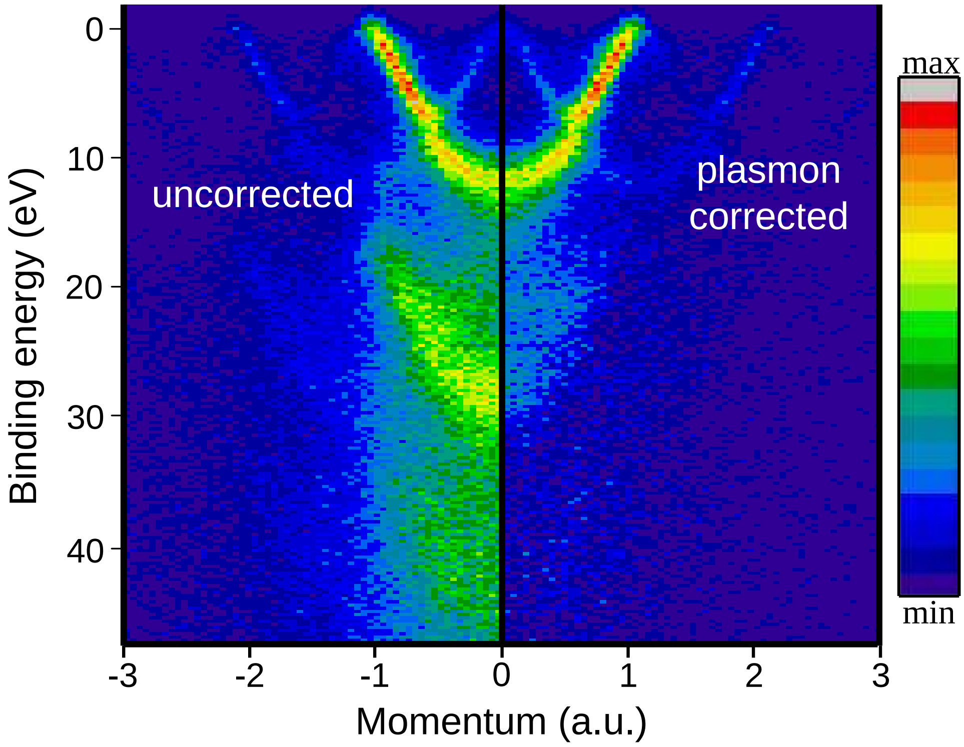

Figure 4.9: A raw experimental spectral function (left) for a 20 nm single crystal Si⟨111⟩ film compared to the same spectral function (right) that has been corrected for plasmon excitations by using a plasmon correction function measured from the samples EELS spectra. Much lower intensity at higher binding energies indicates the removal of most of the plasmon effects.

The inelastic deconvolution function (Eq. 4.3) is used in a deconvolution equation (Eq. 4.4) that was first utilised by Tougaard [94] to remove inelastic scattering contributions from x-ray photoelectron spectroscopy. The deconvolution procedure corrects the spectral function one point at a time by treating the intensity at that point as a true intensity plus intensity which comes from inelastic scattering contribution from intensity at a lower binding energy (ε). This correction procedure starts at the Fermi level ($\varepsilon = 0$) where there is no contribution from inelastic scattering, and moves down to higher binding energy ($\varepsilon + \delta$). Once the entire measured energy range for that binding momentum ($\mathbf{q}$) has been corrected the other binding momenta ($\mathbf{q} + \gamma$) are corrected in the same method.

$$\mathrm{A}(\varepsilon)_{\text{corrected}} = \mathrm{A}(\varepsilon)_{\text{raw}} - a\int_{\mathrm{E}}^{\varepsilon} \rho(\varepsilon-\mathrm{E})\mathrm{A}(E)_{\text{raw}}.\mathrm{dE}. \tag{4.4}$$

The result of using the inelastic scattering correction function can be seen in Fig. 4.9. The uncorrected spectra (left) has extra intensity at intervals of 16.25 eV higher in binding energy, the corrected spectra (right) has large reductions in this intensity which is primarily due to plasmon excitation. Metals typically have a plasmon excitation energy of between 5-20 eV.

4.4 Noble Metals

The term noble metal refers to precious and inert metals such as the group 11 elements in the periodic table, consisting of copper (Cu), silver (Ag) and gold (Au). The group 11 elements are all relatively corrosion resistant and excellent conductors of electricity due to their unusual and stable ground state configuration of $\mathrm{d}^{10}\mathrm{s}^{1}$. Apart from caesium, Au and Cu are the only coloured metals which along with their moderate malleability means they are widely used in the production of coins and as such are commonly referred to as the coinage metals. This term is archaic as modern day coins are produced from a large range of alloys to decrease the malleability and hence increase the coins lifetime. Whilst the term noble metals also refers to other precious metals such as platinum, in this thesis the term noble metal will only be used in reference to Cu, Ag and Au.

The noble metals have face centred cubic (FCC) structures in real space, which transforms to a body centred cubic (BCC) structure in reciprocal (momentum) space through a Fourier transformation. These metals have been widely studied using various experimental techniques and are generally considered to be well understood. Examining the fine detail in the solid state EMS results should give clear indications of the trends down the group 11 elements. Comparison of these trends will give a good determination of how well we understand EMS and how well theory can describe them. With each metal having the same valence electronic configuration and crystal structure, differences should come from the increasing system complexity, arising from increasing atomic mass and increasing electronic density. EMS should be able to shed some light on the effect of the many body interactions as the system complexity increases.

4.4.1 SMD's

The experimental spectral momentum densities were measured for Cu, Ag and Au along three high symmetry crystal directions ($\langle 100\rangle$, $\langle 110\rangle$, $\langle 111\rangle$). Experimentally the high symmetry directions were accessible by the preparation of a single crystal sample with a $\langle 110\rangle$ surface normal (Fig. 4.10). By a simply rotation about the surface normal the $\langle 100\rangle$ (Γ-X), $\langle 110\rangle$ (Γ-K), and $\langle 111\rangle$ (Γ-L) directions were aligned along EMS measurement direction (y-axis).

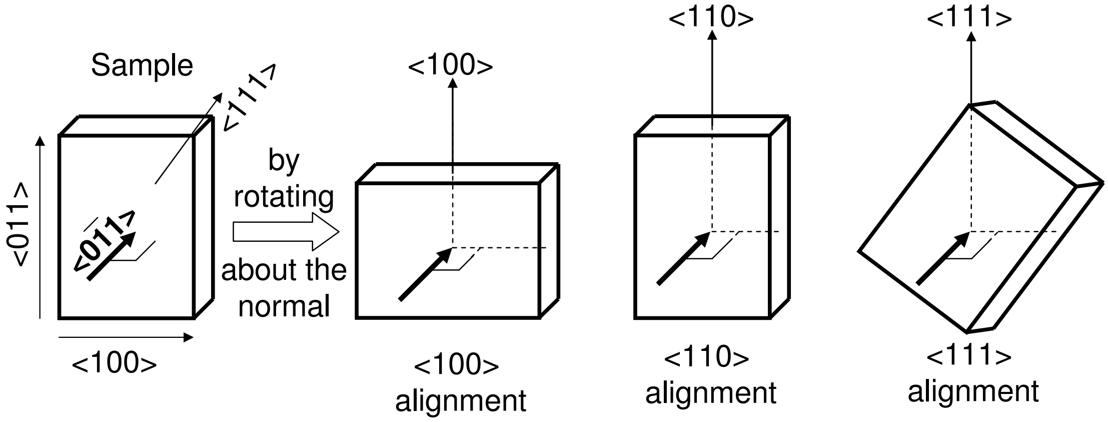

Figure 4.10: Using a single crystal sample with a $\langle 0\bar{1}1\rangle$ surface normal (bold arrow), we can achieve the y-axis orientations (measurement directions) across the surface (non-bold arrow) of $\langle 100\rangle$ (Γ-X), $\langle 110\rangle$ (Γ-K), and $\langle 111\rangle$ (Γ-L) by rotation about the surface normal.

The experimental SMDs (Fig. 4.11) are displayed with the binding energy of the valence electron along the vertical axis and the momentum of the valence electron along the horizontal axis. The colour on the SMDs represent the electron density at any particular energy and momentum combination, with red being areas of high intensity and dark blue being areas of low intensity.

Single crystal samples have a clear anisotropy which can be seen in the SMDs (Fig.

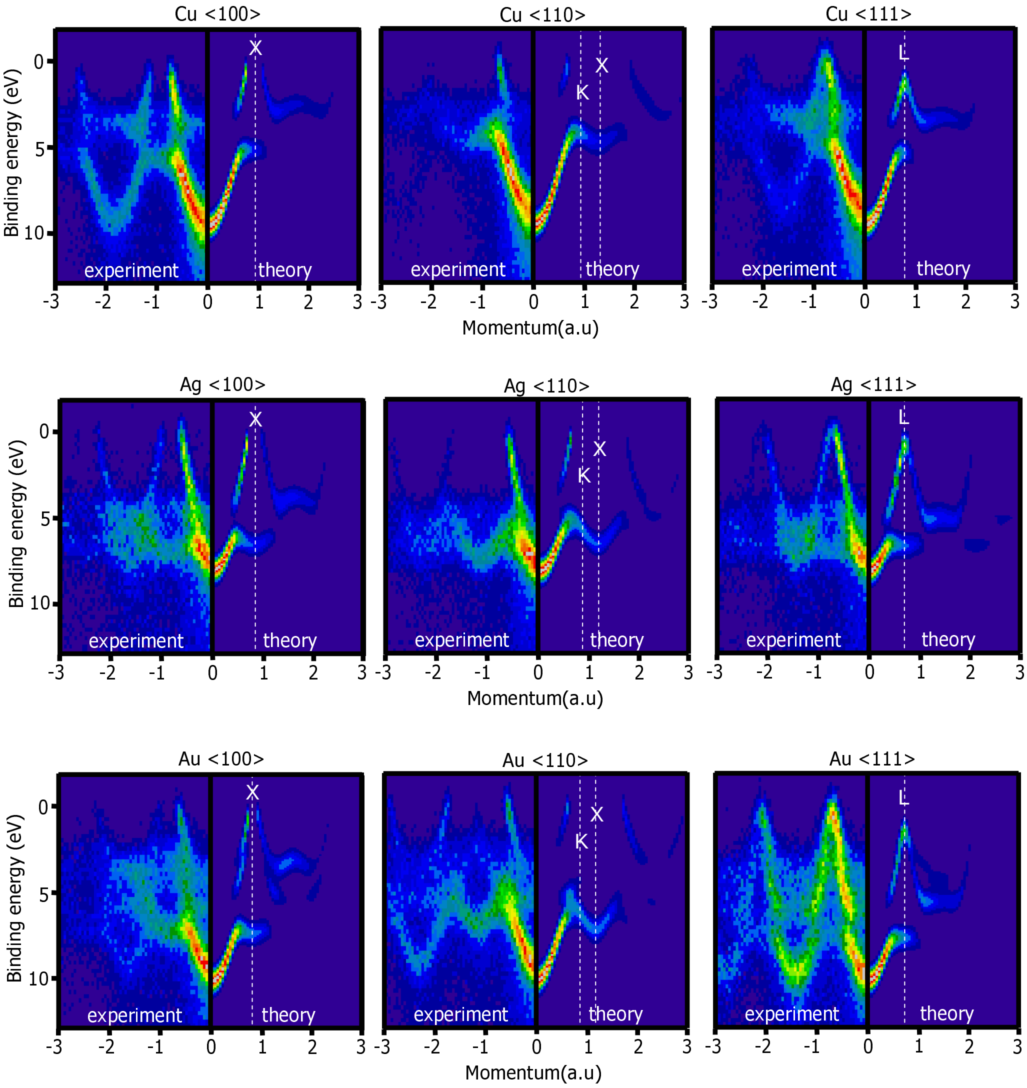

Figure 4.11: The raw (not corrected for diffraction effects) experimental SMDs (left) compared to the theoretically calculated SMDs (right). The colour refers to the electronic density at a specific energy and momentum combination within the target, with red being areas of high intensity and blue being areas of low intensity. The white dashed lines seen in the theory SMDs are high symmetry crystallographic points.

4.11) when measuring along different directions through the crystal. The anisotropy in the single crystal originates from the differences in interatomic spacing, resulting in different electronic densities and hence electronic structures. The BCC reciprocal lattice means the shortest reciprocal lattice vector (**G**) is along the $\langle 111 \rangle$ direction, and hence the band gap ($\frac{\mathbf{G}}{2}$) is at the smallest momentum value. The dispersion relation of the sp-band, which is free electron like (E $\propto \mathbf{q}^2$), means that the BZ boundary crossing occurs at the highest binding energy (lowest energy) value. The band gap is seen at the L-point in the $\langle 111 \rangle$ direction and the Fermi level lies in the band gap region. In the $\langle 100 \rangle$ and $\langle 110 \rangle$ directions the band gap is above the Fermi level and is not seen in the occupied ground state electronic structure.

The sp-hybridised band extends from the Fermi level down to the valence band minimum and is parabolic in shape. The sp-bands symmetry about the Γ-point ($\mathbf{q}$ = 0 au) allows the experimental SMD to be folded to increase statistics. The intensities seen in all SMD's between 2-8 eV that are less dispersed and extend out to much higher momenta are the d-bands. For Au the spin-orbit interaction produces additional splitting and distortion in the d-bands. Where the sp-band and d-bands intersect there is a hybridisation of the spd-bands that leads to a reduction of the electron-electron Coulomb repulsion energy by maximising the electron-electron separation. The reduction in Coulomb repulsion energy stabilises the solid, and the spd-hybridisation causes a gap in the parabolic sp-bands. The spd hybridisation effect is much stronger in Ag and Au than it is in Cu, due to relativistic effects [96, 97]. These relativistic effects are caused by a heavy nuclei increasing the relativistic mass of the s and p band electrons which contracts their orbit around the nucleus which consequently leads to a stronger screening of the nuclear attraction and hence an expansion of the d bands [98]. The resulting lower Coulombic attraction of the d-bands broadens them as can be seen down the columns of SMDs in fig 4.11. This affect increases proportionally to the square of the atomic mass (Z^2), so the effect is far stronger for Au than it is for Ag and stronger for Ag than it is for Cu.

The band gap arising from the periodicity of the crystal lattice, as discussed earlier (section 4.2), can not be seen in these SMDs as the upper band from the Brillouin zone induced band splitting is above the Fermi level and hence unoccupied. In the $\langle 111 \rangle$ SMDs the lower band from the band splitting is fully occupied below the Fermi level. The position at which the Brillouin zone splitting occurs can be seen as the fold over point of the sp-band. Quantitative values of the G vector that creates these band gaps will be determined from momentum profiles in section 4.4.2.

A clear difference between theoretical and experimental SMDs is the intensity out at higher momenta. The experimental results have much higher intensity than theory predicts, this difference can be explained by theory not including multiple scattering effects, or underestimating the d-band intensity, or electron correlation effects or some combination of all three. Diffraction effects have been previously discussed and as diffraction is an experimental effect the theoretical calculations do not include any diffraction. Theory may be either underestimating the d-band intensity or the effect of diffraction on the d-bands. As the d-bands are less dispersed in energy, diffraction will still contribute to their measured intensity. In mean-field (Hartree Fock) theory the electron interacts with the average electron density. In reality the electron interacts with other electrons, not their average density. The difference between the mean-field solution and the exact solution is referred to as "correlation effects". These correlation effects can change the dispersion of the bands and their momentum densities. Electron correlation is such a complex effect that no theory has been able to accurately and correctly predict the electron correlation effect for a range of targets. Alternatively the discrepancies in the d-band intensity between the EMS experiment and the LDA theory may have simply originated from theory underestimating the intensity of the Bloch functions at higher binding energy [99]. This excess intensity at higher momentum will be examined more closely (Sec. 4.4.2) in an attempt to extract the intensity due to electron correlation.

An interesting trend of the group 11 elements is the band width of the sp-bands. Treating the lone, outer most, s-orbital electron as a free electron electron, the depth of the s-band ($\mathrm{E_F}$) should be proportional to the valence band electronic density $\left(\frac{\mathrm{N}}{\mathrm{V}}\right)$ to the power of two thirds ($\mathrm{E_F} \propto \left(\frac{\mathrm{N}}{\mathrm{V}}\right)^{\frac{2}{3}}$, Tab. 4.1). This implies that Cu should have a larger band width than both Ag and Au. The valence bandwidth of Cu is larger than Ag, but is smaller than Au which opposes the free electron gas trend. This is an indication that Au deviates from the free electron gas description because of relativistic effects and d-band interactions. This trend will be examined more closely in section 4.4.3.

In general the theoretical description of the SMDs is reasonably good. The shape of the bands match quite well and the prediction of the relative intensity of the bands is

Metal	Valence electronic density (10^{22}/cm^3)	Calculated bandwidth (for free electron gas, eV)	Valence bandwidth (EMS values, eV)
Al	18.06	11.63	11 [51]
Cu	8.47	7.00	8.7
Ag	5.86	5.48	7.6
Au	5.90	5.51	9.5

Table 4.1: The valence densities of a free electron like metal should govern the valence bandwidths. The free electron bandwidth and EMS measured bandwidth is in agreement for Al, which is a very free electron-like metal, but they quickly deviate for the heavier metals indicating the relativistic behaviour of the heavier metals.

good for all the cases despite the systems varying in complexity. There are some minor discrepancies which will be examined more closely in the following sections.

4.4.2 Momentum Profiles

Momentum profiles can be obtained from the EMS measured SMDs by integrating over an energy interval and graphing the resulting intensity against the measured momentum of the bound electron. The energy intervals can range from between 0.25 eV (the data bin size) up to typically 100 eV (effective summed energy range of the channel plates), if needed the experimental configuration can be altered to measure over much larger or smaller ranges.

By integrating over the full valence electron binding energy range (-2 to 13 eV for the noble metals) the integrated momentum profiles of the valence electrons are obtained (Fig. 4.12). The EMS integrated momentum profiles are the equivalent of the intensity of a line through the 3-dimensional electron momentum density, which can be measured through reconstructing a series of Compton scattering measurements [100]. Given the limited energy range of integration the EMS momentum profiles presented here only incorporate the valence electrons ($d^{10}s^1$). In each of the plots the experimental data is plotted both with and without diffraction corrections and compared to theory.

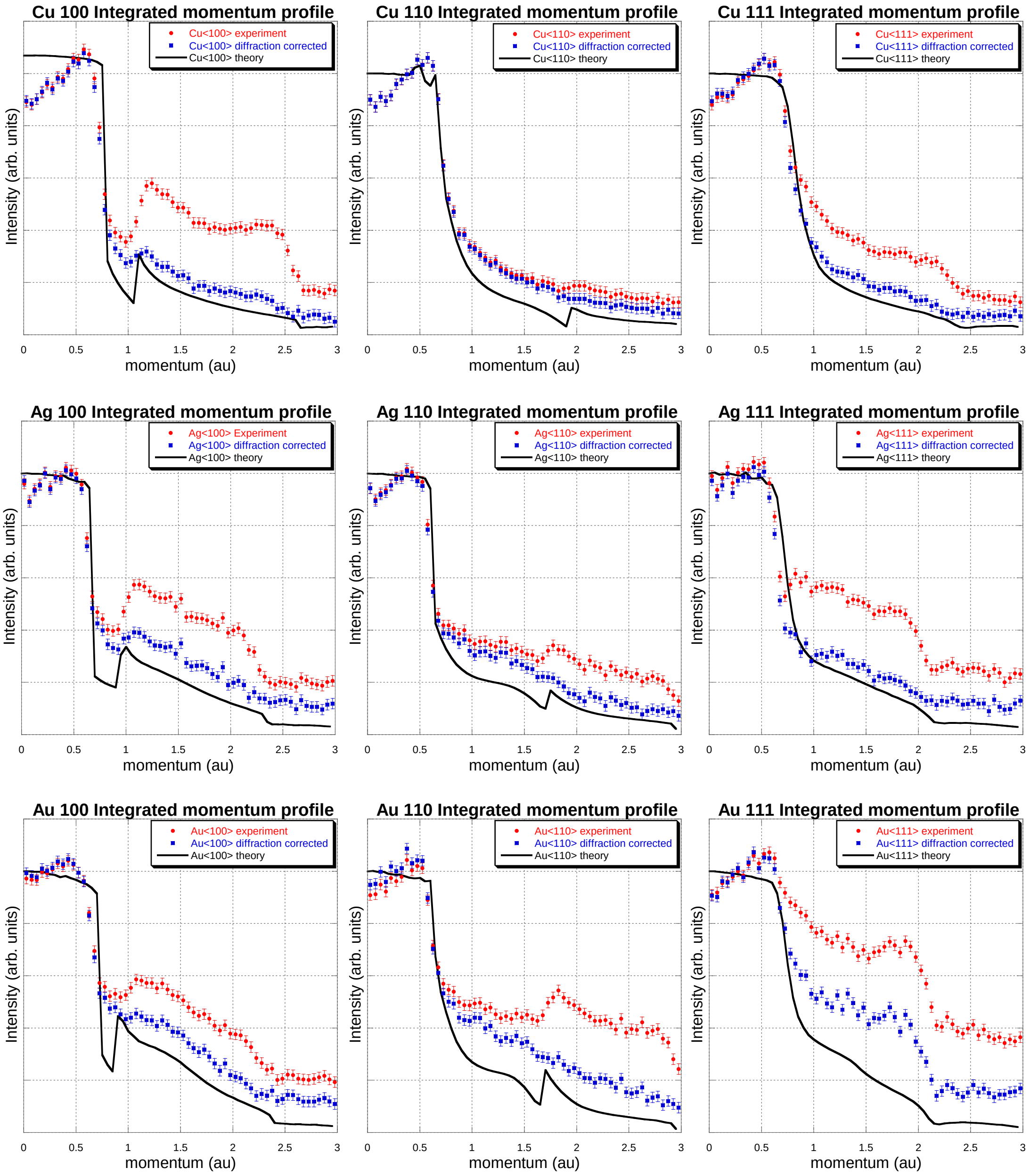

Figure 4.12: The EMS momentum profiles of the three measured high symmetry directions of the noble metals (●), which have been integrated over the valence bands. They have been corrected for diffraction effects (●), and compared to the FP-LMTO, LDA theory (-). The difference in the momentum profile intensity at higher momentum can be partly attributed to an incorrect electron correlation correction used in the theory.

The raw EMS data points (●, Fig. 4.12) have considerably more intensity at higher momentum values than theory (-, Fig. 4.12). Most of this extra intensity is due to diffraction effects from the incident or one of the outgoing electron waves interacting with the periodic atomic cores in the solid. Diffraction effects that occur along the measurement vector can be measured and corrected for, the diffraction corrected EMS spectra (blue dots, Fig. 4.12) match the theory more accurately than the raw experimental data. In all cases there is still more intensity in the diffraction corrected experimental spectra than theory predicts. There are three possible main sources of the extra intensity. The first is it could be caused from diffraction contributions that are not along the measured direction ("out-of-plane" diffraction), and hence have not been corrected for. The second is from electron correlation in the d-band electrons, which will cause the d-band to be more dispersed in real space and thus more concentrated in momentum space. A third effect could be incoherent elastic scattering, which is elastic scattering that is not shifted by a complete **G** vector. The out-of-plane diffraction contributions are hard to determine as very small alignment changes can severely change the contribution from this effect. For the case of Cu $\langle 110 \rangle$ diffraction effects were very small, which implies that out-of-plane diffraction effects would also be quite small, yet there is still a considerable amount of extra intensity at higher momenta than theory estimates. This implies that theory may under predict the effect of electron correlation in the noble metals. As the electronic systems become more complex it is seen that the gap in the intensity predicted by theory and the diffraction corrected experimental spectra becomes larger. As the atomic cores increase in size the out-of-plane diffraction is expected to become more intense. At this stage it is impossible to extract the full "out-of-plane" diffraction contribution, and thus impossible to determine the full effect of electron correlation.

There is a sharp increase in intensity in the $\langle 100 \rangle$ (at 0.8-1.0 au) and $\langle 110 \rangle$ (at 1.7-1.9 au) integrated momentum profiles (Fig. 4.12), this feature corresponds to where the sp-band cuts through the Fermi level. The sp-band moves from a momentum value where the sp-band is above the Fermi level (unoccupied) to a higher momentum value where the sp-band again drops below the Fermi level and is occupied, resulting in a sharp increase in electron intensity at the transitional momentum value. The description of this effect is supported by the $\langle 111 \rangle$ spectra that do not have this feature. In the $\langle 111 \rangle$ directions the sp-bands do not cross the Fermi level, and hence there is no dramatic change of intensity.

There is a large discrepancy between the experimental and theoretical intensity in the integrated momentum profiles at the Γ-point ($\mathbf{q}$=0). The difference in this intensity is purely an experimental result that arises from lifetime broadening at the valence band minimum. All the experimental and theoretical spectra were integrated from -2 to 13 eV, this meant however that for Cu and Au, which have an sp-band binding energy on the order of 9 eV at the Γ-point, quasi-particle energy broadening near the bottom of the valence band will shift intensity from the sp-band outside of the integrated energy range. When electrons are ejected they leave behind a positively charged region that perturbs the wave function of the electrons around it. This positive hole has a finite lifetime which leads to an energy broadening effect commonly referred to as lifetime broadening. A bound electron that is ejected from a bound state leaves an empty "hole" which is more energetically favourable for electrons that are less tightly bound. For a hole near the bottom of the valence band there are many less tightly bound electrons that can cascade into the created "hole", thus there are many possible transitions (final states). The large number of decay channels means there is a distribution of final state energies which results in a larger energy distribution of measured binding energies. The energy distribution is known as lifetime broadening, and it is a large effect at the bottom of the sp-band. A hole created near the Fermi level has very few transitions (final states) available to fill the hole, meaning the effect of lifetime broadening near the Fermi level is very minimal. This lifetime broadening is a correlation effect between the electrons, and can only be calculated using a many-body theory. Many-body theories are computationally very expensive, especially for electronic systems as large as the noble metals.

An alternative many body computation (eg. a cumulant expansion) can be used to model the lifetime broadening of a free electron gas. The only input parameter into the cumulant expansion theory calculation is the electron density, and through iterative cycles the input parameter can be adjusted so the resulting free electron parabola matches the band width of the sp-band from Cu. The effect of lifetime broadening can be obtained and then added to the spectral momentum densities calculated for the noble metals from the

FP-LMTO code. This simplified calculation works remarkably well for free electron like metals (eg. Al). Cu however has d-electrons, and spd-hybridisation which perturbs Cu away from the free electron like model. Surprisingly the model still works reasonably well for Cu, but more accurate results can be expected from a complete many-body calculation.

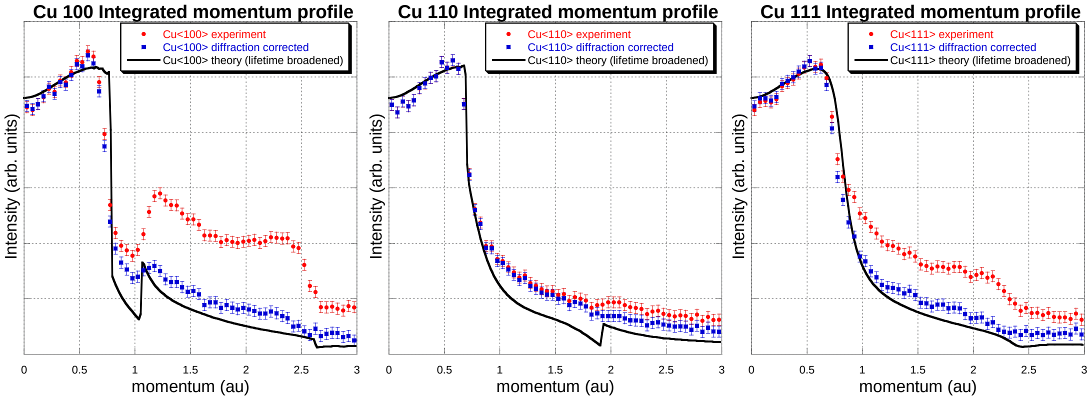

Figure 4.13: The integrated experimental Cu momentum profiles are compared to a lifetime broadened LDA calculation. The lifetime broadening strongly broadens the base of the sp-hybridised band around the Γ-point, shifting intensity near the Γ-point to binding energies outside the range of the integrated momentum profile. The raw experimental data (●), diffraction corrected experimental data (●) and FP-LMTO with lifetime broadening (-) are shown.

In Fig. 4.13, the lifetime broadening effect has been added to the theoretical calculation for Cu, and the integrated (-2 to 13 eV) momentum profile has been determined. Some intensity at the Γ-point has been lost as it now lies outside of the integrated energy range. The agreement between theory and experiment is greatly improved when lifetime broadening is accounted for.

The advantage of EMS over the reconstructed 3D Compton profiles is that EMS can differentiate over energy intervals which resolves more information about the target. By integrating over a 1 eV interval near the Fermi energy, the diffraction of the sp-hybridised band in the first Brillouin zone out to higher order Brillouin zones can be seen, and from this information the reciprocal lattice vector ($\mathbf{G}_{\text{exp}}$) can be measured. The reciprocal lattice vector is generally well known, so the EMS measurement of **G** is used as a cross check, so that the sample is well aligned. In the $\langle 111 \rangle$ directions the sp-band does not

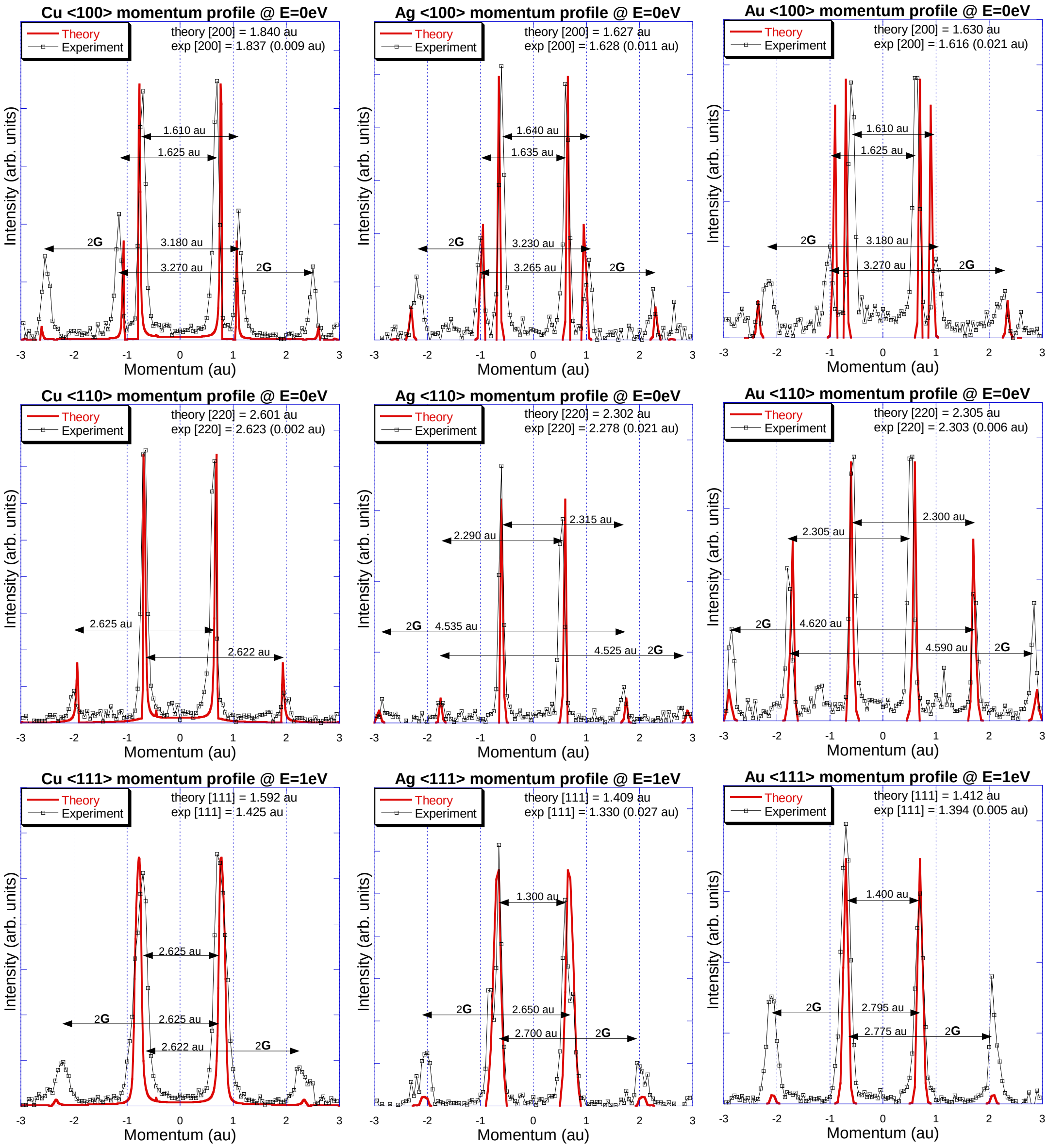

Figure 4.14: Momentum profiles taken from the raw SMDs (not corrected for diffraction effects) at 1 eV energy window near the Fermi level. The distance between the diffracted peaks (higher order BZ peaks) and the first order BZ peaks is $\mathbf{G}_{\text{exp}}$. In each plot the experimental $\mathbf{G}_{\text{exp}}$ (with statistical error) is compared to the theoretically determined $\mathbf{G}$. The raw experimental data (☐) and the FP-LMTO theoretical curves (-) are shown. The measurement and the FP-LMTO calculations should only coincide in magnitude if diffraction effects were negligibly small.

pass through the Fermi level as previously discussed so the momentum profile (Fig. 4.14) is taken at 1 eV below the Fermi level, which is where the occupied sp-band first appears.

The momentum profiles at the Fermi level (Fig. 4.14) are shown with the momentum vector between the sp-hybridised band in the first Brillouin zone and the corresponding diffracted peaks. This distance in momentum space between the diffraction peaks has been compared to the well known **G** value, which can be determined from the real space lattice spacings which are easily measured and calculated. In all the $\langle 100\rangle$ and $\langle 110\rangle$ measurements the EMS determined $\mathbf{G}_{\mathrm{exp}}$ agrees with the theoretical value to within the experimental data bin size (0.05 au). In the $\langle 111\rangle$ measurements the EMS determined $\mathbf{G}_{\mathrm{exp}}$ vectors are less than the theoretical values. This discrepancy is attributed to the fact that the momentum profile peaks are wider due to the bands folding over rather than cutting through the Fermi level. The intensity of the band decreases as the band moves out to higher momentum so the intensity at the inside of the $\langle 111\rangle$ Fermi level momentum profile peak is larger than at the outside. Resulting in the fitting of the peak to yield a smaller momentum value than where the band fold over point actually is. Thus the experimentally determined $\mathbf{G}_{\langle 111\rangle}$ will always under predict the real value, a trend which is clearly visible in Fig. 4.14. Moving down the group 11 elements (in Fig. 4.14) an increase in the intensity of the diffraction peaks is evident. This originates from the atomic cores becoming larger and thus the diffraction cross section increases. The exception to this trend is the Cu$\langle 100\rangle$ measurement which is attributed to the sample being thicker than normal.

4.4.3 Energy Profiles

Integrating the SMD over a limited momentum range (0.05 au) and presenting the resulting intensity as a function of binding energy yields the energy profile of the valence electrons for any specific crystalline direction, which will yield the band intensities of a small volume in momentum space. This analysis technique accurately determines the binding energies of the bands at key crystallographic positions, such as the Γ, X ($\langle 100\rangle$ BZ boundary), K ($\langle 110\rangle$ BZ boundary) or L ($\langle 111\rangle$ BZ boundary) points for a FCC structure.

For any single crystal sample (or even a polycrystalline sample) the Γ-point (at $\mathbf{q} = 0$

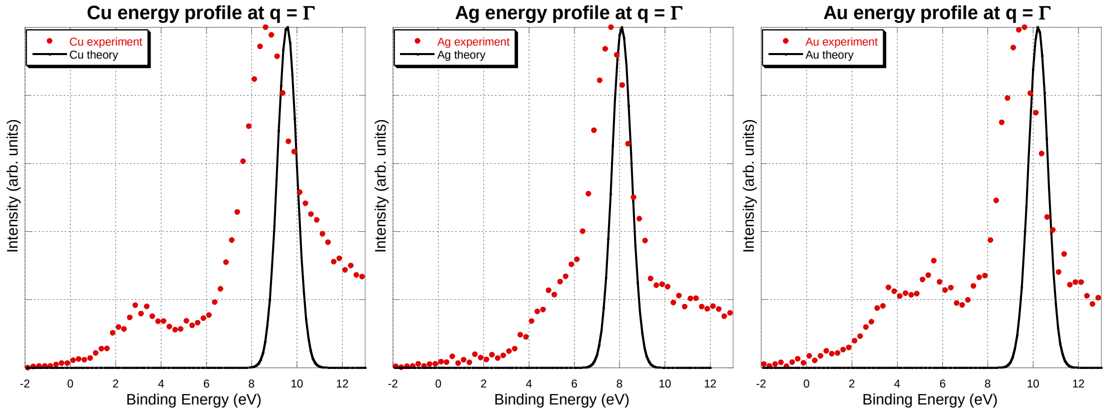

Figure 4.15: The energy profiles integrated over a 0.05 au range about the Γ point (**q**=0). The experimentally measured EMS spectra (●) is compared to the FP-LMTO DFT calculation (-). Theory can be seen to consistently over predict the sp-band binding energy at this point. The large peak is the bottom of the sp-band, the other peaks at lower binding energy come from out of plane diffraction that creates some intensity in d-bands that would otherwise have a spectral weight too low to be measured in the first Brillouin zone.

au) is a common point, hence the Γ-point spectra for all three high symmetry directions will be the same for a specific sample. Determining the peak position at the Γ-point will give the sp-band minimum, and for the three noble metals the $\langle 100\rangle$ and $\langle 110\rangle$ measurements the valence band width will be obtained, as they are occupied up to the Fermi level. Experimentally there is a difference in energy between the surface of a sample and point in space outside the sample, this level is referred to as the vacuum level (or work function) and for Cu, Ag and Au it is on the order of 4 eV. This vacuum level creates an offset in the measured energy scale that can be corrected for by visually realigning the Fermi level with the sharp intensity drop off in the experimental spectra that correspond to the Fermi level. The experimental resolution (1 eV), means that some intensity will lie above the Fermi level, this makes alignment a little difficult and introduces a source of error into the measured band widths and band levels. The quoted experimental error (± 0.2 eV) in band positions comes from the accuracy in the fitting of the peak and determining the Fermi level. Another EMS group from Flinders University quotes an error of ±0.2 eV due to experimental resolution and fitting uncertainties [18, 101].

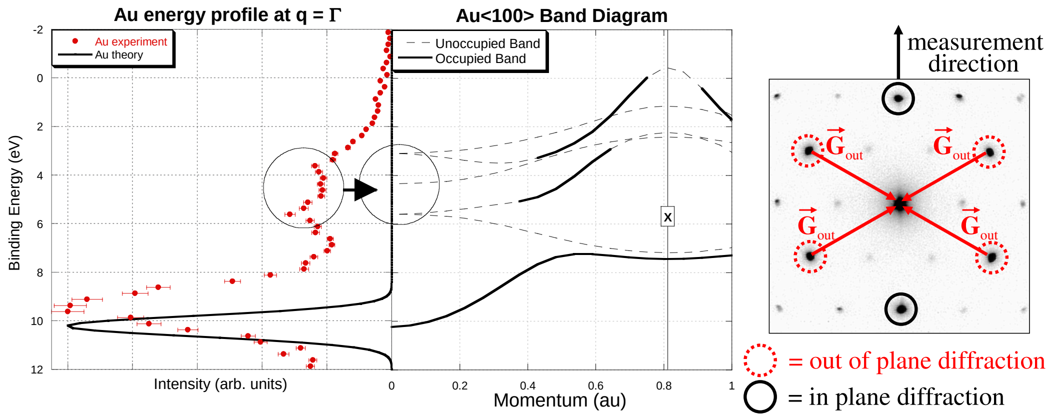

Figure 4.16: The energy profile (left) for Au at $\mathbf{q} = 0$ is shown next to the band diagram (centre) using the same energy axis. The peaks from the theoretically estimated unoccupied d-bands are indicated. The intensity in these bands come from diffraction effects that are not along the measurement vector as shown by the red vectors in the electron diffraction image (right). Theoretically there are 3 d-band energy levels at $\mathbf{q} = 0$, only 2 of those are experimentally resolved.

The energy profiles of the noble metals at the Γ-point (q = G, Fig. 4.15) have extra peaks at lower binding energy that correspond to bands that are estimated by theory to have zero intensity in the first Brillouin zone (BZ). These peaks are caused by diffraction that shifts a copy of the experimental spectrum that is $\Gamma + \mathbf{G}_{in/out}$ in any direction (Fig. 4.16). This allows EMS to measure the d-band positions that would otherwise have too small of a spectral weight in the first BZ (Γ_{7+} and Γ_{8+}). The Γ-point band positions were measured from the energy plots (Fig. 4.15) and are presented in Tab. 4.2.

In all three samples the sp-bands (Γ_{6+}) are the strongest signal in the Γ-point energy profiles (Fig. 4.15) for both experiment and the plotted LDA theory [89]. The sp-band (Γ_{6+}) is the most intense signal in the EMS measurement which is in contrast to the ARPES experiment where the sp-band is weakest. Despite the differences in signal strength the EMS data and ARPES data agree within the EMS experimental resolution (0.2 eV). The experimental measurements are compared to three different theoretical calculations, there is a non-ab initio self consistent charge density (SCCD) calculation [102] which was calculated by iteratively varying the exchange potential until the calculated band structure was in good agreement to the ARPES data. There is a FP-LMTO LDA cal-

Symmetry label	EMS data (this work)	ARPES data	LDA theory [89]	SCCD theory [102]	LDA + SIC [103]
Cu Γ_{6+}	8.72	8.60 [104]	9.56	8.75	8.80
Cu $\Gamma_{7+,8+}$	3.00	3.42-3.65 [104, 105, 106]	3.20	3.34,3.54	2.93,3.09
Ag Γ_{6+}	7.60	7.44 [107]	8.11	7.21	-
Ag $\Gamma_{7+,8+}$	5.20	5.48-6.16 [107, 108]	4.93	5.37,5.82	-
Au Γ_{6+}	9.45	-	10.24	9.01	-
Au Γ_{8+}	5.85	5.90 [109]	5.60	5.75	-
Au Γ_{7+}	3.90	4.45 [109]	4.34	4.33	-

Table 4.2: Experimental and theoretical values for the Γ_{6+}, Γ_{7+}, and Γ_{8+} band positions that are common to all single crystal directions. The error in the EMS Γ_{6+} band positions are estimated to be $\approx$0.2 eV, the other bands are expected to have a much larger error ($\approx$ 0.4 eV) due to poor statistics. All values are given in eV.

culation [89], which is known to overestimate the Γ-point binding energies of sp-bands in metals [110] and overestimate the energy dispersion of the d-bands [103], due to the non-zero cancellation of the self-Coulomb energy and the self-exchange-correlation. The third theory is an LDA calculation that has a self interaction correction (SIC) applied which ideally corrects for any non-zero cancellation in the self-Coulomb energy and self-exchange-correlation.

The sp-bands are well estimated by the SCCD theory (Tab. 4.2), however the results of the calculation [102] had to be unjustifiably shifted by 0.2 eV to get this agreement. The SCCD estimation of the sp-band binding energy appears to become worse as the system complexity increases. The LDA theory, overestimates the Γ-point sp-band binding energy in all cases, however the system complexity does not seem to affect the LDA calculations comparison with experiment. The LDA calculation with SIC [103] is in better agreement with the experimental sp-band binding energy data for Cu. Commonly the disagreement of the LDA calculation with sp-band binding energies has been attributed to self-energy effects [111]. The improved comparison with the SIC corrected LDA theory indicates that it is a combination of both self interaction and self energy effects in the LDA calculation that leads to poor approximation of the sp-band binding energy.

The Γ-point d-bands (Γ_{7+}, Γ_{8+}) of Cu and Ag were unresolved in the EMS measurement due to the low intensity which was reliant upon out of plane diffraction to occupy those bands, so those bands are seen as a single peak. The Au d-bands were separable because of their larger energy separation caused by a larger spin-orbit interaction. Comparison of the two experimental data sets show that the measured EMS d-band positions are lower in binding energy and for the case of Au show a larger spin-orbit splitting than the experimental ARPES results, the cause of the discrepancy is uncertain. Further EMS measurements of the Cu and Ag samples in extended momentum space, where these d-bands have a higher spectral weight, will yield a more accurate determination and most likely separation of the Γ_{7+} and Γ_{8+} bands. A description of using EMS to measure out into extended momentum space can be found in Vos *et. al.* [37, 40]. The calculated LDA d-band positions are lower in binding energy than the ARPES measured d-band positions, indicating that the metallic screening is overestimated in the LDA calculation. When the SIC is introduced to the LDA calculation the disagreement between the d-band positions estimated by theory and measured by experiment only become larger.

High Symmetry Points

In solid state physics the high symmetry directions, $\langle 100\rangle$, $\langle 110\rangle$, and $\langle 111\rangle$ are more commonly referred to as the Γ-X, Γ-K, and Γ-L respectively. These high symmetry points (X, K, L) are at a Brillouin zone boundary (see Fig. 4.17). Previously theorists only had ARPES data to compare their calculated band diagrams against, now with the improvement of the EMS technique to a point where the complete band diagram can be accurately determined (1.0 eV, 0.1 au resolution) in one measurement, there are two different experimental techniques that can enhance the understanding of valence electrons in many electron systems. The X, K, and L symmetry points for these noble metal systems were analysed and compared to both the available ARPES data points and different types of theory.

The energy profiles at the crystallographic points (X, K, L) are integrated over a 0.05 au momentum window (Fig. 4.18), the experimental spectrum (●) is overlaid on the theoretical calculation (-). In the X and K-point energy profiles the sp-band is above the

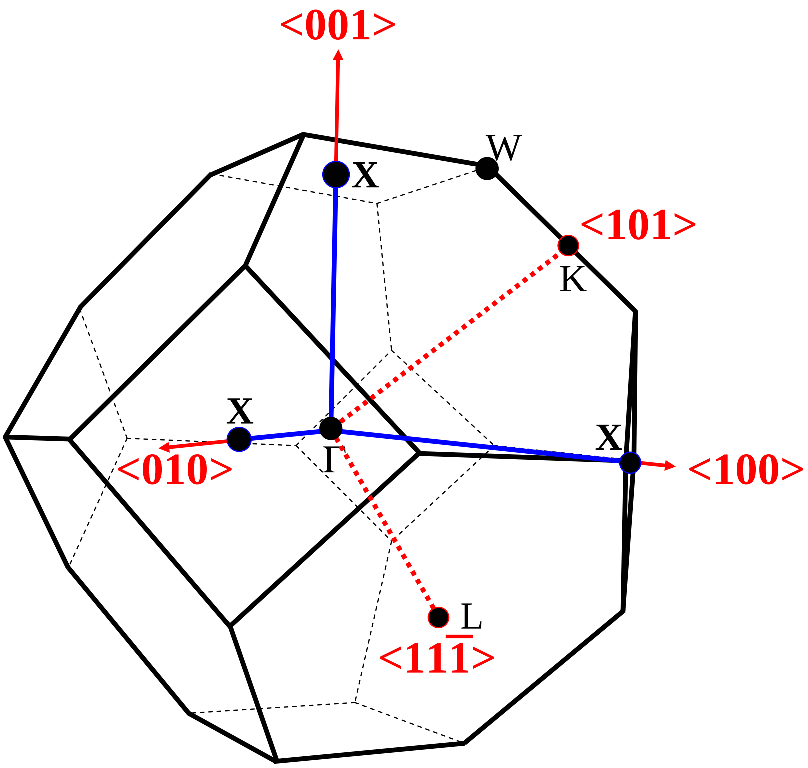

Figure 4.17: A 3D representation of the first Brillouin zone boundary with the key crystallographic points (X,K,L) indicated. The measured directions $\langle 100 \rangle$ (Γ-X), $\langle 110 \rangle$ (Γ-K), and $\langle 111 \rangle$ (Γ-L) are shown with vectors.

Fermi level and hence unoccupied, so in those energy profiles only contributions from the d-bands are seen. In the case of the L-point ($\langle 111 \rangle$) spectra the sp-band is below the Fermi level and folds over at this point, so the sp-band and the d-band peaks are visible. The binding energies of the sp-bands (L-point spectra only, L_{6-}) and the d-bands ($X_{6+,7+}$, $K_{6+,7+}$, $L_{4+,5+,6+}$) were determined from the experimental energy profiles (Fig. 4.18) and compared to experimental ARPES data and an LDA theory [89] and an SCCD theory [102] (Tab. 4.3).

The L_{6-} point is the sp-band local maximum (in terms of binding energy) in the three dimensional band structure, thus any slight sample misalignment or surface disorder will severely affect the position of this band by moving it to a lower binding energy. The EMS values for the L_{6-}-point are much lower than the ARPES values, indicating that there may possibly be either a slight misalignment of the sample, or there is some surface disorder

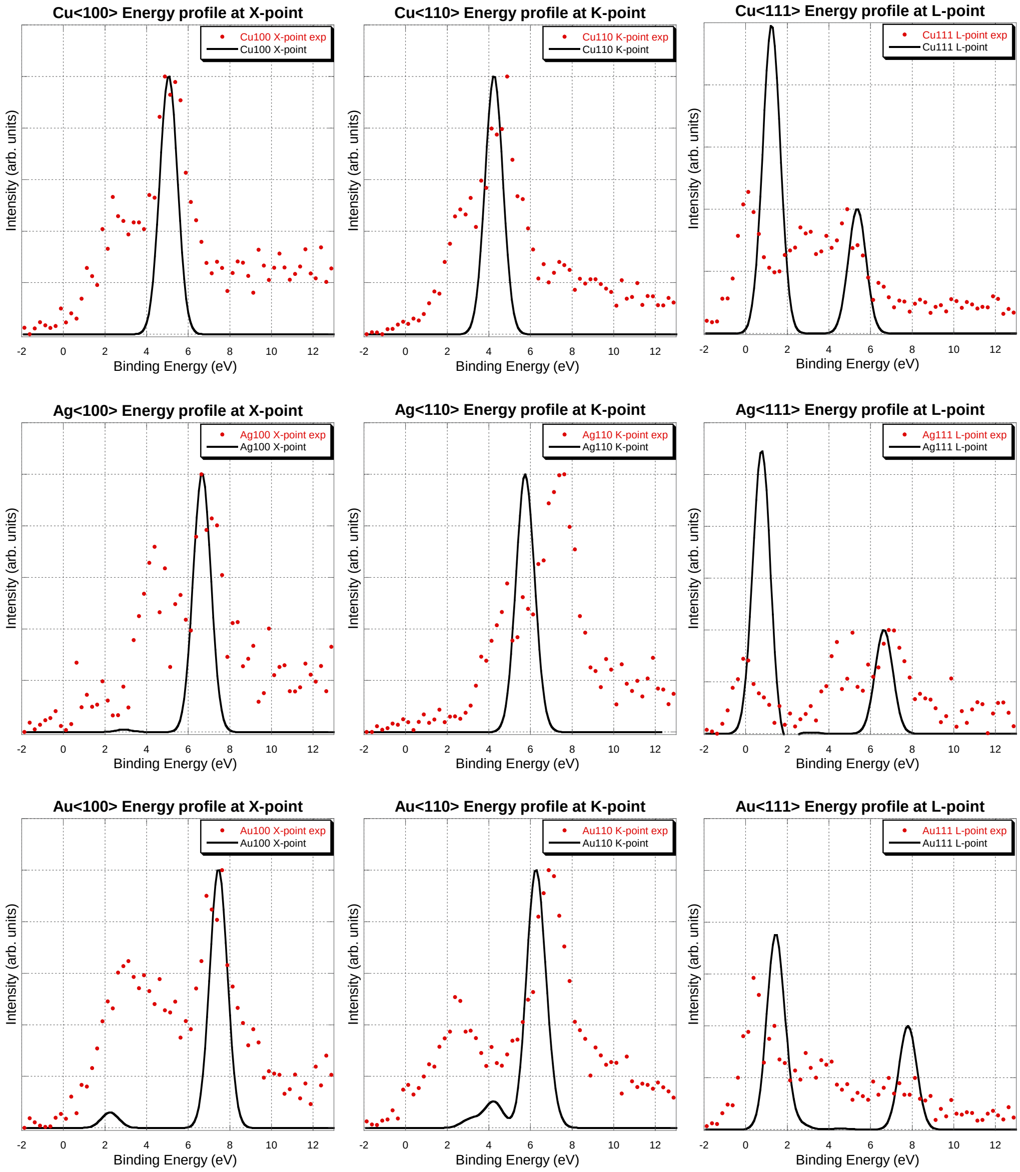

Figure 4.18: The energy profiles of the key crystallographic points that lie on the first Brillouin zone boundary along each direction. The experimental EMS data (●) is compared to the FP-LMTO DFT calculation (-). The peaks in the $\langle 100\rangle$ and $\langle 110\rangle$ direction correspond to the d-bands, the first peak in the $\langle 111\rangle$ direction is due to the sp-band.

effects in the EMS measurement, however the EMS values agree very well with the SCCD theory, that was tailored for the ARPES measurements. This implies that perhaps the real L_{6-}-point binding energies are likely to be somewhere between the EMS and ARPES results. The LDA theory overestimates the L-point sp-band binding energy, indicating that self energy effects are strong at this point. The differences between experiment and the LDA calculation for the L_{6-}-points appear to be consistent with increasing system complexity.

The EMS measured d-bands (Tab. 4.3) for the crystal points energy plots (Fig. 4.18), are more complicated than the sp-bands. There are numerous d-bands at each crystal-point that are slightly separated in binding energy due to spin-orbit coupling, that is larger for heavier elements. In the EMS measured crystal-point energy-plots (Fig. 4.18), one d-band has a high intensity as it has a large spectral weight, whilst the other bands are not measured as they have a very low spectral weight at the first BZ boundary, we still measure some intensity due to out of plane diffraction (Fig. 4.16). Due to the narrow energy splitting, and low occupation of some of the d-bands, not all the d-bands were resolved, and hence in the EMS spectra some bands are grouped together (Tab. 4.3).

In the EMS X-point spectra (Fig. 4.18) the high binding energy X_{6+}-point is the most intense d-band in the first BZ boundary, and the overall agreement between ARPES, EMS, and the two theories is quite good. The other X-point d-bands (X_{7+},X_{6+}, X_{7+}), have low intensity in the EMS measurement, and they are all higher in binding energy than measured by ARPES and estimated by the LDA and SCCD theory. The differences between the EMS and ARPES d-bands are on the order of the EMS band energy resolution (0.2 eV), but the LDA theory consistently underestimates the binding energy of the three lower binding energy d-bands. The LDA discrepancy is consistent with theoretical findings that LDA overestimates the d-band dispersion due to self interaction corrections [103, 111], and overestimates the effect of metallic screening [103].

In the K-point and L-point spectra all the EMS measured d-bands agree well with the available APRES measurements. Comparing experimentally measured d-bands to the LDA calculations, it appears that the LDA d-bands are generally underestimated, and the dispersion is overestimated, which is consistent with the findings of the X-point results.

It is clear that generally the EMS and ARPES measurements are in agreement, there are some discrepancies in the L-point sp-band binding energies where EMS is expected to measure a binding energy lower than expected. There is also some discrepancies in the

Symmetry label	EMS data (this work)	ARPES data	LDA theory [89]	SCCD theory [102]
X-point bands				
Cu X$_{7+}$	2.42	1.98-2.05 [104, 105, 106]	1.63	2.01
Cu X$_{6+}$		2.00-2.12 [104, 105, 106]	1.63	2.16
Cu X$_{7+}$		2.30 [104, 106]	1.78	2.33
Cu X$_{6+}$	5.21	5.15-5.20 [104, 105, 106]	5.06	5.14
Ag X$_{7+}$	4.31	3.82 [108]	2.80	3.71
Ag X$_{6+}$		4.12 [108]	2.80	4.05
Ag X$_{7+}$		4.36 [108]	3.04	4.25
Ag X$_{6+}$	6.87	7.30 [108]	6.64	7.00
Au X$_{7+}$	-	1.60 [112]	1.15	1.72
Au X$_{6+}$	3.21	-	2.23	2.77
Au X$_{7+}$		-	2.42	3.00
Au X$_{6+}$	7.33	-	7.45	7.27
K-point bands				
Cu K$_{7+}$	2.45	2.10-2.15 [104, 106]	1.83	2.26
Cu K$_{6+}$		2.50 [104, 106]	2.21	2.66
Cu K$_{7+}$		2.95-3.00 [104, 106]	2.93	3.06
Cu K$_{6+}$	4.62	4.45-4.60 [104, 106]	4.52	4.59
Ag K$_{7+}$	4.75	4.10 [113]	3.09	4.05
Ag K$_{6+}$		-	3.62	4.57
Ag K$_{7+}$		4.86 [113]	4.20	4.87
Ag K$_{6+}$	7.34	6.59 [113]	6.19	6.60
Au K$_{7+}$	2.66	-	1.95	2.51
Au K$_{6+}$	6.95	-	6.87	6.65
L-point bands				
Cu L$_{6-}$	0.04	0.90 [105]	1.19	0.39
Cu L$_{4+,5+,6+}$	3.14	2.24-2.25 [104, 105, 106]	1.77	2.21-2.32
Cu L$_{6+,4+,5+}$		3.27-3.70 [104, 105, 106]	3.22	3.41-3.62
Cu L$_{6+}$	5.02	-	5.29	5.04
Ag L$_{6-}$	0.07	0.30 [114]	0.71	0.03
Ag L$_{4+,5+}$	4.26	3.96-4.22 [106, 107]	3.03	4.01
Ag L$_{6+}$		4.20 [107]	3.03	4.23
Ag L$_{6+}$	5.11	5.53 [107]	4.96	5.44
Ag L$_{4+,5+}$		5.82 [107]	4.96	5.91
Ag L$_{6+}$	7.08	6.94 [107]	6.62	6.74
Au L$_{6-}$	0.35	-	1.37	0.37
Au L$_{6+}$	3.45	-	2.49	3.02
Au L$_{6+}$	7.35	-	7.72	7.14

Table 4.3: Experimental and theoretical binding energies (eV) for the valence bands at the X, K and L crystallographic points in Cu, Ag and Au points. Multiple bands that are grouped together to one energy level, are unresolved because of either the energy resolution or poor statistics.

lower binding energy X-point d-bands, where EMS measures them at slightly higher binding energy than ARPES. Comparison between experimental results and the LDA theory reveals that the LDA theory overestimates the d-band dispersion, overestimates the sp-band binding energy, and underestimates the d-band binding energy. The overestimation of the sp-band and d-band dispersion is generally a sign that the self-Coulomb energy and the self-exchange correlation energy are not completely cancelling [103, 111, 115]. SIC corrections, which were introduced in the Cu Γ-point measurement (Tab. 4.2), showed a remarkable improvement in those discrepancies. The underestimation of the d-band binding energy is typical of a relaxation shift [103], perhaps indicating that the metallic screening in these systems are overestimated by the LDA calculations. The SCCD calculation, whose exchange potential was artificially varied to achieve reasonable comparisons with ARPES results, shows a better general agreement to the experimental results which is expected. As the target system becomes more complex the SCCD calculation shows a decrease in the agreement, whilst the LDA calculation is consistent in the relative disagreement.

Linear Density of States

Integrating over the entire momentum range (-3 to +3 au) will produce the linear density of states (linear-DOS). Photoemission experiments (at high energy) measure the density of states (DOS) over all momentum space, where as EMS measures a more resolved linear-DOS which is the density integrated along a vector in momentum space (the direction of the momentum transfer the EMS measurement), the vector has a projected momentum width of ≈ 0.1 au. EMS is more sensitive to the sp-band electrons, primarily because of their concentration over the measured momentum range. Alternatively photoemission measurements are more sensitive to the d-bands and to surface effects, so comparison between the DOS and linear-DOS is not applicable due to the differences in the two measurements.

The EMS measured linear-DOSs are compared to the FP-LMTO LDA calculation

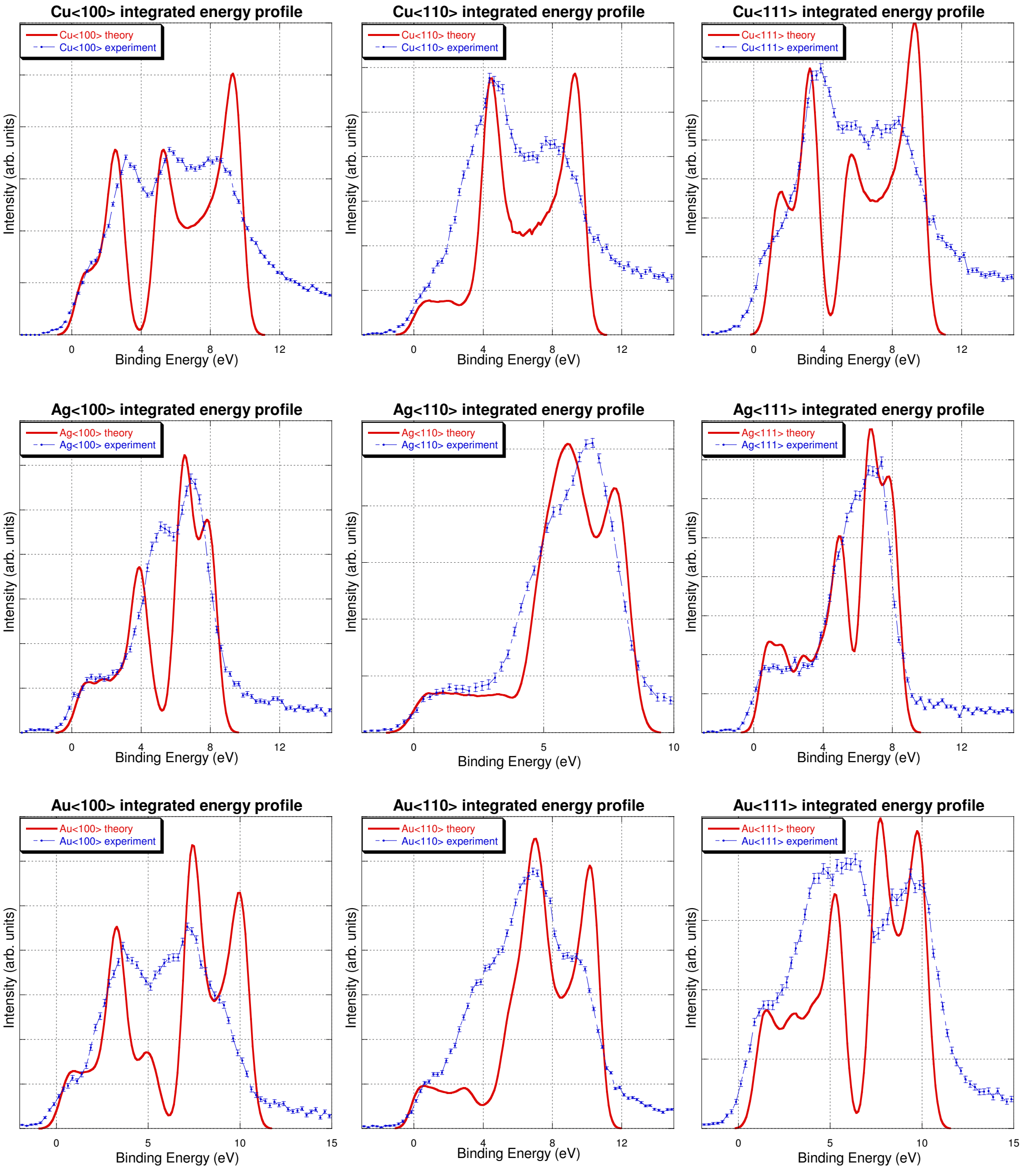

Figure 4.19: The EMS valence linear-DOS integrated over the momentum range of -3 to +3 au. The experimental points (•) are plotted with statistical error and compared to the FP-LMTO LDA calculation (-) which has not been corrected for lifetime broadening.

(Fig. 4.19) performed by Anotoli Kheifets [89]. At first glance the agreement between theory and experiment appears to be extremely poor, the relative peak intensities, the peak positions at higher binding energy and the width of the peaks appear to be in poor agreement. These discrepancies can be explained by effects that have already been mentioned. Lifetime broadening effects will broaden these linear-DOS peaks more at higher binding energy, as previously explained, meaning that the heights of the peaks at higher binding energies (ie. the sp-band at the Γ-point) will be more strongly affected than peaks near the Fermi level. The difference in the highest binding-energy peak position (sp-band at the Γ-point) is attributed to the LDA code being known for overestimating the binding energy at the Γ-point for metals [115, 116].

The binding energy of the d-band peaks either side of the band minimum in each plot and the s-band peak near the Fermi level are in reasonable agreement. The EMS spectra measures a much less pronounced band minimum than is predicted by theory which may be attributed to the LDA calculation over predicting the spin-orbit splitting of the d-bands creating a more pronounced minimum. Alternatively it could be due to experimental effects such as surface disorder of the sample, out of plane diffraction, or inelastic losses from the d-band intensity, all of which adds extra intensity around the d-bands. In the energy profiles at the Γ-X, Γ-K, and Γ-L points (Fig. 4.18), the d-bands are more closely matched with theory, and the less complex system of Cu is better described by the ab-initio LDA theory. The same effects are seen in the EMS valence linear-DOS plots (Fig. 4.19).

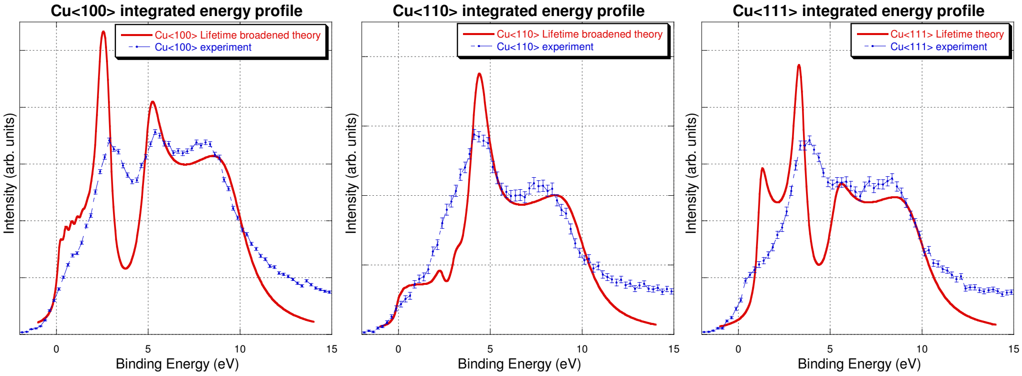

Figure 4.20: The EMS valence linear-DOSs for single crystal copper (●) compared to the LDA, lifetime broadened calculation (-). Much better agreement at higher energies are seen compared to the non-lifetime broadened theory in Fig. 4.19

The lifetime-broadened LDA theory is compared to the three measured directions of Cu in Fig. 4.20. There is a much better match in the shape of the linear-DOS at higher binding energy. A point of concern is still the large difference in the intensity of the peaks near the Fermi level, and the intensity in the band minimum region. Underestimating the experimental energy resolution or the lifetime broadening near the Fermi level would explain these differences. The theoretical calculation is the sum of the intensities along a line in momentum space, the measurement samples a volume of momentum space along a line due to the finite momentum resolution (0.1 au). The effect would be to disperse the sp-band near the Fermi level, lowering the height of the peak in the energy plot and decreasing the measured intensity in the band minimum region.

In the Cu$\langle 111\rangle$ linear-DOS (Fig. 4.20) the major concern is the experimental intensity near the Fermi level that should not be there due to the presence of the band gap. There are two possible experimental causes for this extra intensity, either the sample was slightly misaligned and hence a direction near the $\langle 111\rangle$ was measured. This explanation is unlikely as the diffraction images show that the sample was aligned to within 1^o. The other experimental cause would be surface disorder. This region in the linear-DOS is highly sensitive to surface disorder as zero intensity is only predicted in this region for $\langle 111\rangle$ aligned samples, and disorder of any type (polycrystalline, or another single crystal direction) would give intensity in this area. Surface disorder contributing a noticeable intensity to the measured SMD would also explain the excess experimental intensity in the spd-hybridised minimum in the sp-band ($\approx$ 4 eV, Fig. 4.20).

Core Level Spectra

The outer core level spectra obtained from the EMS experiment is plotted in Fig. 4.21, with the X-ray photoelectron spectroscopy (XPS) measured values indicated by the dashed and solid lines [117]. These core levels are measurable in the valence band EMS measurements of the noble metals as the 2D detectors measure over a large energy window ($\approx$100 eV, summed range). The core levels were at the extreme of the energy window in these measurements and hence they are not as statistically accurate as the valence band part of the spectra. Core levels are localised near the nucleus in real space which makes them very dispersed in momentum space and hence a weaker signal in EMS due to the limited momentum range (-3 to +3 au). XPS is much more able to measure the core levels, as it can sample a lot more of momentum space at once, the XPS values (vertical lines, Fig. 4.21) are shown for their position and also for their relative heights in the Cu and Ag spectra [118]. It has been estimated for XPS measurements that the $p_{\frac{1}{2}}$ Cu (3p) and Ag (4p) are only around 20 % of the intensity of the $p_{\frac{3}{2}}$ peaks [118].

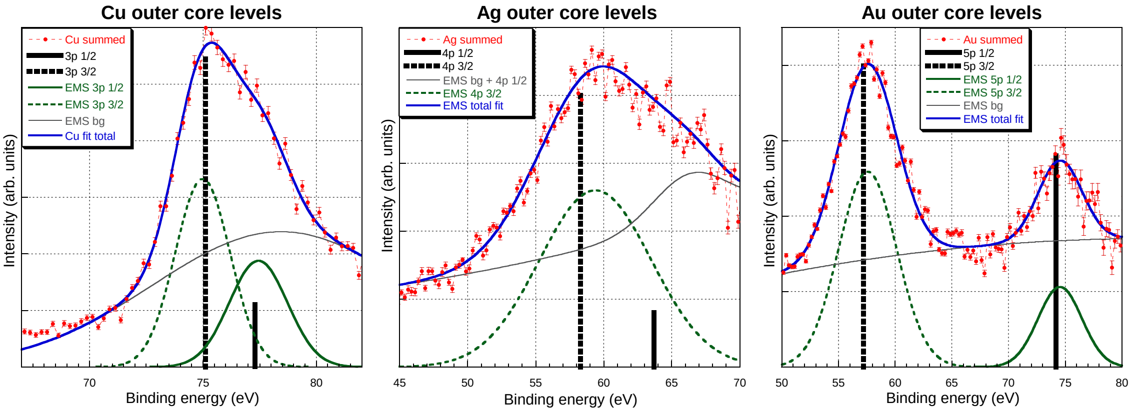

Figure 4.21: The noble metals core levels, the EMS experimental data (●) is fitted with a line of best fit (-) and compared to the XPS measured values (bar plots). The height of the XPS data is not indicative to relative intensities, as they are not precisely known.

Experimental agreement (Tab. 4.4) is much better for Au, where the two core levels are well separated and can be more easily fitted. For the Cu and the Ag core level spectra the spin orbit splitting is small and the EMS measured core level peaks overlap, causing some difficulty in fitting the EMS spectra. The difficulty in fitting, relative intensity ratios and smaller statistics all contribute to the poor agreement between the EMS results and more reliable XPS core levels. The advantage of this EMS measurement is that the peak positions are measured relative to the Fermi level that is obtained in the same measurement.

The width of these peaks can be attributed to a combination of lifetime broadening, shake-up and configuration interaction effects [118, 120]. Lifetime broadening has been previously explained, shake-up effects are when some of the energy used to eject a core level electron is used to excite a valence electron into an unoccupied band, this energy loss causes a broadening in the measured core-level energies. Configuration interaction is a term used to describe the mixing of electronic states in a many-body system. It has

Core Level	EMS (eV)	XPS (eV) [117]	Semiempirical theory (eV) [119]
Cu $3p_{\frac{1}{2}}$	77.15±0.64	77.3	73.6
Cu $3p_{\frac{3}{2}}$	74.98±0.37	75.1	73.6
Ag $4p_{\frac{1}{2}}$	-	63.7	62.6
Ag $4p_{\frac{3}{2}}$	58.84±0.40	58.3	55.9
Au $5p_{\frac{1}{2}}$	74.54±0.29	74.2	71.7
Au $5p_{\frac{3}{2}}$	57.52±0.26	57.2	58.7

Table 4.4: The EMS measured p core levels of the noble metals compared to the XPS measured values and a semiempirical theory. The error shown on the EMS value is a combination of statistical and fitting error, and accuracy in the determination of the Fermi level. The theory is from a semiempirical calculation by Larkins [119]

been shown that to accurately describe initial and final states of solids a combination of many states is needed [120]. The mixing of states leads to a dispersion of the measured binding energy levels. For the core levels (Fig. 4.21) the broadening of the XPS linewidths due to lifetime broadening effects have been calculated and in some cases experimentally measured [118]. As the lifetime broadening effects are internal to the sample, the effect of the probe should be independent, thus the EMS broadening should be similar to the XPS broadening. These effects for the noble metals have been calculated (measured) for Cu 1.5-5 eV (1.5-2.0 eV), Ag 8-13 eV (4-8 eV) and Au (>2.4 eV) [118]. There is great discrepancy between the calculated and measured lifetime broadening effects of the core levels, but Fuggle and Alvarado [118] concluded that various decay mechanisms were severely overestimated in theory and could lead to errors of up to 200%. Also attributed to the broadening of the core levels is a small contribution from multiplet splitting from interaction with the spin moment in the valence level [121]. As the noble metals have the same valence band moment, with only 1 unpaired electron, this contribution to broadening is expected to be very small and consistent across all the noble metals. It is clear from these values that the core level lifetime broadening effect is much larger in Ag than it is in Cu and Au, which is supported with the EMS measured core-levels (Fig. 4.21).

The splitting of the core-level increases as one moves down the group 11 noble metals (Fig. 4.21). This observed splitting is attributed to the spin-orbit coupling with the ionic core. As the ionic core increases in size down the group 11 elements, it is also expected that the spin-orbit splitting increases, which is consistent with EMS results.

4.4.4 Band Diagrams

EMS directly measures the complete valence band SMD for a sample in one measurement. From the EMS measured SMD the occupied ground state band structure can be determined for the bulk electrons. The ARPES technique can be used to measure an angle resolved energy distribution curve (AREDC), from which points on the band diagram can be extracted. Through several ARPES measurements the complete band structure can be measured. ARPES emits low energy electrons, which in effect reduces the sample depth from which it is capable of measuring the band structure. How strongly the surface effects affect the measured band structure in an ARPES measurement is not exactly known, comparing ARPES data to EMS data should help to clarify the effect of the surface.

The EMS measured band diagrams for the noble metals (Figs. 4.22-4.24) are compared to a LDA theory [89] with solid lines representing the bands calculated to have a large spectral weight, and with dashed lines representing the bands calculated to have a very low spectral weight. The EMS measured points are shown by red dots with the error bars associated with fitting and statistical errors, for the entire EMS band diagram, but these statistical errors do not include any associated with general offsets. These general energy errors come from two main causes;

1. The assignment of the Fermi level which can be assigned from the measurement of the core level or from visual alignment with the sudden drop off of intensity at E_F, either method introduces an offset error of up to 0.2 eV.
2. Incorrect methodology in the fitting of the energy plots to extract the band diagram

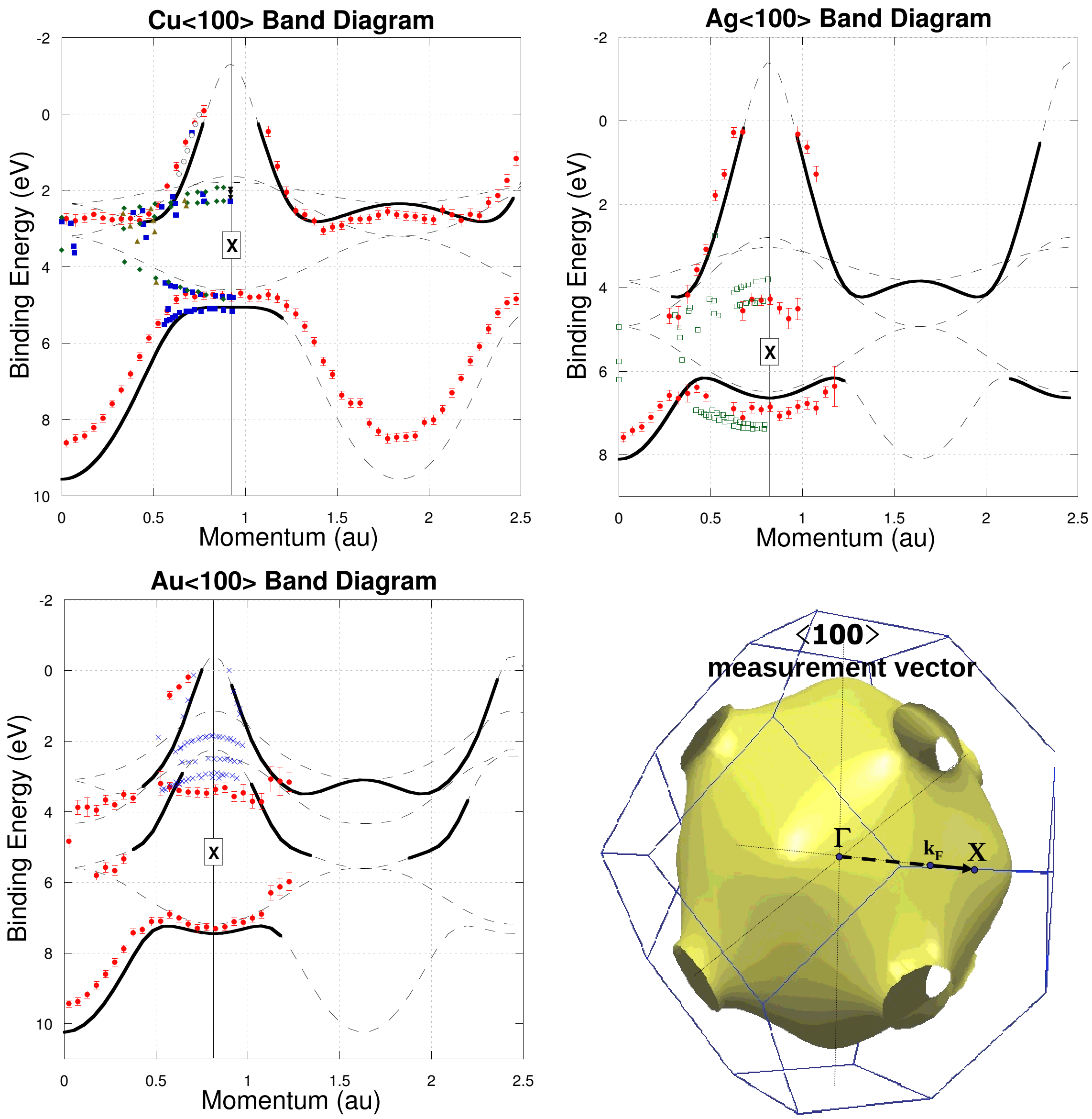

Figure 4.22: The band diagrams for the ⟨100⟩ measurements on the noble metals. The EMS results (●) and various ARPES references (other data points) are compared to the LDA calculation of Kheifets [89], where the bands with heavy spectral weighting (**-**) and the bands with very little spectral weighting (- -) are indicated. The Fermi sphere of a FCC noble metal is shown with the measured ⟨100⟩ vector and crystal symmetry points (■ and **X**) represented. The ARPES references are taken from; ■ = Courths *et. al.* [122], ♦ = Dietz *et. al.* [123], ▲ = Courths *et. al.* [22, 108, 108, 122], ▼ = Balmann *et. al.* [124], ○ = Knapp *et. al.* [105], □ = Wern *et. al.* [113], × = Wern *et. al.* [125].

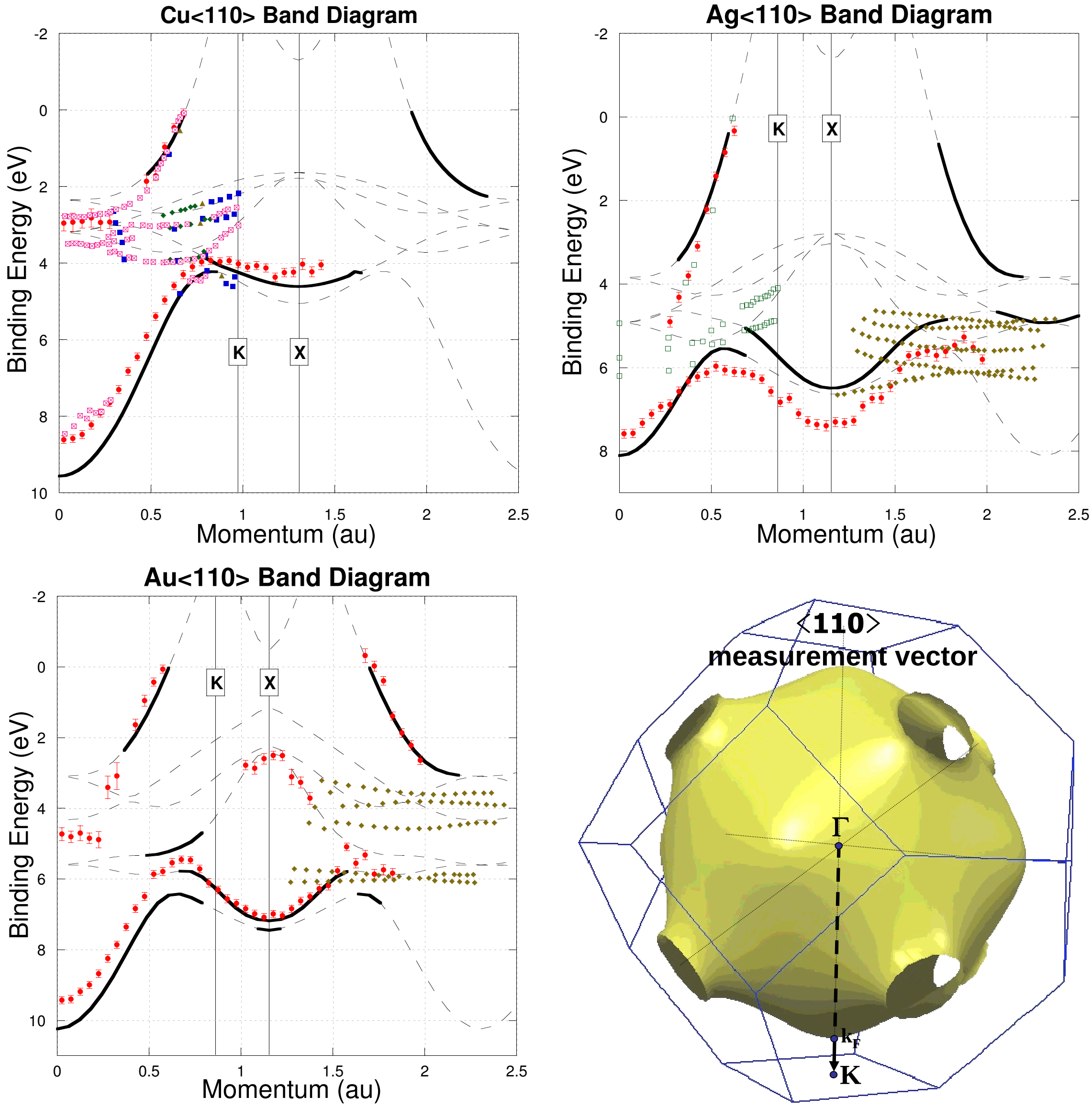

Figure 4.23: The band diagrams for the $\langle 110\rangle$ measurements on the noble metals. The EMS results (red dots) and various ARPES references (other data points) are compared to the LDA calculation of Kheifets [89], where the bands with heavy spectral weighting (**-**) and the bands with very little spectral weighting (- -) are indicated. The Fermi sphere of a FCC noble metal is shown with the measured $\langle 110\rangle$ vector and crystal symmetry points (■ and **K**) represented. The ARPES references are taken from; ■ = Courths *et. al.* [122], ♦ = Dietz *et. al.* [123], ▲ = Courths *et. al.* [22, 108, 106, 122], ☒ = Thiry *et. al.* [104, 126], □ = Wern *et. al.* [113], ♦ = Courths *et. al.* [127].

points, as there are many complex processes occurring such as multiple scattering, lifetime broadening and diffraction, it is difficult to know the precise fitting function

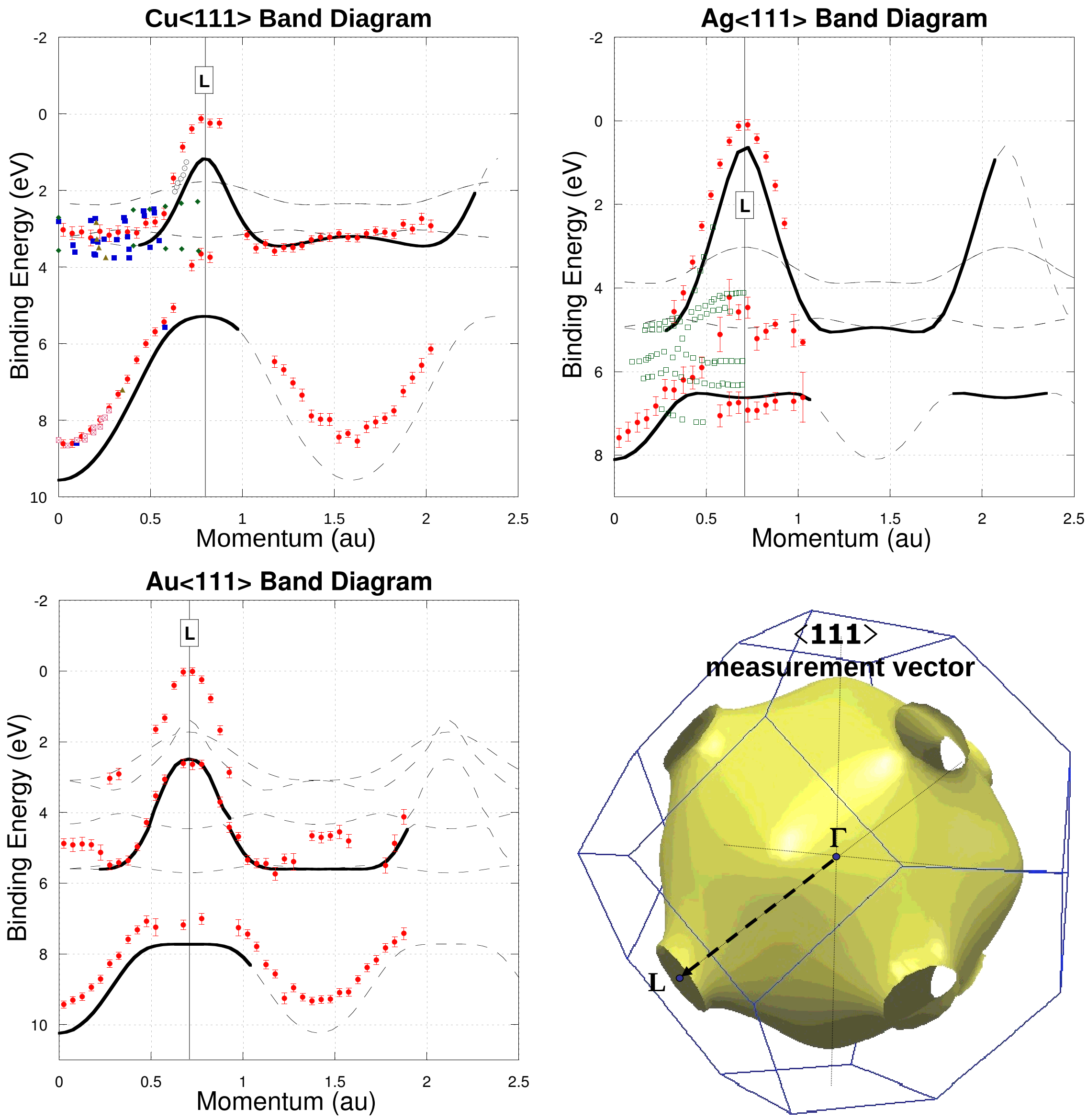

Figure 4.24: The band diagrams for the $\langle 111 \rangle$ measurements on the noble metals. The EMS results (red dots) and various ARPES references (other data points) are compared to the LDA calculation of Kheifets [89], where the bands with heavy spectral weighting (-) and the bands with very little spectral weighting (- -) are indicated. The Fermi sphere of a FCC noble metal is shown with the measured $\langle 111 \rangle$ vector and crystal symmetry points (■ and **L**) represented. The ARPES references are taken from; ■ = Courths *et. al.* [122], ♦ = Dietz *et. al.* [123], ▲ = Courths *et. al.* [22, 108, 106, 122], ○ = Knapp *et. al.* [105], ⊠ = Thiry *et. al.* [104, 126], □ = Wern *et. al.* [113].

to use, it is estimated that an offset error of up to 0.2 eV can be introduced.

There is also the signal-to-noise ratio which is typically very good but in points where the spectral weighting of a band is very low then signal-to-noise can add extra errors that can come from a poor fitting function due to the complexity of the background noise, the majority of this error is included in the statistical error bars plotted in the band diagrams (Figs. 4.22-4.24). The error bars show on the band diagrams only include the statistical error as a result of further measurements will reduce these error bars, a further offset error of 0.28 eV must also be taken into account for each data point, which comes from the two sources of error added in quadrature.

The EMS and LDA band structures are compared to ARPES data from several references, in all these publications it is believed that the bulk band structure was measured. It is noticeable that the majority of the ARPES data points are for the d-bands, which is the strongest signal for ARPES, due to the localisation in real space. Alternatively in the EMS data it is the sp-bands dominate, thus the EMS and ARPES measurements should be used in tandem to obtain the most accurate experimental band diagram.

The EMS data fits the shape of the bands quite well in most cases, however there appears to be large offsets in energy between the LDA theory and the EMS/ARPES data. The ARPES data suggests that the LDA calculation underestimates the binding energy of the d-bands, again indicating a problem in the LDA theory to accurately model the metallic screening in these systems. The EMS data suggests that the valence band width is overestimated by the LDA theory, which is consistent with the LDA theory not including SIC effects. For the sp-bands in all the Cu and Ag measurements, the data points that have been measured by ARPES compares very well with the EMS data. Most of the ARPES points (Figs. 4.22-4.24) have been previously compared (Courths *et. al.* [22]) to a self consistent charge density (SCCD) DFT calculation [102]. The SCCD calculation was not an ab-initio calculation and used experimental ARPES data points as a reference to determine the amount of exchange correlation. So it is with little surprise that the SCCD band diagram matched the ARPES data extremely well. This still indicates that the SCCD calculation is a better estimate for the EMS measured band diagrams of Cu than the ab initio LDA calculation, but a first principles theory is imperative as experimental results will not always be available.

Comparing the EMS results to the LDA calculation, it is seen that for the $\langle 100 \rangle$ and $\langle 110 \rangle$ measurements (Figs. 4.22 and 4.23) there is a good agreement at the top of the sp-band near the Fermi level. Whilst there is a general agreement in shape for the bottom of the sp-band in those measurements, there appears to be a graduated offset that is largest at the higher binding energy. The EMS measured d-bands in the $\langle 100 \rangle$ spectra (Fig. 4.22) are higher in binding energy by up to 1 eV than what the LDA calculation estimates, a trend also seen in the ARPES measured d-bands of Ag and Au. The calculation of Eckardt *et. al.* [102], shows a good agreement with these ARPES d-bands, indicating that self energy corrections, or electron correlation effects along with the modelling of the metallic charge screening from the nucleus are contributing to the poor description of the d-bands in the LDA calculation.

For the $\langle 111 \rangle$ measurements (Fig. 4.24), there is a clear difference at the top of the sp-band near the Fermi level, which is attributed to an experimental problem with surface disorder contaminating the experimental results. The bottom of the sp-band shows the same offsets as was seen in the $\langle 100 \rangle$ and $\langle 110 \rangle$ measurements. Again the Cu $\langle 111 \rangle$ d-bands show a good comparison between theory and experiment, but moving to more relativistic samples in Ag and Au there is again some large differences of up to 1.3 eV in the case of Ag $\langle 111 \rangle$, this difference was not seen in the comparison of the ARPES points to the theory of Eckardt *et. al.* [102] in a publication of Wern *et. al.* [113].

4.4.5 Trends and Disparities

The group 11 noble metals of Cu, Ag and Au are three systems of varying complexity, which is seen by analysing the sp-band width. Cu shows a close comparison to the free electron band width (Tab. 4.1), whilst Ag and Au become increasingly more relativistic. The effects of the larger nucleus in these increasing complex systems are reflected by the size of the d-band splitting in the band diagrams (Figs. 4.22 - 4.24). These noble metals have the same valence electron configuration ($d^{10}s^{1}$) yet still have vastly different SMDs due to the difference in complexity of the systems. As such these targets will provide a good test of both the EMS and ARPES experimental techniques in comparison to each other, and also for the comparison of these experimental results to theoretical calculations.

EMS is a bulk sensitive process which measures the strongest intensity from bands that are denser in momentum space (sp-bands), due to the limited momentum range in which it is measured over. ARPES is more of a surface sensitive process which measures the strongest intensity from bands that are denser in positional space (d-bands). Typically ARPES measured band structures are used in comparison to theoretical calculations, but with the more sp-band and bulk sensitive EMS technique, both ARPES and EMS could be used in conjunction to measure more accurate band structures. These two different experimental techniques measure relatively similar band positions (Tab. 4.3) and band diagrams (Figs. 4.22 - 4.24). There are slight discrepancies in some of the d-band positions in which EMS measures through out of plane diffraction effects (Fig. 4.16), and hence is a weak signal, in which case the ARPES results are expected to be more accurate. Alternatively some slight differences in the sp-band positions are expected to be measured more accurately with the EMS experiment, due to the increased sp-band sensitivity.

Comparison between the combined EMS and ARPES experiments and the LDA calculations in this chapter has shown some consistent failures on the part of the LDA theory. The sp-band width and sp-band position is consistently overestimated by theory which is attributed to a problem in the cancellation of the self-Coulomb and self-exchange correlation effects [103, 111, 115]. The same self energy effects are attributed to the LDA theories overestimation of the d-band dispersion. These assumptions are verified by the observed improvement (Tab. 4.2) of an LDA theory with a SIC that accommodates for the self energy effects. The LDA theory also consistently underestimates the position of the d-bands which is attributed to the LDA theory overestimating the effect of metallic screening from the nucleus [103]. Despite the LDA theory having consistent problems, the positive sign is that the LDA theory was consistently able to estimate the band structures of all these systems of varying complexity. The errors associated with the LDA theory were of a similar order for all the bands in all the samples, indicating that the LDA theory was able to handle the increase in system complexity.

Chapter 5

Disordered Semiconductors and Alloys

Results for the disordered states of silicon (Si) and germanium (Ge) will be presented in order to examine the differences between their amorphous and polycrystalline electronic structure, a comparison which only EMS can provide. Experimental investigations into the complete valence electronic structure of these two states can yield information that has not previously been measured.

The second half of this chapter will examine alloys of nickel (Ni) and copper (Cu) in varying concentrations. A close examination of the change in the electronic structure of the NiCu alloys, as they vary in composition, should obtain information about the nature of the valence electrons.

5.1 Semiconductors in Disordered States

EMS measures the real momentum of the bound electron (**q**) rather than the crystal lattice reduced momentum (**k**) which is measured in photonic techniques such as ARPES. This gives EMS the ability to measure the electronic structure of disordered states as well as single crystal states which have already been presented (see chapter 4). Samples can be prepared in amorphous, polycrystalline or single-crystal forms; each is expected to have a different electronic structure resulting from differences in the degree of short and long range order. Single crystal samples have both short and long range order in the atomic lattice. A polycrystalline sample consists of many small randomly orientated single crystals separated by grain boundaries. Typically amorphous samples have very limited short order and no long range order, which makes them extremely difficult to model with theory. The amorphous state of a semiconductor however is not typical, amorphous semiconductors exist in a special state referred to as a continuous random network (CRN) [128]. In the CRN state each atom has a co-ordination number of 4, but the orientation of the 4 nearest neighbour atoms is still somewhat randomized creating a range of bond angles and bond lengths [129] that vary by as much as 2 % and 10 % respectively [130, 131]. An ideal amorphous semiconductor exists in a perfect CRN state, in reality there is a slight deviation from this picture, with the introduction of dangling bonds, and multi-member rings that create slight variations in electronic density through out the sample [132].

The polycrystalline form of Si and Ge can be approximated theoretically by a spherical average of all possible single crystal directions. A spherical average of theoretical calculations from a 16 by 16 mesh of polar and azimuthal angles has been shown to be the required mesh size for convergence [133]. For amorphous semiconductors it is the CRN that has raised much theoretical interest [134, 135, 136, 137, 138]. In a realistic semiconductor amorphous state there is expected to be a reasonable concentration of dangling bonds [132] which should have an effect on the electronic structure. The questions arise; what effects do these dangling bonds have? And with partial short range order in the amorphous state, how different are the electronic structures of the amorphous and polycrystalline state semiconductors?

5.1.1 Si and Ge Results

Amorphous Si (a-Si) and amorphous Ge (a-Ge) samples were prepared by evaporation onto a thin (35 Å), free standing amorphous carbon (a-C) film [139]. The sample was positioned so that the contribution of a-C to the results was minimised. That was achieved by facing the a-C side of the sample towards the incident electron beam, so that the outgoing EMS electrons from an event happening in a-C region would most likely undergo several multiple scattering events which would shift the a-C results outside of the measured energy and momentum window. Diffusion of the C into either the Si or Ge samples is expected to be negligible due to the extremely low solid solubility values (10^{14} cm^{-3}) [140, 141], and alloying of the Si or Ge with the C substrate is expected to be weak [142]. The island growth formation of the semiconductor films onto the a-C substrate has no effect on the amorphous results, as the thickness of the deposited Si and Ge layers (10-20 nm) is more than enough to ensure complete coverage of the substrate. Considering the pre-mentioned factors the semiconductor samples are expected to produce high quality EMS spectra.

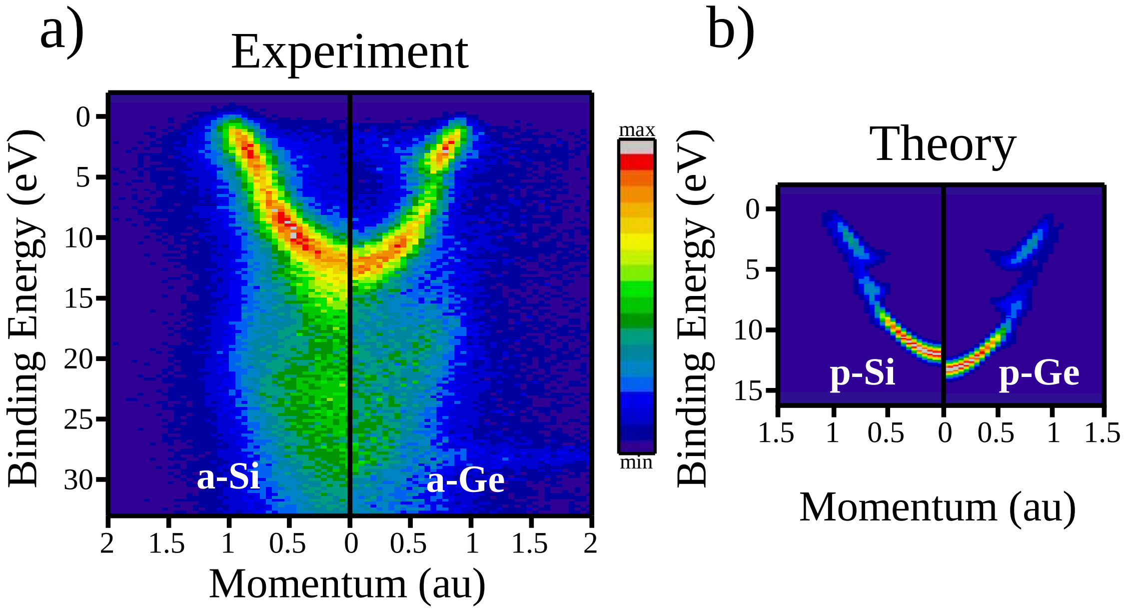

Figure 5.1: a) The EMS measured SMDs of a-Si (left) and a-Ge (right). Red areas represent high electronic density, blue areas represent zero electronic density. A band gap is visible in a-Ge, in a-Si the same band gap is suppressed. b) The theoretical SMDs for polycrystalline Si and Ge, showing reasonable similarities to the experimental amorphous spectra.

The measured SMDs from amorphous Si and Ge are presented in Fig. 5.1: a, and are compared to LDA calculations of the SMDs for polycrystalline Si and Ge [133] (Fig. 5.1: b). The experimental Si spectra shows much more intensity at higher binding energy, which is due to quasi-particle lifetime effects and inelastic scattering effects such as plasmon excitation. Ge appears to have less multiple scattering, but the presence of the 3d core level at $\approx$ 28 eV is visible as a faint band that extends out to high momentum. The Si spectra appears to have more complex inelastic energy features, which could be due to a thicker sample, or the presence of more disorder (dangling bonds) in the CRN structure.

The experimental band widths of Ge (12.8 eV) and Si (12.4 eV) are closer to the theoretical LDA values [133] which were calculated for polycrystalline Ge (13.1 eV) and Si (11.9 eV). LDA is well known to underestimate the band gap, however this underestimation is associated with an incorrect conduction band position due to local screening potentials and self energy effects [110]. The valence band position is fairly well estimated in its energy level and width even with small variances in exchange potentials and self energy effects [110]. More accurate, many-body GW calculations show the top of the valence band shifting upwards by up to 0.5 eV, so if any discrepancy is expected for the valence bandwidths of these more covalent systems it would be an underestimation by the LDA calculation. In Si the LDA calculation does underestimate the valence bandwidth in comparison to the EMS measurements, but only by a small amount (0.5 eV) and the same trend is not seen for Ge.

The lack of periodicity in the amorphous state means that the electronic structure can not be described by Bloch functions. Theorists have attempted to use other methods to describe the electronic structure of the CRN arrangement. Bose *et. al.* used a large and disordered unit cell [134], whilst Hickey *et. al.* used a Greens function technique [135]. There are major differences between the results of these two methods of calculation. Most noticeably is the occupation near the Fermi level, as these samples are semiconductors, one would expect there to be a band gap near the Fermi level, which is calculated in the crystalline case. Hickey *et. al.* calculated an extremely low density of states minimum (10^{-3}), which separated the valence band from the conduction band. Hickey *et. al.* explained that for a finite sample size they are uncertain as to whether there is just a very low minimum in the density of states or an absolute gap. Bose *et. al.* [134], calculated considerable intensity in the band gap region for amorphous Si. Bose *et. al.* attributes this intensity in the band gap region to a problem in the recursion method of his calculation and also to the way his calculation treats the interstitial region, although they don't exclude the possibility of states occurring in the band gap region.

A polycrystalline sample is expected to have dangling bonds at the grain boundaries, but that number is miniscule compared to the dangling bonds present in the amorphous sample. The effect of these dangling bonds on the EMS spectra would plateau the EMS intensity near the Fermi level, instead it is seen that the intensity drops off rather sharply in accordance with our energy resolution (1 eV). It can hence be concluded from the EMS measurement that if states do exist in the band gap region then they are less intense than the statistical accuracy (< 4 %), or these states are not occupied in our sample.

The last feature that will be discussed in the amorphous Si and Ge SMDs (Fig. 5.1: a), is the presence of a gap in the "parabolic" sp-band at ≈ 5 eV. The origin of this gap comes from the first BZ induced splitting in the band, this band gap will be referred to as the first BZ band gap to avoid confusion with the band gap between the valence and conduction bands near the Fermi level. In the single crystal case the first BZ band gap occurs at $\mathbf{q}_t = \frac{1}{2}\mathbf{G}_t$ (where t is any direction), for the polycrystalline case, if the momentum and energy value of the first BZ band gap is close in all directions (for the BZ surface see Fig. 4.22: bottom right) then the band gap will survive the spherical averaging over all directions [143]. In the polycrystalline LDA calculations the first BZ band gap is more pronounced for Ge than it is for Si, the same trend is seen for the EMS measurements on the amorphous semiconductors. The presence of dangling bonds, or multi member rings, both which alter the localised electronic density [132], is expected to tone down the presence of the first BZ band gap, which would explain why the first BZ band gap is more noticeable in the polycrystalline theory compared to the amorphous experiment (Fig. 5.1).

Annealing amorphous Ge or Si to over 500 °C will cause a crystallisation of the sample into a polycrystalline arrangement [144]. Annealing thin Ge samples, of a few monolayers, also initiates island formation [145], however given the thickness of the a-Ge sample (10-20nm) island formation is not expected to be a problem. Annealing also increases

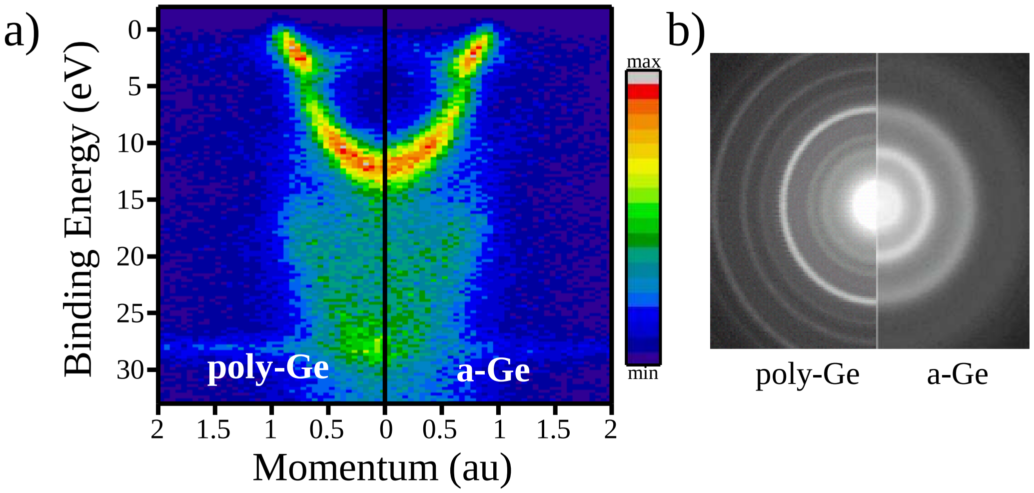

Figure 5.2: a) The EMS SMDs of p-Ge (left) and a-Ge (right), in the p-Ge spectra the band minimum (≈ 5 eV) is more defined, whilst the inelastic scattering and the 3d core level are more intense. b) The electron diffraction images of the two samples; used to confirm that recrystallisation into the p-Ge form was complete.

the solid solubility and the a-C substrate, though even the temperature increased solid solubility (2×10^{14} cm^{-3} at 900 °C)[140] is too small to contribute to the results. Annealing was used to produce polycrystalline Ge (p-Ge) samples, the polycrystalline state was confirmed by electron diffraction (Fig. 5.2: b). The polycrystalline diffraction pattern is a 360° smearing of the single crystal diffraction pattern, resulting in sharp concentric circles. The a-Ge diffraction pattern has much broader diffraction rings originating from a larger distribution of bond lengths and angles. The large differences in the electron diffraction patterns (Fig. 5.2: b) confirm the differences in the states of the two samples, it is thus surprising that the SMDs (Fig. 5.2: a) look quite similar, and it is only upon closer inspection that some minor differences can be noticed.

The slope of the sp-hybridised band, near the Fermi level (Fig. 5.3), to a loose approximation can be an indication of atomic order. The band gap in the polycrystalline sample is formed from Bragg reflection at the second BZ boundary and bends the band towards the boundary. Hence the slope of a band gap created from periodic crystal structure in the polycrystalline sample would be less steep. A band produced from a more disordered sample would have less crystal structure and the resulting sp-band would be

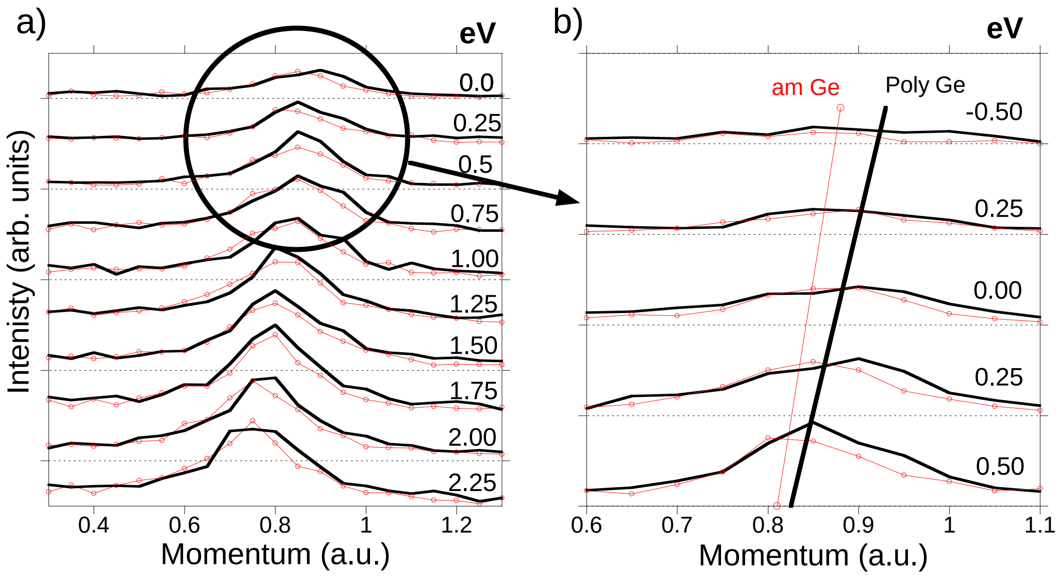

Figure 5.3: a) The momentum profiles for a-Ge and p-Ge at different binding energies near the Fermi level, showing the slope in the sp-hybridised band. b) A closer look at the differences in the slope of the sp-hybridised band of the amorphous and polycrystalline spectral functions.

more free-electron-like in nature, and should have a steeper parabolic tail from the dispersion relation $E \propto q^2$. The polycrystalline slope (13.3 ± 3.6 eV/au) is much smaller than the amorphous slope (20.4 ± 8.1 eV/au) (Fig. 5.3). This electronic structure effect could be an experimental indication of the differences in crystalline order between the two samples.

The first BZ band gap (Fig. 5.4) is seen around 5.5 eV for both the amorphous EMS spectrum and the polycrystalline EMS and LDA spectra, however there is a difference in position of the sp-band peaks for the amorphous and polycrystalline spectra. The sp-band peaks in the amorphous Ge spectrum are closer together and the high binding energy peak is flatter than in the polycrystalline spectrum. Both of the experimental spectra have much more intensity trailing off to higher binding energy than predicted by theory, this extra intensity is due to quasi-particle lifetime broadening as discussed previously.

The largest difference is the depth in the density of states minimum at the first BZ band gap, theory predicts much less intensity in this region than is measured by EMS. This could be due to the experiment having a poorer energy resolution than expected,

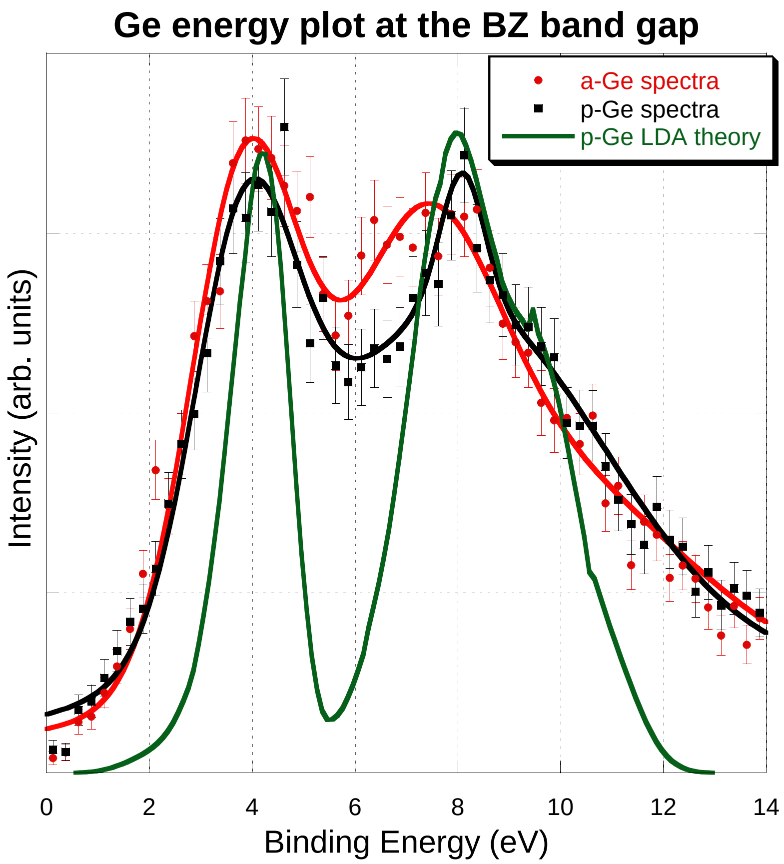

Figure 5.4: A comparison of the BZ band gap in the a-Ge (●), p-Ge (■) and LDA calculated (-), spectra taken over the momentum range $0.6 < \mathbf{q} < 0.7$. The BZ band gap is narrower and less well defined in the a-Ge sample.

quasi-particle lifetime broadening dampening the effect of the minimum, or the presence of dangling bonds. The LDA theory is a spherical average of all single crystal directions [133], and thus doesn't account for the presence of any dangling bonds which are caused by crystal defects, grain boundaries or a large amount of surface disorder in the polycrystalline case, or by multi member rings which exists naturally in the amorphous case [132]. The presence of these dangling bonds changes the localised electronic density which can introduce states in the BZ band gap region. The BZ band gap is clearly more pronounced in the polycrystalline spectra than it is for the amorphous Ge spectra (Fig. 5.4), indicating that dangling bonds/disorder is at least partly responsible for the differences, as quasi-particle lifetime effects and experimental resolution effects are expected to be similar for both EMS measurements. This result implies that it is imperative that theoretical calculations on amorphous semiconductor systems include the effects of dangling bonds.

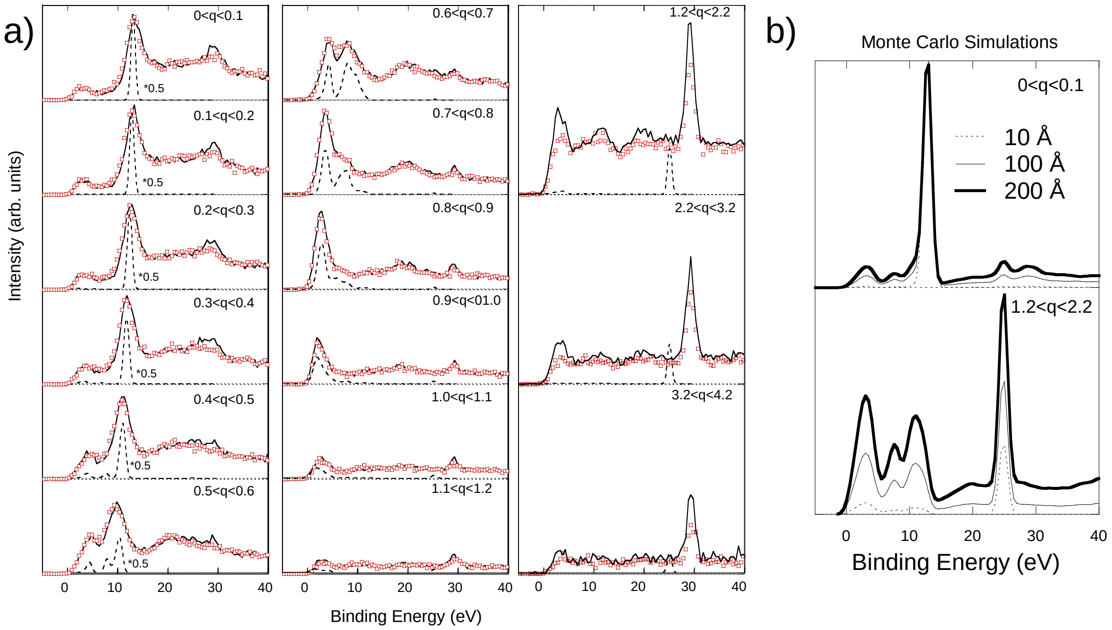

Figure 5.5: a) The energy profiles of a-Ge (squares), p-Ge (thick line) and LDA theory (dashed line). Differences between the a-Ge and p-Ge spectra are seen in the $0.6 < \mathbf{q} < 0.7$ energy profile at the band minimum ($\approx$ 4 eV), and in the higher momentum plots at the 3d core level (28 eV). b) Monte Carlo simulations of the relative heights of the 3d core level as a function of sample thickness after normalisation at the valence band. The relative intensity of the 3d core level is higher for thicker samples.

The SMDs for amorphous and polycrystalline Ge (Fig. 5.2) show a difference in intensity for the 3d core levels. The intensity of the 3d core level ($\approx$ 28 eV) in the p-Ge spectra is systematically higher than the a-Ge at higher momentum. This difference in the 3d core level intensity was determined to be a purely experimental effect. Both the a-Ge and p-Ge were normalised to the valence bands at zero momentum (Γ-point). Thus the extra 3d intensity in the p-Ge spectra could also be a drop in the valence band intensity in the a-Ge spectra. Elastic scattering in the valence bands shifts intensity from the first BZ to a higher order BZ, resulting in a lower intensity in the valence bands. In the less dispersive 3d core level bands, which have a measurable spectral weight at higher momentum, the same elastic scattering contributions can also shift intensity from higher order BZs back into the first BZ, resulting in a higher measured intensity in the

3d bands. The relative height of the 3d-band therefore becomes an indication of the sample thickness, this hypothesis was tested with a Monte Carlo calculation [146], using the results from a FP-LMTO calculation [133] on p-Ge. The results of the Monte Carlo calculations (Fig. 5.5: b) for p-Ge of different sample thicknesses were normalised at the sp-band intensity at q = 0 au. Still at higher momentum ($1.2 < q < 2.2$ au) the 3d-band contribution ($\approx$ 25 eV) is much more intense for the thicker samples. Thus the difference in the core level intensity between a-Ge and p-Ge (Fig. 5.5: a) can be attributed to sample thickness.

The theoretical calculation for p-Ge (dash line, Fig. 5.5:a), shows a good estimation of the experimental valence band peak positions. A variation in intensity could also be attributed to the same elastic scattering effect that reduces the effective intensity of the experimental valence bands. The EMS experimental 3d core level (28 eV) is much higher in binding energy than the estimated FP-LMTO LDA calculation (25 eV). DFT is well known to consistently underestimate the binding energy of the semi-core levels in semiconductors (by up to 5 eV [110]) due to self energy effects, so the theoretical underestimation of the binding energy of the 3d level is not unexpected.

5.1.2 Semiconductor Summary

The SMDs of the amorphous and polycrystalline semiconductors were remarkably similar, in the LDA polycrystalline calculations the first BZ band gap survives. The BZ band gap surviving in the amorphous state of these semiconductors implies that the variation in bond lengths and angles in the CRN is small enough to preserve a similar electronic density throughout the sample. The only (non-experimentally induced) minor differences existed in the region of the inelastic multiple scattering, the first BZ band gap and near the Fermi level. The inelastic scattering intensity may be partly attributed to the change in density between the amorphous state and the more tightly packed polycrystalline state [147], however it is much more likely to be attributed to the experimental effect of differences in sample thickness. The increased intensity in the density of states in the first

BZ band gap region in the amorphous Ge spectrum is caused by the presence of dangling bonds which introduces extra states. The slope of the sp-band near the Fermi level (Fig. 5.3) was more steep for the a-Ge sample, indicating that it's electronic structure is slightly more free-electron in nature.

The CRN structure of amorphous semiconductors is extremely difficult to theoretically model, two of the most common models is a large disordered unit cell [134, 138] (super-cell theory), and an equation of motion method [135] (Green's function technique). The EMS spectra showed very little intensity around the Fermi level, so it is unlikely that there is a large number of states in the band gap region that lie below the Fermi level. The super-cell theory of Bose *et. al.* [134] shows considerable intensity in the band gap region, whilst the Greens function technique of Hickey *et. al.* [135] shows a much better agreement with the EMS measurement. A similar sort of agreement between those two calculations and the EMS measurement occurs with the intensity in the BZ band gap region. The super-cell theory overestimates the intensity, whilst the Greens function technique shows a minimum in the BZ band gap region that is similar to that seen in the EMS measurement. An LDA calculation from polycrystalline Ge estimates a very deep minimum at the BZ band gap (Fig. 5.5), as the LDA calculation doesn't include dangling bonds or any other form of disorder. Theoretical calculations of the electronic structure of amorphous semiconductors must include the effects of dangling bonds, as the most noticeable differences between polycrystalline and amorphous spectra is caused by the increase in the density of these dangling bonds.

5.2 Disordered Alloys

Alloys are solids that are made of two or more constituent atoms. They can come in ordered complexes that have repeating unit cells, that can create quite complicated electronic structures due to the shorter resulting reciprocal lattice vectors. Alloys can also be formed in a random pattern, where the constituent species readily intermix and do not form large repeating unit cells. The latter shall be labelled disordered alloys, and in this chapter the disordered alloy of Ni and Cu will be examined.

5.2.1 Ni and Cu Alloys

Ni and Cu are both FCC metals with only slightly different lattice constants, if one forms an alloy of these two elements the atoms remain in a FCC lattice, but the positioning of the Cu and Ni atoms on these lattice sites displays no order. In this study the Ni-Cu alloy system was investigated through varying compositions of each component. The NiCu samples used in this section were prepared via vapour deposition onto amC substrate of both Ni and Cu simultaneously in the ANU evaporation unit as detailed in section 2.4.2. As mentioned in section 2.4.2 the rate of evaporation on both Ni and Cu can be well controlled to create reasonably accurate alloys within 10 % error margins of the composition, which can be checked by measuring the relative ratio of the core levels in an EMS measurement. It is well known that evaporation of most metals will lead to a polycrystalline sample, the crystalline states of the samples were checked via measuring their electron diffraction patterns, which showed concentric circles indicating their polycrystalline state.

The NiCu alloy structure has been shown to have only a very small change in the lattice constant [148], which leads to the assumption that NiCu is an ideal binary substitutional alloy [149] where no ordered complexes are formed. The simplicity of this alloy system will enable EMS to determine the nature of the localisation of the sp and d electrons in Ni and Cu.

5.2.2 Results

NiCu alloys were produced with Cu concentrations of 0, 30, 50, 70 and 100 %. EMS was then used to measure the SMDs of the valence electrons of these alloys, which included the 3p core levels that were used to determine a more precise composition of Ni and Cu.

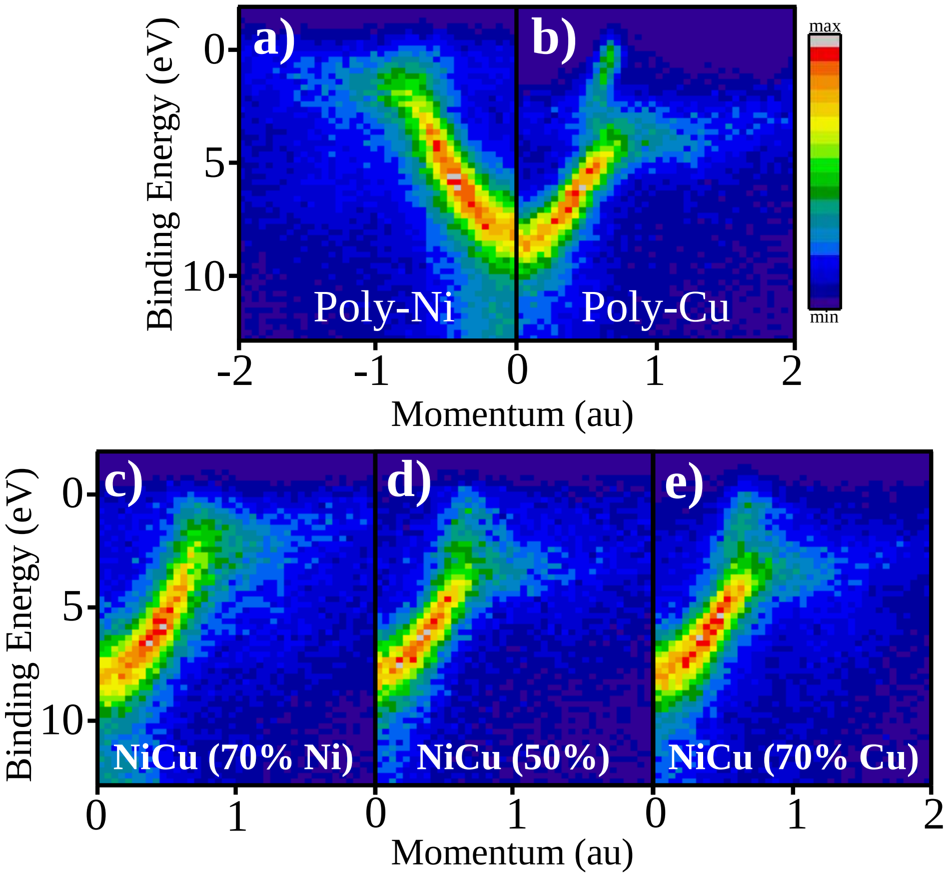

Figure 5.6: The measured SMDs for the NiCu alloys with a Cu concentration of a) 0 %, b) 100 %, c) 30 %, d) 50 %, and e) 70 %. The d-bands which are less dispersed and spread out to higher momentum near the Fermi level can be seen to evolve slowly through the varying composition. The only difference in the sp-bands is the position of the hybridisation band gap that is induced by the position of the b-bands.

The measured valence SMDs are presented in Fig. 5.6, showing the progression of the SMDs as the alloy changes in composition. The dispersed, parabolic sp-band is reasonably similar between the cases of pure Ni (Fig. 5.6: a) and pure Cu (Fig. 5.6: b). The only noticeable difference in the sp-band is the hybridization induced band gap, which is caused by the position of the d-bands. In pure Ni the DOS minimum, due to spd-band hybridisation, is very close to the Fermi energy, as the concentration of Cu increases through the series of alloys the hybridized spd-band gap moves lower in binding energy until the pure Cu case where it is at around 2 eV. The similarities between the sp-bands through all the alloys indicate that the sp-band electrons are not localised around the nuclei and that they form a mixed NiCu sp-band. The d-bands, which are less dispersed and extend out to much higher momentum, show a vast difference between the pure Ni spectrum and the pure Cu spectrum. In Ni the d-bands are much closer to the Fermi energy (0 - 2 eV), whereas in Cu the d-bands are lower in binding energy (2 - 4 eV), in the alloyed samples (Fig. 5.6: c,d,e) the d-bands seem to be much broader in energy range (0 - 4 eV).

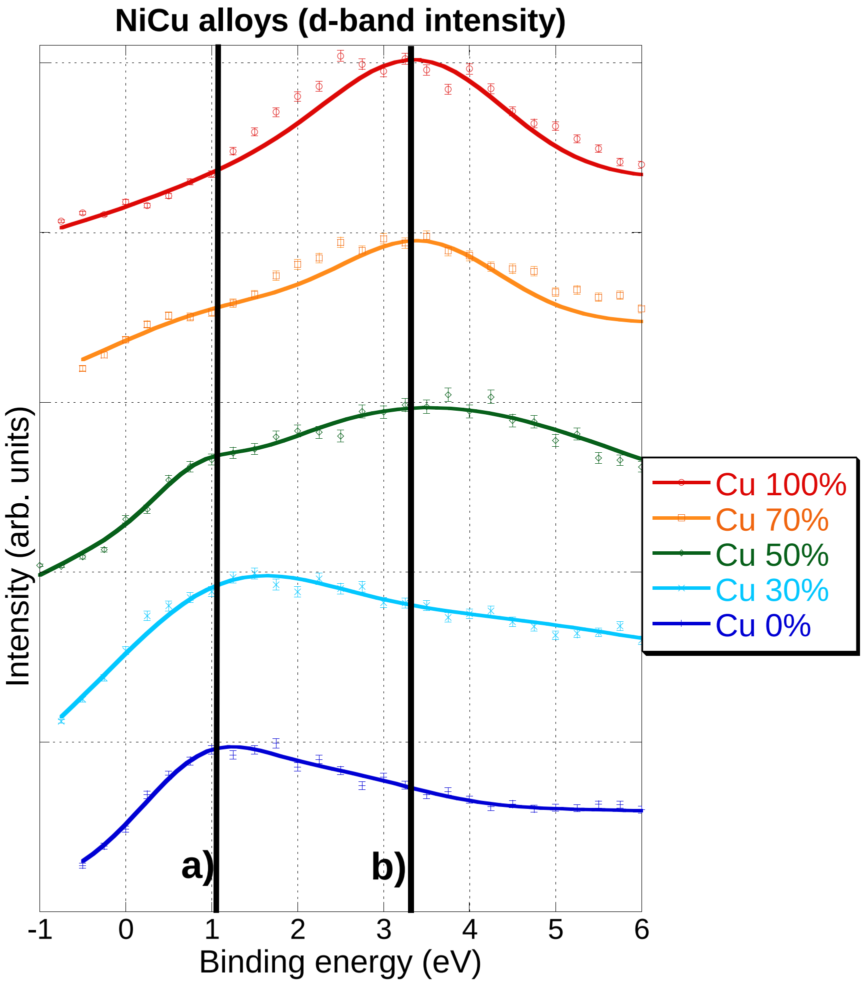

Figure 5.7: The integrated intensity from 1 to 3 au, in this range the spectrum is dominated by d-electrons. It is shown as a function of binding energy for the various alloys. The rough central position of the dispersed d-band for pure Ni is shown by the line marker (a), the rough central position of the dispersed d-band position for pure Cu is shown by the line marked (b). The two individual peaks vary in size depending on the composition of the alloy. The line through each set of data point is a guide to the eye.

In Fig. 5.7, the d-bands are examined more closely by plotting the d-band intensity as a function of binding energy as measured over the momentum range $1 < \mathbf{q} < 3$ au. The Ni d-bands are quite dispersed over the measured momentum range so the peak position is roughly indicated by the line labeled (a), and is measured in the pure Ni spectrum (Fig. 5.7: bottom). The Cu d-bands are also quite dispersive over the measured momentum range so their rough central position is indicated by the line marked (b), as measured from the pure Cu spectrum (Fig. 5.7: top). The energy profile of the d-bands for the alloys, show the two separate peaks for both the Ni and Cu d-electrons, whose variation in intensity is consistent with the variation of the percentage of Ni and Cu respectively. The two clear d-band peaks indicate that the d-band electrons are atomic like in behaviour as they maintain the characteristic binding energy of their parent nuclei, rather than alloying into an average of the d-band binding energy of the sum of the nuclei. These EMS measurements finding the atomic like behaviour of the d-band electrons is consistent with the super-cell calculations of Sommers *et. al.* [150].

5.2.3 NiCu Alloy Summary

The EMS spectrometer was used to examine the alloying trends of the binary substitutional alloy system of Ni-Cu. The simplicity of the alloy, enabled the examination of the behaviour of the valence electrons. The sp-band electrons were found to be more de-localised and adopted the average of the electronic structure of the surrounding nuclei. The d-band electrons were found to be more atomic like in nature, as they adopted the electronic structure of their parent nuclei, this result is consistent with the super-cell calculations of Sommers *et. al.* [150]. The super-cell theory is now outdated and it has been shown that Greens functions techniques under the framework of the Korringa-Kohn-Rostoker coherent potential approximation (KKR-CPA) have proven accurate for many substitutional alloy systems including NiCu [151, 152].

The use of EMS to examine the developing trends in alloys has shown that EMS will be a useful technique for more complex systems, and may be possible to examine such effects as phase transitions in such complex materials as Mott-Hubbard insulators.

Chapter 6

Spin Dependent Effects

The construction and implementation of the spin polarised electron source (Chap. 3) has afforded the EMS laboratory to begin to examine spin dependent effects in solids. For an unpolarised electron source the electron spin orientation is randomised over all directions, so no spin dependent effects in the differential cross section of any electron scattering technique are seen. For a polarised electron source there are two spin interactions that are introduced in an electron scattering experiment, a spin interaction between the incident polarised electron and the nucleus of the target, and a spin interaction between the incident electron and the bound electrons in the target system.

The electron-nucleus spin interaction at high energy is more commonly known as Mott scattering, where the spin-magnetic moment of the incident electron couples with the orbit of the nuclear charge (LS coupling). This coupling causes an asymmetry in the scattering cross section, so for the EMS laboratory configuration which measures in plane scattering angles of ± 44.3 ° from the incident direction, there will be a left/right asymmetry.

The electron-electron spin interaction involves an electron-electron collision and when only one of the outgoing electrons is detected, the technique is referred to as electron-Compton scattering. The electron-electron elastic scattering cross section from a magnetic material is given by Vriens [153];

$$\begin{aligned}\sigma(\mathbf{k}_1) = \ & \tfrac{2k_1k_2}{k_0}\int\int \rho_E(\mathbf{k}_1+\mathbf{k}_2-\mathbf{k}_0)\times\left(\tfrac{1}{K^4}+\tfrac{1}{S^4}-\tfrac{1+\cos\varphi_{0,1}}{K^2S^2}\right)\times \\ & \delta(k_0^2-k_1^2-k_2^2-E)dEdk_2. \qquad (6.1)\end{aligned}$$

Where only one of the outgoing electrons is measured so the cross section is integrated over all binding energies (E) and over the momentum of the second electron (K_2) and $\varphi_{0,1}$ is the angle between the spins of the two interacting electrons. For symmetric scattering conditions of an in plane scattering angle (ϑ) of ≈ 45 °, the transfer momentum ($K = k_0 - k_1$) is equal to the change of momentum ($S = k_0 - k_2$), so the spin dependent term simplifies to;

$$\left(\frac{1-cos\varphi_{0,1}}{K^4}\right). \qquad (6.2)$$

The spin term indicates that the incident polarised electrons will not interact with bound electrons that have the same spin orientation, as the cross section goes to zero; this is a consequence of the Pauli exclusion principle. Thus electron Compton scattering with a 100 % polarised incident electron beam and a magnetised sample can be used to selectively measure the spin up and spin down momentum distribution.

In this chapter the spin dependent scattering of a polarised electron from the nucleus will be examined, and Sherman functions (spin asymmetries) will be measured. The preparation of a thin free standing magnetised Fe sample will be discussed and then results from electron-electron scattering from the ferromagnetic sample will be presented. The chapter will conclude with a feasibility study into the possibilities of measuring the complete spin-polarised spectral functions of ferromagnetic materials.

6.1 Mott Scattering

The EMS spectrometer can measure a left and right asymmetry for high energy elastic scattering (Fig. 6.1), with an electron detectors positioned either side of the direction of the incident electron.

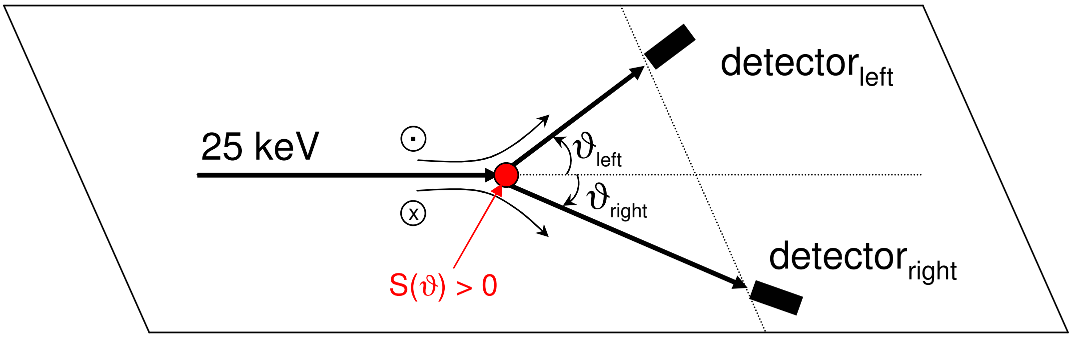

Figure 6.1: The experimental configuration for an elastic Mott scattering experiment. Showing the incident electrons spin direction out of the plane (⨀) and into the experimental plane (⨂), and the resulting preferential outgoing direction due to spin-orbit interactions for a sample with a S(ϑ) $>$ 0 [55].

For an elastic scattering experiment with a polarised incident electron beam the experimental cross section (Mott scattering cross section) is given by;

$$\sigma(\vartheta,\xi) = \mathrm{I}(\vartheta)\,[1 - \mathrm{PS}(\vartheta)\sin\xi]\,. \tag{6.3}$$

Where I(ϑ) is the differential cross section from an unpolarised incident electron beam, P is the degree of polarisation of the incident electron beam, S(ϑ) is the Sherman scattering function at the experimental angle ϑ (44.3 °), and ξ is the angle between the propagation of the outgoing electrons and the polarisation axis, which in this experimental configuration is always 90 °, so $\sin\xi = 1$. The measured asymmetries will be directly proportional to the polarisation degree of the incident electron beam and the Sherman function of the target. The Sherman functions for these experimental parameters were calculated for Au, Cu, Fe and C (Fig. 6.2) using a freely available computer program that uses a Dirac partial-wave calculation (ELSEPA [83]). The degree of polarisation of the incident electron beam was determined by using the well known Sherman function of Au (see Chap. 3), and was determined to be 21 %. The results of the Sherman function calculations (Fig. 6.2), as expected, shows that the heavier elements have a larger Sherman function due to their higher nuclear charge and thus stronger spin-orbit interaction.

From the calculations of the Sherman functions it is clear that Au will give a much larger asymmetry in the differential cross section measurement than Cu and C will. Ex-

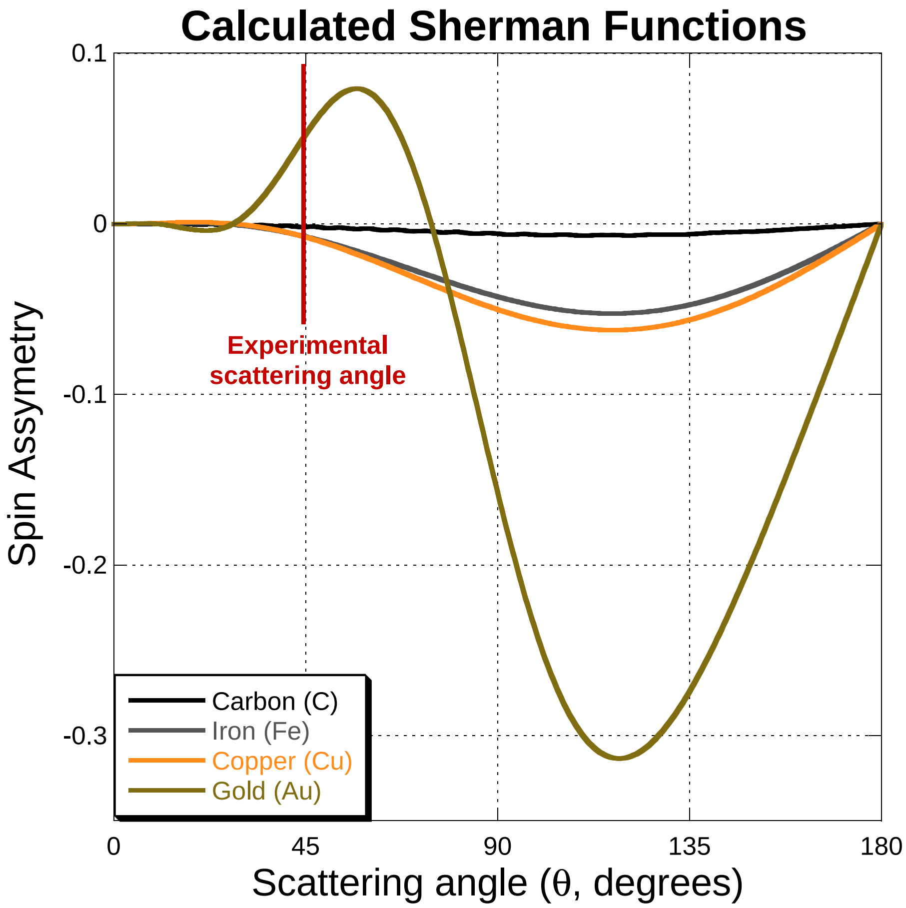

Figure 6.2: The Sherman functions for Au, Cu, Fe and C, calculated over a range of scattering angles for an incoming energy of 25 keV. The experimental scattering angle (44.3 °) is indicated with a red line. As expected the targets with a higher nuclear charge have the largest Sherman functions.

perimental measurements of the Mott scattering asymmetry (Sherman function), which are corrected for the experimental degree of polarisation of the incoming electron beam (0.21), were performed for C, Cu and Fe using the experimental configuration shown in Fig. 6.1. The experimental energy resolution was on the order of 0.5 eV, and only counts measured from the elastic peak were used to determine the experimental Mott asymmetry, minimising the effects of any low energy inelastic fine structure effects on the measured Sherman function. After every minute the measured number of counts were stored into an array and the spin polarisation of the incident electron beam was flipped, this minimised any differences in the detector efficiency and any fluctuations in the incident beam current so that there was minimal adverse effects on the experimental results.

Sample	Nuclear charge	S(44.3 °) calculated [83]	S(44.3 °) measured
C	6	-0.18 %	-0.56 ± 0.49 %
Fe	26	-0.72 %	-0.82 ± 0.12 %
Cu	29	-0.74 %	-0.69 ± 0.28 %
Au	79	5.32 %	5.32 ± 0.16 %

Table 6.1: The Sherman functions expressed as a percentage for C, Fe, Cu and Au samples, measured at a scattering angle of 44.3 ° and an incident energy of 25 keV. The Sherman function for Au was used in determining the degree of polarisation in the electron gun so that is exact by definition. The calculations [83] are in reasonable agreement with the experimental measurements, given the large errors associated with the lighter elements.

The experimental error given in Tab. 6.1 only includes statistical errors in the determination of the Sherman function, other sources of error, such as the error in the degree of polarisation of the electron beam have not been included. The theoretical Sherman function was calculated for a sample of zero thickness, however, the experiment was performed on a sample approximately 10-20 nm thick. The determination of Sherman functions from non-zero thicknesses can deviate by as much as 5 % [82] from the zero thickness value due to multiple scattering effects. These multiple scattering effects were minimised by only using counts from the elastic peak (i.e. electrons that did not suffer inelastic scattering) in the determination of the Sherman function.

Given the associated errors, the experimental and theoretical Sherman functions are in reasonable agreement for the heavier elements of Au, Cu and Fe. The lighter element of C is still within the large experimental error of the calculated value. The large experimental error for C arises from a combination of a smaller asymmetry value and a lower nuclear charge and hence a smaller Mott scattering cross section which leads to lower countrates. The lower number of counts and smaller asymmetry value lead to a larger statistical uncertainty.

6.2 Preparation of a Magnetised Fe Sample

The following sections will deal with the incident polarised electrons interacting with the bound electrons in a single crystal magnetic Fe sample, as the magnetic Fe sample is anisotropic, special attention must be paid to sample preparation and orientation. The single crystal magnetic Fe sample was commercially purchased from the University of Aarhus, and was grown on a NaCl [111] surface normal crystal by evaporation deposition. This growth mechanism is well known to produce an iron sample with a [110] surface normal through the Nishiyama-Wasserman mechanism [154]. The experiments performed in the EMS laboratory examine directions that are perpendicular to the surface normal, and the growth mechanism allows for two crystal directions to be parallel to the surface along the long edge of the NaCl [111] substrate (Fig. 6.3).

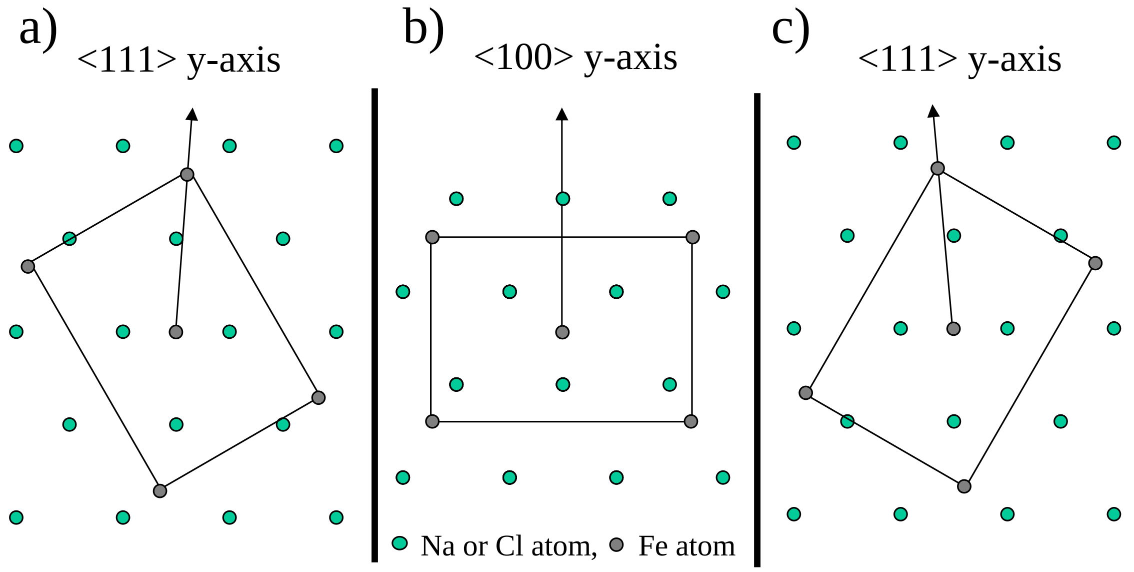

Figure 6.3: The three possible Fe[110] surface normal growth mechanisms due to the three-fold symmetry of the NaCl[111] surface normal substrate. There are slight lattice mismatches which are nullified by the misalignments in the Fe growth, known as Nishiyama-Wasserman growth [154]. a) and c) result in an experimental y-axis orientation of Fe$\langle 111\rangle$, whilst b) results in an experimental y-axis orientation of Fe$\langle 100\rangle$. Both the growth orientations are possible.

In Fig. 6.3, the y-axis corresponds to the measured direction in the EMS spectrometer, which is also the axis of magnetisation. The Fe$\langle 100\rangle$ (y-axis) growth mechanism (Fig.

6.3: b), has a small lattice mismatch (x-axis $\approx$ 3 %, y-axis $\approx$ 1 %) which is nullified by a combination of crystal strain at the interface, and a slight out of plane tilt in the direction of the Fe[110] surface normal. The Fe$\langle 111\rangle$ (y-axis) growth mechanism (Fig. 6.3: a and c) is a little more strained (x-axis $\approx$ 1 %, y-axis $\approx$ 12 %) than the Fe$\langle 100\rangle$ growth, and involves a slight rotation around the [110] surface normal, so the resulting experimental y-axis is not precisely orientated along the Fe$\langle 111\rangle$ direction. The Fe$\langle 111\rangle$ y-axis orientation is still possible because of the out of plane tilt incorporated in the Nishiyama-Wasserman growth.

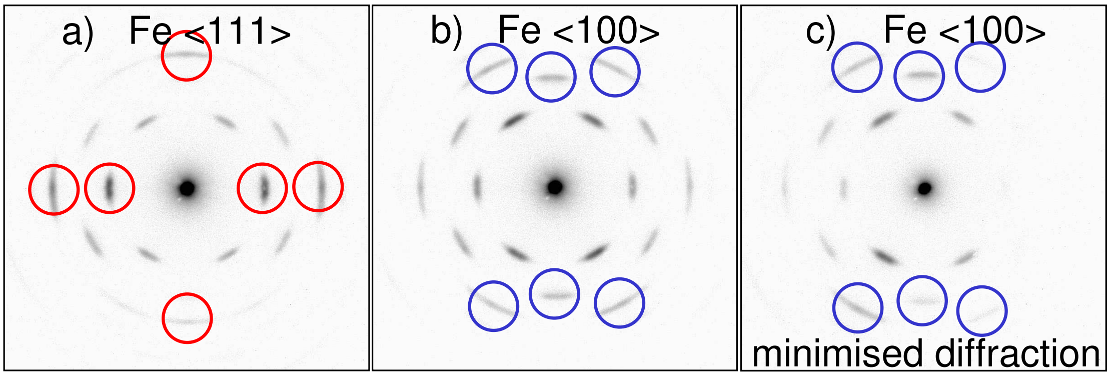

Figure 6.4: Diffraction images taken at different points across the same magnetised Fe sample. a) The diffraction pattern indicates a $\langle 111\rangle$ y-axis arrangement, as shown by the characteristic $\langle 222\rangle$ diffraction spots (◯) b) The diffraction pattern indicates a primarily $\langle 100\rangle$ y-axis arrangement as shown by the characteristic $\langle 110\rangle$ and $\langle 211\rangle$ diffraction spots (◯). c) By slightly rotating the sample about the measurement direction, diffraction is minimised, the transmission experiments were performed in this configuration.

The sample was then magnetised along the y-axis (100) orientation prior to being placed inside the experimental chamber and thinned in the same manner as the other single crystal samples (see Chap. 4). The sample was magnetised, by an iron core electromagnet with an internal magnetic field of 2 T, that had a 15 mm air gap in which the sample was placed. The magnetic field was obtained by applying 10 A across three solenoids that were in series, which varied from 160-300 turns. Applying the magnetic field for 30 seconds proved more than long enough to magnetise the Fe sample. The sample was mounted onto a specially made copper sample holder and the magnetisation of the Fe sample was measured with a magnetometer both before and after magnetisation and before and after experimental measurements were performed. Prior to magnetisation the sample produced a net zero magnetic field, after magnetisation a field on the order of 20 nT was measured approximately 1 cm from the sample. After the experiment was performed the magnetic field of the Fe sample was again measured and was similar to the magnetic field measured prior to the experiment

High energy electron diffraction patterns were taken in situ on the prepared magnetic Fe sample (Fig. 6.4) to examine the samples orientation. By scanning across the sample and measuring high energy electron diffraction images, it can be seen that there are regions where the y-axis is orientated along Fe $\langle 111\rangle$ (Fig. 6.4: a), and regions where the y-axis is primarily orientated along $\langle 100\rangle$ (Fig. 6.4: b). The magnetic Fe sample was positioned so that the y-axis was in a $\langle 100\rangle$ orientation and then rotated about the y-axis by ≈ 3 °, to minimise the amount of diffraction (Fig. 6.4: c). The effect of diffraction on the Compton profile could in principle be nullified by tilting the sample in combination with rotation to setup a two-beam case [155], although there was no ability to tilt the sample in the EMS spectrometer.

The transmission mode experiments in the following sections were performed on the sample position which produced the diffraction image shown in Fig. 6.4: c). The results are expected to be primarily for a magnetised Fe$\langle 100\rangle$ sample, but any translational movement of the sample through vibrations in the building could introduce magnetic Fe $\langle 111\rangle$ results into the measurement.

Spin-polarised electron-energy-loss-spectroscopy (SPEELS) and spin polarised EMS measurements would be performed along the y-axis of the magnetised Fe sample (Fig. 6.5: b), which corresponds to a $\langle 100\rangle$ (Γ-H, Fig. 6.5: a) orientation. Magnetic electron-Compton profiles are measured along the momentum transfer direction, which is in the xz-plan (Fig. 6.5) of the experiment at 45 ° to the surface normal, and corresponds to a $\langle 100\rangle$ (Γ-H, Fig. 6.5: a) orientation.

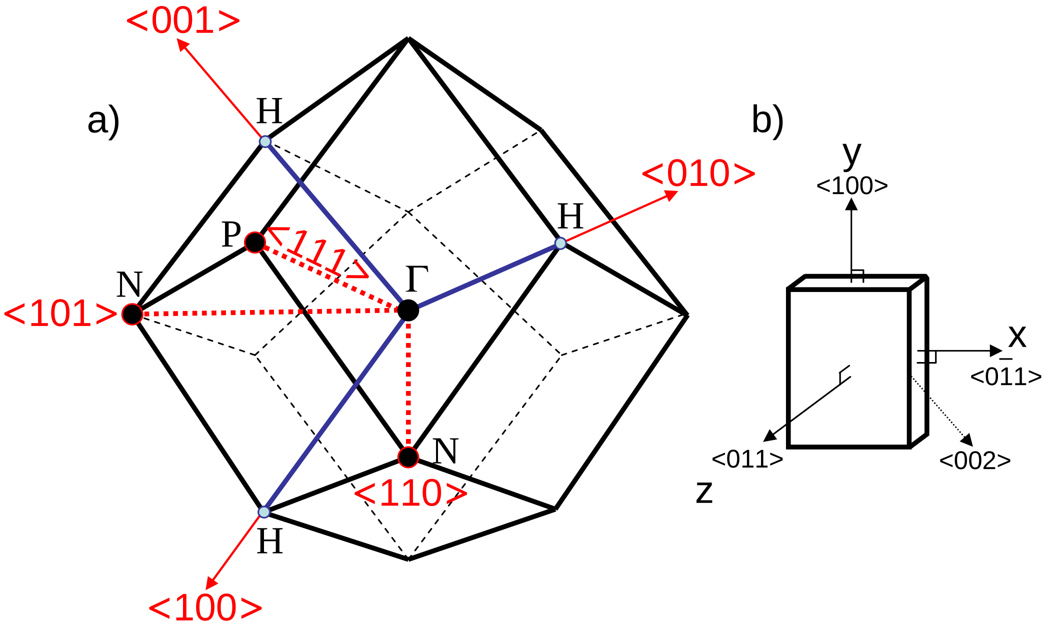

Figure 6.5: a) The first Brillouin zone boundary for a body centred cubic (BCC) structure, showing the high symmetry (100, 110, and 111) directions with the corresponding high symmetry crystal points (**H**, **N** and **P**) respectively. b) The sample orientation as positioned in the spectrometer, with the incident electron beam coming in along the surface normal $\langle 011 \rangle$, the y-axis measured in an EMS experiment $\langle 011 \rangle$, and the momentum transfer vector $\langle 002 \rangle$ of which the projection is measured in an electron-Compton scattering experiment.

6.3 Spin Polarised Electron Energy Loss Spectroscopy

Spin polarised electron energy loss spectroscopy (SPEELS) is an experimental technique that can resolve spin dependent information about the target. The experiment is the same as an EELS measurement with the distinct difference of having either an incident electron beam that is polarised [156, 157], or a spin polarised detection system [158], or in some cases both [159, 160]. The polarised incident electron beam gives rise to spin specific transitions at a low energy loss [161]. The spin dependent processes can be divided into two types of processes, those that flip the incident electron's spin (flip) and those that do not flip the incident electron's spin (non-flip). Flip scattering processes (Fig. 6.6: a) involve the incident electron occupying an empty state above the Fermi level and transferring its energy to a bound electron with opposite spin, which is ejected, creating an electron-hole pair (Stoner excitation) [161]. Non-flip processes (Fig. 6.6: b) can involve both direct or exchange scattering. Direct, non-flip scattering occurs via dipole scattering (when the incident electron has long-range electric field interactions with the electrons in the target) or impact scattering (when the incident electron penetrates into the sample and is directly scattered). Exchange scattering also occurs via impact scattering. The combination of these different types of spin dependent inelastic scattering produces small features in the SPEELS spectrum. The cross sections of these spin dependent inelastic scattering processes is many orders smaller than plasmon excitations and thus are most noticeable at very small energy loses where the elastic peak no longer dominates and before the first plasmon excitation is too intense.

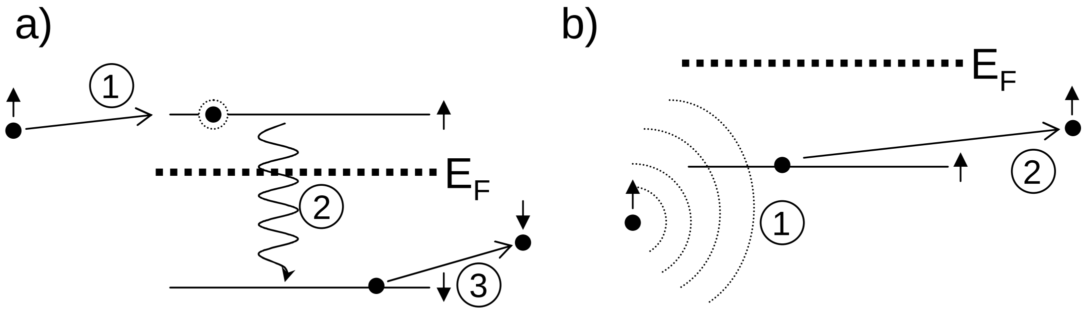

Figure 6.6: a) The spin-flip (Stoner excitation) scattering process broken into three stages. The incident ↑ electron occupies an empty orbital (1), couples with a ↓ electron below the Fermi level (2), ejecting the ↓ electron. b) A Non-flip scattering process, shows the long range electric field fluctuations that can eject a bound electron of the same spin orientation, whilst the incident electron is still well outside the target.

Previous studies into inelastic spin dependent features in SPEELS spectrums [162, 163, 164, 165] have shown quite broad and featureless spectra. The field of SPEELS became stagnant in the mid 90's, and was maligned to a field for theorists to study. In 2006 a study by Komesu *et. al.* [166] on the SPEELS spectra on magnetic Fe showed signs of peaks associated with Stoner excitations in both the minority and majority spin spectra.

The experiment of Komesu *et. al.* [166] has the same scattering angle (45 °) and a slightly worse energy resolution (0.6 eV, compared to 0.5 eV) than the EMS spectrometer.

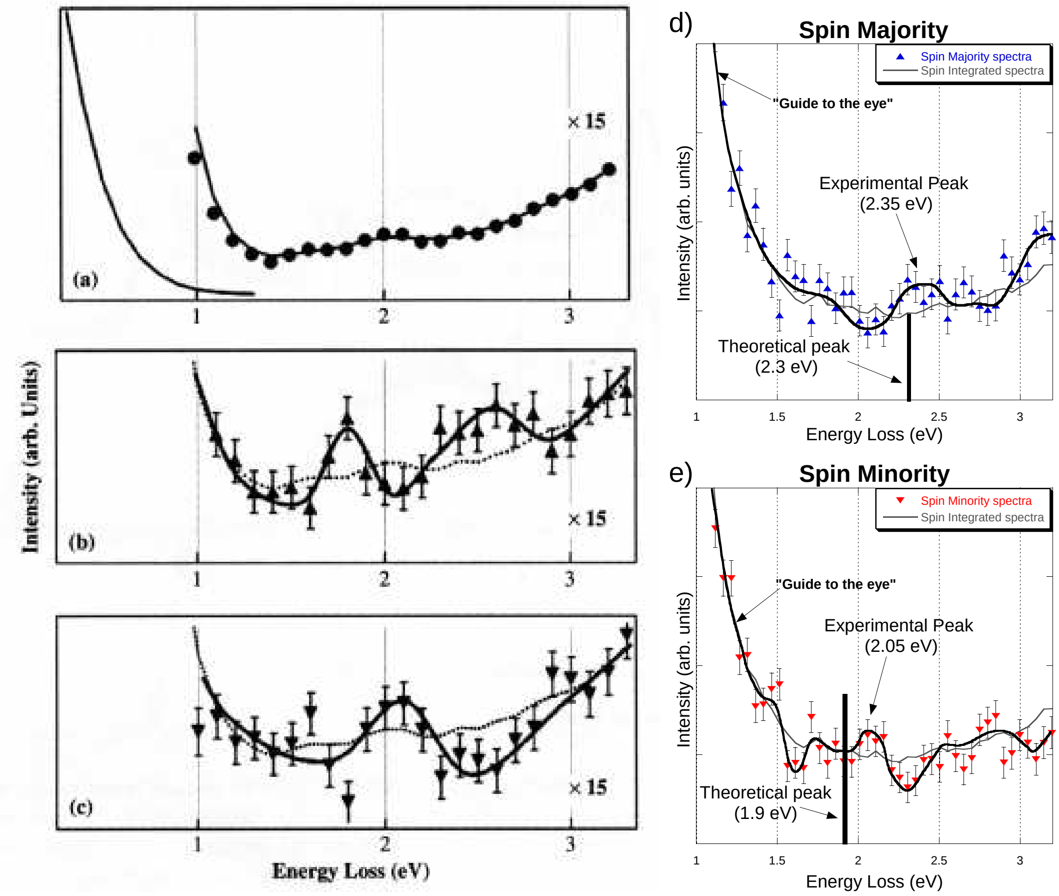

Figure 6.7: The spin integrated (a), spin majority (b) and spin minority (c) SPEELS spectra of Komesu *et. al.* for the Γ-H direction of magnetised Fe. The spin majority and spin minority spectra which were measured by the left/right scattering from the Mott polarimeter have been rescaled to the same height as the spin integrated spectra, hence the larger error bars. The results of this study are presented in the same fashion with the spin majority (d) and spin minority (e). The calculated Stoner excitations and direct transitions [167] are shown in the spin majority (d) and spin minority (e) spectra for this study.

The main differences were the experiment of Komesu *et. al.* was performed at 300 eV, making his experiment more sensitive to Stoner excitations and direct transitions. The ANU experiment required much higher energy (25 keV) as it was performed in transmission mode. Another difference is that Komesu had a Mott polarimeter after the interaction region so they could separate out the spin contributions after the interaction region, whilst the EMS spectrometer has a spin polarised electron source (21 %). In an effort to support the data of Komesu *et. al.* which was performed on a Γ-H magnetised Fe sample, a SPEELS experiment in the same direction of magnetised Fe ($\langle 100\rangle$, Γ-H) was performed in the EMS spectrometer. In the EMS measurements the spin-flip (Stoner excitations) are initiated by spin-down incident electrons, in keeping with the nomenclature of Komesu this spectra is labelled as “majority spectra”. Alternatively, direct transitions are initiated by incident electrons that are spin-up, that EMS spectra was labelled as “minority spectra”. The two data sets are both presented in raw EELS spectra, as an spin integrated EELS spectra and “spin-up” and “spin-down” EELS spectra, they are compared in Fig. 6.7.

The experimental results of Komesu *et. al.* for the minority spin state (Fig. 6.7: c) has a feature measured at 2.1 eV which agrees quite well with the calculated feature at 2.3 eV [167]. The calculated 2.3 eV feature corresponds to a Stoner excitation between the unoccupied $\Delta_2^{\downarrow}$ and the occupied $\Delta_2^{\uparrow}$ states, which would appear in the minority spin states spectra due to the spin-flip interaction. The majority spin state spectra (Fig. 6.7: b) of Komesu *et. al.* shows two features near 1.8 eV and 2.6 eV. Komesu *et. al.* believe that those features are due to direct transitions which is a non-flip process. Photoemission spectra [168] has measured band positions that would predict a direct transition peak of 2.8 eV, that would agree well with the 2.6 eV feature (Fig. 6.7: b).

The experimental results of this study of the spin-polarised electron-energy-loss spectrum measured with the spin vectors of the incident and bound electrons along the Γ-H ($\langle 100\rangle$) direction in magnetised Fe produces some results which are in mild agreement to that of Komesu *et. al.*. The majority spectra (Fig. 6.7: d) which shows spin-flip excitations such as Stoner excitations, has one obvious feature at 2.35 eV, which compares well to the theoretical value (2.3 eV) for the $\Delta_2^{\downarrow} - \Delta_2^{\uparrow}$ Stoner excitation. This Stoner transition was measured at 2.5 eV by Komesu *et. al.*, and the two energy levels were measured at 2.8 eV apart by photoemission data [168]. It is plausible that there maybe a peak below 2 eV, that would correspond with the measurement of Komesu (1.8 eV) and could be due to the $\Delta_5^{\downarrow} - \Delta_5^{\uparrow}$ Stoner transition that has a theoretical value of 2.1 eV [167]. The validity of this second feature is dubious at best.

The minority spectra from this study (Fig. 6.7: e) corresponds to direct transitions, that is transitions that involve the incident spin-up electron colliding with a spin-down bound electron. One obvious feature (2.05 eV) that may be attributed to a direct $\Delta_2^{\downarrow} - \Delta_5^{\downarrow}$ excitation. Calculations by Callaway and Wang [167] show this feature to be at 1.9 eV, and the study of Komesu *et. al.* [166] show this feature to be at 2.0 eV.

Poor statistical resolution and less sensitivity raises the question whether these features are actual Stoner excitations or are from a combination of statistical inaccuracies, incomplete incident polarisation or other inelastic processes. The position of the features in both this study and the study by Komesu *et. al.* [166] do agree well with theory and other experimental measurements [167, 168]. Due to the poor statistical accuracy and clarity of these features especially in this study but also in the study of Komesu *et. al.*, it is not entirely convincing as to whether these peaks can be decisively attributed to Stoner excitations and direct transitions.

6.4 Magnetic Compton Scattering

To examine the electron-electron spin interaction of a spin polarised electron source and a solid target, a Compton scattering experimental configuration can be setup (Fig. 6.8) in the EMS spectrometer. Only one outgoing electron is measured which results in measuring a planar projection of the target electron's momentum along the momentum transfer vector (**K**).

Using non-relativistic terms, the energy transfer can be given as;

$$\begin{aligned} \mathrm{E}_{\mathrm{final}} - \mathrm{E}_{\mathrm{initial}} &= \frac{(\mathbf{q}+\mathbf{K})^2}{2m} - \frac{\mathbf{q}^2}{2m} \\ \mathrm{E}_{\mathrm{transfer}} &= \frac{\mathbf{K}^2}{2m} + \frac{\mathbf{q}\cdot\mathbf{K}}{m}. \end{aligned} \tag{6.4}$$

Where $\mathrm{E}_{\mathrm{transfer}}$ is the energy lost by the incident electron, and by fixing the incident electron energy at 50 keV and measuring the outgoing electron at 25 keV at a scattering angle of 44.3 ° the $\mathrm{E}_{\mathrm{transfer}}$ is equal to the momentum transfer term $\left(\frac{\mathbf{K}^2}{2m}\right)$, hence the bound

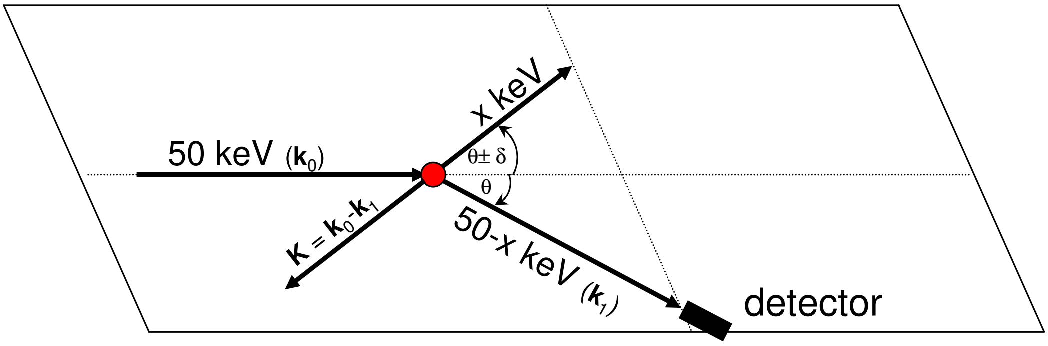

Figure 6.8: a) The experimental configuration for a Compton scattering experiment (Section 1.3). Showing the incoming electron (50 keV) colliding with and ejecting a target electron. One of the outgoing electrons is measured at the experimental scattering angle of 44.3 ° (θ). The momentum transfer vector (**K**) is shown, and is the projection vector of the measured momentum profile.

electron's momentum (**q**) projection onto the momentum transfer (**K**) is zero. Thus the momentum of the bound electrons projection on to the momentum transfer vector can be determined by the change in energy of the outgoing electron away from the 25 keV.

$$\mathrm{E}_{\mathrm{outgoing}} - 25\ \mathrm{keV} = \frac{\mathbf{q}\cdot(\mathbf{k}_0 - \mathbf{k}_1)}{m}. \tag{6.5}$$

This experimental configuration has been used to previously record the electron-Compton scattering profile of carbon [169].

Compton scattering is more typically performed with synchrotron radiation such as γ-rays or X-rays, the advantage of photonic probes is that there is very little Bragg-Compton coupling of the incident probe. That is, there are almost no diffraction effects from the incident beam. The idea of using electrons as probes for measuring the Compton profiles of solids was first discussed and used by Williams *et. al.* in 1981 [170], who stated that electron Compton scattering has a huge advantage arising from the strength of the interaction. The electron Compton scattering cross section is up to 5 orders of magnitude higher than the X-ray Compton scattering cross section, and the incident electron flux can be orders of magnitude higher than the X-ray flux produced from synchrotron radiation. There were concerns expressed over the effect of multiple scattering, and thus samples would have to be very thin to avoid the Compton scattering contribution from being immersed by other scattering mechanisms. The double differential cross section for electron

Compton scattering [171] is given by;

$$\frac{\partial^2\sigma}{\partial E\partial\Omega} = (2\pi)^4\sum_b |T_{ba}|^2\delta(E_0 - E_1 + E). \tag{6.6}$$

Where E_0 is the energy of the incident electron, E_1 is the energy of the outgoing electron and E is the energy transfer. T_{ba} is the transition matrix element for the total initial state of the system (a) and the total final state of the system (b). The expression for the transition matrix element becomes very complicated very quickly, especially with inclusion of Bragg-Compton channel coupling [172], a full expression for the spin integrated transition matrix element can be found in Schattschneider *et. al.* [171]. Vriens [153] has shown that when using polarised incident electrons, the electron-electron scattering cross section introduces a spin dependent term that for our EMS spectrometer configuration reduces to $\left(\frac{2}{K^4} - \frac{1+(\cos\varphi_{0,1})}{K^4}\right)$ (Eq. 6.2). Where $\varphi_{0,1}$ is the angle between the spins of the incident electron (0) and bound electron (1). In a ferromagnetic sample the bound electrons are either spin $\uparrow$ or spin $\downarrow$, and for a spin polarised electron source the electrons are either spin $\uparrow$ or spin $\downarrow$. This means the angle between the spins of the incident and bound electrons will either be 0 °, in which case the cross section is zero ($\sigma \rightarrow 0$), or the angle between the spins of the incident and bound electron will be 180 °, in which case the cross section is twice that of a spin integrated system ($\sigma \rightarrow 2\sigma_{\text{unpolarised}}$).

This is an interesting result as it states that if the incoming beam is 100 % polarised the countrate is entirely due to the target electrons with opposite spin orientation. The magnetic electron-Compton profile is thus entirely dependent upon the spin of the bound electron. Compared to magnetic X-ray Compton scattering where the spin dependent term in the cross section is on the order of 1 % compared to the non-spin dependent terms, commonly labelled as the "charge" terms [173]. Theoretically, magnetic electron-Compton scattering is 100 times more sensitive to spin dependent effects and several orders of magnitudes more intense than X-ray Compton scattering. In reality incident electron beams are not 100 % polarised (21 % in this study), and multiple scattering obscures the electron-Compton scattering cross section.

Magnetic Compton profiles are defined as the difference of the spin up ($\uparrow$) and the spin down (↓) projected momentum densities [174];

$$J_{mag}(\mathbf{q}_z) = \int\int [n\uparrow(\mathbf{q}_z) - n\downarrow(\mathbf{q}_z)]\mathrm{dq}_x\mathrm{dq}_y. \tag{6.7}$$

To ensure the magnetic Compton profiles are accurate the spin-up and spin-down Compton profiles must be measured in the same absolute scale, this meant the EMS spectrometer had to be modified. The Faraday cup that measures the incident beam current (see Section 2.1), had a charge integrator added that produced an output pulse for every 5 pC of incident electron charge. This pulse, generated at the positive HV potential, was transmitted to ground as an optical pulse and then sent to the data collection terminal. The data collection software was programmed to record data as a function of the accumulated incident electron charge, in this manner Compton profiles could be measured as a function of incident electron charge and two separate measurements on the same sample could be directly compared.

In the EMS spectrometer magnetic Compton scattering experiments were performed at the momentum projection value of **q** = 0 for both Au and magnetised Fe ⟨100⟩ (Γ-H) at two scattering angles (± 44.3 °) for a spin-up and spin-down incident electron beam. Magnetised Fe should yield positive asymmetries for both scattering directions due to the spin components in the cross sections; Au should yield zero asymmetry as the bound electrons' spins are not aligned. The results for this experiment are shown in Table 6.2, as a percentage of asymmetry.

Sample	Asymmetry in left detector	Asymmetry in right detector
magnetised Fe	-1.27 ±0.1 %	-1.04 ±0.1 %
Au	-1.12 ±0.1 %	+0.99 % ±0.1 %

Table 6.2: The ↑-↓ asymmetry in magnetised Fe is as expected, there is a higher cross section for spin up incident electrons at both the scattering angles ± 44.3 °. For Au however there is a large asymmetry that changes sign for the two measured scattering angles. This is a Mott-scattering effect, and the percentage of the asymmetry is similar to what was seen in the Au Mott scattering experiment. These measured asymmetries have not been corrected for the limited degree of polarisation of the incident electron beam (0.21).

The results for magnetised Fe are as expected, when the sample is magnetised in the spin up (↑) direction, as the Compton scattering cross section is much higher for spin down (↓) incident electrons, and thus the spin ↑ - spin ↓ spectra will result in a negative asymmetry. For Au, where there is no preferential spin direction, there is expected to be no asymmetry at either detector. Surprisingly a relatively large asymmetry (Tab. 6.2) is seen in the measurement from both scattering angles, and these asymmetries are opposite in sign. This type of asymmetry is typical of the size and magnitude of the electron-nucleus Mott scattering experiment that was performed on Au where spin-orbit interaction creates a preferential scattering direction dependent upon incident electron spin polarisation. For this asymmetry to be accountable by a Mott scattering mechanism either the incoming or outgoing electron would have to lose 25 keV in order to be detected, as Mott scattering is an elastic scattering process. With such a large intensity attributed to multiple scattering it is clear that to measure magnetic Compton profiles of Fe the thinnest possible sample is required. This contribution from Mott scattering would also explain the slight difference in spin asymmetries seen for both detectors in the electron Compton scattering of Fe (0.23 %), which is a fifth of the asymmetry difference seen for Au. This ratio of the intensity of the Mott scattering asymmetry is close to the expected asymmetry (Tab. 6.1) of these two samples.

To understand the size of the inelastic background in the raw Compton profiles, two spin integrated Compton profiles were measured for the same magnetised Fe sample, one in transmission mode and one in reflection mode (Fig. 6.10). The effective sample thickness of these two measurements depends on the distance the incident and outgoing electrons traverse and the energy they posses due to the high energy mean free path relationship (MFP $\propto$ E) [95, 175]. The transmission mode configuration has an average effective thickness of 1.91 x $\mathrm{MFP}_{50\,\mathrm{keV}}$, whilst in reflection mode the effective thickness of the sample increases to 3.92 x $\mathrm{MFP}_{50\,\mathrm{keV}}$ (Fig. 6.9). Using the effective thicknesses of the two modes the sample in the reflection mode experiment was 2.05 times thicker. The results (Fig. 6.10) show that the Compton profile of the thinner sample has a background on the order of 1.43 times the Compton signal, whilst the thicker sample had a background on the order of 2.87 times the Compton signal. At $\mathbf{q} = 0$ the differences between the spin-

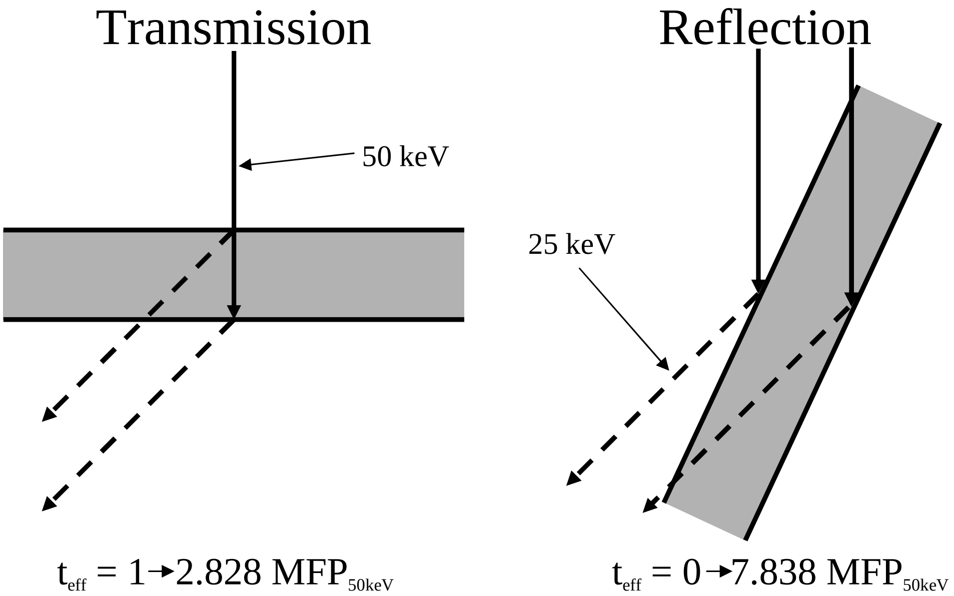

Figure 6.9: The kinematics the magnetic Compton profile experiment. Showing the minimum and maximum possible pathlengths of the electron through the sample for the transmission mode (a) and the reflection mode (b). Taking mean free paths into account the same sample measured in a reflection mode experiment would be 2.05 times thicker.

up and spin-down Compton profiles was on the order of 2 % for the thin sample and 1.2 % for the thick sample, indicating that the background does not have the same proportion of spin asymmetry as the Compton profile. The multiple scattering background acts to dampen the spin dependent asymmetry in the magnetic Compton profiles.

There are experimental problems with diffraction effects (Bragg scattering) that can contribute to the measured Compton profile, as the incoming or outgoing electrons can undergo diffraction which changes their scattering angle. With these diffraction effects a measured Compton profile will be a superposition of many Compton profiles where the diffraction angle and the Compton scattering angle add up to the measured in plane angle of 44.3 ° (θ) and the measured out of plane angle of 0 ± 3.25 °, which is where our detector is situated. The effect is that the measured Compton profile includes partial intensity from a set of Compton profiles measured at both different crystalline directions and measured over a different Compton scattering angle. For disordered samples this effect is not as noticeable, for single crystalline samples where electron correlations are not spheri-

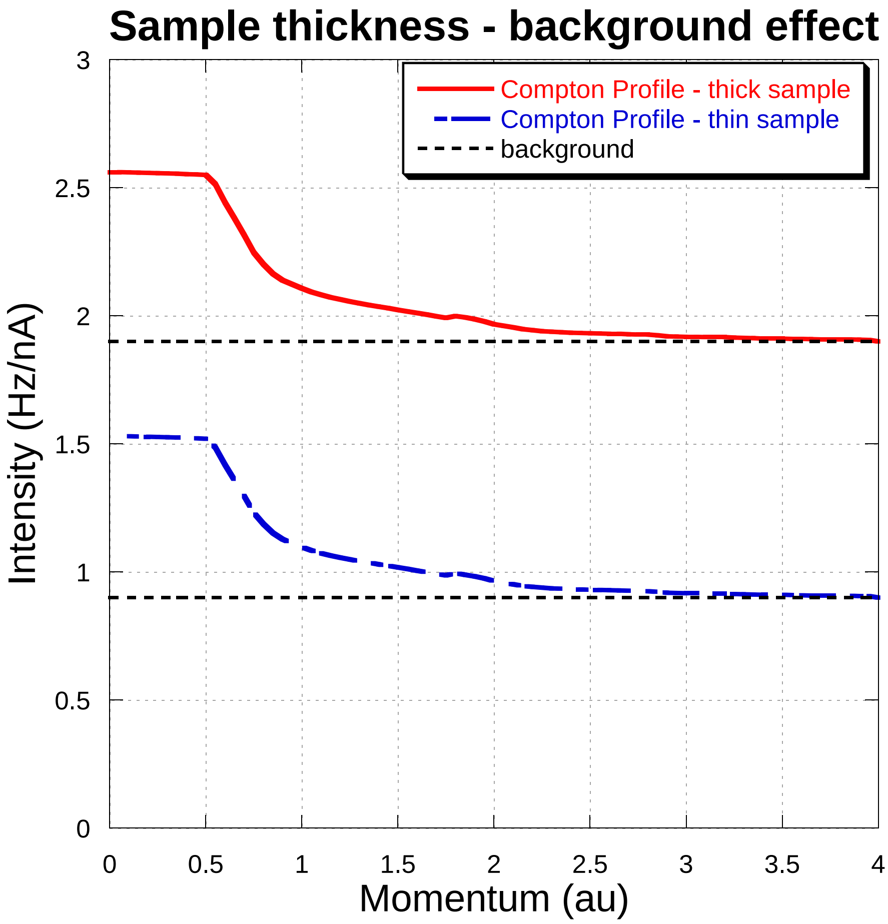

Figure 6.10: The measured (spin-integrated) Compton profile for a thick magnetised Fe sample (-), which shows that 74 % of the signal is due to other processes. The measured Compton profile of the same magnetised Fe sample but in a different experimental geometry that effectively decreases the samples thickness by a factor of 2.65 (-). The background signal has reduced to 58 % of the total signal.

cally averaged, valence electrons are not uniformly distributed, and different crystalline directions measure noticeably different Compton profiles [155] these diffraction effects can severely contaminate results.

Lam and Platzman [176] developed a correction for electron correlation in Compton profiles, which gives a better agreement between theory and experiment, especially for states above the Fermi radius, but even this correction was for isotropic systems, and small discrepancies still exist for anisotropic measurements. The differences seen in this study are far larger than other reported differences in anisotropic systems [155], so diffraction effects are a large contribution to the background, the size of which will be determined later.

Experimentally, diffraction effects can be minimised and in some cases negated by using the crystal symmetry to nullify Bragg-Compton coupling [172] by setting up a so called "two-beam" case [155]. This is done by rotating and tilting the sample away from the zone axis which produces Bragg scattering, and using the crystal symmetry to measure along an equivalent crystalline direction. In the EMS spectrometer there is no facility for tilting the sample, and thus a two beam case could not be utilised.

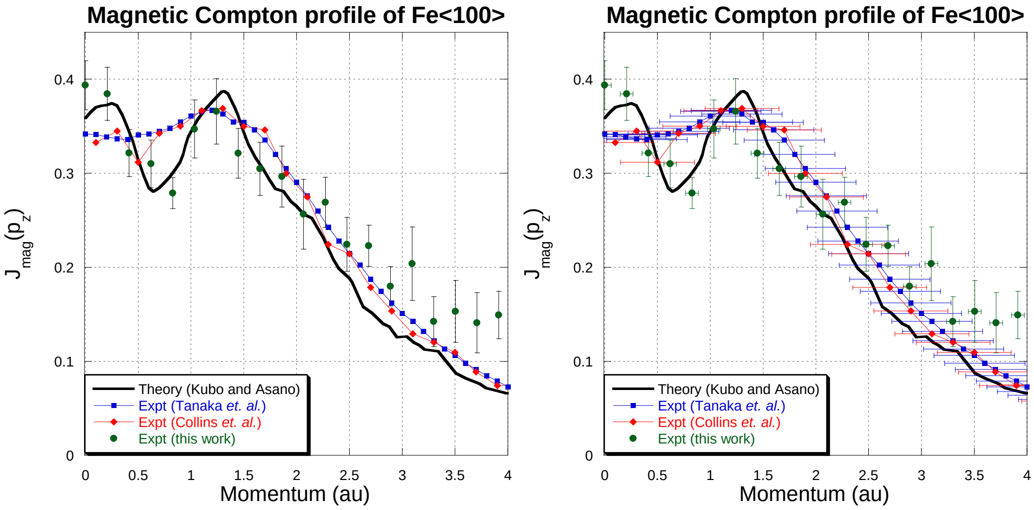

Figure 6.11: Left: The magnetic electron-Compton profile of magnetised Fe (●), that has been averaged over both detectors, from this study is compared to the magnetic Compton profiles measured by Tanaka *et. al.* (■) [177] and Collins *et. al.* (♦) [178], and the LDA calculations by Kubo and Asano (-) [179]. The local minimum in the spin asymmetry at 0.6 au is seen in the electron Compton data but not in the photon Compton data. Right: The experimental Compton profiles shown with their relative momentum resolution. The poor momentum resolution of the photon based Compton profiles (0.7-0.76 au) could explain why the local minimum in the spin asymmetry is seen more clearly in the electron-Compton data (0.12 au).

By repeating the electron-Compton scattering experiment and taking the difference between the spin up and spin down spectra we can measure the magnetic electron-Compton profiles (Eq. 6.7). The measured magnetic electron-Compton profiles for the magnetised

Fe $< 110 >$ sample has been compared to experimental magnetic photon-Compton profiles [177, 178] and an LDA calculation [179] (Fig. 6.11). In these measurements the photon based magnetic CPs are scaled so the area covered from ± 8 au is equal for the number of unpaired electrons in the sample (2.2 in magnetised Fe [178]). Electron CPs suffer from Bragg-Compton coupling which adds extra intensity to the CP at higher momentum as will be discussed later, so comparison of the magnetic electron CPs is performed by scaling the theory to match the value of the experiment at lower momentum values, as opposed to the area integration technique that X-ray Compton scattering uses.

The error bars (Fig. 6.11: Right) for the electron-CPs and photon based CPs are vastly different. The momentum resolution in the case of electrons comes from two components; the momentum resolution from the geometry of the experiment (0.1 au) and the momentum resolution from the measured energy range (0.068 au), give a total momentum resolution for the electron-CPs of 0.12 au. The experimental photon-CPs had quoted resolutions of 0.76 au [177] and 0.7 au [178]. The statistical accuracy in the photon-CPs ($\approx$ 1 %) is on the order of the size of the data points, statistical accuracy is good due to long measurement times and hence a high number of measured counts (typically 10^8). The electron-CPs in this study were measured over a short period of time, typically 1 hour per data point, the incident electron flux was kept low to increase the stability of the electron gun, and hence the count rates were low. The lower total number of counts decreased the statistical accuracy, and hence the electron-CPs have large statistical error bars. With refinement of the electron-CP technique in the EMS spectrometer, much higher count rates will be attainable and a statistical improvement on the order of 3-4 times will be possible without increasing the data acquisition time.

A DFT calculation using a local spin density approximation (LSDA) of the magnetic CP for magnetised Fe$\langle 100\rangle$ [179] is presented along with the experimental data (Fig. 6.11). The calculation shows a minimum in the spin asymmetry, for the Fe$\langle 100\rangle$ projection, at around 0.6 au. The 0.6 au minimum is attributed to the outer most d-band which are the least tightly bound [179], which is anisotropic due to electron-correlation effects. CPs are planar projections, so there are also Fermi surface topology effects at the projection 0.6 au along the Fe$\langle 100 \rangle$ that attribute in part to the 0.6 au minimum in the spin asymmetry. The overestimation of the depth of the 0.6 au asymmetry minimum feature in theory compared to photon-CPs has been partially attributed to errors in the LSDA [180]. The electron-CP measurement presented in this work suggests that the minimum is deeper than measured in the photon-CPs (Fig. 6.11: Left). When considering the momentum resolution of the photon-CPs (Fig. 6.11: Right), it is possible that this feature is dampened due to the 0.2 au and 1.3 au peaks. The statistical accuracy of the electron-CPs would have to be increased and a measurement with a finer momenta grid would have to be performed to decisively comment on the depth of the asymmetry feature.

At higher momentum the magnetic electron-Compton profile deviates from both the theory and photon-CPs. There are two extra contributions to the measured intensity, that effect the electron-CPs much more than the photon-CPs, that can account for the deviation in the electron CP. The first is Bragg-Compton coupling, which occurs when either the incoming or outgoing electron is Bragg scattered (diffracted) in addition to being Compton scattered which was discussed earlier. The effect of the diffraction is to shift intensity out to higher momentum which was also seen in the EMS results, so more intensity at higher momentum ($\mathbf{p}_z$) is expected due to Bragg-Compton coupling.

The second effect is unique to the EMS spectrometer and is due to the influence of the inelastic Mott scattering contribution which was discussed earlier. Magnetic Fe has a negative Sherman function (-0.82 %), thus incident spin up electrons will be preferentially deflected to the right, and alternatively incident spin down electrons will be deflected to the left. The effect can be seen in the raw electron Compton profiles (Fig. 6.12: a), where the gap between the spin-up and spin-down Compton profiles is larger in the right detector than it is in the left detector. Mott scattering will therefore artificially increase the intensity measured for the right detector (spin down) and left detector (spin up) spectra, which will increase the magnetic Compton profiles measured in the right detector and decrease the magnetic Compton profiles measured in the left detector (Fig. 6.12: b). The Mott effect is equal and opposite, so the left and right magnetic electron-Compton profiles can be averaged to minimise the effect of Mott scattering, however as one detector

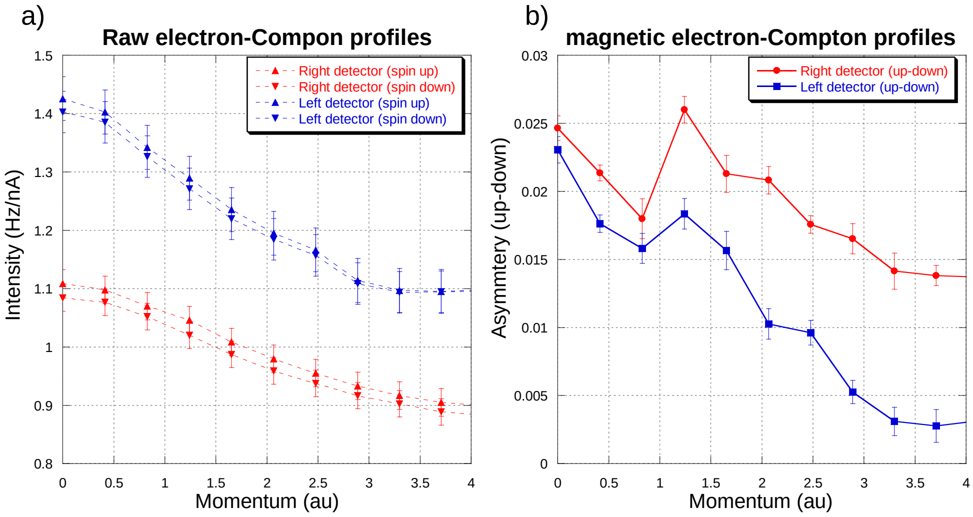

Figure 6.12: a) The raw electron-Compton profiles for both the left and right detectors measured with both a spin-up and spin-down incident polarised electron beam. The left detector has much a higher countrate due to increased detector efficiency. Also note that the y-axis does not start at zero. b) The magnetic electron-Compton profiles as measured by each detectors, the right detector has a much higher asymmetry that is attributed to Mott scattering contributions.

is more efficient than the other a small proportion remains in the final magnetic electron-Compton profile (Fig. 6.11). The Left detector is more sensitive, so the remnants of the Mott scattering effect on the magnetic electron-Compton profile actually reduces the asymmetry at higher momentum. So diffraction effects which are responsible for the excess intensity at higher momentum in the magnetic Compton profile (Fig. 6.11) will be dampened by the Mott scattering effect. The diffraction intensity is hence a larger than first expected from the magnetic Compton profiles (Fig. 6.11).

The size of the Mott scattering contribution can be used to roughly determine the intensity of the inelastic contribution to the background of the raw Compton profiles. The difference between the measured magnetic electron-Compton profiles (Fig. 6.12: b) relates to approximately 0.007 Hz/nA. The Mott scattering contribution is expected to be 0.82 % (Tab. 6.1) of the total inelastic contribution, thus the inelastic background is approximately 0.85 Hz/nA (0.007/0.0082), given that the total background is approximately 1 Hz/nA, that means the Mott scattering contribution to the background is 85 % of the total background (Fig. 6.12: a). Thus the diffraction contribution is approximately 15 % of the total background or 0.15 Hz/nA, which is half as large as the Compton signal (0.30 Hz/nA).

In summary, initial progress towards measuring magnetic electron-Compton profiles in the EMS spectrometer has been made. Further developments of the technique in this spectrometer will be able to increase the statistical accuracy, and different energy configurations will be able to increase the momentum resolution down to 0.1 au. Further and more detailed measurements into the magnetic Compton profiles of Fe $\langle 100 \rangle$ after these improvements have been made will be more conclusive to experimentally resolving the depth of the spin asymmetry minimum in the magnetic Compton profiles. Better sample preparation is required to avoid any contributions from the Fe $\langle 110 \rangle$ domains that exist in small quantities in the present sample. The orientation uncertainties may contribute to the apparent depth of the 0.6 au minimum by increasing the size of the 1.2 au peak. At present it is difficult to determine if the depth of the asymmetry minimum is either overestimated by theory due to errors in the LSDA or is experimentally under resolved in photon based magnetic Compton profiles due to momentum resolution restraints.

6.5 Future Possibilities of Spin Polarised EMS

By measuring the second outgoing electron in a Compton scattering experiment the projection of the momentum density is resolved into a momentum vector, and the experiment becomes electron momentum spectroscopy (Fig. 6.13). By using a spin polarised incident electron beam and a ferromagnetic sample the spin dependent term in the electron-electron scattering cross section simplifies into to either 0 or 2 depending on whether the two electrons' spin orientation is parallel or anti-parallel respectively.

The spin dependent cross section for EMS is given by Vriens [153], and for the symmetric experimental geometry Vriens cross section simplifies to;

$$\sigma(E, \mathbf{k}_1, \mathbf{k}_2) = \frac{2k_1k_2}{k_0K^4}\rho_E(\mathbf{k}_1 + \mathbf{k}_2 - \mathbf{k}_0) \times (1 - \cos\varphi_{0,1})\delta(k_0^2 - k_1^2 - k_2^2 - E). \quad (6.8)$$

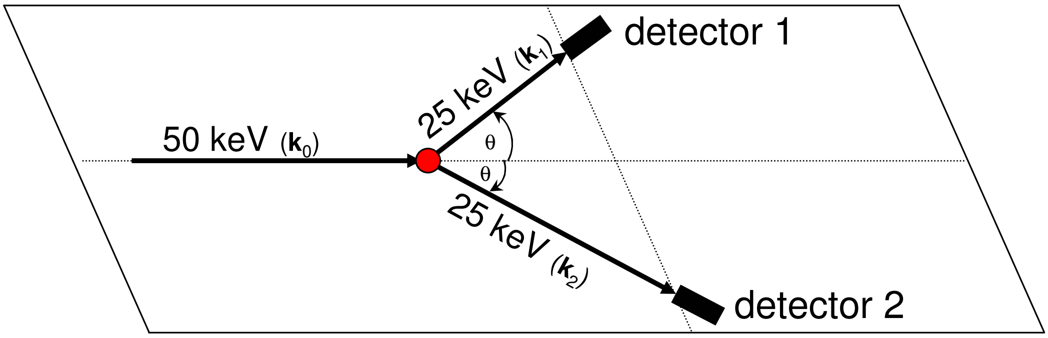

Figure 6.13: The schematic layout for a SPEMS experiment. Both the outgoing electrons are now measured, the incident electron beam is spin polarised and the sample magnetisation is perpendicular (up) to the experimental plane. The conservation of energy and momentum enables the experiment to measure a vector in momentum space that is in the direction of magnetisation.

Where two outgoing electrons are measured, so compared to the electron-electron scattering cross section (Eq. 6.1), k_2 is known and the binding energy of the bound electron is known (E), so there is no need to integrate over any variables. $\varphi_{0,1}$ is the angle between in spin of the incident electron and the spin of the bound electron, thus $1 - \cos\varphi_{0,1}$ (and hence the cross section σ) is either 0 when the two electrons' spins are parallel, or 2 (and hence $2\sigma_{\mathrm{unpolarised}}$). So spin polarised electron momentum spectroscopy (SPEMS) can be used to probe spin dependent states, such as the spin-up and spin-down states in ferromagnetic materials.

The experimental configuration for this experiment is identical to that shown and explained earlier (Chap. 2), with the exception of the exchange from the unpolarised electron gun to the spin polarised electron gun (Chap. 3). SPEMS experiments require the gun to be held at 25 keV for several days, whilst maintaining high emission current that is constant and well focussed. The spin polarised gun required a residual Cs flux to maintain its emission, however the Cs flux eventually coats the insulators, causing a HV breakdown which causes the experiment to fail. At present the spin polarised electron gun must undergo major modifications to achieve the stable emission whilst held at a high potential, however a theoretical investigation was performed to determine if the spin dependent effects are measurable with the present spectrometer, given the experimental resolution.

The question remains how much does the reduced degree of polarisation of the incident electron beam and multiple scattering effect the spin-up and spin-down differences?

Theoretical calculations of the spectral momentum densities (Fig. 6.14) for the spin-up and spin-down states in magnetised Fe were performed by Anotoli Kheifets using a LMTO code [89].

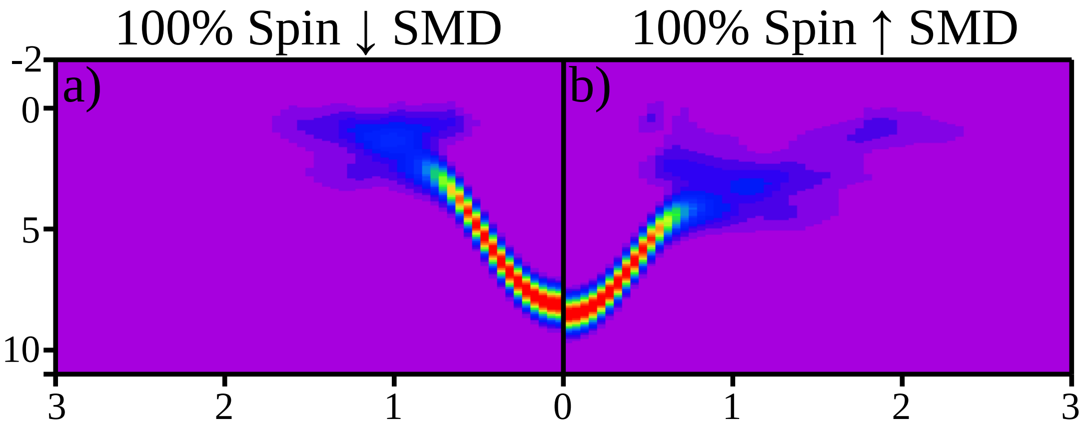

Figure 6.14: The SMDs for the spin-down (a) electrons and the spin-up (b) electrons in an Iron sample that is magnetised in the up direction. There are large differences in the position of the d-band intensities, and a noticeable difference in the sp-band minimum at q = 0.

There is quite a considerable difference in the position of the d-bands for the 100 % spin-up and 100 % spin-down cases. To transform these theoretical calculations into the expected experimental results the effect of the degree of polarisation of incident electron beam must be taken into account. A 21 % incident polarisation means that 60.5 % of the electrons are aligned in the preferential spin direction, and 39.5 % of the electrons are aligned in the non-preferential spin direction. As shown in Eq. 6.8, the spin-up incident electrons will only interact with spin-down electrons in the target, and vice versa for spin-down incident electrons. That means for a spin-up polarised incident electron beam the measured SPEMS spectral momentum density will measure 60.5 % of the spin-down spectral momentum density and 39.5 % of the spin-up spectral momentum density, and vice versa for the spin-down polarised incident electron beam.

The expected experimental SMDs (Fig. 6.15) have been convoluted to the experimen-

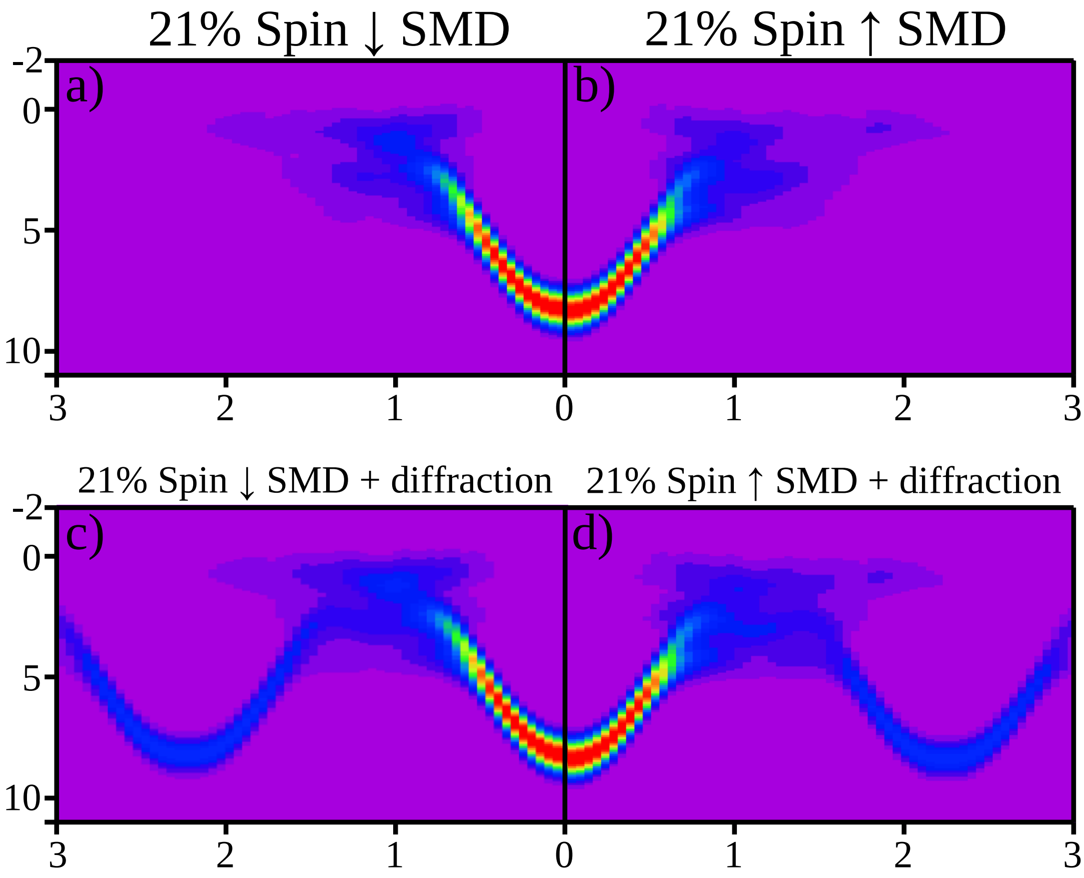

Figure 6.15: The expected experimental SMDs for an "up" magnetised Fe sample with an incident electron beam that is 21 % polarised. The differences between the spin-down (a) and spin-up (b) SMDs are much smaller, the d-band distribution looks very similar and the sp-band offset at q = 0 is now very small. Adding experimental diffraction effects into these theoretical calculations (c: spin-down, d: spin-up) doesn't appear to dampen the asymmetry any further, due to the different energy levels of the ↑ and ↓ d-bands.

tal resolution of 1 eV and diffraction effects have been added at an intensity of 20 % of the theoretical intensity, more complex effects such as quasi-particle lifetimes have been omitted from this theoretical examination. It is clearly seen that the spin-down SMD (Fig. 6.15: c) is very similar to the spin-up SMD (Fig. 6.15: d). The mixing effect introduced from the incomplete spin polarisation of the incident electron beam has made these two SMDs almost too similar to differentiate.

The spin-up minus spin-down asymmetry SMD's that would be experimentally mea-

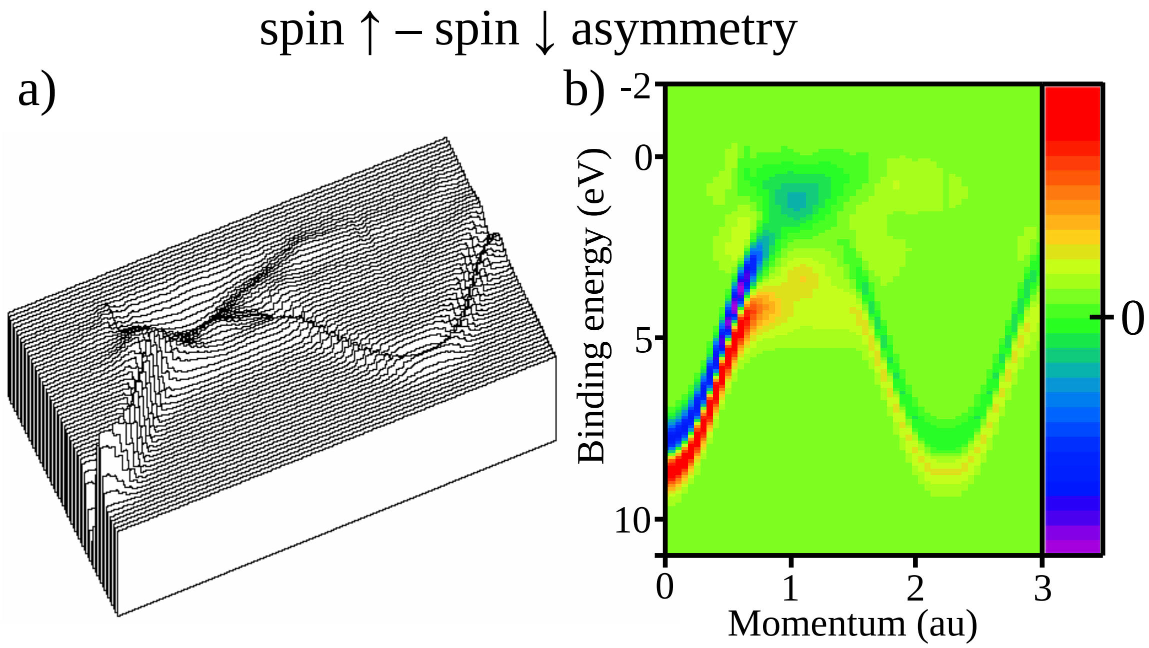

Figure 6.16: The spin-up minus spin-down SMD asymmetry for "thought experiments" taken with a 21 % polarised incident electron beam and with a typical diffraction intensity contribution of 20 %. The asymmetry is shown as a contour surface plot (a), and a two-dimensional colour coded SMD plot (b) with an colour-intensity scale indicated. The largest asymmetry is around the sp-bands, there is still asymmetry seen around the d-bands, despite the added diffraction

sured given the current electron beam polarisation, experimental resolution and typical in-plane diffraction contributions are shown in Fig.6.16. The largest spin asymmetry would be expected to be seen around the d-bands near the Fermi level, however due to measured spin-state mixing from the incomplete polarisation of the incident electron beam the spin asymmetry is smaller than in the sp-bands. The largest spin asymmetry is around the sp-band, primarily as those bands are the most intense. The asymmetry effect from the spin-down sp-band is seen as a negative contribution in the contour plot (Fig. 6.16: a), or as a blue and in the colour coded SMD (Fi.g 6.16: b). The asymmetry effects from the spin-up band is seen as a positive contribution in the contour plot (Fig. 6.16: a), or as a red band in the colour coded SMD (Fi.g 6.16: b). The diffraction effects of the sp-band only adds intensity back onto the band, and thus the spin asymmetry is clearly visible as the spin-up and spin-down sp-bands split by as much as 0.4 eV at $\mathbf{q} = 0$ due to spin-orbit coupling.

The spin-up sp-band electrons in the magnetised Fe sample have a band position of 8.3 eV at **q** = 0 (Fig. 6.17: a), compared to the spin-down sp-band electrons that have a binding energy of 7.9 eV at **q** = 0. When the incident electron beam is not 100 % polarised, there is a mixing of these two bands in the measured SMD, at 21 % polarisation the bands are only separated by 0.12 eV. When looking at the energy plots of the sp-band asymmetry (at **q** = 0), at 100 % polarisation the intensity of the asymmetry spectra is half of the total sp-band intensity. At 21 % incident polarisation the measured sp-bands are closer and hence the asymmetry is much smaller (only 10 % of the total sp-band intensity). The intensity of the asymmetry would be on the order of our statistical resolution in a typical EMS measurement, and this investigation does not include quasi-particle lifetimes that add inelastic intensity to the sp-band that would further hinder the asymmetry measurement.

For a strained GaAs polarised electron source, incident polarisations of at least 50 % are commonly reported [181, 182], at this degree of incident polarisation the measured sp-band splitting would be 0.22 eV. The intensity of the asymmetry would also increase, due to the increased band-splitting, to over 25 % of the raw sp-band intensity (Fig. 6.17: b). This still does not include lifetime broadening effects, but it is expected that, even with lifetime broadening effects, an asymmetry at this degree if polarisation should be observable.

The largest spin dependent effects in magnetised Fe are in the d-bands, however the lower experimental d-band intensity measured in EMS and the incomplete polarisation of the electron beam make the spin asymmetry effects in the d-bands difficult to resolve. For a SPEMS experiment the biggest effects are expected to be seen in the sp-band spin-orbit splitting, however at the current experimental incident polarisation the mixing of the bands and the lifetime broadening in the sp-band will make it difficult to measure. It is expected that at a higher incident polarisation ($\approx$ 50 %) the asymmetry of the sp-band should be measurable, despite lifetime broadening effects. The current experimental resolution (1 eV) will make the splitting of the sp-bands difficult to measure, but at higher degrees of incident polarisation a clear difference in the binding energy of the sp-band at

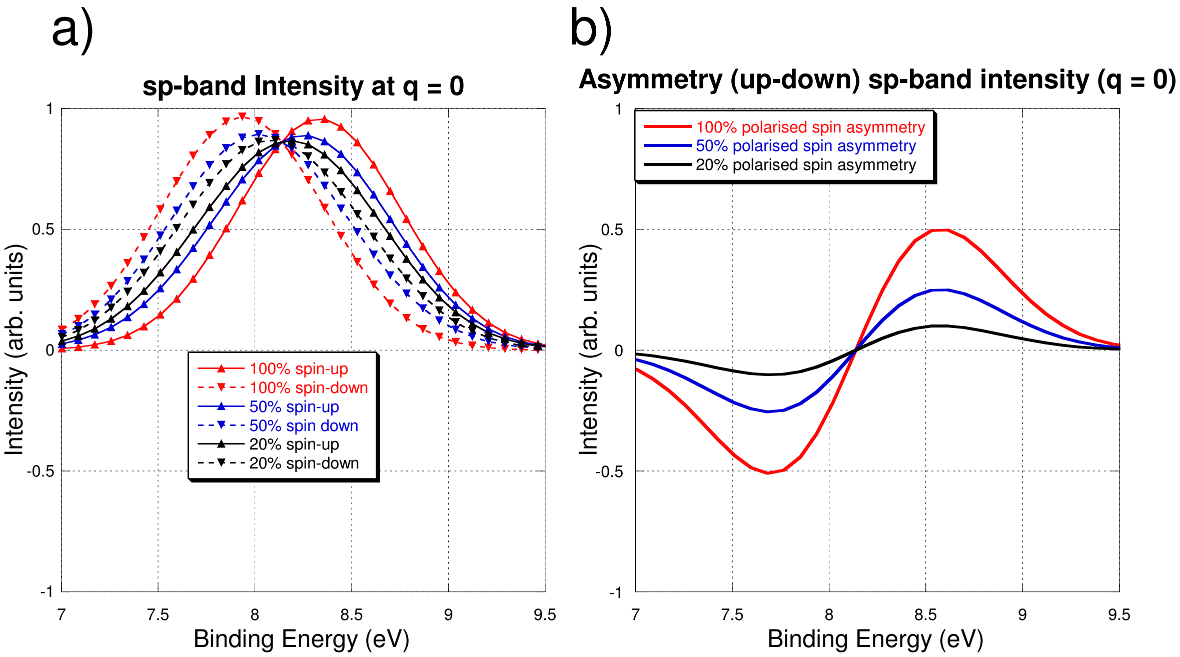

Figure 6.17: a) The simulated sp-band intensity at **q** = 0 for different degrees of incident spin polarisation. The spin-up and spin-down refers to the spin of the bound electrons. For a 100 % polarised incident electron beam there is a clear splitting (0.4 eV), for the current experimental polarisation (21 %) the splitting is hardly resolved. b) The expected spin asymmetry (spin-up minus spin -down) for the different degrees of polarisation. For 100 % polarisation the asymmetry is half the intensity of the raw sp-band. At 21 % polarisation the asymmetry intensity is around 10 %.

q = 0 should be observable.

Chapter 7

Conclusions

This chapter is a summary of the results that have been presented throughout this thesis. Firstly the results presented in chapters 4-6 will be summarised, and then secondly the present state of EMS will be summarised with suggestions for future studies and the further advancement of the field.

The results of the single crystal noble metals, presented in chapter 4, show that EMS can measure the anisotropy of the electronic structure of single crystal samples by independently measuring along different crystalline directions. The EMS measurements of the noble metals (Cu, Ag and Au) were compared to a LDA FP-LMTO calculation. The DFT theory consistently overestimated the band width of the sp-band, which has been attributed to self energy effects. The DFT theory also overestimated the amount of dispersion in the d-bands, which was concluded to be due to the self interaction correction effects. Inclusion of a self interaction correction term to the LDA theory showed a much better agreement in the dispersion of the d-bands for Cu. The LDA theory generally underestimated the binding energies of the d-bands; this has been attributed to problems in the modeling of the metallic screening. Comparison between the ARPES and EMS experimental data for these three systems have shown that EMS measures a much more intense signal for the sp-band and is typically considered more accurate for those bands, whilst the ARPES technique is more sensitive to the d-bands and is typically considered more accurate there. With EMS a bulk sensitive technique and ARPES generally a surface sensitive technique, it is clear that both experiments are complimentary to each other and are required to accurately measure the complete electronic structure of solids.

The results for the semiconductors (Si and Ge) in chapter 5 highlight the ability of EMS to measure spectral functions of solids in a disordered state, unlike ARPES which requires long range crystalline order. This feature of EMS was utilised to measure the polycrystalline and amorphous states of Si and Ge. These semiconductors are of interest as they exist in a special amorphous state known as a continuous random network, and EMS is currently the only technique that can measure the full spectral function of this state. Theorists approach this unique state in many interesting ways; it was found in this study that typically the Green's function techniques were found to be a better match to the EMS data than the super-call theories were. The differences between the experimental measurements of the amorphous and polycrystalline states were found to be quite minimal. The most noticeable difference was an increase of states in the first Brillouin zone induced sp-band gap for the amorphous sample, this effect was attributed to the larger number of dangling bonds in the CRN structure which introduced states into that region.

EMS was also utilised to track the changes in the spectral function of a NiCu alloy across varying compositions of each component. NiCu is a quintessential substitutional alloy, and as such it is a very simple test subject, it was found in this study that the sp-bands are delocalised in nature and tend to adopt a hybrid structure of the two constituent species. The d-bands were found to be quite localised in nature and kept the characteristic structure of their constituent atom. This was a test study which will hopefully evolve to more complex targets, and as such be able to track the rapid changes across transitions of interest such as Mott-Hubbard insulators.

In chapter 6 the spin-polarised electron source, that was designed, built and commissioned during this project, was used to progress the EMS technique into the field of studying spin-dependent phenomena. The ANU EMS spectrometer was used in conjunction with the new spin polarised electron source to measure the spin-polarised electron-energy-loss spectra of magnetised Fe. It was found at low energy loss there is some spin dependent structure that may correspond to spin dependent Stoner excitations. Comparison with the work of Komesu is in agreement with this study and exhibits similar features, these features are extremely small and given the larger error bars in the spin dependent spectra it is still uncertain whether they can be clearly attributed to Stoner excitations.

In the study of the magnetic electron-Compton profiles (Sec. 6.4) the interesting feature of the electron-electron scattering cross section is the spin dependent term which varies from 0 to 2 dependent upon the alignment of the bound electron and incident electron spins. In ferromagnetic samples the only two possible alignments are parallel ($\sigma \rightarrow 0$) or anti-parallel ($\sigma \rightarrow 2$). This means that the intensity of the spin dependent phenomena for ferromagnetic samples is only restricted upon the degree of polarisation of the incoming electron beam. This is large in comparison to Photon based techniques such as magnetic Compton scattering, where typically only 1 % of the signal is due to spin dependent phenomena. The EMS spectrometer was used to measure the magnetic electron-Compton profile of magnetised Fe, it was found that multiple scattering was a limiting factor in the resulting spectrum; still a clear magnetic Compton profile was measured. This technique showed great promise, for a spectrometer specifically designed to measure magnetic electron-Compton profiles, a 2-beam case can be set up to nullify the effect of multiple scattering, and an incident electron beam with a higher degree of polarisation can be used. These modifications will allow magnetic electron-Compton profiles to be measured accurately.

Also presented in chapter 6 was a feasibility study into a new field of spin-polarised electron-momentum-spectroscopy (SPEMS), which was based on the current experimental resolution, diffraction and typical countrates. It was determined that the limiting factor was the mixing of states; that is incomplete polarisation of the incident electron beam. With the current spin polarisation (21 %) it would be difficult to see differences in the spin dependent spectra of magnetised Fe. It was concluded that polarisations on the order of 50 % were required to see the differences in the binding energies of the sp-bands and d-bands. The high voltage instability of the new spin polarised electron source made it impossible to currently attempt this experiment.

The experimental technique of EMS has progressed to the point where the ANU EMS spectrometer can measure the spectral function of the valence electrons of a target within three to four days with resolutions of 1 eV and 0.1 au. Advancements in electron cathodes to limit the space-charge effect at the cathode is expected to improve the energy resolution further. Advancements in sample preparation techniques will increase the range of targets, which is now limited by the target thickness restriction ($\approx$ 20 nm). EMS is a very robust technique, it can measure, equally well, spectral functions from crystalline or disordered solids, and there is no question that the technique is bulk sensitive. In combination with ARPES a complete and accurate picture of the surface and bulk spectral functions can be accurately measured for all the valence electrons. Future studies should further explore spin polarised phenomena, which requires an electron polarised gun with a polarisation of at least 50 %. Future studies should also develop the ability to track alloys through different transitions, again the limiting factor in these future studies will be sample preparation.

Author's publications

- Bowles, C., Went, M. R., A. S. Kheifets and Vos, M. "Direct measurement of spectral momentum densities of ordered and disordered semiconductors by high energy EMS" AIP Conference Proceedings 811:167 (2006),
- Nixon, K. L., Vos, M., Bowles, C. and Ford, M. J. "Measuring the electronic structure of disordered overlayers by electron momentum spectroscopy: the Cu/Si interface" Surface and Interface Analysis 38:1236 (2006),
- Vos, M., Bowles, C., Kheifets, A. S. and Went, M. R. "Band structure of silicon as measured in extended momentum space" Physical Review B 73:085207 (2006),
- Vos, M., Bowles, C., Kheifets, A. S. and Went, M. R. "Electron momentum spectroscopy of light and heavy targets" Journal of Electron Spectroscopy and Related Phenomena 149:20 (2005),
- Bowles, C., Kheifets, A. S., Sashin, V. A., Vos, M. and Weigold, E. "The direct measurement of spectral momentum densities of silicon with high energy (e, 2e) spectroscopy" Journal of Electron Spectroscopy and Related Phenomena 141:95 (2004),
- Vos, M., Bowles, C., Kheifets, A. S., Sashin, V. A., Weigold, E. and Aryasetiawan, F. "Measurement of the electronic structure of crystalline silicon by electron momentum spectroscopy" Journal of Electron Spectroscopy and Related Phenomena 137-40:629 (2004),
- Vos, M., Kheifets, A. S., Bowles, C., Chen, C., Weigold, E. and Aryasetiawan, F. "Electronic structure of copper studied by electron momentum spectroscopy" Physical Review B 70:205111 (2004),
- Vos, M., Sashin, V. A., Bowles, C., Kheifets, A. S. and Weigold, E. "Probing the spectral densities over the full three-dimensional momentum space" Journal of Physics and Chemistry of Solids 65:2035 (2004).

Bibliography

[1] V.G. Neudachin, G.A. Novoskoltseva, and Yu.F. Smirnov. *Sov. Phys. JETP*, 28(3):540–543, 1969.

[2] U. Amaldi, A. Egidi, R. Marconero, and G. Pizzella. *Rev. Sci. Instrum.*, 40(8):1001–1004, 1969.

[3] R. Camilloni, A. Giardind Guidoni, R. Tiribelli, and G. Stefani. *Phys. Rev. Lett.*, 29(10):618–621, 1972.

[4] E. Weigold, S.T. Hood, and P.J.O Teubner. *Phys. Rev. Lett.*, 30(11):475–478, 1973.

[5] E. Weigold and B. Lohmann. *Phys. Lett. A*, 86(3):139–141, 1981.

[6] N.M. Persiantseva, N.A. Krasil'nikova, and V.G. Neudachin. *Sov. Phys. Jetp*, 49(3):530–535, 1979.

[7] A.L. Ritter, J.R. Dennison, and R. Jones. *Phys. Rev. Lett.*, 53(21):2054–2057, 1984.

[8] J. Lower, S. M. Bharathi, Yu Chen, K. J. Nygaard, and E. Weigold. *Surf. Sci.*, 251:213–217, 1991.

[9] M. Vos. *Aust. J. Phys.*, 51:609–618, 1998.

[10] C. Kittel. Wiley, 7th edition, 1996.

[11] C. Gao, A.L. Ritter, J. Dennison, and N.A.W. Holzworth. *Phys. Rev. B*, 37(8):3914–3923, 1998.

[12] P.J. Storer et. al. *Rev. Sci. Instrum.*, 65(7):2214–2226, 1994.

[13] S.A. Canney, M.J. Brunger, I.E. McCarthy, P.J. Storer, S. Utteridge, M. Vos, and E. Weigold. *J. Elec. Spec. Rel. Phenom.*, 83:65–76, 1997.

[14] E. Weigold et. al. *Aust. J. Phys.*, 49:543–554, 1996.

[15] M. Vos, S.A. Canney, I.E. McCarthy, S. Utteridge, M.T. Michalewicz, and E. Weigold. *Phys. Rev. B*, 56(3):1309–1315, 1997.

[16] M. Vos et. al. *J. Elec. Spec. Rel. Phen.*, 87:231–251, 1998.

[17] Z. Fang, S. Matthews, S. Utteridge, M. Vos, S.A. Canney, X. Guo, I.E. McCarthy, , and E. Weigold. *Phys. Rev. B*, 57:12882–12889, 1998.

[18] V.A. Sashin, H.E. Dorsett, M.A. Bolorizadeh, and M.J. Ford. *J. Chem. Phys.*, 113(18):8175–8182, 2000.

[19] M. Vos and E. Weigold. *J. Elec. Spec. Rel. Phenom.*, 112:93–106, 2000.

[20] J.B. Pendry. *Surf. Sci.*, 57:679–705, 1976.

[21] S. Sahrakorpi A. Bansil, M. Lindroos and R.S. Markiewicz. *New Journal of Physics*, 7:140, 2004.

[22] R. Courths and S. Hufner. *Phys. Rep.*, 112(2):53–171, 1984.

[23] I.E. McCarthy and E. Weigold. *Rep. Prog. Phys.*, 51:299–392, 1988.

[24] A. Tadich, L. Broekman, J. Riley, R. Leckey, S. Homolya, A.E. Smith, T. Seyller, K. Emtsev, and L. Ley. *J. Elec. Spec. Rel. Phenom.*, 144:515–518, 2005.

[25] T. Greber, T.J. Kruetz, P. Schwallerand E. Wetli, and J. Osterwalder. *Rev. Sci. Instrum.*, 68(12):4549–4554, 1997.

[26] M.J. Cooper. *Rep. Prog. Phys.*, 48:415–481, 1985.

[27] J.P. Carbotte and H.L. Arora. *Canad. J. Phys.*, 45:387–402, 1967.

[28] R.N. West. *Adv. Phys.*, 22:263–383, 1973.

[29] N. Shoitani N. Sakai M.J. Cooper, P.E. Mijnarends and A. Bansil. Oxford series on synchrotron readiation. Oxford Press, 2004.

[30] I.E. McCarthy and E. Weigold. *Phys. Rep.*, 27(6):275–371, 1976.

[31] M.A. Coplan, J.H. Moore, and J.P. Doering. *rev. of mod. phys.*, 66(3):985–1014, 1994.

[32] E. Weigold and I.E. McCarthy. Physics of Atoms and Molecules. Kluwer Academic, 1999.

[33] I.E. McCarthy and E. Weigold. *Rep. Prog. Phys.*, 54:789–879, 1991.

[34] W.F. Ford. *Phys. Rev. B*, 133:1616–1621, 1964.

[35] M. Vos and I.E. McCarthy. *Rev. Mod. Phys.*, 67:713–723, 1995.

[36] M. Vos, G.P. Cornish, and E. Weigold. *Rev. Sci. Instrum.*, 71(10):3831–3840, 2000.

[37] M. Vos, V.A. Sashin, C. Bowles, A.S. Kheifets, and E. Weigold. *J. Phys. Chem. of Sol.*, 65(12):2035–2039, 2004.

[38] J.L. Labar. *Microscopy and Analysis*, 75:9–11, 2002.

[39] C. Chen, M. Gale, A.S. Kheifets, M. Vos, and M.R. Went. *accepted to J. Phys: Condens. Matter*, 17:1, 2005.

[40] M. Vos, C. Bowles, A.S. Kheifets, and M.R. Went. *Phys. Rev. B*, 73(8):085207, 2006.

[41] R.E. Imhof, A. Adams, and G.C. King. *J. Phys. E*, 9:138–142, 1975.

[42] T.J.M. Zouros and E.P. Benis. *Applied Phys. Lett,*, 86:094105, 2005.

[43] J.H. Moore, C.C. Davies, and M.A. Coplan. Addison-Wesley, 1983.

[44] C.E. Kuyatt and J. Arol Simpson. *Rev. Sci. Instrum.*, 38(1):103–111, 1967.

[45] R.S. Caprari. *Meas. Sci. Technol.*, 6(7):1063–1064, 1995.

[46] J.L. Wiza. *Nucl. Instr. and Meth.*, 162:587–601, 1979.

[47] M. Lampton and C.W. Carlson. *Rev. Sci. Instrum.*, 50(9):1093–1098, 1979.

[48] B. Zimmerman. Kluwer Academic, 1970.

[49] M. Vos. *Ultramicroscopy*, 92:143–149, 2002.

[50] D. Roy and D. Tremblay. *Rep. Prog. Phys.*, 53:1621–1674, 1990.

[51] M. Vos, , A.S. Kheifets, V.A. Sashin, E. Weigold, M. Usuda, and F. Aryasetiawan. *Phys. Rev. B*, 66:155414, 2002.

[52] M. Inokuti. *Rev. Mod. Phys.*, 13(3):297–347, 1971.

[53] R.D. Doherty, D.A. Hughes, F.J. Humphreys, J.J. Jonas, D. Juul Jensen, M.E. Kassner, W.E. King, T.R. McNelley, H.J. McQueen, and A.D. Rollett. *Materials Sci. and Engin. A*, 238:219–274, 1997.

[54] D. Turnbull and J.C. Fisher. *J. Chem. Phys.*, 17(1):71–73, 1949.

[55] J. Kessler. Springer series on atoms and plasma. Springer-Verlag, 2nd edition, 1985.

[56] E.L. Garwin, D.T. Pierce, and H.C. Siegmann. *helv. phys. acta*, 47:393, 1974.

[57] D.T. Pierce, F. Meier, and P. Zurcher. *app. phys. lett.*, 26(12):670–672, June 1975.

[58] G. Lampel and C. Weisbuch. *sol. stat. comm.*, 16:877–880, 1975.

[59] D.T. Pierce, F. Meier, and P. Zurcher. *phys. lett. A*, 51(8):465–466, may 1975.

[60] R. Calabrese, V. Guidi, G. Lamanna, and L. Tecchio. *J. Phys. III France*, 2:473–480, 1992.

[61] R. Calabrese et. al. *Rev. Sci. Instrum.*, 65(2):343–348, Feb. 1994.

[62] K. Togawa et. al. *Nucl. Instr. and Meth. in Phys. Res. A*, 414:431–445, 1998.

[63] K. Aulenbbacher et. al. *Nucl. Instr. and Meth. in Phys. Res. A*, 391:498–506, 1997.

[64] E. Mergl, E. Geisenhofer, and W. Nakel. *Rev. Sci. Instrum.*, 62(10):2318–2321, 1991.

[65] T. Nakanishi et. al. *Nuc. Instr. and Meth. in Phys. Res. A*, 455:109–112, 2000.

[66] T. Matsuyama, H. Takikita, H. Horinaka, K. Wada, T. Nakanishi, S. Okumi, T. Nishitani, T. Saka, and T. Kato. *Jap. J. applied phys.*, 43(6A):3371–3375, 2004.

[67] A. Janotti and S.H Wei. *applied phys. lett.*, 81(21):3957–3959, 18 nov. 2002.

[68] J.R. Chelikowsky and M.L. Cohen. *Phys. Rev. Lett.*, 32:674–677, 1974.

[69] J.J. Uebbing and L.W. James. *J. applied phys.*, 41(11):4505–4516, oct. 1970.

[70] L.W. James, G.A. Antypas, J. Edgecumbe, R.L. Moon, and R.L. Bell. *J. of Appl. Phys.*, 42(12):4976–4980, 1971.

[71] G. Leveque and M. Nouaoura. *Eur. Phys. J. AP*, 4(2):227–233, 1998.

[72] R.L. Bell. Monographs in electrical and electronic engineering. Oxford University Press, 1973.

[73] D.T. Pierce, R.J. Celotta, G.C. Wang, W.N. Unertl, A. Galejs, C.E. Kuyatt, and S.R. Mielczarek. *Rev. Sci. Instrum.*, 51(4):478–499, apr. 1980.

[74] H. Al-Khateeb, B.G. Birdsey, T.C. Bowen, A.S. Green, M.E. Johnston, and T.J. Gay. *Rev. Sci. Instrum.*, 70(10):3882–3885, oct 1999.

[75] J.X. Zhou, D.E. Golden, J.E. Furst, and D.W. Mueller. *Nuc. Instru. Meth. Phys. Res. B*, 56:1171–1172, 1991.

[76] D.T. Peirce and F. Meier. *Phys. Rev. B*, 13(12):4584–5499, June 1976.

[77] F.C. Tang, M.S. Lubell, K. Rubin, A. Vasilakis, M. Eminyan, and J. Slevin. *Rev. Sci. Instrum.*, 57(12):3004–3011, dec. 1986.

[78] M. Succi, R. Canino, and B. Ferrario. *Vacuum*, 35(12):579–582, 1985.

[79] C.K. Sinclair, E.L. Garwin, R.E. Kirby, and A. Roder. *Vacuum*, 31(10):553–556, 1981.

[80] C.J. Ruan. *Chin. Phys.*, 12(5):483–487, may 2003.

[81] D. Durek, F. Frommberger, T. Reichelt, and M. Westermann. *App. Surf. Sci.*, 143:319–322, 1999.

[82] G.D. Fletcher, T.J. Gay, and M.S. Lubell. *Phys. Rev. A*, 43:911–923, 1986.

[83] F. Salvat, A. Jablonski, and C. Powell. *Comp. Phys. Comm.*, 165:157–190, 2005.

[84] T. Nakanishi, K. Dohmae, S. Fukui, Y. Hayashi, I. Hirose, N. Horikawa, T. Ikoma, Y. Kamiya, M. Kurashina, and S. Okumi. *japanese journal of applied physics*, 25(5):766–767, may 1986.

[85] P.A. Hayes, D.H. Yu, and J.F. Williams. *Rev. Sci. Instrum.*, 68(4):1708–1713, apr. 1997.

[86] F. Machuca, Z. Liu, Y. Sun, P. Painetta, W.E. Spicer, and R.F.W Pease. *J. Vac. Sci. Technol. B*, 20(6):2721–2725, nov/dec 2002.

[87] K.A. Elamrawi and H.E. Elsayed-Ali. *J. Vac. Sci. Technol. A*, 17:823–831, 1999.

[88] R. Calabrese et. al. *Appl. Phys. Lett.*, 65(3):301–302, July 1994.

[89] A.S. Kheifets, D.R. Lun, and S.Yu Savrasov. *J. Phys. C.*, 11(35):6779–6792, 1999.

[90] J.P. Biersack and J.F. Ziegler. In *The stopping and ranges of ions in matter*, volume 1. Pergamon Press, Oxford, 1985.

[91] M.R. Went and M. Vos. *J. Elec. Spec. Rel. Phenom.*, 148:107–114, 2006.

[92] M.R. Went, M. Vos, and A.S. Kheifets. *submited to elsevier science*, 2006.

[93] S. Tougaard. *Solid State Commun.*, 61(9):547–549, 1987.

[94] S. Tougaard. *Phys. Rev. B*, 34(10):6779–6783, 1986.

[95] M. Vos, A.S. Kheifeits, and E. Weigold. In D.H. Madison and M. Schulz, editors, *Correlations, polarization and ionization in atomic systems*, pages 70–75. Melville, New York, 2002.

[96] P. Wahl. *PhD thesis*, 2005.

[97] N. Christensen and V. Heine. *Phys. Rev. B*, 32(10):6145–6156, 1985.

[98] P. Pykko. *Angew. Chem. Int. Ed.*, 43(34):4412–4456, 2004.

[99] G.E.W. Bauer and J.R. Schneider. *Phys. Rev. B*, 31(2):681–692, 1985.

[100] N.K. Hansen, P. Pattison, and J.R. Schneider. *Z. Phys. B*, 66:305–315, 1987.

[101] E.A. Mikajlo, K.L. Nixon, and M.J. Ford. *Phys. Rev. B*, 68:233205, 2003.

[102] H. Eckardt, L. Fritsche, and J. Noffke. *J. Phys. F:Met. Phys.*, 14:97–112, 1984.

[103] M.R. Norman. *Phys. Rev. B*, 29(6):2956–2962, 1984.

[104] Y. Petroff and P. Thiry. *Appl. Opt.*, 19(23):3957–3963, 1980.

[105] J.A. Knapp, F.J. Himpsel, and D.E. Eastman. *Phys. Rev. B*, 19:4952–4964, 1979.

[106] R. Courths, V. Bachelier, B. Cord, and S. Hufner. *Solid state commun.*, 40:1059–1063, 1981.

[107] P.S. Wehner, R.S. Williams, S.D. Kevan, D. Denley, and D.A. Shirley. *Phys. Rev. B*, 19:6164–6171, 1979.

[108] R. Courths, V. Bachelier, and S. Hufner. *Solid state commun.*, 38:887–889, 1981.

[109] K.A. Mills, R.F. Davis, S.D. Kevan, G. Thornton, and D.A. Shirley. *Phys. Rev. B*, 22(2):581–592, 1980.

[110] F. Aryasetiawan and O. Gunnarsson. *Rep. Prog. Phys.*, 61:237–312, 1998.

[111] Y. Kubo, Y. Sakurai, and N. Shiotani. *J. Phys.: Condens. Matter*, 11:1683–1695, 1999.

[112] P. Szczepanek and R. Glosser. *Solid State Commun.*, 15(8):1425–1429, 1974.

[113] H. Wern, R. Courths, G. Leschik, and S. Hufner. *Z. Phys. B - Condensed Matter*, 60:293–310, 1985.

[114] R.C. Jaklevic and J. Lambe. *Phys. Rev, B*, 12(10):4146–4160, 1975.

[115] Y. Kubo. *J. Phys. Chem. Solids*, 66:2202–2206, 2005.

[116] A. Yamasaki and T. Fujiwara. *J. Phys. Soc. Japan*, 72(3):607–610, 2003.

[117] J.C. Fuggle and N. Martensson. *J. Elec. Spec. Rel. Phen.*, 21:275–281, 1980.

[118] J.C. Fuggle and F.Alvarado. *Phys. Rev. A*, 22(4):1615–1624, 1980.

[119] F.P. Larkins. *Atomic data and nuclear data tables*, 20:311–387, 1977.

[120] J.C. Fuggle. In B. Crasemann, editor, *AIP Conf. Proc. 94: X-Ray and Atomic Inner-Shell Physics*, pages 661–675, 1982.

[121] C.S. Fadley and D.A. Shirley. *Phys. Rev. A*, 2(4):1109–1120, 1970.

[122] R. Courths, B. Cord, H. Wern, and S. Hufner. *Physica Scripta*, T4:144–147, 1983.

[123] E. Dietz and D.E. Eastman. *Phys. Rev. Lett.*, 41:1674–1677, 1978.

[124] A. Baalmann, H. Przybylski, M. Neumann, and G. Borstel. *Phys. Rev. B*, 27:6669–6675, 1983.

[125] H. Wern, G. Leschik, U. Hau, and R. Courths. *Solid State Commun.*, 50(7):581–586, 1984.

[126] P. Thiry, D. Chandasris, J.Le. Cante, C. Guillot, P. Pinchaux, and Y. Petroff. *Phys. Rev. Lett.*, 43:82–85, 1979.

[127] R. Courths, H. Wern, U. Hau, B. Cord, V. Bachelier, and S. Hufner. *J. Phys. F: Met. Phys.*, 140:1559–1572, 1984.

[128] W.H. Zachariasen. *J. Am. Chem. Soc.*, 54:3841–3851, 1932.

[129] K. Tanaka and R. Tsu. *Phys. Rev. B*, 24(4):2038–2050, 1981.

[130] E. Kim. *Phys. Rev. B*, 59(4):2713–2721, 1999.

[131] S.C. Moss and J.F. Gracyk. *Phys. Rev. Lett.*, 23:1167, 1969.

[132] J.M. Ziman. *J. Phys. C*, 4:3129–3142, 1971.

[133] A. S. Kheifets and Y. Q. Cai. *J. Phys. C*, 7(9):1821–1833, 1995.

[134] S.K. Bose, K. Winer, and O.K. Andersen. *Phys. Rev. B*, 37(11):6262–6277, 1988.

[135] B.J. Hickey and G.J. Morgan. *J. Phys. C*, 19:6195–6209, 1986.

[136] F. Wooten, K. Winer, and D. Weaire. *Phys. Rev. Lett.*, 54(13):1392–1395, 1985.

[137] S. Kugler, K. Kohary, K. Kadas, and L. Pusztai. *Solid State Commun.*, 127:305–309, 2003.

[138] G. Allan, C. Delerue, and M. Lannoo. *Phys. Rev. B*, 57(12):6933–6936, 1998.

[139] I. Equivias, J. Sanz-Maudes, J. Sangrador, and T. Rodriguez. *J. Vac. Sci. Technol. A*, 3(4):1791–1796, 1985.

[140] R.F. Scholz, P. Werner, U. Gosele, and T.Y. Tan. *Appl. Phys. Lett.*, 74(3):392–394, 1999.

[141] F. Watanabe, K. Ohmura, S. Kawai, and T. Motooka. *J. Cryst. Growth*, 222:1–8, 2001.

[142] A. Yamada, N. Miyazono, and M. Konagai. *Jpn. J. Appl. Phys.*, 38(1):2566–2568, 1999.

[143] M. Vos, Bowles. C., A.S. Kheifets, V.A. Sashin, E. Weigold, and F. Aryasetiawan. *J. Elec. Spec. Rel. Phen.*, 137:629–632, 2004.

[144] J.R. Parsons and R.W. Balluffi. *J. Phys. Chem. Solids*, 25:263–272, 1964.

[145] I. Suzumura, M. Okada, A. Muto, Y. Torige, H. Ikeda, A. Sakai, S. Zaima, and Y. Yasuda. *Thin Solid Films*, 369:116–120, 2000.

[146] M. Vos and M. Bottema. *Phys. Rev. B*, 54(8):5946–5954, 1996.

[147] K. Zeppenfeld and H. Raether. *Z. Physik*, 193:471–478, 1966.

[148] B.R. Coles. *I. Inst. Metals*, 84(9):346–348, 1956.

[149] N.J. Shevchik and C.M. Penchina. *Phys. Stat. Sol. B*, 70:619–623, 1975.

[150] C.B. Sommers, H.W. Myron, and F.M. Mueller. *Solid State Commun.*, 36:411–414, 1980.

[151] A. Andrejczuk L. Dobrzynski J. Kwiatkowska F. Maniawski A. Bansil, S. Kaprzyk and E. Zukowski. *Phys. Rev. B*, 57(1):314–323, 1998.

[152] S. Kaprzyk P.E. Mijnarends A. Bansil, B. Barbiellini. *J. Phys. Chem. of Solids*, 61:2191–2197, 2001.

[153] L. Vriens. *Phys. Rev. B*, 4(9):3088–3093, 1971.

[154] A.M. Begley, D. Tian, F. Jona, and P.M. Marcus. *Surf. Sci.*, 280(3):289–297, 1993.

[155] P. Jonas and P. Schattschneider. *Microsc. Microanal. Microstruct.*, 4:63–85, 1993.

[156] J. Kirschner, D. Rebenstorff, and H. Ibach. *Phys. Rev. Lett.*, 53(7):698–701, 1984.

[157] Y.U. Idzerda, D.M. Lind, D.A. Papaconstantopoulos, G.A. Prinz, B.T. Jonker, and J.J. Krebs. *Phys. Rev. Lett*, 61(10):1222–1226, 1988.

[158] H. Hopster, R. Raue, and R. Clauberg. *Phys. Rev. Lett.*, 53(7):695–697, 1984.

[159] J. Kirschner. *Phys. Rev. Lett*, 55(9):973–976, 1985.

[160] K.-P. Kamper, D.L. Abraham, and H. Hopster. *Phys. Rev. B*, 45(24):335–346, 1992.

[161] R. Saniz and S.P. Apell. *Phys. Rev, B*, 63:014409, 2000.

[162] D. Venus and J. Kirschner. *Phys. Rev. B*, 37(4):2199–2211, 1988.

[163] D.L. Abraham and H. Hopster. *Phys. Rev. Lett.*, 62(10):1157–1160, 1989.

[164] H. Hopster and D.L. Abraham. *Phys. Rev. B*, 40(10):7054–7058, 1989.

[165] T.G. Walker and H. Hopster. *Phys. Rev. B*, 48(5):3563–3566, 1993.

[166] T. Komesu, G.D. Waddill, and J.G. Tobin. *J. Phys.: Condens. Matter*, 18:8829–8836, 2006.

[167] J. Callaway and C.S. Wang. *Phys. Rev. B*, 16(5):2095–2195, 1977.

[168] E. Kisker, K. Schroder, W. Gudat, and M. Campagna. *Phys. Rev. B*, 31(1):329–339, 1985.

[169] M. Vos, C. Bowles, A.S. Kheifets, and A.S. Went. *J. Elec. Spec. Rel. Phenom.*, 149:20–28, 2005.

[170] B.G. Williams, G.M. Parkinson, C.J. Eckhardt, and J.M. Thomas. *Chem. Phys. Lett.*, 78(3):434–438, 1981.

[171] P. Schattschneider and A. Exner. *Ultramicroscopy*, 59:241–253, 1995.

[172] P. Schattscneider, P. Jonas, and M. Mandl. *Microsc. Microanal. Microstruct.*, 2:367–375, 1991.

[173] J.E. McCarthy, M.J. Cooper, V. Honikimaki, T. Tschentscher, P. Suoritti, S. Gardelis, K. Hamalainen, S.O. Manninen, and D.N. Timms. *Nucl. Instr. and Meth. in Phys. Res. A*, 401:463–475, 1997.

[174] M.J. Cooper and J.A. Duffy. *J. Phys. Chem. Solids*, 61:345–352, 2000.

[175] S. Tanuma, C.J. Powell, and D.R. Penn. *Surface and Interface Analysis*, 20(1):77–89, 1993.

[176] L. Lam and P.M. Platzman. *Phys. Rev. B*, 9(12):5122–5127, 1974.

[177] Y. Tanaka, N. Sakai, Y. Kubo, and H. Kawata. *Phys. Rev. Lett.*, 70(10):1537–1540, 1993.

[178] S.P. Collins, M.J. Cooper, D. Timms, A. Brahmia, D. Laundy, and P.P. Kane. *J. Phys.: Condens. Matter*, 1:9009–9020, 1989.

[179] Y. Kubo and S. Asano. *Phys. Rev. B*, 42(7):4431–4446, 1990.

[180] M. Tokii and M. Matsumoto. *J. Phys.: Condens. Matter*, 18:3639–3646, 2006.

[181] Y. Mamev. *Nucl. Instr. Meth. Phys. Res. A*, 536:289–294, 2005.

[182] A.N Ambrajei, J.E. Clendenin, A. Yu. Egorov, Yu.A. Mamev, T. Marayama, G.A. Mulhollan, A.V. Subashiev adn Yu. P. Yashin, V.M. Ustinov, and A.E. Zhukov. *Appl. Surf. Sci.*, 166:40–44, 2000.